Measurement of the Brout-Englert-Higgs boson couplings in its diphoton decay channel with the ATLAS detector at the LHC

Estelle Scifo

Université Paris-Sud

École doctorale : Particules Noyaux Cosmos
Laboratoire de l'Accélérateur Linéaire

Discipline : Physique des particules

Thèse de doctorat

Soutenue le 11 juillet 2014 par

Estelle Scifo

Measurement of the Brout-Englert-Higgs boson couplings in its diphoton decay channel with the ATLAS detector at the LHC

M. Marc Escalier	(Co-directeur de thèse)
M. Louis Fayard	(Directeur de thèse)
M. Massimiliano Grazzini	(Examinateur)
Mme. Chiara Mariotti	(Rapporteur)
M. Aleandro Nisati	(Rapporteur)
M. Achille Stocchi	(Président du jury)
M. Guillaume Unal	(Examinateur)

Parce qu'ils ont aiguisé ma curiosité,
M'ont transmis persévérance et envie d'apprendre,
En donnant sans compter et sans jamais reprendre,
Je dédie ma thèse à mes parents adorés.

Parce qu'ils sont toujours là pour me conseiller,
Font l'incommensurable effort de me comprendre,
M'orientent jour après jour sans condescendre,
A ce travail mes amis ont contribué.

Pour m'avoir fait découvrir la beauté des sciences,
Aider à épancher ma soif de connaissances,
Mes professeurs ont eux aussi leur place ici.

Enfin, à tous ceux qui partagent leurs sourires,
Embellissant mes journées, je tiens à offrir,
Le mot de la fin par le plus grand des mercis.

Abstract

After the Higgs boson discovery in the first LHC data, the focus is now on its properties measurement. Among these properties, its couplings are of particular importance since any deviation from the expected value can be an indication of new physics, beyond the Standard Model.

This thesis is oriented towards the Higgs couplings measurements with the ATLAS experiment, using the diphoton decay channel. Selected diphoton events are classified into different categories to disentangle the five Higgs production modes by tagging the objects produced in association with the Higgs boson: two jets for the VBF production mode, lepton and missing transverse energy for the higgsstrahlung (WH and ZH), b-jets for ttH, the remaining events being mostly produced via the dominant production mode ggH.

The impact of the Higgs p_T modelling in the ggH production mode is also investigated. Theoretical developments provide predictions of the p_T shape at NNLO+NNLL accuracy, including top and bottom mass effects in the loop up to NLO+NLL, implemented in the `HRes` program. A reweighting technique to take into account these latest theoretical improvements is derived, taking into consideration the correlation with the number of jets. Its impact on the final measurement is estimated to be of the order of a few percent.

The final couplings results based on 4.5 fb^{-1} at 7 TeV and 20.3 fb^{-1} at 8 TeV do not show any significant deviations from the Standard Model. The couplings, measured at Higgs mass measured by the combination of the $H \to \gamma\gamma$ and $H \to ZZ^* \to 4l$ channels in ATLAS ($m_H = 125.4 \pm 0.4$ GeV) do not show any statistically significant deviation from the Standard Model: The observed signal strength $\mu = \frac{\sigma^{obs}}{\sigma^{exp}}$ is found to be:

$$\mu = 1.17^{+0.27}_{-0.27} = 1.15^{+0.23}_{-0.23} \text{ (stat.)} \, ^{+0.10}_{-0.08} \text{ (syst.)} \, ^{+0.12}_{-0.08} \text{ (theory)}$$

The ratio of the observed number of events in each production mode to the expected ones are measured at:

$$\mu_{ggH} = 1.32 \pm 0.32 \text{ (stat.)} \, ^{+0.13}_{-0.09} \text{ (syst.)} \, ^{+0.19}_{-0.11} \text{ (theory)}$$
$$\mu_{VBF} = 0.8 \pm 0.7 \text{ (stat.)} \, ^{+0.2}_{-0.1} \text{ (syst.)} \, ^{+0.2}_{-0.3} \text{ (theory)}$$
$$\mu_{WH} = 1.0 \pm 1.5 \text{ (stat.)} \, ^{+0.3}_{-0.1} \text{ (syst.)} \, ^{+0.2}_{-0.1} \text{ (theory)}$$
$$\mu_{ZH} = 0.1 \, ^{+3.6}_{-0.1} \text{ (stat.)} \, ^{+0.7}_{-0.0} \text{ (syst.)} \, ^{+0.1}_{-0.0} \text{ (theory)}$$
$$\mu_{ttH} = 1.6 \, ^{+2.6}_{-1.8} \text{ (stat.)} \, ^{+0.6}_{-0.4} \text{ (syst.)} \, ^{+0.5}_{-0.2} \text{ (theory)}$$

Keywords: Standard Model, Higgs, LHC, ATLAS, couplings, photon

RÉSUMÉ

Après la découverte du boson de Higgs par les expériences ATLAS et CMS au LHC, annoncée le 4 juillet 2012 au CERN, l'heure est maintenant à la mesure des propriétés de cette nouvelle particule pour vérifier sa compatibilité avec le boson scalaire prédit par le Modèle Standard. Son couplage aux autres particules est une mesure importante car toute déviation par rapport à la valeur prédite par la théorie peut être le signe d'une nouvelle physique, au delà du Modèle Standard.

Cette thèse présente la mesure des couplages du boson de Higgs dans son mode de désintégration en deux photons, utilisant l'ensemble des données collectées en 2011 (4.5 fb^{-1} à 7 TeV) et 2012 (20.3 fb^{-1} à 8 TeV) par le détecteur ATLAS. Les événements sont classifiés en fonction des objects produits en association avec le Higgs : deux jets pour la production VBF, lepton et énergie transverse manquante pour le higgsstrahlung (WH et ZH) et jets de b pour le ttH, les événements restants étant produits majoritairement par le mode de production dominant ggH.

L'impact de la modélisation du moment transverse du Higgs, dans son mode de production par fusion de gluons, est aussi estimé. Les derniers développements théoriques dans ce domaine permettent d'atteindre une précision à l'ordre NNLO+NNLL, avec la prise en compte de l'effet des masses finies des quarks top et bottom dans la boucle jusqu'à l'ordre NLO+NLL, implémentée dans le programme HRes. Une méthode de pondération est dérivée pour prendre en compte ces dernières avancées, en prenant en compte la corrélation avec le nombre de jets.

Les résultats finaux sont en bon accord avec les prédictions du Modèle Standard, en prenant en compte les barres d'erreur. À la masse mesurée par la combinaison des canaux diphoton et quatre leptons dans ATLAS, $m_H = 125.4 \pm 0.4$ GeV, la section efficace totale ramenée à celle attendue par le Modèle Standard est :

$$\mu = 1.17^{+0.27}_{-0.27} = 1.15^{+0.23}_{-0.23} \text{ (stat.) } ^{+0.10}_{-0.08} \text{ (syst.) } ^{+0.12}_{-0.08} \text{ (theory)}$$

et le rapport du nombre d'événements mesurés pour chaque mode de production à celui prédit par le Modèle Standard est :

$$\mu_{ggH} = 1.32 \pm 0.32 \text{ (stat.) } ^{+0.13}_{-0.09} \text{ (syst.) } ^{+0.19}_{-0.11} \text{ (theory)}$$
$$\mu_{VBF} = 0.8 \pm 0.7 \text{ (stat.) } ^{+0.2}_{-0.1} \text{ (syst.) } ^{+0.2}_{-0.3} \text{ (theory)}$$
$$\mu_{WH} = 1.0 \pm 1.5 \text{ (stat.) } ^{+0.3}_{-0.1} \text{ (syst.) } ^{+0.2}_{-0.1} \text{ (theory)}$$
$$\mu_{ZH} = 0.1 ^{+3.6}_{-0.1} \text{ (stat.) } ^{+0.7}_{-0.0} \text{ (syst.) } ^{+0.1}_{-0.0} \text{ (theory)}$$
$$\mu_{ttH} = 1.6 ^{+2.6}_{-1.8} \text{ (stat.) } ^{+0.6}_{-0.4} \text{ (syst.) } ^{+0.5}_{-0.2} \text{ (theory)}$$

Mots clés : Modèle Standard, Higgs, LHC, ATLAS, couplages, photon

CONTENTS

Introduction

<blockquote>
“ Il mondo è un bel libro,
ma poco serve a chi non lo sa leggere. ”

<div align="right">CARLO GOLDONI</div>
</blockquote>

The Brout-Englert-Higgs boson (or Higgs boson) quest was one of the most exciting one during the last 50 years. Its mass is not predicted by the theory and the recent searches cover a large mass range, from about 100 GeV to several hundreds of GeV. The LEP and Tevatron experiments were able to set limits on the allowed mass range and showed that the low mass region ($114 \lesssim m_H \lesssim 150$ GeV) is favoured. The LHC collider, in the LEP tunnel at CERN, and the experiments scrutinizing the collision products were designed to maximize the sensitivity to a potential Higgs signal.

Thanks to the great LHC and detectors performances, a new particle, compatible with the Standard Model Higgs boson, was discovered at a mass $m_H \approx 125$ GeV and announced in a joint meeting with the ATLAS and CMS experiment on July 4$^{\text{th}}$, 2012. This is a major achievement of the Standard Model but this is not the end of the LHC adventure. First, the new particles properties, spin and parity, have been measured to confirm its scalar nature. Its mass is also measured, and used as an input to confront its measured couplings to the other Standard Model particles to the theory.

The diphoton decay mode, together with the $H \to ZZ^* \to 4l$, was one of the leading channels for the Higgs discovery, achieving a 5σ significance by itself with the full 2011 and 2012 dataset recorded by ATLAS. Due to the large number of observed signal events, it is also primordial for most of the Higgs properties measurements.

Among the Higgs properties that need to be measured, its couplings are of great importance since any deviation from the Standard Model expectations can be a sign for physics beyond the Standard Model. The work presented in this thesis is devoted to the measurement of the Higgs couplings, through the $\gamma\gamma$ channel. This is achieved thanks to the isolation of each production mode in the observed events, tagging the objects produced in association with the Higgs boson in the VBF, VH and ttH production modes.

This document is organized as follows. *My personal contribution are described in italic.*

In a first chapter, the Standard Model and the Brout-Englert-Higgs mechanism giving mass to the gauge bosons are outlined. Expected Higgs boson production cross-sections at the LHC and decays are also summarized. The statistical tools, essential to interpret the analysis of the probabilistic collisions taking place at the LHC, are outlined in Chapter 2.

The second part describes the experimental set-up. Chapter 3 recalls the LHC functioning and data-taking conditions in 2011 and 2012. Chapter 4 presents the design of the ATLAS detector dictated by its physics programme. The objects reconstruction principles and efficiencies during the LHC first run are also described. A dedicated chapter, Chapter 5, details the status of the ATLAS electromagnetic calorimeter, from the data acquisition and quality to the final photon calibration. The pointing technique, derived to reconstruct the unconverted photons direction using the electromagnetic calorimeter longitudinal segmentation is also discussed. *The last part of this chapter describes the study I have made*

about strange oscillations observed in the pointing technique. I have tested several scenarios to understand their origin and derived a correction of this effect.

The core of the analysis is described in the third part, starting from the photon performances in ATLAS, applied to the $H \rightarrow \gamma\gamma$ search channel in Chapter 6. The different cuts performed to reduce the jet faking photon contamination are presented, followed by a background decomposition from data driven methods. After a description of the statistical model and systematics uncertainties, the results of the searches for the Higgs and first measurements are summarized and compared with other decay channels and experiment. *Before the discovery, I re-investigated the kinematics cuts on the photons, needed to be re-evaluated due to trigger constraints. I then moved to the background understanding with Drell-Yan studies and developed a semi-data driven method to estimate this background in each of the categories. I also give an interpretation of the spurious signal term, technique used to choose the best background parametrization.* Chapter 7 shows the couplings analysis in the diphoton channel, detailing the events categorization and the results of the analysis of the full 2011+2012 dataset representing 4.5 fb^{-1} at $\sqrt{s} = 7$ TeV and 20.3 fb^{-1} at $\sqrt{s} = 8$ TeV. *I was particularly interested into the categories involving leptons, first studying the one-lepton category background, leading to the inclusion of a new cut on the electron-photon invariant mass. I then moved to dilepton category trying to isolate the ZH production mode with the leptonic decay of the Z boson. Here, I have performed the analysis from the cut definition to the background estimation. The statistical treatment also had to be done carefully due to the very low number of expected and observed events in this category. This is handled technically thanks to the introduction of ghost events. Finally, I participated to the global fit of all categories to get the final result on the global and individual signal strengths from this analysis, obtaining results in good agreement with the published ones. I also participated to the numerous tests that were performed on the results. I provided informations about the dependence of the signal strength with the Higgs mass, the compatibility between the mass measured in 2011 and 2012 datasets, and the pull of the nuisance parameters.* This analysis does not show any statistically significant deviations from the Standard Model expectations.

The fourth part is about the Higgs transverse momentum description at the simulation stage. The tools to compute expected inclusive and differential cross-sections are outlined in Chapter 8 in the context of the Higgs p_T modelling in the gluon fusion production mode. Chapter 9 describes the impact of the Higgs p_T modelling on the $H \rightarrow \gamma\gamma$ analysis, and explain the reweighting technique used in the analysis to take into account the last theoretical development in the area (NLO+NLL accuracy in the exact theory considering finite top and bottom mass in the loop and NNLO+NNLL in the effective theory). The related uncertainties are also discussed. *After re-initiating the discussion with theorists, I followed the theoretical improvements implemented in the successive `HRes` versions and tested their impact on the $H \rightarrow \gamma\gamma$ analysis by using a reweighting technique.*

Part I

Theory overview

STANDARD MODEL
OF PARTICLE PHYSICS

❝ Nous voyons la force se matérialiser, l'atome s'idéaliser, ces deux termes converger vers une limite commune, l'univers retrouver ainsi sa continuité. ❞

HENRI BERGSON

Chapter content

Physics is a scientific discipline that tries to understand how natural phenomena can happen, formulating rules and models. Particle physics is the field that concentrates on the question of the composition of matter and the interactions between its constituents at the smallest reachable scale.

This question has been a motivation for scientists for a long time and the representation of matter has evolved a lot since early indication of such thoughts, tracked back to Antiquity. The guiding line for scientists to understand what is the structure of matter and how its constituents interact has always been simplicity, with a lot of successes: the atom was reduced to only electron, proton and neutron. Then the last two, with a lot of other particles, were explained in terms of smaller particles named quarks. On the interactions side, electricity and magnetism were combined to form electromagnetism, before electromagnetism and weak interaction unification in the electroweak framework.

The Standard Model of particle physics provides a mathematical formulation to this particle and interaction content. When completed by the Brout-Englert-Higgs mechanism to explain particle masses, the Standard Model is our current best global understanding of matter behaviour.

1.1 SM constituents

1.1.1 Quick historical overview

What is the matter made of? Finding an answer to this apparently simple question is not that easy and a lot of people have been involved since the first Greek philosophers and scientists up to nowadays to build a coherent model consistent with the observations.

The ancient Greek philosophers were the first to make hypotheses about the matter composition that came to us through the centuries. They already made the assumption that day to day matter was made of other constituents, that differs depending on the material considered. At that epoch, and for about 20 centuries, the dominant theory was that matter is made of four elements – earth, fire, water and wind – each of them being present in different, continuous, proportion in the various known materials. Another doctrine also emerged during Antiquity, especially in the 5th century B.C. with Leucippus and Democritus, according to which matter is made of small and indivisible building blocks, called atoms, but the atomistic theory took time to be fully established and adopted by the scientific community.

Progresses in this domain highly benefited from progresses in other fields. For example, chemistry was a source of inspiration thanks to the classification concepts developed stating from the 19th century. Optics and other technical fields bring the necessary knowledge to build experiments, essential to establish the theories that were proposed along the years. Making the microscopic world visible to our human eyes with lenses is a key moment in the history of science.

A new era of experimental innovation in the search for the matter composition started at the end of the 18th century. Several discoveries were made almost simultaneously changing drastically our vision of matter. First, the electron appeared to Thomson in 1897 as a electric arc in vacuum. In the same year, other type of radiations were discovered, ending with the famous discovery of radioactivity by Becquerel in 1896 followed by the work of Pierre and Marie Curie. In the meantime, models have emerged to explain those observations based on the atomistic theory. Thanks to the Geiger and Marsden experiment in 1909 and the following explanation by Rutherford, the atom model as we know it today was almost finalized: a neutral structure with a central positively charged nucleus and negative electrons orbiting around it.

At the beginning of the 20th century, quantum mechanics appeared with its surprising novelties. Particles are no more considered as point-like with well defined position and momentum, but are associated to waves functions interpreted as a probability of presence at a given position. The so-called particle-wave duality is illustrated by the Young experiment in 1801 for photons and light. In this conception, the atomic model changes in the sense that electrons do not really turn around the nucleus on stable trajectories but are distributed with probabilities forming a cloud around the nucleus

with fuzzy contours.

In the 1930's, the number of particles starts to grow quickly because of new observations. Indeed, thanks to new experimental techniques to detect microscopic particles coming from cosmic rays interacting with the Earth's atmosphere, new kind of particles were observed (among which pions π and kaons K). A new model was needed to understand the role of these new particles, that seem not to be necessary for the ordinary matter to exist. This was done with the quark model, stating that the proton, neutron and lot of newly discovered particles were not elementary in the sense that they can be divided into smaller pieces, called quarks. At that time, the observed particles only allowed to predict the existence of three quarks called up, down and strange; it is now known that three other flavours are needed in the Standard Model: charm, bottom and top quarks, all of them have been observed.

The quarks and the electrons are, as far as we know today, elementary. They have the common property to have spin $\frac{1}{2}$ and obey the Fermi-Dirac statistics, hence called fermions.

To fully understand matter behaviour, knowing the nature and properties of the interactions between its constituent is fundamental. In particle physics, interaction between two matter particles is seen as the exchange of mediator particles, with integer spin and commonly called bosons.

Today, a limited number of particles are sufficient to describe the matter at the subatomic scale: fermions are matter constituents and bosons, the force carriers, depicted in the next sections.

1.1.2 Fermions

Matter particles are classified into two categories: the leptons, particles sharing some properties with the electrons, and the quarks. Particles are also categorized into three families, each family containing two leptons and two quarks, with increasing masses.

The first family is made of everyday matter constituents, *i.e.* the electron, the up and down quarks and the electronic neutrino. Neutrinos are massless particles (in the Standard Model), introduced to ensure energy conservation in nuclear reactions and whose existence was demonstrated by experiments during the last century. This matter content is completed by four other quark flavours, associated with new leptons. Particles in the second (third) family have the same properties than their counterparts in the first (second) family, except for their mass which is found to be larger, sometimes by several order of magnitude.

The second family contains the muons, similar to the electron with higher mass. It also contains the muonic neutrino and two quarks, called charm and strange quarks. Finally the third family is made of the tau, its associated neutrino, and two heavy quarks: the top and bottom. This is summarized in the table 1.1 where the mass of each particle is also specified.

Antimatter: in reality, one needs to add one antiparticle per elementary particle in the table 1.1. These antiparticles have properties similar to their associated particle, except for some of their quantum numbers, such as the electric charge, that have opposite sign.

Thus, the Standard Model relies on 24 elementary elementary particles for the matter content.

		1st family	2nd family	3rd family
Leptons		Electronic neutrino ν_e ($\approx 10^{-6}$)	Muonic neutrino ν_μ ($\approx 10^{-6}$)	Tauic neutrino ν_τ ($\approx 10^{-6}$)
		Electron e^- (0.511)	Muon μ^- (105.7)	Tau τ^- (1,776)
Quarks		up u ($2.3^{+0.7}_{-0.5}$)	charm c ($1,275 \pm 25$)	top t ($173,500 \pm 0,890$)
		down d ($4.8^{+0.7}_{-0.3}$)	strange s (95 ± 5)	bottom b ($4,180 \pm 30$)

Table 1.1: *Elementary fermions of the Standard Model. In parenthesis, their mass in MeV [1].*

1.1.3 Bosons

Four interactions are needed to explain all the observed phenomena of the subatomic world so far (see Table 1.2):

- Electromagnetic interaction is mediated by photons and acts only between charged particles, meaning that neutral particles such as the neutrinos are not sensitive to this interaction. It is a long range interaction that makes it noticeable at the human scale.

- Strong interaction range is of the order of the nucleus radius (10^{-15} m). It is the most powerful interaction among the four fundamental interactions. Strong interaction explains why two protons, both positively charged, can be bounded in nuclei. The mediators for strong interaction are the eight gluons. In the same way that for electromagnetism, each particle has a strong charge, called colour, and only those who have non-zero strong charge are sensitive to the strong interaction. In practice, this includes only the quarks and gluons themselves.

- Weak interaction, last one included in the Standard Model, is needed to explain why some nuclei are not stable and decay via radioactivity. Its is mediated by three gauge bosons: the neutral Z and two charged $W^\pm$. All particles are sensitive to weak interaction, although the processes dominated by weak interaction are rare because of the small intensity of this interaction at low energy.

- The last interaction that has been identified is gravity. Similarly to the attraction between planets, each particle is attracted by its neighbour, with an intensity proportional to the mass of the protagonists. Unfortunately, all attempts to include this interaction in the Standard Model and describe it with the same mathematical framework have failed. However, at the subatomic level, this interaction has a negligible intensity compared to the other forces – its relative intensity with respect to the strong force is only 10^{-40}. That's why, for the processes we are interested in during this thesis, it can be safely neglected.

Interaction	Electromagnetic	Strong	Weak
Boson	Photon γ	Gluons g	$W^\pm, Z^0$
Mass $[MeV]$	(0)	(0)	($80\text{-}90 \times 10^3$)
Intensity wrt strong	10^{-2}	1	10^{-13}
Range	∞	$\approx 10^{-15}$	$\approx 10^{-15}$

Table 1.2: *Interactions and force carriers of the Standard Model. Relative intensity with respect to the strong interaction is given at low energy.*

This closes the qualitative description of the Standard Model. But the Standard Model can not be reduced to a table. It relies on precise mathematical concepts such as symmetries and their application to quantum field theory, that the following sections attempt to present briefly.

The mathematical foundations of the Standard Model were formulated by Glashow [2], Salam and Ward [3] and finally Weinberg [4] in the 60's to explain the behaviour of matter in the quantum field theory framework, and in 1964, Brout-Englert [5] and Higgs [6–8] exposed their idea to give a mass to the gauge bosons, operation that was not yet possible in the Standard Model framework. Historical reviews can be found in [9, 10].

1.2 From classical physics to gauge invariance

1.2.1 Lagrangian and least action principle

Classical systems and subatomic particles dynamics are based on the same hypothesis: the least action principle. The action $\mathcal{S}$ is a well-defined quantity. For a classical system composed of N particles i, it can be defined as in as a functional[1] of the quantity L (Equation 1.1), where the q_i denotes the ith particle coordinates and $\dot{q}_i$ is the time derivative of q_i: $\dot{q}_i \equiv \frac{dq_i}{dt}$.

$$S = \int L(q_i(t), \dot{q}_i(t), t)dt \tag{1.1}$$

L is the system Lagrangian, that is expressed in classical physics as the difference between kinetic and potential energy. For a particle of mass m in the external potential V it is expressed by:

$$L = T - V$$
$$= \frac{1}{2}m\dot{\vec{q}}^{\,2} - V(\vec{q})$$

Least action principle states that among all possible paths, the system will choose the one that minimize the variation of the action. For a system with initial state A (*i.e.* $A = \{t^A, q_i^A\}$) and final state B, the path from A to B should satisfy:

$$\delta S = \delta \int_A^B Ldt = 0 \tag{1.2}$$

which leads to the Euler-Lagrange equations of motion for each particle i:

$$\frac{\partial L}{\partial q_i} - \frac{d}{dt}\frac{\partial L}{\partial \dot{q}_i} = 0 \tag{1.3}$$

This classical interpretation of the Lagrangian can be extended to particle physics, where particles can no more be described by their position q and velocity $\dot{q}$.

As it has been noticed at the beginning of the 20th century, classical mechanics is not successful in describing subatomic particles. It has to be replaced by quantum mechanics, which is a non intuitive theory based on probabilities, but very successful in describing the phenomena observed at small scales.

Among the particularities of quantum mechanics, one is particularly interesting for predicting their motion: the impossibility to determine precisely the position and kinematics of a particle at the same time. This means that the Lagrangian formalism developed in the previous paragraph will not be applicable. Hopefully, this formalism can be extended to quantum mechanics, where particles are described by fields ϕ.

Another subtlety is related to the relativistic nature of the particles in high energy physics. A theory relying on quantum mechanics and special relativity is then necessary. Such a mathematical framework exists in the Quantum Field Theory where particles are described by fields defined in all points of the four-dimension space-time of special relativity. An interpretation of this field formalism

---

[1] Meaning that the action is a function of the Lagrangian at all time and position, not only one point.

tells us that the field amplitude represents the probability for a particle to be present in a given point of space and time.

In this framework, the Lagrangian L is replaced by a Lagrangian density $\mathscr{L}$ such that $L = \int \mathscr{L} d^3 x$. For simplification, in the rest of this document, $\mathscr{L}$ will be called Lagrangian. The covariant notations will also be used, *i.e.* the coordinate index in the four-dimension space are labelled with a Greek letter (usually μ or ν) and the derivative with respect to the μth coordinate is written $\frac{\partial}{\partial x_\mu} \equiv \partial_\mu$. With these notations, the Lagrangian becomes:

$$L(q_i(t), \dot{q}_i(t), t) \rightarrow \mathscr{L}(\phi, \partial_\mu \phi, x_\mu)$$

From the observation that the action becomes $S = \int \mathscr{L} d^4 x$ (where the three spatial coordinates and the time coordinate are treated on the same scale) one deduces that the Lagrangian $\mathscr{L}$ is of dimension[2] $[E^4]$ and has to be Lorentz invariant to ensure Lorentz invariance of the action that governs the physics of the system.

The same reasoning as for the classical case leads to the equivalent of the Euler-Lagrange equations governing the system dynamics:

$$\frac{\partial \mathscr{L}}{\partial \phi} - \partial_\mu \frac{\partial \mathscr{L}}{\partial(\partial_\mu \phi)} = 0 \tag{1.4}$$

Dirac Lagrangian: A free fermion ψ is fully described by the Dirac Lagrangian of Equation 1.5 resulting in the dynamic rule of Equation 1.6. A fermion field is described by a four-dimension field ψ. The γ are four-dimension Dirac matrices that can be expressed in term of the three 2-by-2 Pauli matrices σ:

$$\gamma^0 = \begin{pmatrix} \mathbb{1} & \mathbb{0} \\ \mathbb{0} & \mathbb{1} \end{pmatrix}, \gamma^k = \begin{pmatrix} \mathbb{0} & \sigma^k \\ -\sigma^k & \mathbb{0} \end{pmatrix}$$

$$\mathscr{L}_\psi = \bar{\psi}(i\,\not{\partial} - m)\psi \tag{1.5}$$

where,

- $\bar{\psi} = \psi^\dagger \gamma^0$ with $\psi^\dagger$, the Dirac adjoint of ψ

- $\not{\partial} = \gamma^\mu \partial_\mu$

$$(i\gamma_\mu \partial^\mu + m)\psi = 0 \tag{1.6}$$

1.2.2 Symmetries & groups

Before going further into the details of particle physics, it is important to introduce the notion of symmetries that govern the building of the theory.

Symmetries play an important role in many fields of physics: they can be used to simplify a problem like in the Gauss theorem of electromagnetism or predict the existence of new particles with the quark model. More profound implications of symmetries are formulated by the Noether's theorem, according to which a conserved quantity can be associated to each continuous symmetry of a system. In particle physics, it will be shown that imposing a system to be invariant under a precise symmetry is sufficient to make the force carriers appear in the mathematical formulation.

A symmetry is an operation that does not change a system. It can be geometric, like rotation in space, or internal referring to internal degree of freedom of the considered system such as spin. All possible transformations of one kind are gathered into a mathematical object $(\mathcal{G}, \cdot)$ called group if satisfying some mathematical criteria such as closure, meaning that if g_i and g_j are two elements of

---

[2]In natural units where $c = \hbar = 1$, meaning that $[Length] = [Time] = \frac{1}{[Energy]} = \frac{1}{[Mass]} = \frac{1}{[Temperature]}$.

the group, the product $g_i \cdot g_j$ should also belong to the same group. Moreover, if the system ends up in the same state after the application of two successive transformations, whatever order is used, *i.e.* $g_i \cdot g_j = g_j \cdot g_i$, then the group is said to be commutative or abelian, otherwise it is a non-abelian group.

Each group can be represented by matrices. A finite number of them, called generators, is needed to totally define the group.

Two kinds of groups are useful for the following discussion: groups dealing with continuous symmetries such as rotations $\mathcal{R}$, and groups of discrete symmetries such as parity $\mathcal{P}$. The first one are described by Lie groups. The matrices defining a Lie group can be written $U = e^{\alpha^a T_a}$ where α^a are continuous parameters and T_a are the symmetry group matrix generators. It turned out that defining how these generators commute is enough to fully define the group algebra, usually written as $[T^a, T^b] = f^{abc} T_c$ where f^{abc} are the structure constants.

Among the Lie groups, two are mostly used in particle physics: $U(n)$ is the unitarity group containing all $n \times n$ complex matrices with $det|U| = \pm 1$ and $SU(n)$ having the additional requirement that the determinant is positive.

1.2.2.1 Noether's theorem

A crucial aspect of symmetries was discovered by the mathematician E. Noether in 1918: each continuous invariance of a system is associated to a non-observable quantity and a conserved one [11]. For example, with a system invariant under rotations, one cannot define absolute angle. With the Lagrangian formalism, it is straightforward to show that the angular momentum is conserved with respect to time in this case. Table 1.3 shows a few other examples of invariance/unobservable/conserved triplets in the classical world.

Non-observable quantity	Symmetry	Conserved quantity
Absolute direction	Space rotation	Angular momentum
Absolute position	Space translation	Momentum
Absolute time	Time translation	Energy

Table 1.3: *Examples of conserved quantity associated with an invariance of a classical system from the Noether theorem.*

This theorem also holds in field theory. A symmetry of the field yields a conserved current J^μ such that $\partial_\mu J^\mu = 0$.

1.2.2.2 Gauge invariance

The most important invariance in particle physics is the gauge invariance corresponding to a local continuous symmetry represented by the matrix:

$$U = e^{\alpha^a(x) T_a}$$

Ensuring the Lagrangian of a free particle is invariant under such a transformation makes the interaction fields appear in the mathematical formalism. The number of generators of the symmetry group corresponds to the number of force carriers associated to the interaction.

Next part shows how to make the gauge fields appear naturally in the Lagrangian describing a free particle, with the only requirement that this Lagrangian is invariant under a given, local, symmetry.

1.3 Gauge theories

Gauge invariance is first discussed in the simpler case of quantum electro-dynamics (QED). It is then applied to the strong interaction in the quantum chromo-dynamics (QCD) theory.

1.3.1   QED

A free fermion of mass m, associated to the field ψ, is described by the Dirac Lagrangian of Equation 1.5.

Now, one can impose that this Lagrangian is invariant under a local $U(1)$ transformation, meaning that the field transforms as:

$$\psi(x) \rightarrow \psi'(x) = e^{i\alpha(x)}\psi(x) \tag{1.7}$$

Then $\bar{\psi}$ transforms like:

$$\bar{\psi}(x) \rightarrow \bar{\psi}'(x) = \bar{\psi}(x)e^{-i\alpha(x)} \tag{1.8}$$

The Lagrangian after transformation is then:

$$\begin{aligned}
\mathscr{L}'_\psi &= (\bar{\psi}(i\ \not{\partial} - m)\psi)' \\
&= \bar{\psi}'(\partial_\mu\psi') - (m\bar{\psi}\psi)' \\
&= \bar{\psi}'(\partial_\mu e^{i\alpha(x)})\psi + \bar{\psi}'e^{i\alpha(x)}(\partial_\mu\psi) - m\bar{\psi}'\psi' \\
&= \bar{\psi}'e^{i\alpha(x)}(\partial_\mu + i(\partial_\mu\alpha))\psi - m\bar{\psi}\psi
\end{aligned} \tag{1.9}$$

The mass term is invariant under the considered transformation of the field, but this is not the case of the kinematic term. If one wants this term to be invariant as well, the definition of the covariant derivative needs to be adapted.

If we replace ∂_μ in 1.5 by the covariant derivative of Equation 1.10, then the Lagrangian of Equation 1.12 is invariant under the local $U(1)$ gauge invariance defined in Equation 1.7.

$$D_\mu = \partial_\mu + ieA_\mu \tag{1.10}$$

with:

$$A_\mu \rightarrow A_\mu - \frac{1}{e}\partial_\mu\alpha \tag{1.11}$$

$$\mathscr{L}_\psi = \bar{\psi}(i\ \not{D} - m)\psi \tag{1.12}$$

A new field A_μ had to be introduced, that couple to the fermion field Ψ through the term $\bar{\psi}A\psi$. This interaction interaction between the particle associated to the field ψ, the antiparticle associated to $\bar{\psi}$ and the bosonic field A_μ is represented in Figure 1.1. A common example of such interaction is electromagnetism, where the boson is the photon with spin 1.
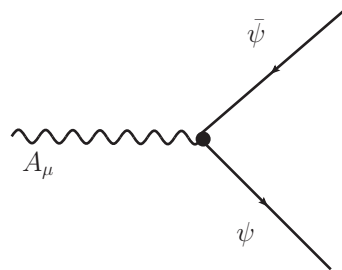
Figure 1.1: *Example of interaction between two fermions via a boson.*

Note that transformation 1.11 corresponds to a gauge transformation that leaves invariant the Maxwell equations of electromagnetism.

To complete the QED Lagrangian, one should consider the field dynamics, governed by the term: $-\frac{1}{4}F_{\mu\nu}F^{\mu\nu}$ where $F_{\mu\nu} = \partial_\mu A_\nu - \partial_\nu A_\mu$ is the electromagnetic tensor.

In practice, the full Lagrangian is never used to compute the cross-section, *i.e.* the probability for a process to happen. An interesting property of QED is used instead: the fact that its coupling constant, or its strength parameter α, is of the order of $\frac{1}{137}$. That means that terms in α^2 are much smaller than terms in α and can be neglected as a first approximation. This technique is known as the perturbation theory since higher order terms only introduce perturbations to the leading order (LO). Perturbation theory works pretty well for QED, whose results have been compared against experiments and the relative agreement is better than 10^{-6} (for the measurement of the anomalous dipole moment of the muon $\frac{g-2}{2}$ for example [1]).

The same gauge invariance mechanism can be used to introduce the other two interactions of the Standard Model, using non abelian groups, following the work of Yang and Mills [12].

The total Standard Model is described by the $SU(3)_c \times SU(2)_I \times U(1)_Y$ algebra, where $SU(3)_c$ refers to the color symmetry leading to the strong interaction and $SU(2)_I \times U(1)_Y$ is the isospin and hypercharge electroweak symmetry.

1.3.2 QCD

Strong interaction theory called Quantum Chromo Dynamics (QCD) with reference to the strong charge that was named colour and can take the values: red (R), green (G) and blue (B) for elementary particles (and $\bar{R}$, etc for antiparticles) while all composite particles are white ($W = R+G+B = \bar{R}+R$).

The same technique of gauge invariance can be applied to introduce the force carrier in the theory, with the notable difference with respect to QED that the local symmetry is $SU(3)_c$, which is a non-commutative group. The basic element of this theory is then represented by a colour triplet and $SU(3)_c$ represents a rotation in the colour space, justifying the subscript c.
For example:

$$\Psi = \begin{pmatrix} \Psi_R \\ \Psi_G \\ \Psi_B \end{pmatrix} \rightarrow \Psi' = \begin{pmatrix} \Psi_G \\ \Psi_B \\ \Psi_R \end{pmatrix} \tag{1.13}$$

The QCD Lagrangian after the gauge symmetry is imposed has the following form:

$$\mathscr{L}_{QCD} = \bar{\psi}(i\,\not{\partial} - \frac{g_S}{2}\mathbf{G}.\mathbf{t} - \mathbf{m})\psi - \frac{1}{4}Tr(G_{\mu\nu}G^{\mu\nu}) \tag{1.14}$$

In this equation 1.14, $G_{\mu\nu}$ is the equivalent to the QED $F_{\mu\nu}$, with non commutative properties. $\mathbf{G}$ represents the bosonic fields of the theory, and $\mathbf{t}$ the generators of $SU(3)$ creating the 8 force carriers called gluons. $\mathbf{m}$ is a diagonal mass matrix.

If one develops this Lagrangian, several possible interaction vertex can be identified. Especially, and contrarily to QED, the gluons themselves carry a colour charge, meaning that a gluon can interact with itself (Fig. 1.2).

(a) $q \rightarrow qg$ (b) $g \rightarrow gg$ (c) $gg \rightarrow gg$
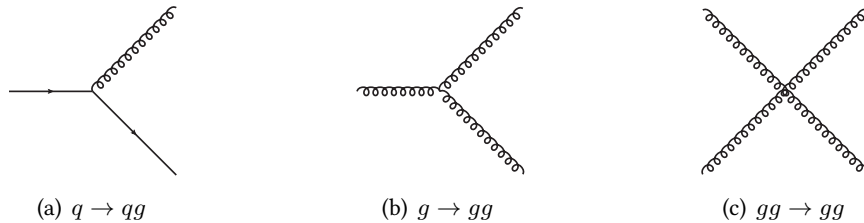
Figure 1.2: *Possible vertices in the QCD theory. Only the first one is possible in QED with photons instead of gluon.*

Running coupling constant The strength parameter of QCD is $\alpha_s = \frac{g_S^2}{4\pi}$. Contrarily to QED, its value is of the order of 0.1 or higher, which means that it will be more complicated for perturbative theory to produce reliable results. Hopefully, the value of α_{em} and α_s are strongly dependant on the energy involved in the process. Their behaviour however are very different and illustrated on figure 1.3(a). The running of the coupling as a function of the energy scale considered (usually chosen to be the transferred momentum in the reaction) and can be expressed as:

$$\alpha(\mu^2) = \frac{\alpha(\mu_0^2)}{1 + \alpha(\mu_0^2)\beta_0 ln\left(\frac{\mu^2}{\mu_0^2}\right)} \tag{1.15}$$

For QED, the β_0 function is $\beta_0^{QED} = -\frac{1}{3\pi} < 0$ while for QCD, $\beta_0^{QCD} = \frac{33-2n_f}{12\pi} > 0$ since n_f is the number of quarks flavour at most equal to 6 in the Standard Model. This yields quite different behaviour for the two interactions. When QED has a small coupling at high energy, QCD coupling increases when energy decreases (Fig. 1.3(a)) leading to peculiar properties:

- Confinement: at small energy and long distance, the coupling is higher. The consequence is that two quarks for example bound in a meson will never be able to be separated: the more you take them away, the more their binding energy increase;

- Asymptotic freedom: at high energy (*i.e.* small distance), the coupling is small. That means that two close particles will almost not see each other, phenomenon known as the asymptotic freedom, since particles are almost free, but only at high energy. In this regime, the coupling constant is small enough to apply perturbative theory: this is the region of perturbative QCD (pQCD).
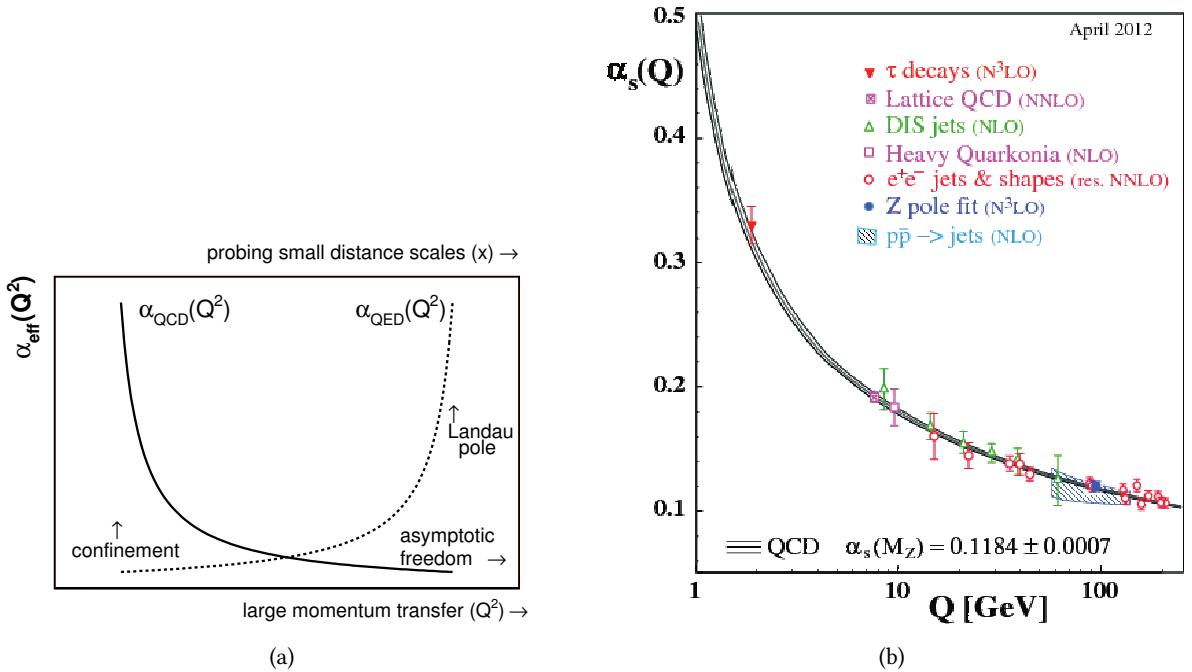
Figure 1.3: *Strong coupling evolution: (a) compared to the QED coupling evolution (schematic) and (b) compared to the various measurements taking as reference the point $\alpha_s(m_Z)$ [13].*

The predictions for the strong couplings are confronted to data with several measurements giving access to its value at different energy scales. Until now, all of them are in good agreement with the theory predictions (Fig. 1.3(b)).

1.4 Electro-weak sector

1.4.1 The weak interaction

The weak interaction was first studied by E. Fermi [14–16] in the 1930's through the radioactive β decay of the neutron:

$$n \rightarrow p + e^- + \bar{\nu}_e$$

It is characterized by a long lifetime of a few seconds compared to the characteristic lifetime of electromagnetic and of the strong induced processes far below the second, which motivated the introduction of a new fundamental interaction. This also suggests that its intensity is quite lower than the usual interactions; it is hence called the weak interaction.

Apart from its weakness, this interaction is characterized by several other new aspects:

- Parity violation: parity is the symmetry that flips the sign of the spatial coordinates. It is also an intrinsic property of particles, that exist on a right-handed and left-handed form (except neutrinos whose right-handed version was never observed). Two kinds of particle mediators are known to exist: the charged ones (later identified with the $W^{\pm}$) and the neutral ones (the Z^0). Experiments such as muons decay and charged pions leptonic decay have shown that the charged currents have a $V - A$ structure (vector minus axial vector) corresponding to a maximal parity violation [17, 18]. Equation 1.16 shows the structure of the matrix element (proportional to the scattering amplitude) for the beta decay in the context of the Fermi 4-point effective interaction as a function of the 4×4 γ matrices:

$$\mathcal{M} \propto G_F (\bar{u}_p \gamma^\mu (1 - \gamma^5) u_n)(\bar{u}_e \gamma_\mu (1 - \gamma_5) u_\nu) \tag{1.16}$$

- Quark mixing: the weak interaction is the only known fundamental interaction able to change the quark flavours. As shown by Cabbibo in 1963 [19] and extended by Kobayashi and Makawa in 1973 [20], the d and s quarks mass eigenstates d' and s' are different from their interaction eigenstates and are related by the CKM matrix:

$$\begin{pmatrix} d' \\ s' \\ b' \end{pmatrix} = V_{CKM} \begin{pmatrix} d \\ s \\ b \end{pmatrix} \tag{1.17}$$

where:

$$V_{CKM} = \begin{pmatrix} V_{ud} & V_{us} & V_{ub} \\ V_{cd} & V_{cs} & V_{cb} \\ V_{td} & V_{ts} & V_{tb} \end{pmatrix} \tag{1.18}$$

1.4.2 Electro-weak gauge theory

The weak interaction is unified to the electromagnetic one in the electro-weak interaction governed by the $SU(2)_I \times U(1)_Y$ symmetry group. Here, I refers to the weak isospin, whose projection I_3 will also be useful in the following, and Y is the weak hypercharge.

Assuming the purely kinetic form of the Lagrangian can be written:

$$\mathscr{L} = i\bar{L}_\ell \gamma^\mu \partial_\mu L_\ell + i\bar{R}_\ell \gamma^\mu \partial_\mu R_\ell \tag{1.19}$$

where L denotes one of the left handed doublet and R the corresponding right handed singlet (*i.e.* not sensitive to $SU(2)_I$ interactions) of Table 1.4. Imposing this Lagrangian to be invariant under $SU(2) \times U(1)$ requires the introduction of new gauge fields $\mathbf{W}_\mu$ (with three components denoted 1,2 and 3) and B_μ by replacing the covariant derivative ∂_μ by:

$$D_\mu = \partial_\mu + i\frac{g}{2}\boldsymbol{\sigma}.\mathbf{W}_\mu + i\frac{g'}{2}Y B_\mu \tag{1.20}$$

where $\boldsymbol{\sigma}$ are the three $SU(2)$ generators, *i.e.* the Pauli matrices.

$U(1)_Y$ gives rise to an interaction carried by the vector boson associated to the field B_μ while the $SU(2)_I$ symmetry creates three bosons W_μ^1, W_μ^2 and W_μ^3. A linear combination of the two neutral fields B_μ and W_μ^3 should be able to reproduce the electromagnetic current A_μ of section 1.3.1, and the neutral current of weak interactions. The generic expressions of Equation 1.21 and 1.22 describe this fact, where θ_W is the weak mixing angle.

$$A_\mu = +B_\mu cos(\theta_W) + W_\mu^3 sin(\theta_W) \tag{1.21}$$

$$Z_\mu = -B_\mu sin(\theta_W) + W_\mu^3 cos(\theta_W) \tag{1.22}$$

The other two components of $\mathbf{W}_\mu$ give rise to the charged fields:

$$W_\mu^\pm = \frac{1}{\sqrt{2}}(W_\mu^1 \mp W\mu^2) \tag{1.23}$$

1st family	2nd family	3rd family	Q	I	I_3	Y
$\begin{pmatrix} \nu_e \\ e^- \end{pmatrix}_L$	$\begin{pmatrix} \nu_\mu \\ \mu^- \end{pmatrix}_L$	$\begin{pmatrix} \nu_\tau \\ \tau^- \end{pmatrix}_L$	0	1/2	1/2	-1
			-1	1/2	-1/2	-1
$\begin{pmatrix} u \\ d \end{pmatrix}_L$	$\begin{pmatrix} c \\ s \end{pmatrix}_L$	$\begin{pmatrix} t \\ b \end{pmatrix}_L$	2/3	1/2	1/2	1/3
			-1/3	1/2	-1/2	-1/3
e_R^-	μ_R^-	τ_R^-	-1	0	0	-2
u_R	c_R	t_R	2/3	0	0	4/3
d_R	s_R	b_R	-1/3	0	0	-2/3

Table 1.4: *Left-handed doublets and right-handed singlet of the weak interaction. I refers to the weak isospin and Y to the weak hypercharge.*

Electromagnetism and weak interaction are now fully unified into a consistent gauge theory. However, the generated bosonic fields W, Z and A do not have a mass term of the form $m\bar{\psi}\psi$, and one cannot add it by hand because it violates gauge invariance. This is in contradiction with the experimental results that find masses of the order of 80-90 GeV for the $W^\pm$ and Z^0 bosons respectively. The gauge symmetry has then to be broken for a mass term to be added safely to the theory.

1.5 EW symmetry breaking: the Brout-Englert-Higgs mechanism

The observed masses of the W and Z bosons and the fact that a mass term violates the gauge invariance of the theory push towards a symmetry breaking of the theory. The most famous, and now proven by experiments, solution to deal with this issue is the Brout-Englert-Higgs mechanism, developed in the 1960's and for which Englert and Higgs were awarded the Nobel prize of physics in 2013. In this section, the spontaneous symmetry breaking mechanism, that was first introduced by Nambu [21, 22], is first illustrated with a global invariance for real and complex field and is then applied the local gauge invariance of the electroweak interaction.

1.5.1 Spontaneous symmetry breaking of a $U(1)$ symmetry

Let's first consider the following simple example of a bosonic Lagrangian in a potential V:

$$\mathscr{L}_\phi = \frac{1}{2}\partial_\mu\phi\partial^\mu\phi - V(\phi) \tag{1.24}$$

$V(\phi)$ has the form shown in Figure 1.4 and can be written:

$$V(\phi) = \frac{1}{2}\mu^2\phi^2 + \frac{1}{4}\lambda\phi^4 \tag{1.25}$$

with $\mu^2 < 0$ and $\lambda > 0$. Such a potential has two minima, *i.e.* two stable solutions for the system.
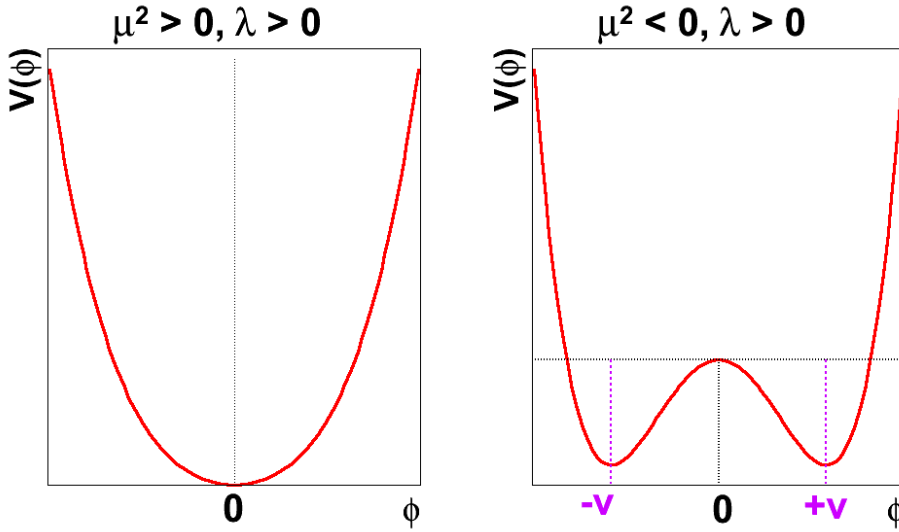
Figure 1.4: *Illustration of the mexican hat Higgs potential in the case of $U(1)$ global symmetry.*

The Lagrangian 1.24 has the property to be invariant under the transformation $\phi \to -\phi$ and such are the solutions of the system corresponding to $\phi = \pm v = \pm \sqrt{\frac{-\mu^2}{\lambda}}$, v being the vacuum expectation value. But the system has to choose one of these solutions, and can not move from one to another once this choice is made. This situation is similar to the bending of a rod illustrated in Figure 1.5: if one applies a vertical force on a beam, nothing will happen until the force reaches a threshold. At that moment, the rod will bend, choosing a special direction among the infinite number of possible directions available due to the rotation symmetry along the beam axis of the system. This phenomena of choosing one out of several symmetric stable solution is known as spontaneous symmetry breaking. The same happens in the case of the Brout-Englert-Higgs mechanism, where, in our simple example, the system has to choose one solution among $-v$ and $+v$.
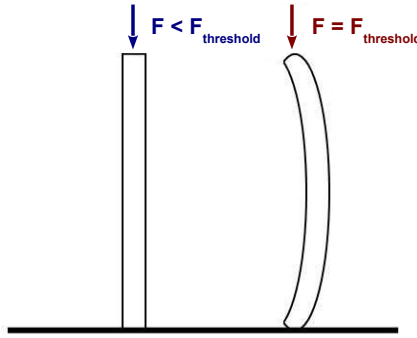
Figure 1.5: *An example of spontaneously broken symmetry: rod bending.*

In the following, the $+v$ solution will be chosen. To understand the consequences of this choice, one can study the system close to the equilibrium, introducing small variations around this minimum:

$$\phi(x) = v + \chi(x), \text{ with } |\chi| << v \tag{1.26}$$

The Lagrangian 1.24 can then be written:

$$\mathscr{L}_\chi = \frac{1}{2}(\partial_\mu \chi)^2 - \lambda v^2 \chi^2 - \lambda v \chi^3 - \frac{1}{4}\lambda \chi^4 + \frac{1}{4}\lambda v^4 \tag{1.27}$$

The newly introduced field χ has an associated mass term $(m_\chi \chi^2)$ with

$$m_\chi = \sqrt{2\lambda v^2} = \sqrt{-2\mu^2}$$

.

Hence, breaking the symmetry by choosing a solution among two possible minima generates a new massive field. This formula for the m_χ was found for the first time by Goldstone in [23], where the mexican hat potential, sometimes called the Higgs potential, was first introduced in particle physics.

1.5.2 Spontaneous symmetry breaking with a complex field

We now repeat the same procedure with a complex field $\phi = \frac{\phi_1 + i\phi_2}{\sqrt{2}}$. Its Lagrangian, given in Equation 1.28 also has a global $U(1)$ symmetry. Its minima are located on a circle in the complex plane such that $\phi_1^2 + \phi_2^2 = \frac{v^2}{2}$.

$$\begin{aligned}
\mathscr{L} &= (\partial_\mu \phi)^* (\partial^\mu \phi) - \mu^2 \phi^* \phi - \lambda(\phi^* \phi)^2 \\
&= \frac{1}{2}(\partial_\mu \phi_1)^2 + \frac{1}{2}(\partial_\mu \phi_2)^2 - \frac{1}{2}\mu^2(\phi_1^2 + \phi_2^2) - \frac{1}{4}(\phi_1^2 + \phi_2^2)^2
\end{aligned} \tag{1.28}$$

As previously, let's choose one of this minima ($\phi_1 = v$ and $\phi_2 = 0$) and expand the Lagrangian around this point $\phi = \frac{v + \eta(x) + i\xi(x)}{\sqrt{2}}$. One ends up with the Lagrangian 1.29 at leading order in η and ξ (removing the constant term are not useful for this discussion)

$$\mathscr{L} = \frac{1}{2}(\partial_\mu \eta)^2 + \frac{1}{2}(\partial_\mu \xi)^2 + \mu^2 \eta^2 \tag{1.29}$$

A mass term appears for the η field, having a mass similar to the previous case $m_\eta = \sqrt{-2\mu^2}$. The other field that needed to be introduced, ξ, remains massless: it is an example of Goldstone boson [23]. This is understood looking at Figure 1.6: the η field corresponds to transverse excitation where energy is needed to move while the ξ field designate excitations along the minimum. In a more general way, the Goldstone theorem [24] states that a massless boson appears in the theory for each broken generator.
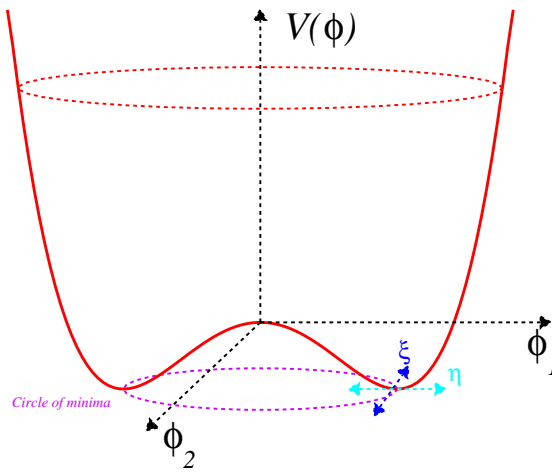
Figure 1.6: *Illustration of the Higgs potential in the complex plane.*

1.5.3   Application to local gauge invariance

In the case of a local $U(1)$ symmetry $\psi \to e^{i\alpha(x)}\psi$, the Lagrangian of Equation 1.12, that contains the gauge generated field A_μ, can be extended around the same chosen minimum. It can be shown that this Lagrangian becomes (without the interaction terms):

$$\mathscr{L} = \frac{1}{2}(\partial_\mu \eta)^2 + \frac{1}{2}(\partial_\mu \xi)^2 - v^2\lambda\eta^2 + \frac{1}{2}e^2v^2 A_\mu A^\mu - evA_\mu\partial^\mu\xi \tag{1.30}$$

Similarly to the previous global $U(1)$ case, this Lagrangian describes a massless field ξ and a massive field η, but it also contains a mass term for the gauge field A_μ, which is the expected result.

The massless Goldstone boson can be suppressed with a trick, using the gauge invariance of the system. Instead of considering the field ϕ, one can use $e^{-i\theta(x)/v}\phi$. Also noticing that the expansion of the field around its minimum can be written $\phi = \frac{(v+h(x))}{\sqrt{2}}e^{i\theta(x)/v}$, the local change of phase of the field ϕ allows to get rid of the massless θ field.

The final Lagrangian then contains the gauge field A_μ that have acquired a mass through this process $m_A = \sqrt{2\lambda}v$ and a massive field h corresponding to the Brout-Englert-Higgs field, that we will most often call Higgs field.

1.5.4   Generation of the gauge boson masses

The application to the Brout-Englert-Higgs mechanism to the $SU(2)_L \times U(1)_Y$ electroweak gauge theory generates masses for the W and Z bosons. This operation breaks the $SU(2)_L \times U(1)_Y$ symmetry but should preserve the $U(1)_{em}$ symmetry that preserves the electric charge Q.

To do so, the Higgs field should have a neutral component, which translates into an $SU(2)_I$ doublet with $|Y| = 1$[3]. be written as $\phi = \begin{pmatrix} \phi^+ \\ \phi^0 \end{pmatrix}$ where both ϕ^+ and ϕ^0 are complex fields [25].

The potential $V(\phi^\dagger\phi) = \mu^2\phi^\dagger\phi + \lambda(\phi^\dagger\phi)^2$ have minima located on the 4-dimension sphere defined by $|\phi^+|^2 + |\phi^0|^2 = \frac{-\mu^2}{2\lambda}$. One has to choose one minimum among this infinite number of possibilities, keeping in mind that the $SU(2)_L \times U(1)_Y$ symmetry has to be broken to generate masses for the W and Z bosons, but the $U(1)_{em}$ symmetry has to be preserved for the photon to remain massless. A suitable choice is to write: $\phi = \begin{pmatrix} 0 \\ \frac{v}{\sqrt{2}} \end{pmatrix}$.

The expansion around the potential minimum can be made directly with the appropriate parametrization in order to eliminate the Goldstone bosons of the theory:

$$\phi \to \frac{e^{\frac{i\boldsymbol{\sigma}.\boldsymbol{\theta}(x)}{v}}}{\sqrt{2}} \begin{pmatrix} 0 \\ v + h(x) \end{pmatrix} \tag{1.31}$$

Expanding the Lagrangian around the potential minimum with this parametrization

$$\begin{aligned}
\mathscr{L} = & \frac{1}{2}\partial_\mu h\partial^\mu h - \frac{1}{2}\lambda v^2 h^2 - \lambda v h^3 - \frac{\lambda}{4}h^4 \\
& + \frac{1}{2}\left[\frac{g'^2v^2}{4}B_\mu B^\mu - \frac{gg'v^2}{2}W_\mu^3 B^\mu + \frac{g^2v^2}{4}\mathbf{W}_\mu\mathbf{W}^\mu\right] \\
& + \frac{1}{v}\left[\frac{g'^2v^2}{4}B_\mu B^\mu h - \frac{gg'v^2}{2}W_\mu^3 B^\mu h + \frac{g^2v^2}{4}\mathbf{W}_\mu\mathbf{W}^\mu h\right] \\
& + \frac{1}{v^2}\left[\frac{g'^2v^2}{4}B_\mu B^\mu h^2 - \frac{gg'v^2}{2}W_\mu^3 B^\mu h^2 + \frac{g^2v^2}{4}\mathbf{W}_\mu\mathbf{W}^\mu h^2\right] \\
& + \dots
\end{aligned} \tag{1.32}$$

---

[3]The $SU(2)_L \times U(1)_Y$ and $U(1)_{em}$ charges are related by the Nishijima relation: $Q = I_3 + \frac{Y}{2}$.

The first line describe the Higgs field dynamics and mass with the common mass expression as a function of the vacuum expectation value $m_H^2 = 2\lambda v^2$. The vacuum expectation value v value can be estimated from the Fermi constant and is ~ 246 GeV.

The last two lines are the formulation of the interactions of this Higgs field with the bosons fields. Finally, the second line unveil the W and Z bosons masses:

- The last term contains the $W^\pm = \frac{1}{\sqrt{2}}(W^1 \mp W^2)$ boson: $m_W = \frac{1}{2}vg$.

- The W_μ^3 and B_μ fiels are mixed together. One of them should reproduce the massless photon field of QED A_μ. The mass of the Z boson can thus be obtained by diagonalizing the matrix using the weak mixing angle θ_W:

$$\frac{1}{4} \begin{pmatrix} g^2 v^2 & -gg'v^2 \\ -gg'v^2 & g'^2 v^2 \end{pmatrix} = M^{-1} \begin{pmatrix} m_Z^2 & 0 \\ 0 & 0 \end{pmatrix} M \tag{1.33}$$

With $M = \begin{pmatrix} cos(\theta_W) & -sin(\theta_W) \\ sin(\theta_W) & cos(\theta_W) \end{pmatrix}$, one deduces that $m_Z^2 = \frac{(g^2+g'^2)v^2}{4}$.

The Z mass can be expressed as a function of the W mass and the weak mixing angle θ_W: $\frac{m_W}{m_Z} = cos(\theta_W)$. Hence, the parameter $\rho_0 = \left(\frac{m_W}{m_Z cos(\theta_W)}\right)^2$ is equal to 1 in the Standard Model at tree level and this observation is confirmed by experiments at the permill precision level [26].

Previous relation also allows to relate the electroweak couplings and the QED charge:

$$g sin(\theta_W) = g' cos(\theta_W) = e \tag{1.34}$$

1.5.5 Fermions masses

The gauge boson masses are explained by the Higgs mechanism but not the fermions ones. Similarly than for gauge bosons, a mass term for fermions of the form $m(\bar{L}L + \bar{R}R)$. violates the $SU(2)_L$ gauge invariance of the Lagrangian and can not be added into the theory by hand. Another trick exists to introduce them in the model through interaction with the Higgs field *via* Yukawa couplings.

Adding a Yukawa coupling between the Higgs field and the leptons to the Lagrangian:

$$\mathscr{L} = -\lambda_e(\bar{L}_\ell \phi R_\ell + \bar{R}_\ell \phi^\dagger L_\ell) \tag{1.35}$$

for the electron case and applying the spontaneous symmetry breaking $\phi(x) = \frac{1}{\sqrt{2}} \begin{pmatrix} 0 \\ v + h(x) \end{pmatrix}$, the Lagrangian becomes:

$$\mathscr{L} = -\frac{\lambda_e v}{\sqrt{2}} \bar{\psi}_\ell \psi_\ell - \frac{\lambda_e}{\sqrt{2}} \bar{\psi}_\ell \psi_\ell h \tag{1.36}$$

The first term gives the electron mass $m_e = \frac{\lambda_e v}{\sqrt{2}}$. The second one is the coupling between the Higgs and the lepton hence proportional to the lepton mass. The same procedure can be repeated for each massive lepton, introducing a constant g for each of them.

The same procedure applies to quarks, with the caveat that, for the up-type quarks, the Higgs field considered is $\phi_c(x) = \frac{1}{\sqrt{2}} \begin{pmatrix} v + h(x) \\ 0 \end{pmatrix}$, corresponding to a rotation of ϕ.

To summarize, the Brout-Englert-Higgs mechanism was able to generate masses for the gauge bosons $m_V = \frac{\lambda_V \cdot v}{2}$, the fermions $m_f = \frac{\lambda_f \cdot v}{\sqrt{2}}$. The cost to pay is the introduction of a new massive field, associated with a new scalar boson (the (Brout-Englert-)Higgs boson) with mass $m_H = \sqrt{2\lambda v^2}$, where the different $\lambda_{V,f}$ quantify the Higgs couplings to the massive bosons and fermions and λ is the Higgs self coupling.

1.5.6 Higgs production and decay

In the Standard Model, the Higgs boson is a spinless particle with even parity ($J^{PC} = 0^+$). Its couplings to other particles are determined by the Higgs mechanism for bosons and a Yukawa potential for fermions. These couplings allow to predict the Higgs production rate in a given collider (that fix the centre of mass energy and the incident particles) together with the possible Higgs decays as a function of the Higgs mass.

1.5.6.1 Decay

The Higgs boson couples to bosons with a strength $\propto m_V^2$ and to fermions with a strength $\propto m_f$. Several possible decay modes are then predicted by the Standard Model, whose relative importance is quantified by the branching ratios $\mathcal{B}r$:

$$\mathcal{B}r_i = \frac{\Gamma_i}{\Gamma_{tot}}$$

where Γ denotes the natural Higgs width in the ith mode or the total of the order of 4.2 MeV at a Higgs mass of 125 GeV (Fig. 1.7).
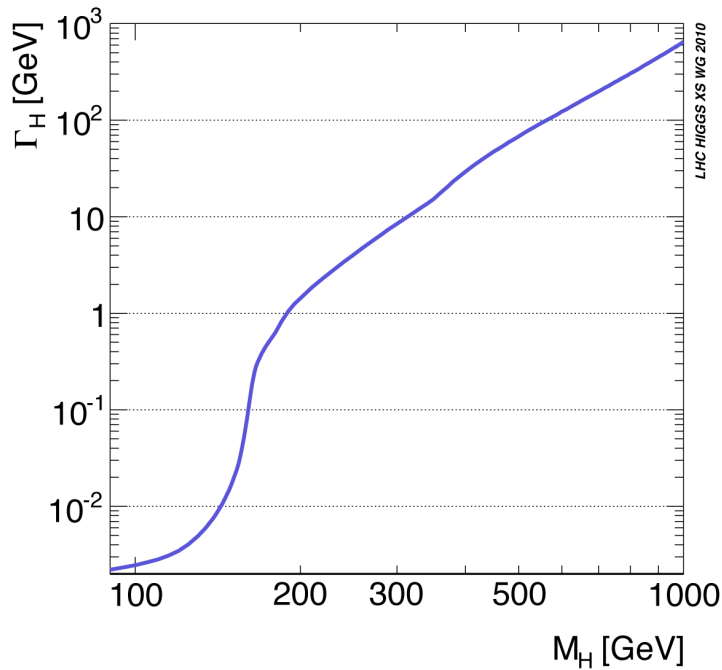
Figure 1.7: *Higgs boson natural width [27].*

Figure 1.8(a) shows the branching ratio for the different Higgs decay modes. They are convoluted by the cross section of the final particles decay in Figure 1.8(b) that shows the relative importance of each observable final state.

In the low mass region ($m_H \lesssim 150$ GeV), the dominant decay modes are $b\bar{b}$ and $\tau^+\tau^-$.

The Higgs does not couple to massless photons, hence the Higgs decay to photons is not possible directly. It happens through loops involving heavy bosons (W) or fermions (where the top quark contribution dominates) (Fig. 1.9). The branching ratio of this decay mode is very small ($\sim 0.2\%$) however, when taking into consideration the probabilities of the different final states (Figure 1.8(b)), it has a non-negligible contribution compared for instance to the ZZ decay, where the Zs decay branching ratios have to be taken into consideration.

(a) $\mathcal{B}r$

(b) $\sigma \times \mathcal{B}r$
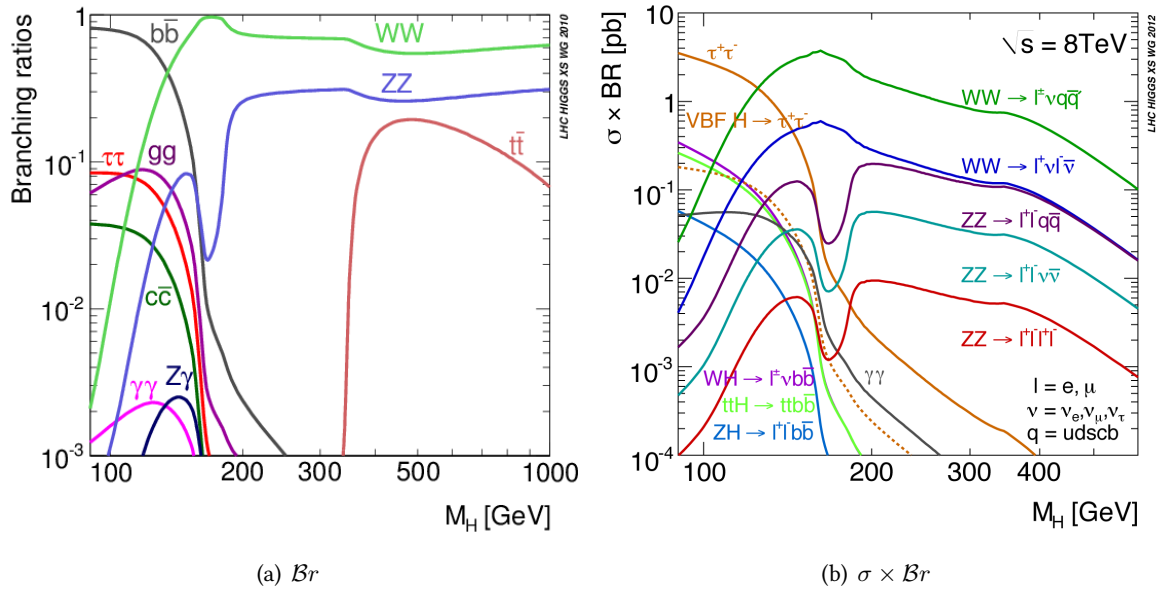
Figure 1.8: *Higgs decay branching ratio in the Standard Model [27]*

(a) (b) (c)
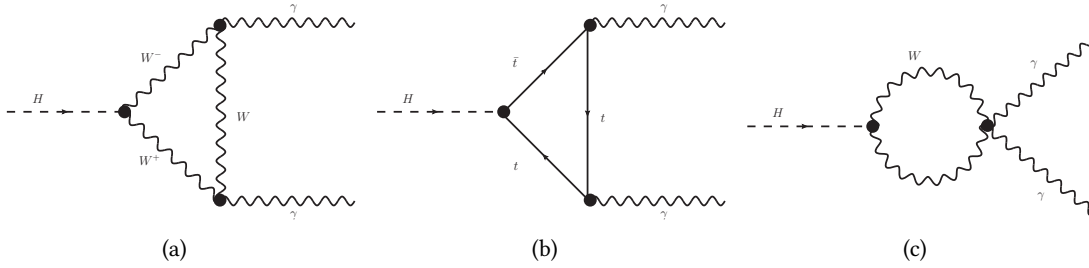
Figure 1.9: *Higgs decay to two photons at lowest order in the Standard Model.*

1.5.6.2 Production

The Higgs production rate is dictated by the collider configuration. In the latter accelerators, where protons and/or anti-protons collide, the main four production modes are drawn in Figure 1.10.

Their importance is quantified by their cross section, related to the number of events produced (see Chap. 3). At the LHC, a proton-proton collider, the main production mode is the gluon fusion (87% for a 126.5 GeV Higgs and a centre of mass energy of $\sqrt{s} = 8$ TeV), followed by the weak Vector Boson Fusion (7.2%), the Higgsstrahlung (3.1% or WH and 1.9% for ZH) and the associated production with top/anti-top pair (0.6%, excluding the $b\bar{b}H$ production which is slightly larger than $t\bar{t}H$). The mass dependence of the cross sections is shown in Figure 1.11. The energy dependence is illustrated in Figure 1.12 (with the $b\bar{b}H$ contribution) where one can see that, as expected $t\bar{t}H$ increases a lot with energy.

(a) Gluon fusion (ggH)

(b) Weak vector boson fusion (VBF)

(c) Higgsstrahung

(d) Associated production with $t\bar{t}$ pair (ttH)
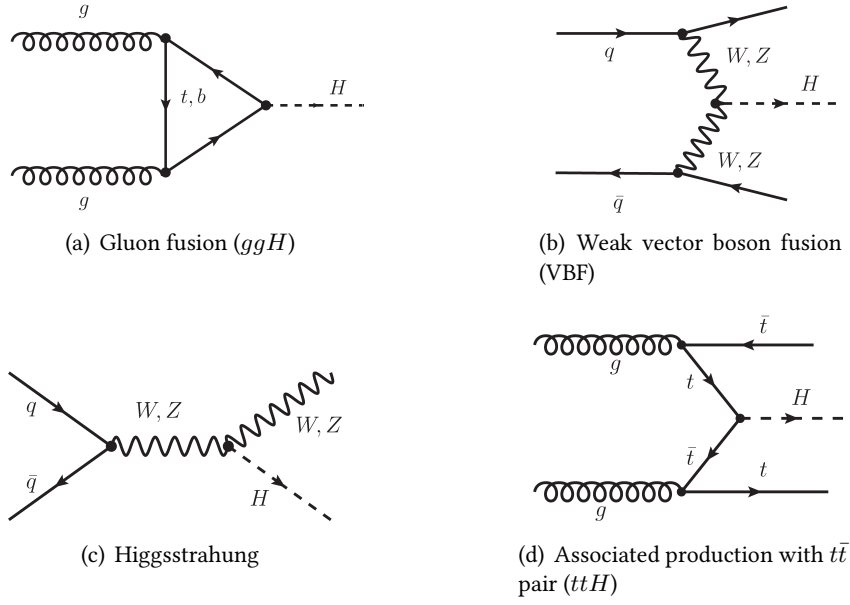
Figure 1.10: *Main Higgs production modes at the LHC.*

(a) 7 TeV

(b) 8 TeV
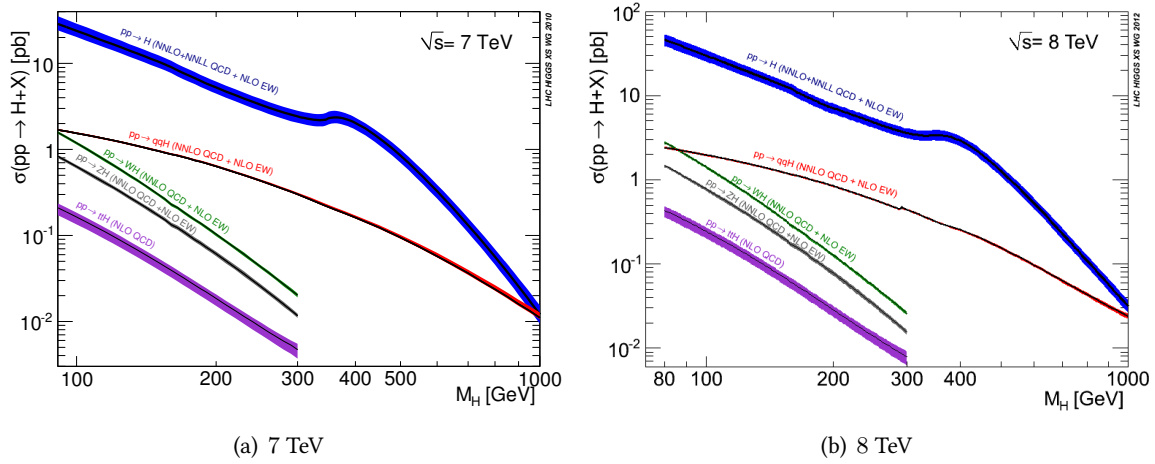
Figure 1.11: *Higgs production cross section for the five main production modes of the Standard Model [27].*
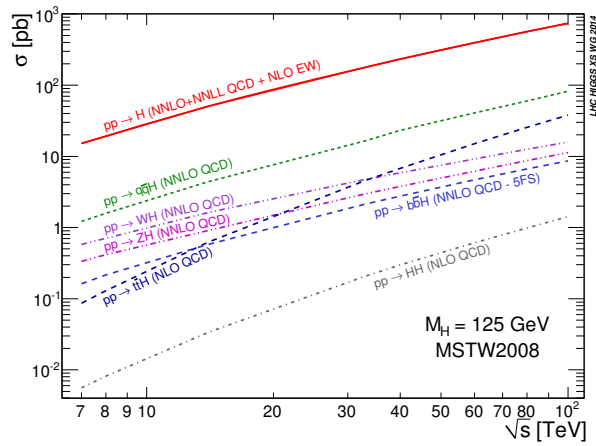
Figure 1.12: *Higgs production cross section as a function of the centre of mass energy $\sqrt{s}$ [28].*

1.5.7 Higgs boson knowledge before the LHC

The Standard Model predicts everything about the Higgs boson except its mass. This is so an important parameter to be measured, which was done intensely at the previous accelerator facilities at CERN (LEP) and in the USA (Fermilab). Theory also provides boundaries on the mass, using vacuum stability and triviality, or helps in finding limits based on high precision electroweak observables.

1.5.7.1 Theoretical limits

Even if the Higgs mass can not be predicted by the theory, several arguments allow to restrict its allowed range:

- Unitarity: the WW scattering cross section diverges as the centre of mass energy increases. This can be avoided by introducing a sufficiently light Higgs boson: $m_H < \left(\frac{8\pi\sqrt{2}}{3G_F} \right)^{\frac{1}{2}} \sim 1$ TeV.

- Triviality: The running of the Higgs coupling as a function of the energy scale (similarly to the running of α_{em} (Equation 1.15) can be written:

$$\lambda(\mu^2) = \frac{\lambda(v^2)}{1 - \frac{3\lambda(v^2)}{8\pi^2} ln\left(\frac{\mu^2}{v^2} \right)} \tag{1.37}$$

and reaches a singularity (Landau pole) at $\mu_L^2 = v^2 exp\left(\frac{8\pi^2}{3v^2} \right)$. The triviality argument states that this frontier should be far enough from the new physics scale. This leads to constraints on the Higgs mass illustrated by the red curve in Figure 1.13.

- Vacuum stability: if the coupling becomes negative, the Higgs potential is no more bounded from below, which leads to an unstable vacuum. Imposing $\lambda(\mu) > 0$ gives other constraints on the Higgs mass illustrated by the green line in Figure 1.13.

These limits are reported on figure 1.13 as a function of the Λ cut-off scale.
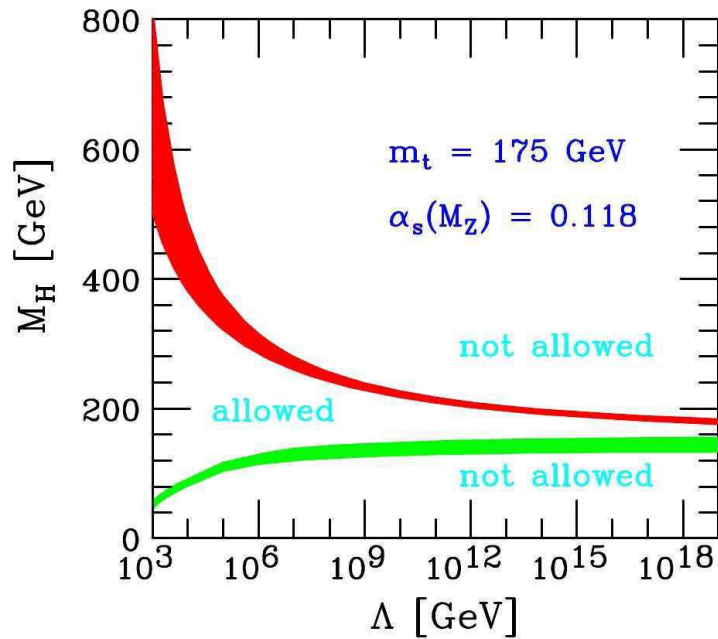
Figure 1.13: *Theoretical limits on the Higgs boson mass [29].*

1.5.7.2 Experimental limits

Before the start of the LHC, previous experiments already allowed to exclude some mass ranges due to the non-observation of a Higgs boson. Figures 1.14(a) and 1.14(b) show the exclusion plots from the LEP (CERN, Geneva) and Tevatron (Fermilab, Chicago). More details about how these plots are made and should be interpreted will be given in chapter 2. The summary of the excluded range after the final analysis of the LEP and Tevatron data is sketched in Figure 1.14(c). This figure includes indirect measurements.

(a) LEP exclusion limit

(b) TeVatron exclusion limit
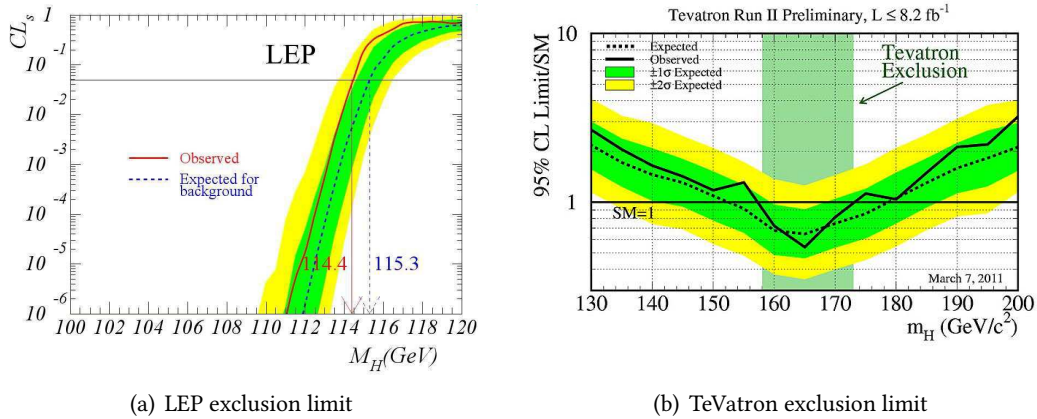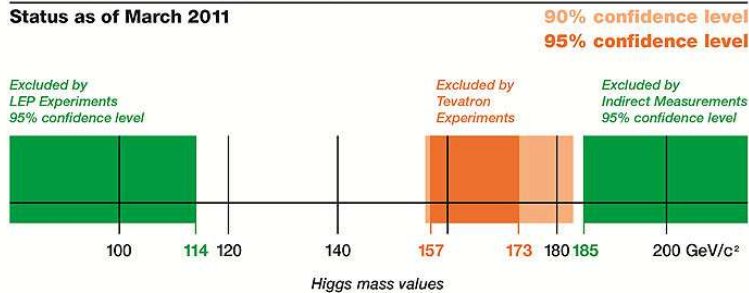
(c) Excluded ranges as of March 2011

Figure 1.14: *Experimental limits on the Higgs mass from LEP (a) [30] and Tevatron (b) [31]. (c) is the summary plot from March 2013.*

The Higgs boson contributes to radiative corrections to high precision electroweak observables (mass of the W and Z bosons, effective weak mixing angle measured in forward-backward and polarization asymmetries in e^+e^- collisions, etc). Thus, constraints on the Higgs mass can be derived from these observations. However, constraints are quite weak because the dependence on the Higgs mass is only logarithmic. The $\Delta\chi^2 = \chi^2 - \chi^2_{min}$ of a fit of the combined data performed by the LEP electroweak working group is shown in Figure 1.15. A 95% CL upper band can be obtained by $\Delta\chi^2 = 3.84$.

The excluded areas as of March 2011 were (with a 95% confidence level (CL)):

$$m_H < 114 \text{ and } 157 < m_H < 173 \text{ and } 185 < m_H \text{ GeV}$$

The first LHC data restricted even more the allowed range, before a 3σ observation happens in December 2011. This observation was confirmed with 2012 data, leading to the announcement of the
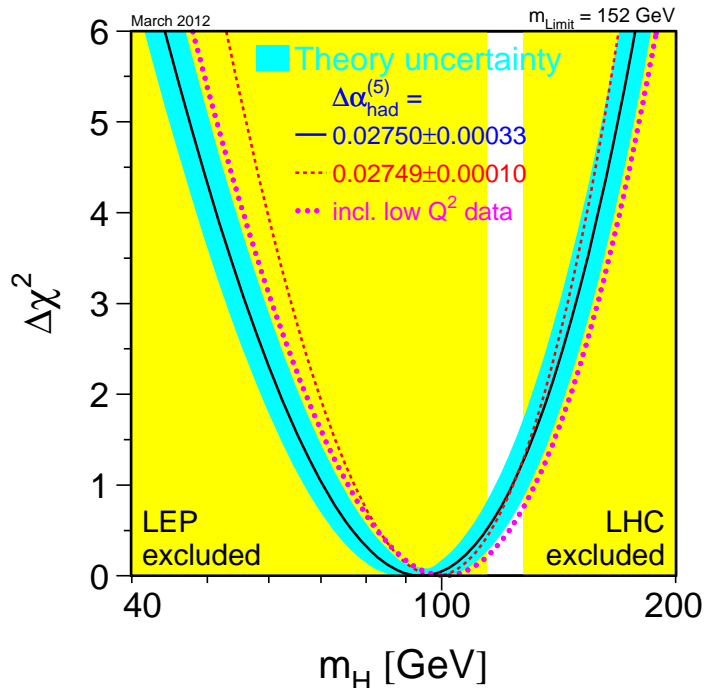
Figure 1.15: $\Delta\chi^2$ *curve derived from precision electroweak measurements as a function of the Higgs-boson mass [32].*

discovery of a boson consistent with a Higgs boson with ~ 125 GeV mass on July 4th, 2012, which is a great achievement of the Standard Model.

1.6 Beyond the Standard Model

The Standard Model allows to explain a lot of observed phenomena. However, it is known that it can not be the final theory of everything and theories beyond the Standard Model exist to overcome its problems.

1.6.1 Standard Model successes

The Standard Model built along the years to include all the observations in a common framework has proven to be well suited in the description of experimental results in most of the cases.

At the end of the 1990's, the Standard Model of particle physics was well established. The LEP electron-positron collider at CERN and the Tevatron proton-antiproton collider at Fermilab, near Chicago, both brought new results validating it. The LEP also allowed to measure the number of fermions families whose associated neutrino has a mass smaller than half the Z mass; it was found to be $N_\nu = 2.9840 \pm 0.0082$ from the combination of all LEP experiments [26]. The W and Z masses are also accurately measured at a precision level of 2.10^{-4} and 2.10^{-5} [1, 33]. At the Tevatron, the top quark, last expected but never observed quark, was discovered and its mass measured [34, 35].

A comparison of the Standard Model parameters measurement to the expected values from a global fit of the Standard Model is shown in Figure 1.16. Almost all these values stay within 2σ of the measured values, only the experimental uncertainties are considered.
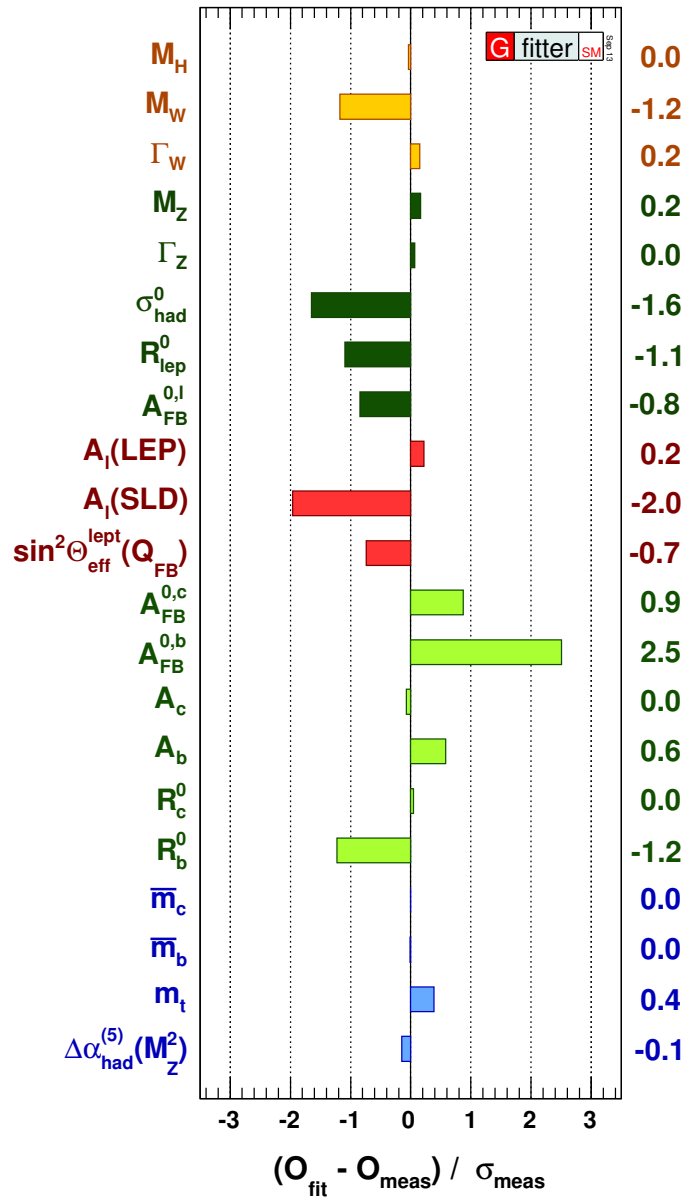
Figure 1.16: *Comparison of the measured values of some Standard Model parameters with the expectations from a global fit [36].*

More recently, Figure 1.17 shows the good agreement reached between the measured cross section of some Standard Model processes by ATLAS (Chap. 4) and the Standard Model predictions.
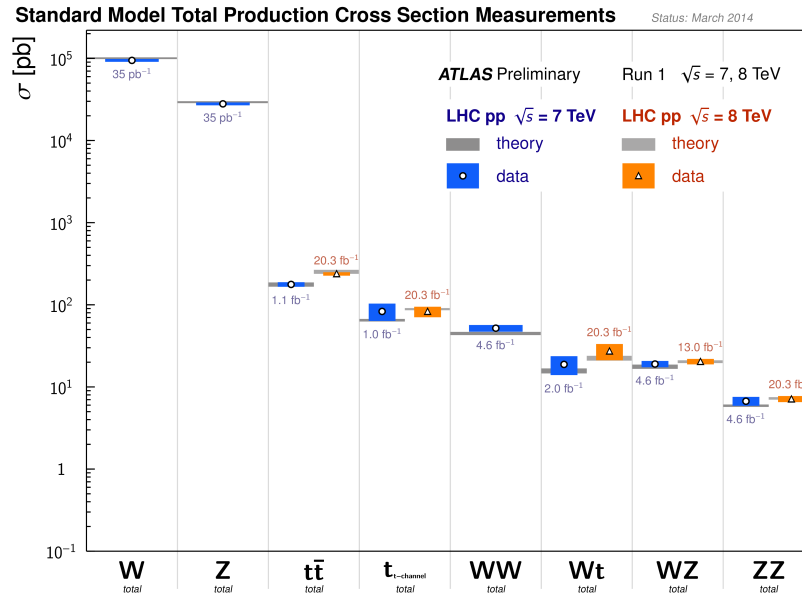
Figure 1.17: *Preliminary cross section of several processes measured by ATLAS and compared to the Standard Model predictions [37].*

1.6.2 Standard Model issues

Nevertheless, the Standard Model suffers from some caveats. Some come from theoretical considerations, others from experimental observations that can not be accommodated through this model. Below are some of these problems:

- Free parameters: the model contains a lot of parameters for which the theory can not provide an estimation. They can be chosen as follows:

  - Interactions: three coupling constants (g and g' in the electroweak sector) and α_s for the strong interaction are not predicted by the model.

  - Lepton sector: each charged lepton mass is also a free parameter (or their coupling to the Higgs field).

  - Quark sector: to the six unpredicted quark masses, one should add the three mixing angles and the free CP violating phase of the CKM matrix.

  - Higgs sector: two new parameters are needed to describe the Higgs potential μ and λ.

- The Standard Model does not incorporate gravity. This translates into an upper scale Λ at which the model is expected not to be correct anymore: close to the Planck scale $\Lambda \sim m_{Planck} \sim \frac{1}{\sqrt{G_N}}$. The hierarchy problem, which wonders why is there 17 orders of magnitude difference between the weak scale and the Planck scale ?

- Neutrino masses: in the Standard Model, neutrinos are massless particles. However, some observed phenomenon such as the neutrino oscillations can be understood only for massive neutrinos. A minimal extension of the Standard Model exists in the see-saw mechanism to get rid of this problem.

- Dark energy/matter: cosmological observations tends to prove that the quantity of observable matter in the universe represents only a small fraction of the total universe mass ($\sim 5\%$) [38]. The remaining mass, called dark matter, accounts for at least 27% of the total universe composition. On top of that, dark energy is also needed to explain the expansion phenomenon,

contributing to another 66% of the universe. The source for dark matter/energy is not known, and can not, *a priori*, comes from Standard Model particles.

- Baryon asymmetry: while particles and anti-particles are expected to behave in the same way, the number of matter particles largely predominate over the anti-matter ones. This can only happen if the CP symmetry is more violated than in the Standard Model.

- Naturalness (or hierarchy problem): when considering loop corrections to the Higgs mass, quadrature divergences appear. Cancelling these terms require a fine tuning of the Higgs bare mass over 16 order of magnitude, which is said not to be a natural solution.

1.6.3 Supersymmetry

Since fermions and bosons loops corrections to the Higgs mass have opposite signs, a solution is to associate a new particle to each Standard Model particle, with same quantum numbers except for its spin, differing by half a unit. This is implemented in the supersymmetry (SUSY) models. If the SUSY symmetry was holding at our current energy scale, a particle and its associated super-partner would have the same mass. Since there is no existing observed candidate for the new super-partners, they should be hidden to the past experiments, *i.e.* very heavy, and SUSY is a broken symmetry. The scale of symmetry breaking is assumed to be smaller than the Planck mass, and often close to the electroweak scale in order to solve the hierarchy problem.

This theory can solve some of the above mentioned issues of the Standard Model.

For instance, a nice feature of SUSY is the convergence of the interaction couplings at high energy scale (Grand Unification), contrarily to what is obtained in the Standard Model (Fig. 1.18).
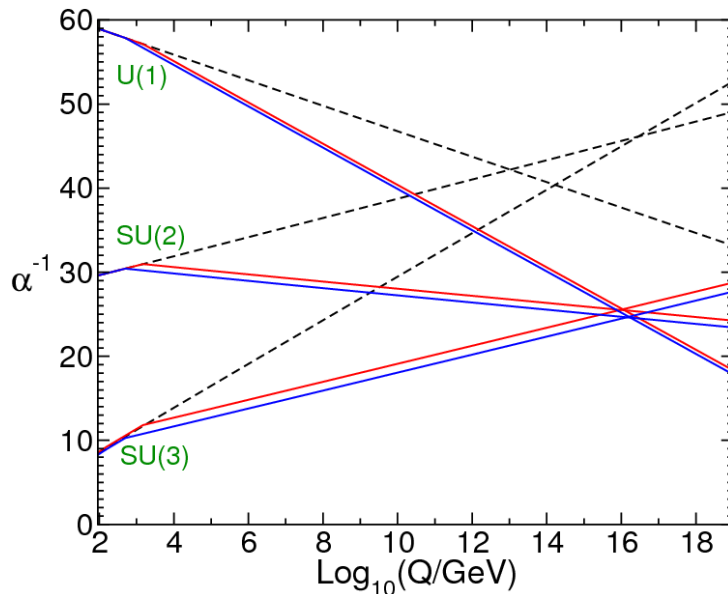
Figure 1.18: *Evolution of the force strength as a function of the energy scale as predicted by the Standard Model and the MSSM [39].*

Experimentally, these particles can manifest themselves through direct production in accelerator experiments such as the LHC. Indeed, most of the SUSY models include a conserved number called R-parity [40, 41], which is 1 for ordinary particles and −1 for super-partners. It follows that there is a Lightest Supersymmetric Particle (LSP) which is present in all super-partner decay final states. This neutral and sterile particle is also a good candidate for dark matter. Indirect searches also make use of the fact that new heavy particles contribute to the loop processes and modify the expected production rates or branching ratios.

1.6.4 Consequences on the Higgs boson

The MSSM (Minimal Super Symmetric Model), which is the simplest SUSY model, requires two Higgs doublets, with vacuum expectation value v_1 and v_2. The ratio of these two vacuum expectation value $\tan(\beta)$ is an important parameter of the model. After symmetry breaking, five physical fields subsist: three neutral bosons h^0, H^0, A^0 and two charged fields H^+ and H^-.

Conclusion

The Standard Model is a theory under construction since the middle of the 20$^{\text{th}}$ century and has proven to be very successful in describing the experimental results. The last missing pieces of this model, the Higgs boson, was discovered at the LHC in 2012, consolidating the Standard Model once again. The starting era of the Higgs sector will hopefully bring new confirmations of this model, or surprises that will force us to update our current vision of matter.

STATISTICAL FRAMEWORK

> **"** *I think it is much more interesting to live with uncertainty than to live with answers that might be wrong.* **"**
>
> RICHARD FEYNMAN

Chapter content

Given the probabilistic nature of the collisions at LHC and the low number of expected events in Higgs searches, a statistical framework to interpret its results is necessary, especially to disentangle a signal from an unfortunate background fluctuation. It is also important for measurement purposes, *i.e.* finding the value of the parameter of interest that best fit the data. For more details, see for instance Ref. [42].

Statistical tools are implemented in the `RooFit` tool-kit [43] part of the `ROOT` data analysis framework [44], intensively used in all this thesis work and in this chapter.

2.1 Model and likelihood

2.1.1 Problem

The first step consist in modelling the problem. For a given final state and experimental conditions, the Standard Model can predict the number of expected events in data, K. The probability to observe

N events in our dataset is given by the Poisson probability law (Fig. 2.1):

$$\mathcal{P}_K(N) = \frac{K^N}{N!}e^{-K} \tag{2.1}$$
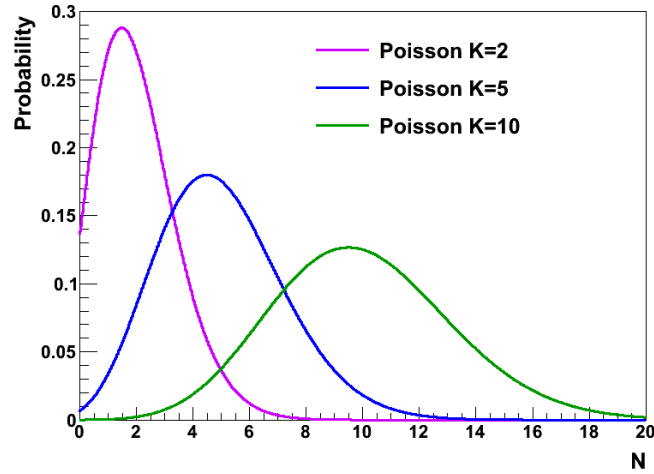
Figure 2.1: *Poisson distribution (NB: $P_K(0) = e^{-K}$).*

In case the data is divided into several bins of a given observable $\mathcal{X}$ (the $\gamma\gamma$ invariant mass for instance), each bin contains n_i events such that $\sum_i n_i = N$. The expected number of signal events in each bin s_i can be predicted and the number of background b_i can be estimated from Monte Carlo studies or data control regions. The total number of expected events in each bin is then $k_i = \mu s_i + b_i$ where μ is the signal strength $\frac{\sigma_{obs}}{\sigma_{exp}}$ (where σ_{exp} is the expected cross-section) which quantifies the number of signal events observed in the data. $\mu = 1$ corresponds to the Standard Model, while $\mu = 0$ corresponds to the case where no signal is observed.

2.1.2 Probablility density functions (pdf)

We assume that the number of events observed in each bin n_i follows a Poisson law with expectation $E[n_i] = \mu s_i + b_i$. The probability (or likelihood) of observing n_i events in bin i is then:

$$\mathcal{L}_i = \frac{(\mu s_i + b_i)^{n_i}}{n_i!}e^{-(\mu s_i + b_i)} \tag{2.2}$$

The probability to observe the full spectrum of the observable $\mathcal{X}$ is given by the product of the probabilities in each of the bins:

$$\mathcal{L}_{binned} = \prod_{i=1}^{N_{bins}} \frac{(\mu s_i + b_i)^{n_i}}{n_i!}e^{-(\mu s_i + b_i)} \tag{2.3}$$

This can be extended to the case of an infinite number of bins, that thus contain either one or zero event, leading to the unbinned likelihood:

$$\mathcal{L}_{unbinned} = \frac{1}{N_{evt}!}e^{-(\mu S + B)} \prod_{i=1}^{N_{evt}} (\mu S f_S(x_i) + B f_B(x_i)) \tag{2.4}$$

where the following notations are used:

- x_i is the measured value of observable $\mathcal{X}$ for event i;

- S and B are the total number of signal and background events;

- f_s and f_b are the probability density functions (*pdf*) of signal and background, each of them being normalized to 1 independently.

In both cases, binned and unbinned, $\mathcal{L}$ quantifies the compatibility between the observed data and the number of predicted events, for a given hypothesis μ.

More on likelihoods formulae:

Other formulae may be used for the likelihood:

- $\mathcal{L}_{unbinned}$ can also be written, in an equivalent way to Equation 2.4:

$$\mathcal{L}_{unbinned} = \frac{1}{N_{evt}!} e^{-(\mu S + B)} (\mu S + B)^{N_{evt}} \prod_{i=1}^{N_{evt}} \frac{1}{(\mu S + B)} (\mu S f_S(x_i) + B f_B(x_i)) \qquad (2.5)$$

This is equivalent to use the normalized *pdf* $\lambda(x) = \frac{\mu f_S(x) + f_B(x)}{\mu S + B}$. Indeed, since f_s et f_b are separately normalized to 1, $\int \lambda(x)dx = \frac{\mu S + B}{\mu S + B} = 1$.

- Equivalence between binned and unbinned likelihood (see also [45]): Let's consider the simple example where the dataset is cut into two regions. The part A contains events from 1 to P, the region B contains events from $P + 1$ to N. If one neglects the factorial, which is independent from the parameter of interest μ and only changes the normalization, the likelihood becomes:

$$\begin{aligned}
\mathcal{L}_{unbinned} &= e^{-(\mu S + B)} \prod_{i=1}^{N_{evt}} (\mu S f_S(x_i) + B f_B(x_i)) \\
&= e^{-(\mu S_A + B_A)} e^{-(\mu S_B + B_B)} \left[\prod_{i=1}^{P} (\mu S \frac{S_A}{S} + B \frac{B_A}{B}) \times \prod_{i=P+1}^{N} (\mu S \frac{S_B}{S} + B \frac{B_B}{B}) \right] \quad (2.6) \\
&= \prod_{i=1}^{N_{bins}} (\mu s_i + b_i)^{n_i} e^{-(\mu s_i + b_i)}
\end{aligned}$$

where $N_{bins} = 2$ and we have used $f_s(x_i) = \frac{S_A}{S}, \forall x_i \in A$ and similar formula for B.

2.1.3 Systematics uncertainties

In a more general way, the likelihood depends on one parameter of interest, here μ, but also on other parameters that are not the measured quantity but are needed to describe the model. This is the case for the parameters describing the signal and background shapes for example. These parameters, called nuisance parameters are grouped together in the notation θ. The likelihood is then:

$$\mathcal{L}_{unbinned}(\mu, \theta) = \frac{1}{N_{evt}!} e^{-(\mu S(\theta) + B)} \prod_{i=1}^{N_{evt}} (\mu S(\theta) f_S(x_i, \theta) + B f_B(x_i, \theta)) \qquad (2.7)$$

To account for systematics uncertainties, the number of predicted signal events is allowed to vary, in a reasonable way, *i.e.* we replace N_s by $N_s \times (1 + \delta\theta)$ where δ is the value of the systematics (in fraction of the event yield) estimated separately and θ is the so-called nuisance parameter, whose default value is 0 (*i.e.* no change of N_s). θ is a free parameter, but one does not want the systematics effect to be far from the expected value determined from physics studies δ. To prevent this, the nuisance parameters are constrained with a Gaussian of mean value $\tilde{\theta} = 0$ and $\sigma \equiv 1$: $\mathcal{G}(\theta, \tilde{\theta}, 1)$. θ is allowed to

vary in the range $\pm 5\sigma$ only. $\tilde{\theta}$ is called global observable. Its default value is 0 but this can be changed in some circumstances.

The form $N_s \times (1 + \delta\theta) \times \mathcal{G}(\theta, \tilde{\theta}, 1)$ allows the number of signal to become smaller than the predicted one. For some parameters, this is not wanted. In such cases, a log-normal form is used instead (see Fig. 2.2):

$$N_s \times exp \left\{ \theta \sqrt{log(1 + \delta^2)} \right\} \times \mathcal{G}(\theta, \tilde{\theta}, 1) \tag{2.8}$$
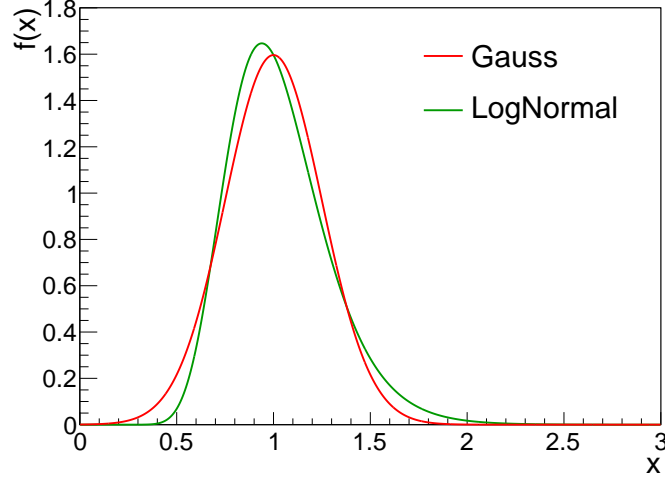
Figure 2.2: *Comparison of log-normal and Gaussian shapes with $\sigma = 0.25$.*

2.1.4 Complete model

The final model introducing all nuisance parameters and constraints is written:

$$\mathcal{M} = N_S \times \prod_{syst} \left[(1 + \delta_{syst}\theta_{syst}) \times \mathcal{G}(\theta_{syst}, \tilde{\theta}_{syst}, 1) \right] \times f_S(x; \theta_{S,shape} + N_B \times f_B(x; \theta_{B,shape}) \tag{2.9}$$

out of which the likelihood is defined:

$$\mathcal{L}_{unbinned}(\mu, \theta) = \frac{1}{N_{evt}!} e^{-(\mu S(\theta) + B)} \prod_{i=1}^{N_{evt}} \mathcal{M}(x_i, \theta) \tag{2.10}$$

As an example in the following, the simple model of Figure 2.3 will be used. It is defined by the following criteria:

- The signal is modelled by a simple Gaussian of fixed peak position and width. The number of signal event is N_S.

- The background normalization N_B is estimated form a fit to data only, from an exponential shape, whose slope is an unconstrained nuisance parameter.

- For illustration purposes, when specified, a 10% systematic uncertainty will be applied on the signal yield efficiency. The associated nuisance parameter is constrained by a Gaussian of width 1 and allowed to vary within $\pm 5\sigma$.
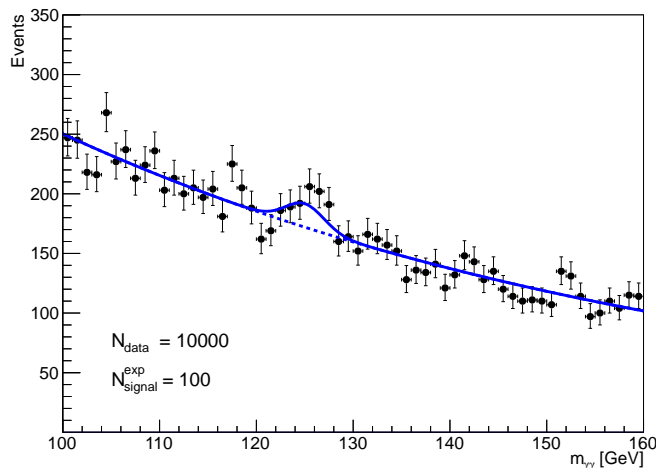
Figure 2.3: *Example of model showing expected signal at $m_H = 125$ GeV and Monte Carlo data. The dashed line shows the background-only pdf.*

2.2 Hypothesis testing and test statistics

2.2.1 Hypothesis

When trying to quantify the agreement of data with a given hypothesis, several cases may arise.

In case no signal was observed, one tries to set a limit on its production cross-section. This is done by rejecting the S+B hypothesis ($\mathcal{H}_0$) versus the B-only hypothesis ($\mathcal{H}_1$).

On the contrary, if an excess of event is observed, one may want to quantify the agreement compatibility of the data with the background-only hypothesis ($\mathcal{H}_0$).

$\mathcal{H}_0$ is called the null hypothesis and is the one we want to validate. This is done by rejecting the alternate $\mathcal{H}_1$ hypothesis.

2.2.2 Test statistics for LHC

Several test statistics can be envisaged, depending on the treatment of the nuisance parameters. The LHC choice is to use a profile likelihood ratio, defined in Equation 2.11. $\hat{\mu}$ and $\hat{\theta}$ designate the values of the parameter of interest μ and of the nuisance parameters θ giving the global maximum of the likelihood $\mathcal{L}$. $\hat{\hat{\theta}}$ is the value of the nuisance parameters that maximize the likelihood for a given value of μ. Since $\mathcal{L}(\mu, \hat{\hat{\theta}}) < \mathcal{L}(\hat{\mu}, \hat{\theta})$, the test statistic of Equation 2.11 is expected to be always positive.

$$q_\mu = -2 \, ln \left(\frac{\mathcal{L}(\mu, \hat{\hat{\theta}})}{\mathcal{L}(\hat{\mu}, \hat{\theta})} \right) = -2 \, ln\lambda(\mu) \qquad (2.11)$$

The value of a test statistic q_μ can be estimated for the observed data. The next question is whether this value is consistent with the μ hypothesis. To quantify this agreement, the distributions of q_μ for the $\mathcal{H}_0$ and $\mathcal{H}_1$ hypotheses are needed.

Note that, this test statistics can be adapted to other parameter of interest than μ.

2.2.3 Distribution from Monte Carlo (toys)

A pseudo-experiment consists in generating a dataset according to expected model, whose nuisance parameters are fitted to the observed data. The parameter of interest μ is fixed to the desired value μ' to get the distribution of q_μ under the hypothesis μ' that is denoted $f(q_\mu | \mu')$. This takes into account the

statistical fluctuation of the data, since the number of generated events follows a Poisson distribution with expectation is the number of observed events in the dataset.

To simulate the systematics uncertainties, the global observables, also called auxiliary measurements, are used [46]. The mean of the Gaussian used to constrain the nuisance parameter are shifted by a random value for each toy (this is called the unconditional ensemble [47]). This changes the estimation of the systematics uncertainty.

The value of the test statistics is then computed for each toy and its distribution can be deduced. This method is very time- and CPU-consuming, especially when the number of event becomes large. In this asymptotic limit, the distribution of the test statistic can be approximated by an analytic function.

2.2.4   Asymptotics formulae for discovery

In the case of discovery, one tries to reject the hypothesis according to which the excess could be done to a background fluctuation. One then tests the background-only hypothesis. To avoid counting the downwards fluctuations as deviations from the expectations, the test statistics is set to 0 if the fitted signal is negative:

$$q_0 = \begin{cases} -2\,ln\lambda(0) & \text{if } \hat{\mu} \geq 0 \\ 0 & \text{if } \hat{\mu} < 0 \end{cases} \tag{2.12}$$

The p-value defined in Equation 2.13 is the probability that the number of observed events in the background-only hypothesis is at least equal to the observed excess in data. If this probability is low, the data looks compatible with the presence of a signal. The p-value is translated into a significance Z, corresponding to the distance to the mean of a Gaussian of width 1, such that the integral of the tail is equal to the p-value (Fig. 2.4). Discovery is claimed when the significance reaches 5σ, *i.e.* a p-value of the order of 10^{-7}. For large S+B, the significance can be further approximated by $S/\sqrt{B}$.

$$p_0 = \int_{q_{0,obs}}^{\infty} f(q_0|\mu' = 0) \tag{2.13}$$
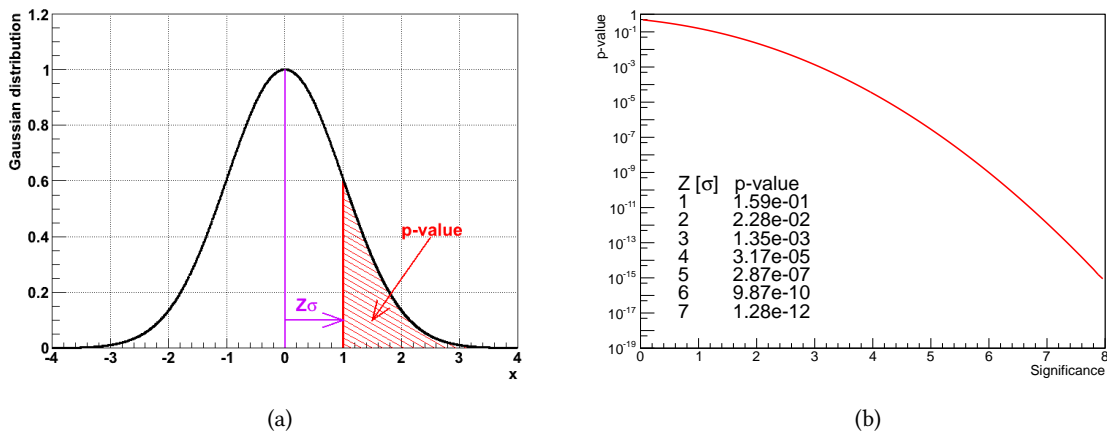
Figure 2.4: *Relation between p-value and significance Z.*

In the case of large statistics, it was shown [48] that the test statistics distribution can be approximated with an analytical form:

$$f(q_0|\mu' = 0) = \frac{1}{2}\delta(q_0) + \frac{1}{2\sqrt{2\pi q_0}}e^{-q_0/2} \tag{2.14}$$

It follows that the significance is simply: $Z = \sqrt{q_0}$.

Same formula can be derived for the more general case $f(q_\mu|\mu')$ (see Ref. [48] for details and demonstrations or [49]). A comparison of the q_μ distributions for two hypotheses is displayed in Figure 2.5 for $N_S = 100$ and $N_{obs} = 10,000$.
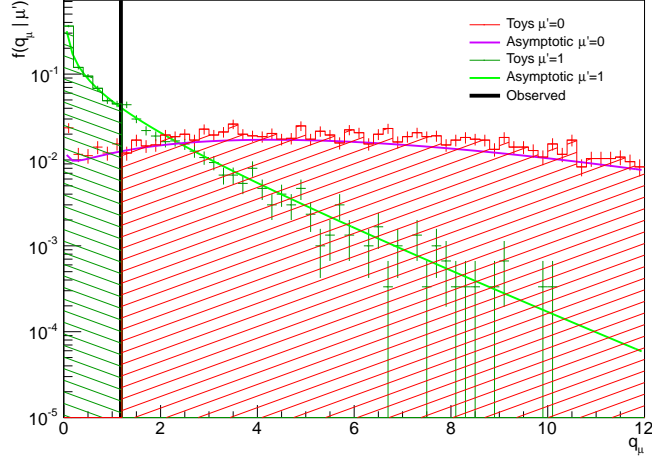
Figure 2.5: *Comparison of the test statistics distribution for two hypothesis, between toys and asymptotic for the model and dataset depicted in Figure 2.3. Green distributions correspond to $f(q_1|\mu' = 0)$ and red distributions represent $f(q_1|\mu' = 1)$. The dashed green area quantifies the agreement between the data (solid black line) and the hypothesis $\mu = 0$, the red area to the hypothesis $\mu = 1$.*

2.2.5 Asimov dataset

The expected values for the parameters are estimated from the so-called Asimov dataset [48]. It is a single representative dataset in which all the statistical fluctuations are suppressed (Fig. 2.6). The number of events in each bin, n_i, is taken to be the expected ones, with a signal strength μ_A. The values of the nuisance parameters are the ones fitted on the real data in the hypothesis μ_A. The same statistical procedure can then be repeated for this dataset, using the test statistics of Equation 2.11.
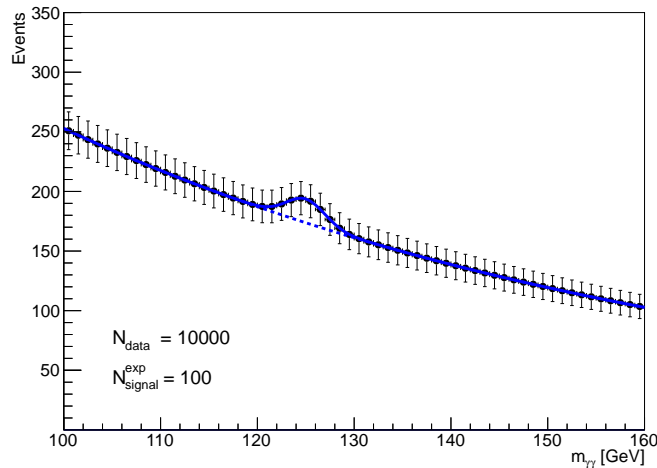
Figure 2.6: *Asimov dataset corresponding to the model of Figure 2.3 with $\mu_A = 1$.*

Categories

It can be shown that dividing the inclusive dataset into categories with different S/B enhances the analysis sensitivity to the signal since the total significance in the case of categories[1] $Z = Z_1 \oplus Z_2$ is larger than the significance of the inclusive dataset. Similarly to the binned case, the likelihood of a categorized dataset is the product of the likelihood is each of the categories, whether they use a binned or unbinned likelihood model.

2.3 Best fit value and profiling

2.3.1 General case

The best fit values $\hat{\mu}$ are obtained by minimizing the likelihood. An iterative way of finding them is to scan the allowed range for the parameter of interest, fix it, and perform a fit of all the remaining parameters. The value of the likelihood one obtains is used to make profile plots as the one illustrated in Figure 2.7.
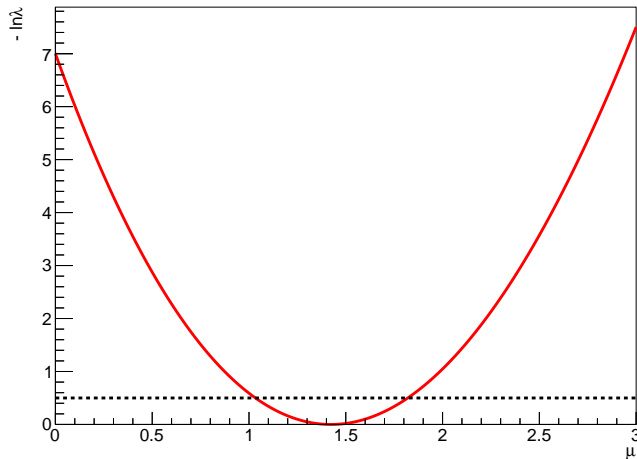
Figure 2.7: *μ likelihood scan (profile).*

When introducing systematics uncertainties into the model, the profile of Figure 2.7 is broadened.

2.3.2 Fit with low number of events

In the cases where there are very few observed events, strange features may happen. Considering for instance the (simulated) dataset from Figure 2.10, the fitted signal is $\mu = -15$, with negative *pdf* in some mass range, which is not physical.

There are several reasons for this behaviour. The first one is the μ dependence of the likelihood. Starting from the unbinned likelihood of Equation 2.4, it can be simplified to (considering only the μ-dependant contributions)

$$\mathcal{L}_{unbinned} = e^{-(\mu S + B)} \tag{2.15}$$

in the case $N_{evt} = 0$. This expression is still valid to a good approximation when the observed events are far from the signal region, where $f_S(x_i) << 1$ for each of the x_i's where the likelihood is evaluated.

The log-likelihood is then:

$$-\ln\left(\mathcal{L}\right) = \mu S + B \tag{2.16}$$

---

[1]Where $\oplus$ designates a quadratic sum.

This dependence is checked in Figure 2.8 where the `RooFit` likelihood is plotted as a function of μ. It is superimposed with the function $\mathcal{Y} = \mu \times S + k$ where k is a constant.

The function $\mathcal{Y}$ tends towards $-\infty$ when $\mu \to -\infty$ such that the minimum of the function corresponds to $\mu \to -\infty$.
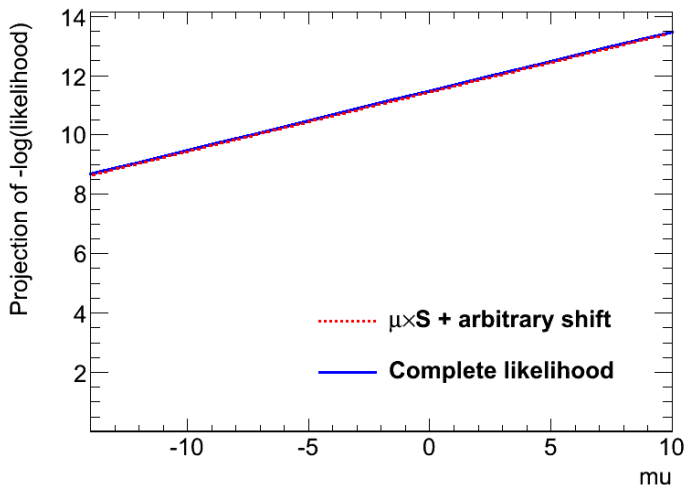
Figure 2.8: *Likelihood dependence with μ with no observed event in the signal region in the case $S = 0.2$.*

In practice, `RooFit` stops the computation when the total number of events become negative: $\mu \times S + B = 0$. Figure 2.9 illustrates this fact by showing the fitted μ as a function of the expected number of signal events S.
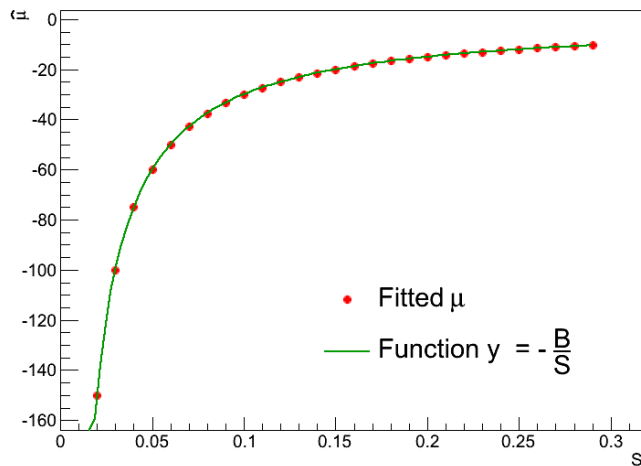
Figure 2.9: *Fitted μ, $\hat{\mu}$, versus the expected number of signal events S when no event is observed in the signal region.*

By definition, a *pdf* can not be negative. For each μ value, `RooFit` test the *pdf* positiveness, but only at mass points given in the dataset. For datasets with no points in large mass range, the *pdf* can become negative in this region without `RooFit` warnings. This problem is solved by adding some events in the signal region with very small weight: they do not modify the likelihood value, but force the program to test the positiveness of the *pdf* in the region where it can become negative, *i.e.* in the region where the sign of μ plays a role [50]. Figure 2.10 shows the result of the introduction of ghost events in the dataset: the fit is stopped at the μ value where the *pdf* touches 0.

(a) Without ghosts

(b) With ghosts
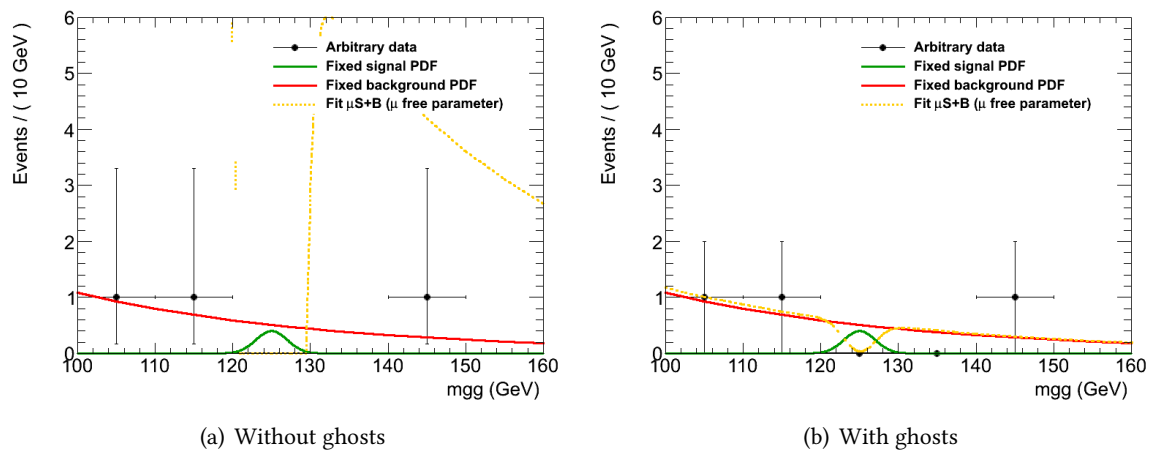
Figure 2.10: *Effect of ghost events. On the left, no ghost are included and the fit is stopped when $\mu = -\frac{B}{S}$. On the right, ghosts are included, allowing the fit to be stopped before the pdf becomes negative.*

Part II

Experimental setup and performances

3

THE LARGE HADRON COLLIDER

> ❝ *When a distinguished but elderly scientist states that something*
> *is possible, he is almost certainly right.*
> *When he states that something is impossible,*
> *he is very probably wrong.* ❞
>
> CLARKE'S FIRST LAW

Chapter content

The Large Hadron Collider (LHC) [51] is the latest particle accelerator located at the European laboratory for particle physics (historically known as CERN) at Geneva, Switzerland. It was foreseen to collide heavy ions and protons at an energy one order of magnitude higher than previous accelerators and a rate thousand times higher. Even though it operated at about half its nominal energy in 2010-2012 it produced an amount of data sufficient for new discoveries by the four detectors examining the products of the collisions.

3.1 Motivations

As was discussed in Chapter 1, at the end of the 1990's, the Standard Model of particle physics was well established and consolidated by experimental observations. However, some troubles persist. For instance, the non-observation of a Higgs boson was really puzzling since, without this scalar boson, the gauge bosons masses can not be explained within the Standard Model framework. Huge efforts were then made to observe a particle compatible with the Higgs boson. Together with other constraints coming from the SUSY side for example, this leads to the design of the largest accelerator up to date.

The LHC can collide protons at a centre of mass energy $\sqrt{s} = 14$ TeV in its nominal configuration. It also has the ability to accelerate heavy ions, mainly lead, for studying the first seconds of the universe with quark-gluon plasmas. The work performed during this thesis is dedicated to the proton-proton collisions studies and the following will only refer to this operating mode.

The beam characteristics driven both by those physical goals and technical constraints are outlined in the next section.

3.2   The machine

3.2.1   Beam and collision characteristics

The restricted constraints from theory or previous experiments motivate physicists to search for new phenomena in a large energy range. The choice for a hadron collider is then natural. Indeed, hadrons are composite particles made of partons, each parton carrying a random fraction of the total hadron energy. The reactions initiated by partons can then cover a large energy range. On top of that, for a given accelerator radius, protons can be accelerated at higher energies than electrons because they loose less energy through synchroton radiations, whose probability is proportional to $m_{particle}^{-4}$.

The choice of a proton-proton instead of proton-antiprotons like at Tevatron is driven by the low production probability, *i.e.* small cross section, of the sought processes. A large number of collisions will then be necessary to observe and study them with enough statistics. Such a high collision rate can not be achieved with anti-protons because they are difficult to produce and they can't be stored for large amounts of time in quantities sufficient to create beams. For this reason, LHC choice is to use protons. However, this required some technological developments as it is not possible for two beams with same charge to move in opposite direction in the same magnetic field. LHC magnets have been designed especially to create a field with opposite sign for each beam (see sec. 3.2.2).

For cost reasons, it was decided to build the LHC in the same circular tunnel occupied by the LEP with a circumference of 26.7 km, at 50 to 150 m underground. Coils are used to bend particle trajectories with a radius related to the magnetic field strength and the particle energy:

$$B\rho \propto \frac{p}{q} \qquad (3.1)$$

where q is the particle charge, p its momentum and ρ the radius of its curved trajectory in the magnetic field B.

This governs the maximal energy a particle can reach in a ring of about 27 km circumference. For a maximal magnetic field of the order of 8 T provided by superconducting magnets (limited by the technology available at the time of the LHC design) and protons with charge $q = e$, the maximal momentum is of the order of 10 TeV. This coarse approximation has to be completed and one has to take into account the energy losses due to the proton radiations. The final expected energy for each proton is 7 TeV at nominal design performances.

Protons are grouped into bunches of 10^{11} to maximize the interaction probability at each bunch crossing. Before each of the four interaction points, the bunches are squeezed, which increase the number of collision per bunch crossing and so the event rate. An event is associated to two colliding bunches, identified with a Bunch Crossing Identifier (BCID).

The main characteristics of the LHC beams are gathered in Table 3.1 for the nominal design performances.

3.2.2   Technical details

The LHC is the larger proton collider in operation as of today provoking collisions at four interaction points. The product of these collisions are detected by the four main experiments on the ring: ALICE is mainly devoted to the heavy ions collisions analysis, concentrating on the quark-gluon plasma observation to understand the first instants of the universe. LHCb is designed for b physics and the CP violation study. CMS and, finally, ATLAS, are general purpose experiments, designed for Higgs and SUSY observation.

LEP previous accelerator was dismantled but other previous CERN accelerators are still used to prepare the beams before injection in the LHC (see Fig. 3.1). Protons in the LHC ring are organized in bunches of 10^{11} protons, bunches are themselves grouped in several bunch trains.

The protons source, an hydrogen gas bottle, is located in front of the linear accelerator LINAC2, bringing the protons from 0 to 50 MeV after the unique hydrogen electron have been unbounded

	Nominal	2010	2011	2012
Circumference		26.7 km		
Injection energy per proton		450 GeV		
$\sqrt{s}$ [TeV]	14	7		8
Luminosity peak (cm^{-2}s^{-1})	10^{34}	2.10^{32}	$3.5.10^{33}$	$7.5 10^{33}$
Bunch per beam k	2808	368	1380	
Protons per bunch N ($\times 10^{11}$)	1.15	1.2	1.45	1.7
Δt (ns)	25	150	50	
Bunch length (along z) [mm]		56		48
Transverse dimension at the interaction point		25 to 12 μm		

Table 3.1: *Main characteristics of the LHC for nominal design. Values reached during LHC Run I are also presented. $\sqrt{s}$ is the centre of mass energy and Δt is the interval between two bunch crossings. Luminosity definition is presented in Section 3.2.3.*
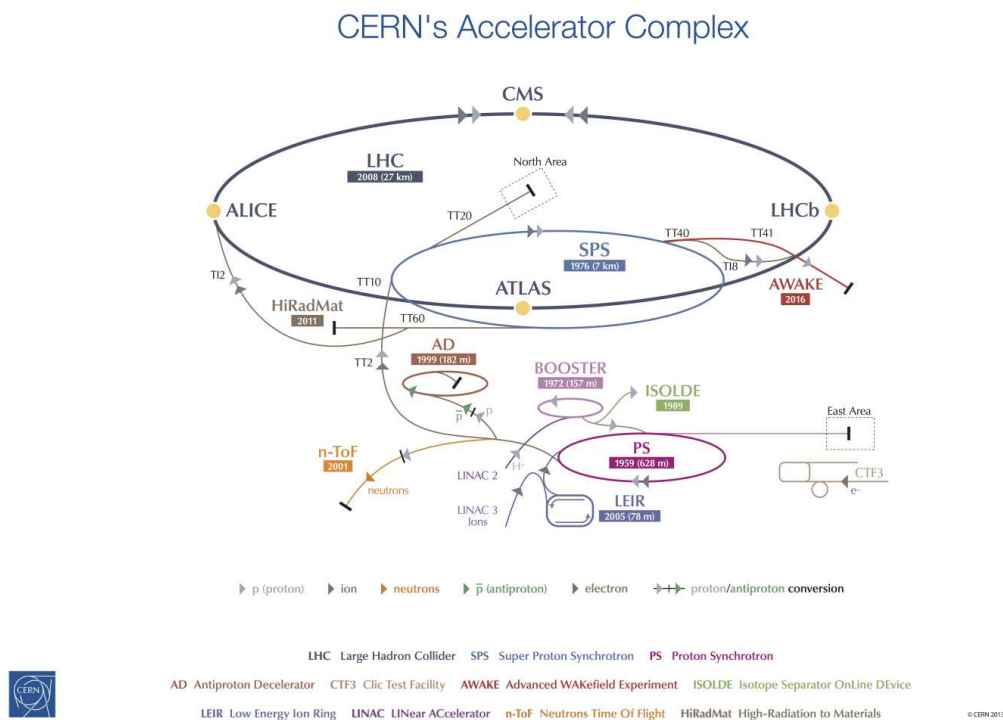
Figure 3.1: *CERN accelerator complex [52].*

from the nucleus. The 80 m long LINAC2 also creates the bunch structure of the beams. Protons are then injected into the 1.57 m circular Proton Synchroton Booster (PSB). When protons are extracted from the PSB, they have a 1.4 GeV energy. The 628 m ring Proton Synchroton (PS) continues the acceleration process in such a way that the particle enter the Super Proton Synchroton with a 26 GeV energy. The SPS, an underground 6.9 km ring, carries on the last pre-LHC threshold by increasing the protons energy up to 450 GeV, after what proton bunches can be injected into the LHC ring, at two injection points (one for each beam), both close to the ATLAS experiment. Around twenty minutes are then necessary to bring the protons to their maximal energy of a few TeV before initiating the collisions.

Beam paths inside the LHC is imposed by a large magnet system: dipoles bend the particle trajectories, while quadrupoles focus the beams. Sextupoles are also necessary to correct for chromaticity effects caused by the energy spread of the particles inside a single beam. All particles are not bent exactly with the same radius by quadrupole, that can cause instabilities after a large number of turns.

The two beams have to be deflected by opposite magnetic fields. This is achieved with dipoles as illustrated in Figure 3.2(a). The resulting magnetic field is also shown in Figure 3.2(b), where the two beam pipes clearly appear, together with the magnetic field sign. For 7 TeV protons, the required magnetic field is 8.3 T, which is achievable only by superconducting magnets operating at a 1.9 K temperature.

(a)   (b)
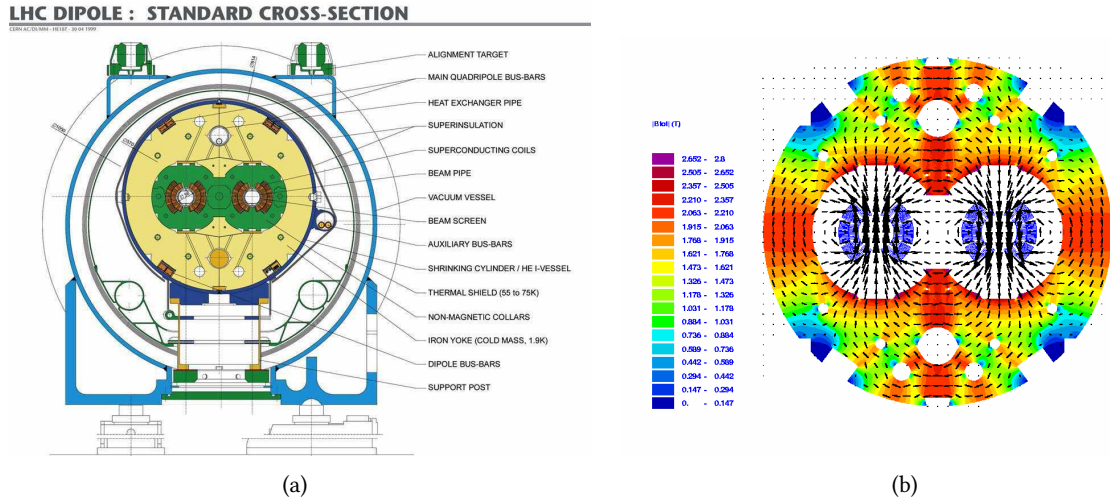
Figure 3.2: *LHC dipoles (a) and the resulting magnetic field (b)* [53]*.*

Special areas require their own magnet system. In the region close to the interaction point, beams are further squeezed in order to increase the effective crossing area and thus the interaction probability. Finally, other magnets are used in the dump region in order to safely extract the beams from the ring.

3.2.3 Luminosity

The instantaneous luminosity is the characteristic parameter of an accelerator. It is directly related to the collision rate through the formula:

$$\frac{dN}{dt} = L \times \sigma \times \epsilon \tag{3.2}$$

where σ is the cross-section of a given process $initial \rightarrow final$ state, ϵ is the detector efficiency and acceptance. L traditional unit is $cm^{-2}s^{-1}$.

The luminosity can also be computed from variables depending only on the beam properties:

$$L = \frac{kN^2 f}{4\pi\sigma_x^*\sigma_y^*}\mathcal{F} \tag{3.3}$$

where:

f is the particle frequency in the ring, close to 11 246 MHz.

N corresponds to the number of protons per bunch $\approx 10^{11}$

k stands for the number of bunches per beam (design value is 2808).

σ^* is the beam size in the transverse plane measured at the collision point: $\sigma_x^* = \sigma_y^* \sim 15 \ \mu$m.

$\mathcal{F}$ is the geometric luminosity reduction factor due to the crossing angle between the beams at the interaction point (nominally $285 \, \mu$rad).

A good knowledge of the expected beam properties give access to a good expectation value for the luminosity. The luminosity can then be used in two ways from formula 3.2: either predict the number of expected background or signal events from a prior cross section value, or measure a cross section from a number of observed events in data.

To reduce the uncertainty on the luminosity and hence on the measured cross sections, its value is monitored regularly during the data-taking period. A method, the Van Der Meer scans, is a technique consisting in measuring the beam transverse dimensions to access the luminosity *via* formula 3.3.

Figure 3.3 shows the globally increasing peak luminosity as a function of the day in 2010, 2011 and 2012.
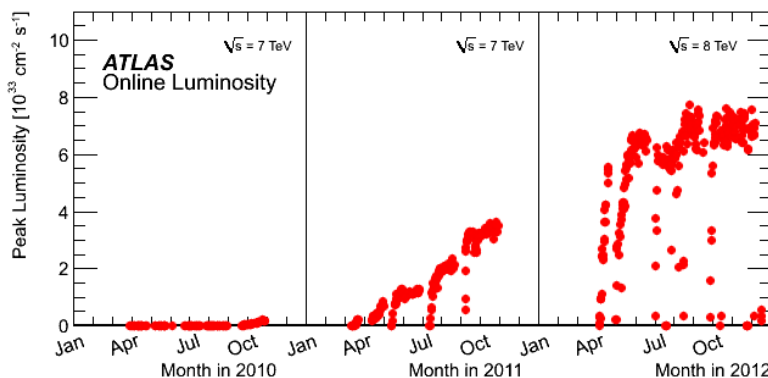
Figure 3.3: *Peak luminosity as a function of time during LHC Run I (2010 to 2012)* [54].

Usually, physics analyses use the integrated luminosity, $\int L dt$, expressed in fb^{-1}, where $1 \, \text{b} = 10^{-24} \text{cm}^2$.

3.3 Expectations for physics

The cross sections of most common processes expected in the Standard Model hypothesis are shown in Figure 3.4 for both pp and $p\bar{p}$ collisions as a function of $\sqrt{s}$. Tevatron 1 TeV energy together with the expected and effective LHC operating energy are highlighted with vertical lines. The cut-off at 4 TeV corresponds to the switch from pp to $p\bar{p}$ initial states.

Colliding hadrons have advantages in terms of energy range able to be probed, but makes precision measurement difficult for several reasons:

- The total energy involved in a collision is not measurable, which makes impossible the application of a total energy conservation law to retrieve missing information. However, experimental techniques, using the transverse energy only, exist and will be detailed in Chapter 4.

- They also suffer from theoretical defects, due to the imperfect knowledge of the hadron structure, described by parton density functions (PDF) (see Chap. 8). This leads to large theoretical uncertainties. However, a lot of theoretical progresses have been recently performed in order to reduce these uncertainties.

- Also due to the hadron substructure, several interactions can occur with a single proton collision: the hard scattering (HS), process involving the highest energy, can be accompanied by other soft interactions between the remaining partons. This phenomenon is called Underlying Event (UE) and is sketched in Figure 3.5.
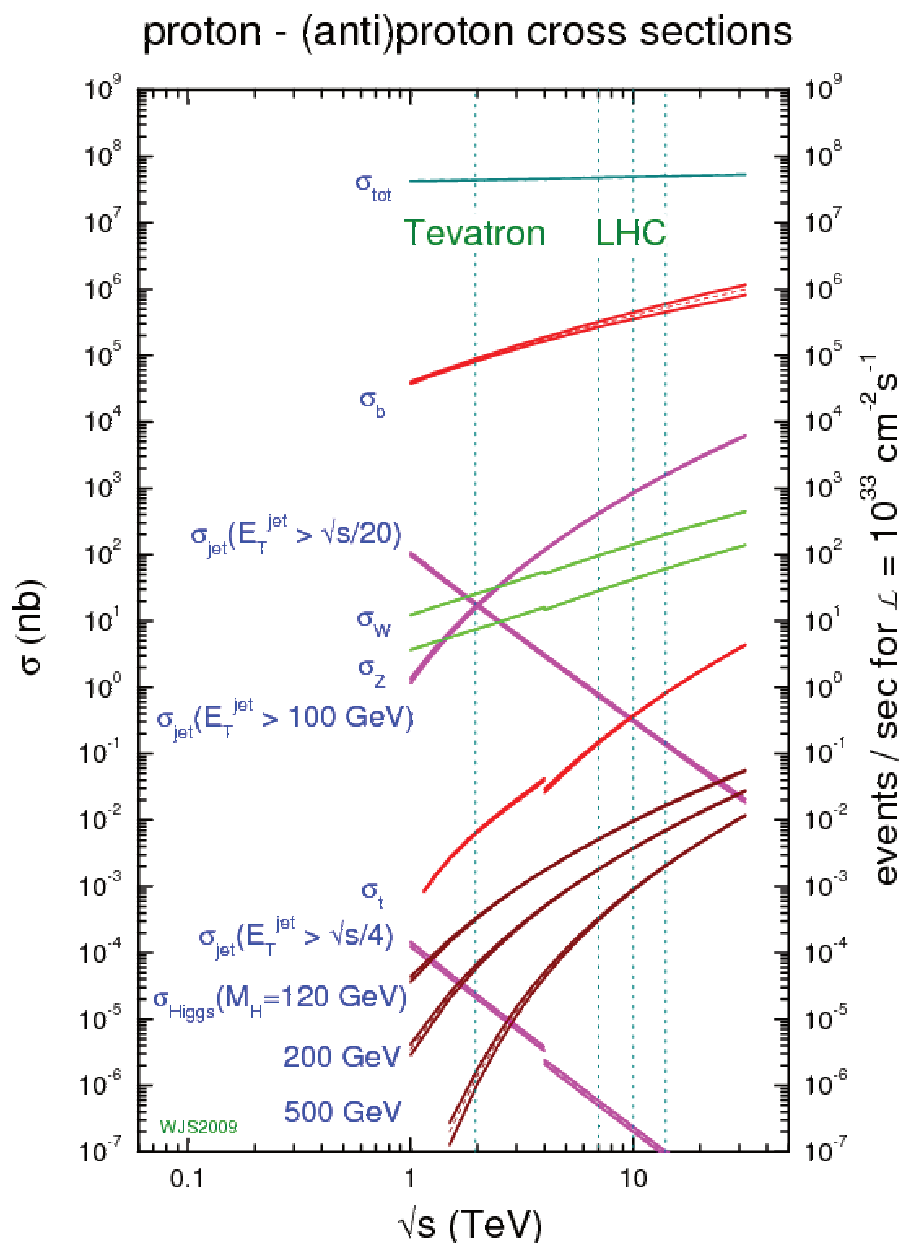
Figure 3.4: *Expected cross section of sought signals and main backgrounds as a function of the centre of mass energy for pp and $p\bar{p}$ collisions. Computations are performed up to NLO or NNLO with the corresponding MSTW2008 parton distribution set [55].*

- As Figure 3.4 shows, the processes of interest such as the Higgs boson production have considerably lower cross section than the pp scattering or the jet production. This require a high luminosity to observe such rare processes.

- The drawback of such a high luminosity is the high number of collisions that can occur in the same bunch crossing, called pile-up and increasing the number of particles detected in each event. The mean number of interaction per bunch crossing is about 20 in 2012 and corresponds to in-time pile-up (interaction between particles in the same bunch crossing than the interesting hard interaction) ant out-of-time pile-up (interactions during previous bunch crossing).
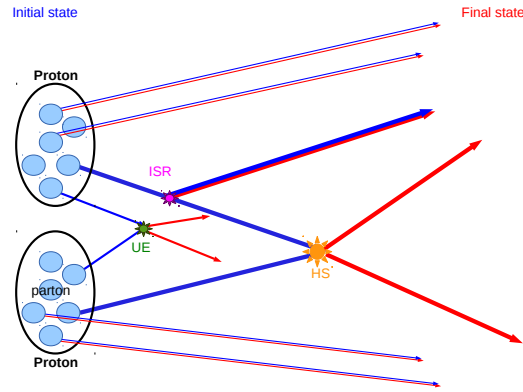
Figure 3.5: *Illustration of a proton-proton collision with a Hard Scattering and one Underlying Event reaction between remaining partons.*

This complicated environment and busy final states bring strict requirements on the detector design and performances.

3.4 Run I

The LHC first started on September 10th 2008. Unfortunately, after a few days of operation, on September 19th, a serious incident caused large damages to the infrastructure that required more than one year to be fixed.

The restart happened in 2010 at a centre of mass energy of 7 TeV. A luminosity of 40 pb^{-1} was collected. The year 2011 continued this campaign at the same centre of mass energy, increasing gradually the instantaneous luminosity. At the end of the year, a record of 5 fb^{-1} had been delivered to the high luminosity experiments.

In 2012, the centre of mass energy was increased to 8 TeV. During the data-taking period from March 2012 to January 2013, the integrated collected luminosity amounts to around 20 fb^{-1}.

Since the beginning of 2013, the LHC operations are paused for a long shut-down (LS1). This gives time to upgrade the machine in order to get it closer to its nominal energy of 14 TeV (probably 13 TeV).

THE ATLAS EXPERIMENT

> *The only way of discovering the limits of the possible is to venture a little way past them into the impossible.*
>
> CLARKE'S SECOND LAW

Chapter content

The ATLAS detector is one of the four main detectors scrutinizing the LHC collisions. Its design was driven by the will to find the mechanism responsible for the electroweak symmetry breaking, the most famous candidate being the Brout-Englert-Higgs mechanism. Other processes were also considered such as the direct search for supersymmetry.

4.1 Physical goals and required performances

ATLAS [56] is a general purpose detector that will observe a large variety of event topologies in proton-proton and heavy ions collisions. Its design takes into account this multi purpose requirements, with highlight on some physical objectives:

- The Higgs sector: the Higgs boson decays to a large number of particles leading to a large variety of final states. Given the huge hadronic activity at the LHC, the most promising ones are the $H \rightarrow \gamma\gamma$ and $H \rightarrow ZZ^* \rightarrow 4l$ with small branching fraction but clear signature. The diphoton channel study requires a very good photon identification, *i.e.* good rejection of particles faking photons such as π^0 (decaying to two collimated photons) in jets. Other channels such as $H \rightarrow b\bar{b}$ would be studied using VH associated production. A reliable b-tagging is thus desirable, correlated to a high precision secondary vertex reconstruction.

- Supersymmetry: events involving supersymmetry would, in the most common models of SUSY, contain a heavy weakly interacting particle that, similarly to neutrinos, would manifest itself through missing transverse energy in the event. To achieve a good resolution on missing transverse energy, good determination of the energy of all other objects including jets is needed.

- B physics: the B sector is also a centre stage to find matter-antimatter asymmetries, that could explain the apparent predominance of matter with respect to antimatter in the universe. In terms of detector performances, studying B mesons requires a good vertex resolution to identify displaced vertex due to the long B lifetime.

- Other processes are also considered. For example, exotic processes such as mini black hole and new heavy boson production that would involve particles with energies up to the TeV scale have also driven the required performance of the detector in terms of energy range at which a high precision energy, momentum and position reconstruction should work.

From these considerations, some constraints on the detector design and required performances can be deduced:

- An efficient displaced vertex finding, *i.e.* a precise track detector as close as possible to the interaction area;

- A good calorimeter system, with high granularity, that allows for a good separation between photons and jets, with a good energy resolution and optimal hermiticity in order not to miss any particles that would create fake missing energy;

- An effective muon detector with precise track measurement in a large momentum range;

- Due to the high luminosity, radiation resistant materials are essential.

These main requirements, combined with overall detector performance, lead to the final design outlined in the next section.

4.2 Physical constraints and design

4.2.1 Overview

Before describing the details of the detector, an overview of its general organization is given.

The processes described above will manifest themselves in the detector as a flow of particles originating from the interaction point and travelling in all directions. This bunch of particles contains only a finite list of stable particles in the sense that they have a lifetime long enough to be directly seen by the detector: electron, photon, muons and jets, created from an outgoing quark or gluon through hadronization. Their associated anti-particles interact with matter in a similar way. For this reason, unless otherwise specified, the term electron will designate in this manuscript both electron and positron; same caveat applies for muon. Other particles such as the Z or Higgs boson will decay into a combination of this list of stable particles before they can be seen by any of the detector subsystem. The task of the detector is to measure the four-momentum and identify each of the stable objects, allowing to retrieve the original particle information.

ATLAS layout is sketched in Figure 4.1. It has a cylindrical shape with its axis along the beam direction, completed by two end-caps at each end. The collision takes place at the interaction point, near the centre of the detector. The detector is made of several sub detectors arranged in four concentric layers. Closest to the interaction point, the tracking detector allows the survey of the charged particles trajectory, then the electromagnetic calorimeter measures the energy of electrons and photons. It is directly followed by the hadronic calorimeter measuring the jet properties. Finally, a specialized muon spectrometer occupies the outermost layer of the detector.

The tracking system, called Inner Detector, is made of several fine segmented layers hit by the charged particles. The connection of these hits forms the particle trajectories. The Inner Detector is immersed in a magnetic field generated by a central solenoid, that bends the particles path, with a curvature depending on their charge (sign) and momentum (radius). The track reconstruction thus allows to measure the particles charge and momentum.

The subsystems aiming at the energy measurement are the calorimeters. They stop most of the incoming particles that are destroyed to create a shower of secondary particles. The electromagnetic calorimeter surrounds the Inner Detector and stops the electrons and photons thanks to bremsstrahlung and conversion processes taking place when an electromagnetic particle goes through matter. The hadrons are more difficult to stop and require an additional hadronic calorimeter after the electromagnetic calorimeter.

Muons still escape from the calorimeters without losing all their energy, that's why a dedicated muon detector is needed at the outermost limit of ATLAS. Another magnetic field is set-up in this area, created by toroidal magnets that gives ATLAS its name (**A T**oroidal **L**HC **A**pparatu**S**).
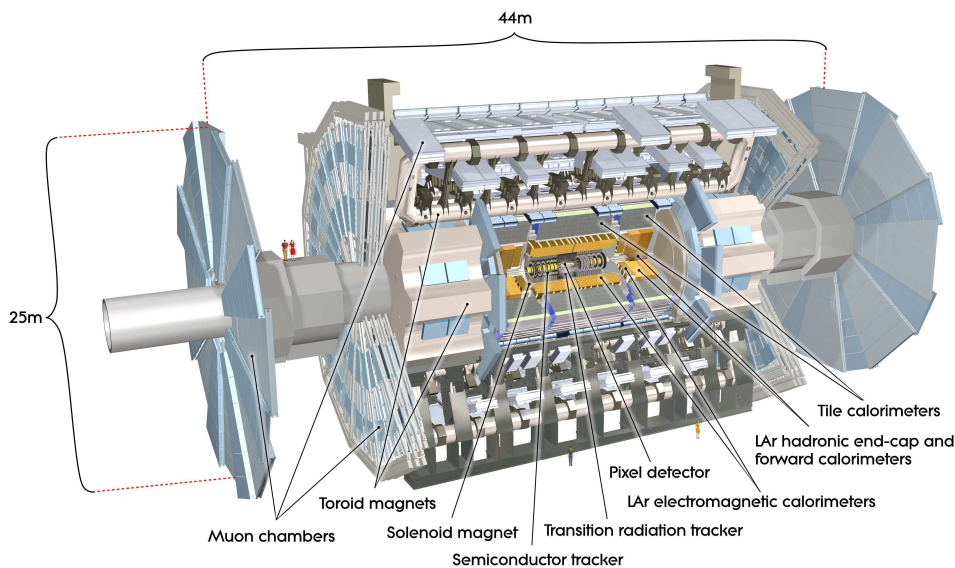
Figure 4.1: *Schematic view of the ATLAS detector with its sub-systems highlighted [57].*

Particle identification is possible thanks to the combination of all sub-detector information: for example, electrons and photons leave similar energy deposits in the electromagnetic calorimeter but electrons have an associated track in the Inner Detector while photons do not as they do not carry electric charge. Figure 4.2 summarizes the basic principles of particle identification.

Quarks and gluons will manifest themselves as jets, bunches of collimated particles. Jets are characterized by a group of non isolated particles (including charged tracks) concentrated in a narrow cone, associated with a large fraction of its energy deposited in the hadronic calorimeter.

Finally, neutrinos are weakly interacting only particles and will not leave any hint of their passage in the detector. The only way to access their presence is to use the momentum conservation law, abusively called energy conservation in the following. In an hadronic collision, the total fraction of the energy entering into the hard process is not accessible because only one parton of each proton is
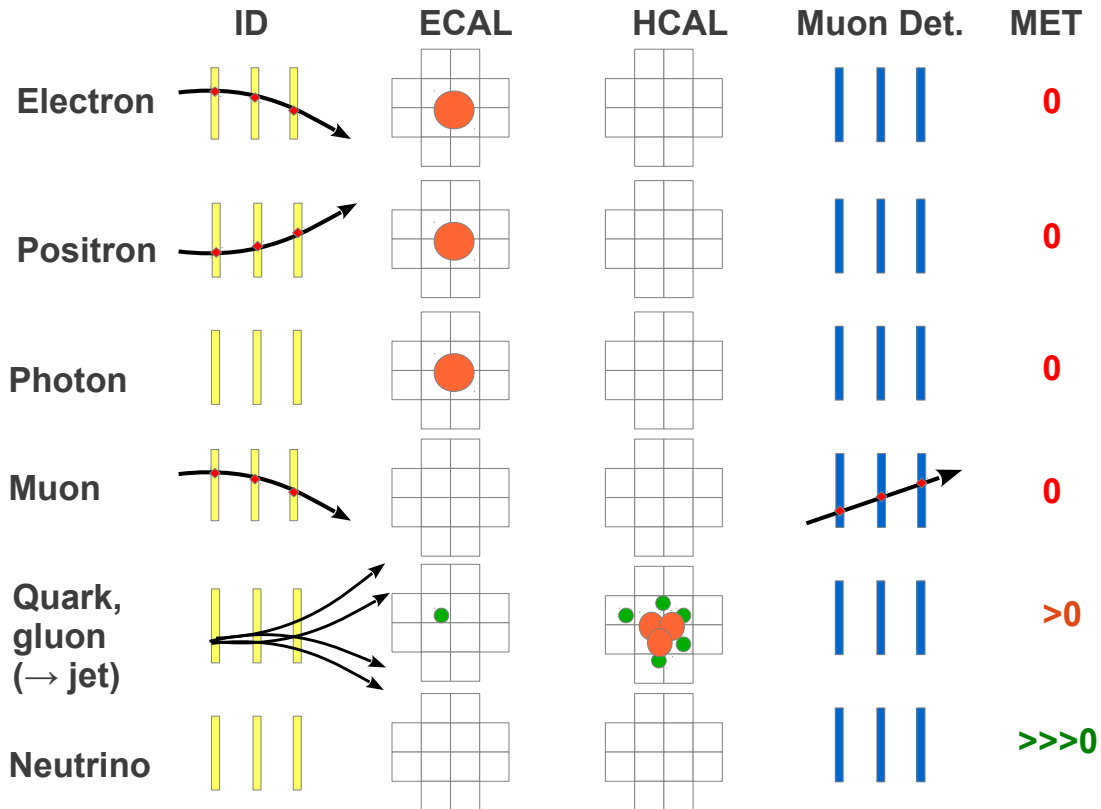
Figure 4.2: *Principle of particle identification by combining the information from all the sub-detectors: Inner tracking Detector, Electromagnetic CALorimeter, Hadronic CALorimeter and Muon Detector. Track bending is shown in the (Rz) plane, i.e. the magnetic field is orthogonal to the sheet. MET stands for Missing Transverse Energy, quantity used to infer the presence of neutrinos in the event. Only the unconverted photons are represented.*

interacting, whose proper energy is not measurable. However, in first approximation, the partons are expected to travel only in the longitudinal direction, meaning that their momentum in the transverse plane is zero. The transverse energy conservation can then be used to infer the presence of neutrinos through the missing transverse energy, MET or E_T^{miss}.

The design of each component has to take into account the optimization of that particular subsystem as well as the overall performances of the detector. For instance, the tracking system should give as many points as possible on the track, without adding too much material in front of the calorimeters to minimize the energy losses before the calorimeters, in places where it is not measurable.

4.2.2 Coordinates

The cartesian coordinate system of ATLAS is defined as follows:

- The x axis is in the horizontal plane, from the detector centre towards the centre of the LHC;

- The positive y axis is the vertical axis pointing upward;

- Finally, the z axis closes the right-handed frame in the beam direction. The side with $z > 0$ is known as the A side, $z < 0$ corresponds to the C side.

Given the cylindrical symmetry of the detector, a more convenient set of coordinates is made of z, completed by the polar angle θ measured from the beam line and the azimuthal angle ϕ around the z axis illustrated in Figure 4.3.
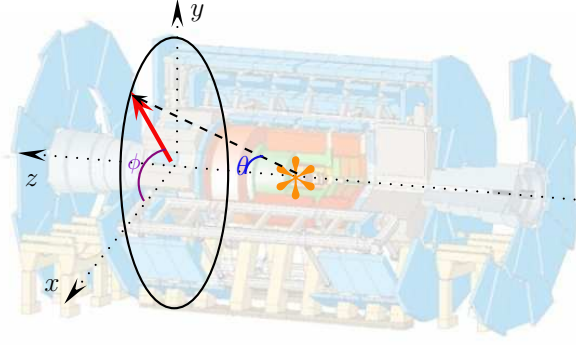
Figure 4.3: *Illustration of the coordinate system in ATLAS. The orange star represents the centre of the detector taken as the origin of all axis.*

The more appropriate set of coordinates usually used to describe particles positions in the detector is (η, ϕ, z), where η is the pseudorapidity, equivalent to the rapidity y for relativistic particles.

The rapidity corresponds to the quantity $y = \frac{1}{2} ln(\frac{E+p_z}{E-p_z})$. Its most interesting property is to be shifted by the same amount for all particles with the same boost along the z axis. That means that the rapidity difference between two particles is a Lorentz invariant under such boosts, which is convenient.

For relativistic particles for which the mass can be neglected, one has $E = p$, which is the case for most of the light particles at LHC, the rapidity can be expressed as a function of the θ angle only (Eq. 4.1).

$$y = \frac{1}{2} ln\left(\frac{E + p_z}{E - p_z}\right) = \frac{1}{2} ln\left(\frac{p + p_z}{p - p_z}\right) = \frac{1}{2} ln\left(\frac{1 + cos(\theta)}{1 - cos(\theta)}\right) = -ln\left(tan\left(\frac{\theta}{2}\right)\right) = \eta \qquad (4.1)$$

η defined as $\eta = -ln\left(tan\left(\frac{\theta}{2}\right)\right)$ is the pseudorapidity of the particle. Its ranges from $-\infty$ to $+\infty$ and is 0 when $\theta = \frac{\pi}{2}$. The limit of coverage of the ATLAS detector is $|\eta| = 4.9$ corresponding to $\theta \approx 0.85$ degrees.

All components of a given observable $\mathcal{O}$ can be expressed as a function of η and ϕ only:

$$\begin{aligned}
\mathcal{O}_x &= \mathcal{O}\,\frac{cos(\phi)}{ch(\eta)} \\
\mathcal{O}_y &= \mathcal{O}\,\frac{sin(\phi)}{ch(\eta)} \\
\mathcal{O}_z &= \mathcal{O}\,tanh(\eta)
\end{aligned} \qquad (4.2)$$

As already mentioned, the transverse plane xy is of particular interest to get the missing transverse energy for example. For each observable $\mathcal{O}$, the projection on the transverse plane is denoted with the subscript T and can also be expressed as a function of the pseudorapidity η the object:

$$\mathcal{O}_T = \sqrt{\mathcal{O}_x^2 + \mathcal{O}_y^2} = \mathcal{O}sin(\theta) = \frac{\mathcal{O}}{ch(\eta)} \qquad (4.3)$$

Finally, one could encounter throughout this document the notion of the ΔR distance in the η-ϕ plane defined as $\Delta R^2 = \Delta\eta^2 + \Delta\phi^2$, which is invariant under z-oriented Lorentz boost.

After these generalities, the next sections describe in detail each of the ATLAS subsystems.

4.2.3 Tracking system

Since the Inner Detector is the first subsystem that particles will see, its design has to satisfy strong constraints:

- High luminosities expected from LHC requires:

  - a fine-segmented detector to have an acceptable occupation rate (around 1,000 particles per bunch collision within $|\eta| < 2.5$ are expected for a typical LHC event);
  - a fast detector able to follow the LHC rate of a collision each 50 or 25 ns;
  - a detector able to survive in a strong radiation environment since this would be the most exposed part of the detector. It is also the most difficult part to change due to access issues.

- It should also be as thin a possible in terms of radiation length X_0. The radiation length quantifies the distance a particle can travel inside matter before interacting and starting its shower.

Taking into account all of these constraints led to the choice of a very fast silicon detector, coupled with a transition radiation detector.

The Inner Detector is made of three independent and complementary detectors. The pixel detector with fine 2-dimension granularity covering the pseudorapidity range $|\eta| < 2.5$ is located closest to the interaction point. It is followed at larger radii by a Semi-Conductor Tracker (SCT) consisting of precision silicon micro-strip detectors for $|\eta| < 2.5$. Farthest from the interaction point, a Transition Radiation Tracker (TRT) covers the region $|\eta| < 2.0$.

The arrangement of the different parts differs in the barrel and in the end-cap regions. In the barrel (Figure 4.4(a)), three concentric layers of pixels detectors are used at radii from 50.5 to 122.5 mm. The SCT is divided into four layers up to $R = 514$ mm. Finally, seventy-three TRT straw planes provide about 36 hits per track and complete the Inner Detector. In the end-caps (Figure 4.4(b)), the different layers are disks installed at fixed z. Each end-cap is made of three pixel, nine SCT disks, completed with one hundred and sixty straw planes. Another view of the Inner Detector is also shown in Figure 4.5.

(a) Barrel   (b) end-cap
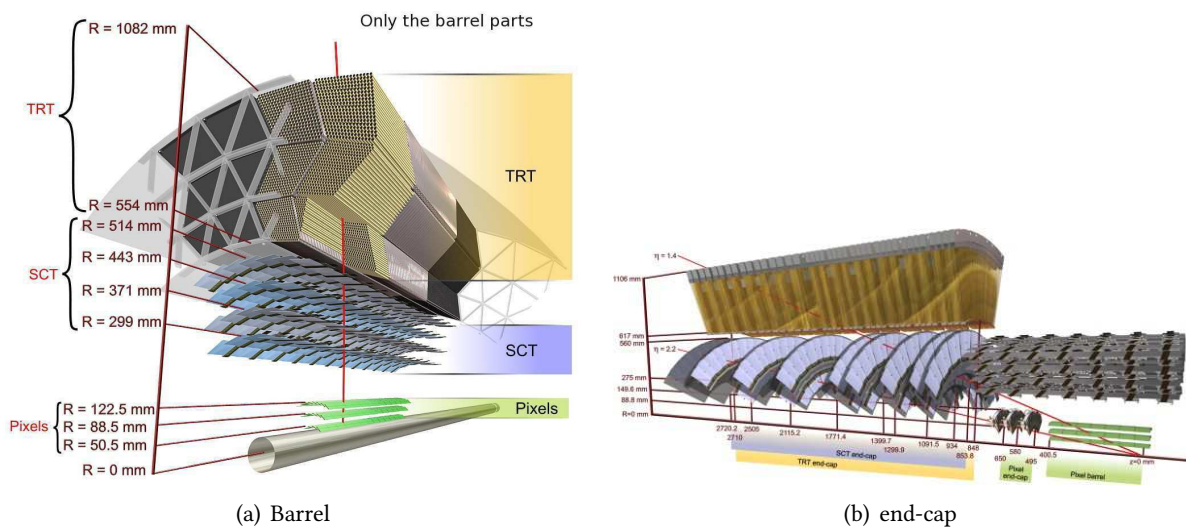
Figure 4.4: *Inner detector structure. A particle track is also drawn for a 10 GeV transverse momentum at $\eta = 0.3$ in the barrel (a) and $\eta = 1.4; 2.2$ in the end-cap (b) [57].*

A solenoidal 2 T field covers the whole Inner Detector and deflects all charged particles within its volume in the xy plane. It is produced by a superconducting coil installed in the isolation vacuum of the electromagnetic calorimeter.

More details about each of the detector functioning and the track reconstruction algorithm are given in the following.

Pixel detector

The pixel detector is the innermost part of the Inner Detector. The three cylindrical layers in the barrel are located at $R = 50.5; 88.5; 122.5$ mm. Similarly the three disks in the end-caps are installed
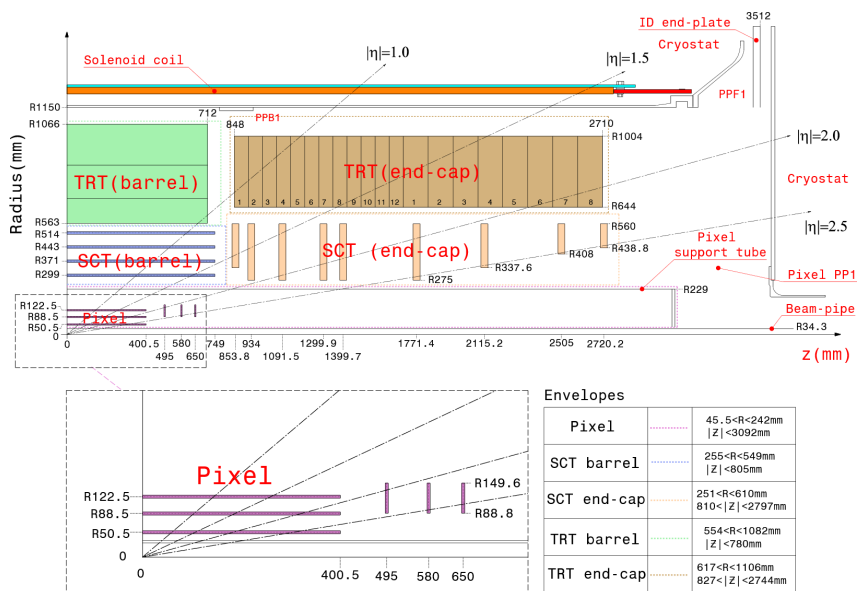
Figure 4.5: *Plan view of a quadrant of the inner detector showing each of the major detector elements with their active dimensions and envelopes. The lower part shows a zoom of the pixel region [57].*

at $z = 495; 580; 650$ mm. It has the highest granularity to achieve a very good spatial resolution. The typical pixel size in R-$\phi \times z$ is 50×400 μm^2 with an intrinsic resolution of the order of 10 μm in the R-ϕ direction and 115 μm in z (R) direction in the barrel (end-cap). The whole Inner Detector contains more than 80 millions pixels.

The first pixel layer located at 5 cm from the beam line is the so called b-layer. It allows a precise determination of the track impact parameter related to a good primary and secondary vertex reconstruction hence important for tagging long-lived b-hadrons. The b-layer is also useful to distinguish between prompt electrons coming from the hard interaction and electrons induced by a photon conversion in the detector material.

In term of resistance to radiations, the first pixel layer is expected to survive 5 years of collisions at luminosity 10^{34} cm^{-2}s^{-1}, the other two layers are less exposed and have an extended longevity of 10 years in the same conditions.

SCT

The SCT provides four more space points per track to increase the efficiency of the pattern recognition and the precision of the p_T measurement. In the barrel, the SCT layers are at fixed radii $R = 299; 371; 443; 514$ mm. In the end-caps, the nine disks layers are located at fixed z from $z \approx 840$ mm to $z \approx 2720$ mm.

With increasing radius and keeping the same η coverage, the area to be covered becomes higher and higher. To avoid having too many readout channels in a region where the occupancy rate is reduced, the pixels are replaced by larger strips with spatial extension 80 μm$\times 12$ cm. In the barrel, the strips are aligned along the beam axis while in the end-caps, they are radial. The intrinsic resolution of the order of 17 μm in the R-ϕ direction and 580 μm in z (R) direction in the barrel (end-cap). The number of readout channels amounts to 6.3 millions.

Transition Radiation Tracker (TRT)

The bulk of the Inner Detector volume is filled by the TRT that extends from $R = 554$ mm to $R = 1082$ mm. The TRT consists of several tens of thousands of drifts tubes (also called straws) of 4 mm diameter, filled with gas. In the barrel, the straws are 144 cm long arranged parallel to the z axis. In the end-caps, straws are 39 cm long and placed radially.

The TRT has a double role. First, an anode located at the centre of each tube provides around 36 additional measurements on each particle track thanks to the particles ionizing the gas. Secondly, the straws are surrounded by fibres with different optical index than the air surrounding them. Particles travelling through the fibre will emit transition radiation (X rays), with a probability proportional to $\gamma = \frac{E}{m}$. This principle is used to discriminate electrons from charged pions, that have a mass ~ 270 times larger.

Material budget

One of the requirement for the Inner Detector is its material thickness in order that the particles do not lose a too large fraction of their energy in that part of the detector. This is characterized by the radiation length X_0 for electrons and photons, and by the interaction length λ for hadronic particles dominated by strong interactions that can be interpreted as the distance those particles can travel through matter before initiating a shower decay.

The total amount of matter in the Inner Detector volume is illustrated in Figure 4.6 in term of X_0 and λ.

(a) X_0 (b) λ
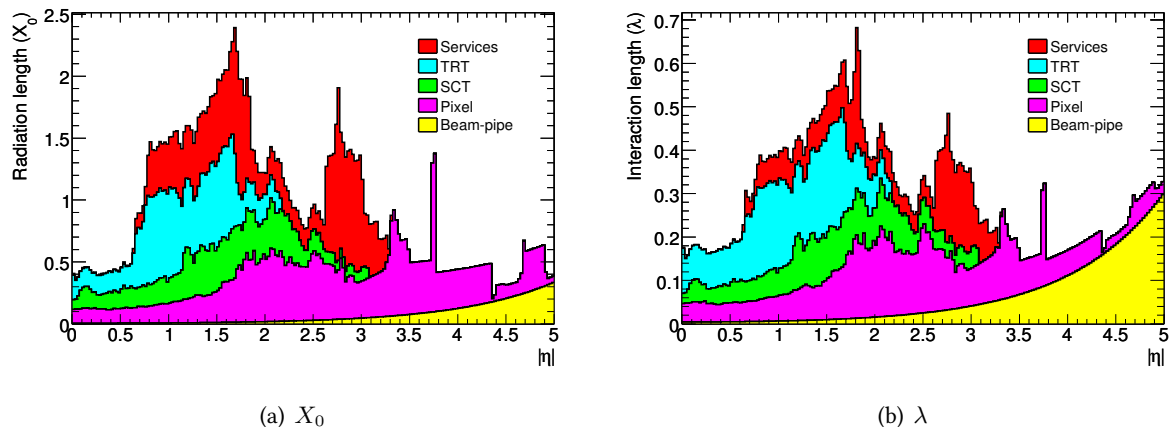
Figure 4.6: *Material in front of the electromagnetic calorimeter in terms of radiation length as a function of the pseudorapidity η and integrated along ϕ [57].*

4.2.4 Calorimetry

The ATLAS calorimeters are made of two main parts covering the region $|\eta| < 3.2$: the electromagnetic calorimeter and the hadronic calorimeter (Fig. 4.7). The former is a LAr (Liquid Argon) sampling calorimeter with a barrel and two end-caps. The latter is further divided into a tile calorimeter in the barrel region and two LAr detectors in the end-cap and forward regions.

An electron or photon penetrating matter initiates an electromagnetic shower or cascade through the bremsstrahlung ($e^\pm \rightarrow e^\pm \gamma$) and conversion ($\gamma \rightarrow e^+ e^-$) processes creating secondary particles with lower energies. This process stops when the energy is no longer sufficient (see Chap 5).
Similar cascades happen with hadrons that interact with matter through inelastic hadron-nuclei interactions. This hadronic interaction length however is usually an order of magnitude greater than the radiation length relevant for electrons and photons, meaning that hadrons will need more matter to be stopped. This is the reason why the hadronic calorimeter is located after the electromagnetic calorimeter.

The electromagnetic calorimeter covers the pseudorapidity region up to $|\eta| = 1.475$ in the barrel and $|\eta| = 3.2$ in the end-caps. Within the region covered by the Inner Detector ($|\eta| < 2.5$), the detector is fine-segmented in order to meet the required performances in terms of particle identification. The
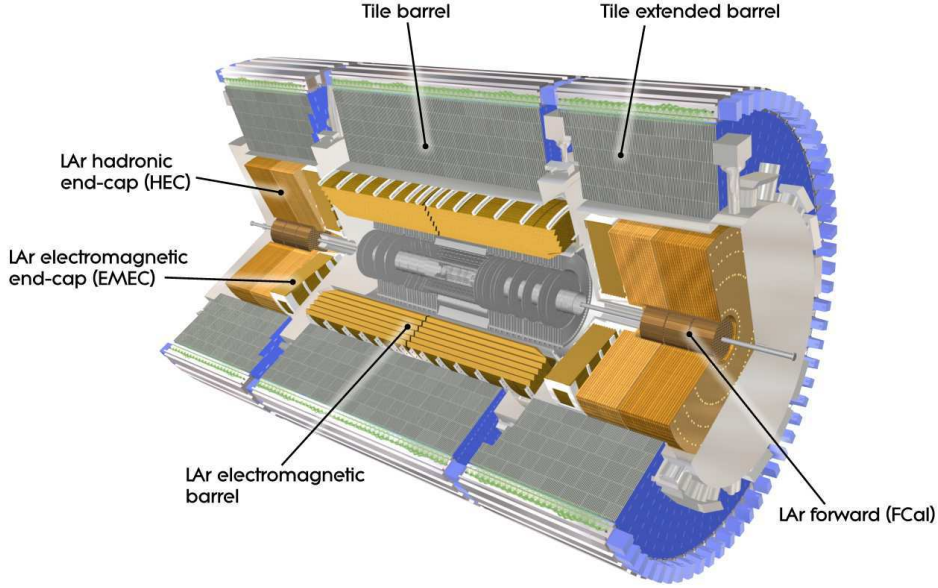
Figure 4.7: *ATLAS calorimeter system including both the electromagnetic calorimeter and hadronic calorimeter. Liquid argon calorimeters are drawn in orange [57].*

hadronic calorimeter has a coarser segmentation which is sufficient given the requirements about jet and E_T^{miss} resolution.

The pseudorapidity coverage and granularity of each calorimeter layer are summarized in Table 4.1.

Electromagnetic calorimeter

The electromagnetic calorimeter is crucial for photon reconstruction. It aims at identifying electrons and photons, with a good rejection with respect to jets and pions, and a good energy resolution. The barrel, consisting of two half-barrels separated by a small gap a $z = 0$, are contained in a single barrel cryostat. The two end-caps are divided between two coaxial wheels each (the outer and inner wheels) and are maintained at the correct operating temperature by two end-cap cryostats. The region $1.37 < |\eta| < 1.56$ suffers from a large amount of dead material. This region, called crack, is ignored by precision analyses, like the pseudorapidity range $|\eta| > 2.5$.

Both the barrel and the end-caps electromagnetic calorimeter are lead-liquid argon sampling calorimeters. Showers initiated in the lead produce secondary particles ionizing the liquid argon. It is segmented into three longitudinal layers:

- the first layer or front consists of strips with the finer granularity in the η direction with dimensions $\Delta\eta \times \Delta\phi = 0.0031 \times 0.1$ in the barrel. The granularity varies with η in the end-caps and goes up to $\Delta\eta \times \Delta\phi = 0.0062 \times 0.1$ for $\eta = 2.4$. This first layer is used to separate a single photon from the two collimated photons coming from a π^0 decay. The size of its cells is dictated by the average separation between these two photons ($\sim 2\frac{m(\pi^0)}{p_T(\pi^0)}$) at a transverse momentum relevant for the $H \to \gamma\gamma$ analysis ($p_T \sim \frac{m_H}{2}$);

- the second layer or middle is where the larger part of the energy is deposited. It is made of cell with size $\Delta\eta \times \Delta\phi = 0.025 \times 0.025$;

- Finally, the back measures the end of the shower with larger cells $\Delta\eta \times \Delta\phi = 0.05 \times 0.025$.

The total thickness is 24 X_0 or more in the barrel and from 25 X_0 up to 35 X_0 in the end-caps, ensuring that electrons and photons are contained within the electromagnetic calorimeter.

In front of these three layers, a thin presampler with $\Delta\eta \times \Delta\phi = 0.025 \times 0.1$ is used in the region $|\eta| < 1.8$ to quantify the energy losses before the calorimeter.

The particularity of the ATLAS electromagnetic calorimeter is to have an accordion geometry of interlaced absorbers and electrodes as illustrated in Figure 4.8 that ensures better azimuthal coverage by avoiding the readout gap between the modules (following an original idea by D. Fournier [58]).
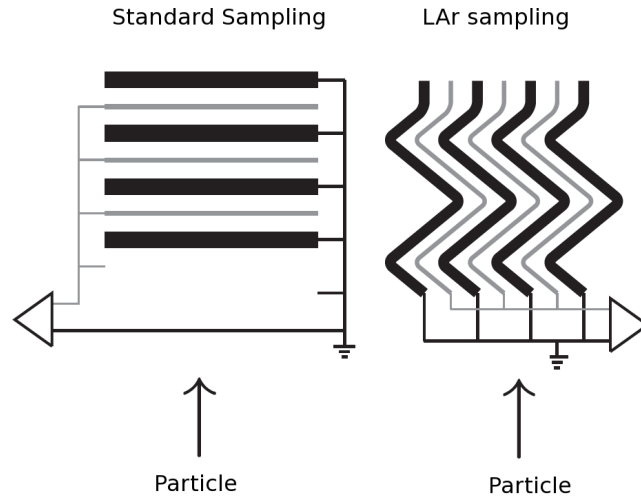
Figure 4.8: *Accordion geometry on the right compared to the standard geometry on the left [59].*
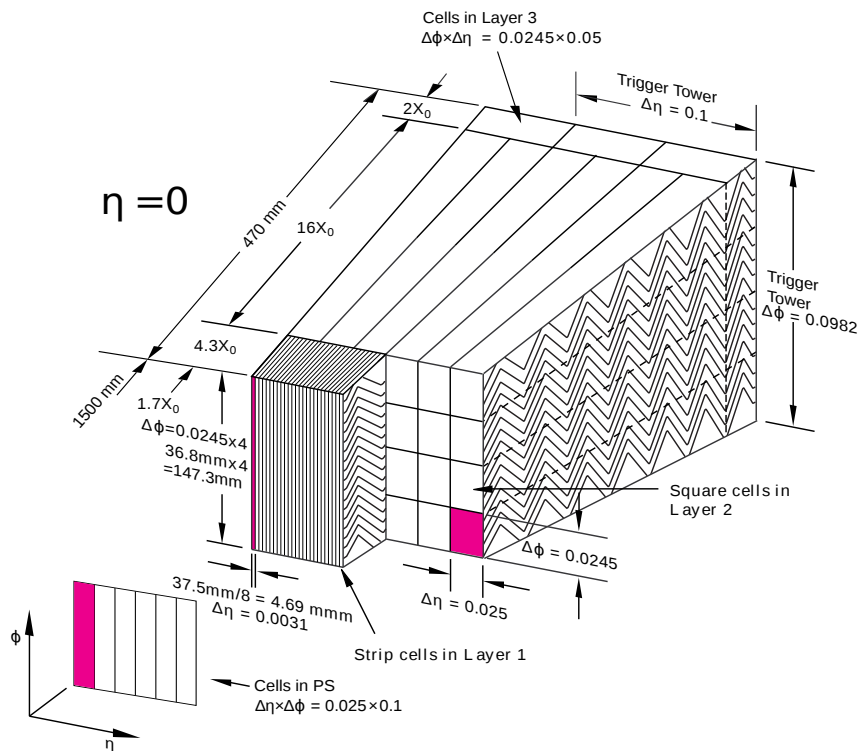
Figure 4.9: *Barrel segmentation in the electromagnetic calorimeter [60].*

The electromagnetic calorimeter is used to identify and measure the energy of photons and electrons. Its functioning is described in more details in chapter 5.

The hadronic calorimeter is an extension of the electromagnetic calorimeter aiming at containing the shower initiated in the late electromagnetic calorimeter by hadrons, *i.e.* jets. It is composed of

three sub-detectors:

Tile calorimeter

The tile hadronic calorimeter covers the pseudorapidity range $|\eta| < 1.6$: one barrel part up to $|\eta| = 1.0$ and two extended barrel. It consists of 14 mm thick iron absorbersand 3 mm plastic scintillators tiles as the active material. It is segmented in depth in three layers, approximately 1.5, 4.1 and 1.8 λ thick for the barrel, and 1.5, 2.6 and 3.3 λ for the extended barrel. The total depth is $\sim 7\ \lambda$ which is safe to ensure a limited hadronic leakage in the muon detectors.

LAr hadronic end-cap calorimeter

At $|\eta| > 1.5$, the end-cap radiation level would cause severe damages to plastic scintillators, which are thus replaced by liquid argon devices. The hadronic end-caps consist of two wheels, each wheels containing two layers. This sysbsystem is located behind the electromagnetic calorimeter end-caps and share the same cryostat. Both wheels consist of an array of copper plates, with a thickness of 25 mm in the first wheel, and 50 mm in the second one. They span the region $1.6 < |\eta| < 3.2$.

LAr forward calorimeter

For better hermiticity of the calorimeters, the coverage is extended with a high density forward calorimeter between $|\eta| = 3.2$ and $|\eta| = 4.8$. Its uses copper and tungsten absorbers and small gap liquid argon active medium. The aim is to retrieve forward particles to reduce the tails in the missing energy measurement.

Electromagnetic calorimeter									
Sub-system	Barrel		EMEC						
$|\eta|$ range	0-0.8	0.8-1.4	1.4-1.8	1.8-2.0	2.0-2.2	2.2-2.4	2.4-2.5	2.5-2.8	2.8-3.2
Presampler	0.025×0.1		-						
Front	0.003×0.1		0.004×0.1		0.006×0.1		$(0.025 - 0.1) \times 0.1$		
Middle	0.025×0.025							0.1×0.1	
Back	0.05×0.025							-	
Lead (mm)	1.53	1.1	1.7						2.2
LAr (mm)	2.1	2.8-0.9							3.1-1.8
$\#X_0$	26-33	21-38	31-35	31-32	32-35	35-41		28-33	33-38
$\#\lambda_A$	1.8-2.5	2.5-3.5	1.8-3.5	1.8					
# cells	109568		63744						
Hadronic calorimeter				
---	---	---	---	---
Sub-system	Tile barrel	Tile extended barrel	HEC	
$	\eta	$ range	0-1.0	0.8-1.7	2.5-3.2	2.5-3.2
Layer 0	-	-	0.1×0.1	0.2×0.2
Layer 1	0.1×0.1	0.1×0.1	0.1×0.1	0.2×0.2
Layer 2	0.1×0.1	0.1×0.1	0.1×0.1	0.2×0.2
Layer 3	0.2×0.1	0.2×0.1	0.1×0.1	0.2×0.2
$\#\lambda_A$	7.5-8.5	5.5-13.5	10	
# cells	5760	4092	5632	

Table 4.1: *Summary of calorimeters characteristics for each layer and pseudorapidity region. Granularity is shown in $\Delta\eta \times \Delta\phi$ space. A "-" indicates that the $|\eta|$ region is not covered by the corresponding layer.*

4.2.5 Muon chambers

The muon spectrometer is the outermost sub-system in ATLAS, allowing for precise muon momentum measurement in a wide p_T range (up to about 1 TeV) thanks to a toroidal magnetic field of about 0.5 T

(1 T) in the barrel (end-cap). It is divided into a barrel part for pseudorapidities up to 1.4 and an end-cap detector covering the pseudorapidity range $1.4 < |\eta| < 2.7$.

The magnetic field in the barrel part up to $|\eta| = 1.0$ is created by 8 superconducting coils (Fig. 4.10(a)). The end-cap region between $|\eta| = 1.4$ and $|\eta| = 2.7$ is covered by another coil system producing a 1 T magnetic field. In the transition region, the field is a superposition of those two contributions.

The tracking and trigger chambers are grouped into three independent stations located at fixed radii in the barrel and fixed z in the end-caps.

(a) xy plane

(b) Rz plane
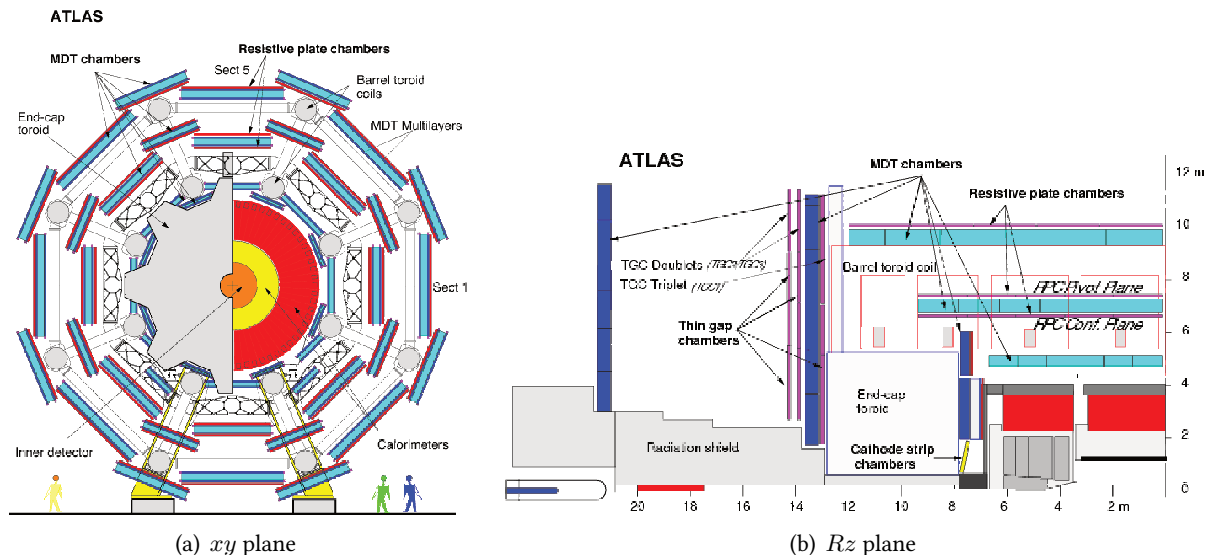
Figure 4.10: *Muon spectrometer [61].*

The precision tracking chambers consist of monitored drift tubes (MDT) and cathode strip chambers (CSC), which can be seen in Figure 4.10(b).

For $|\eta| < 2.7$, Monitored Drift Tube (MDT) chambers are used, which are made of several layers of 30 mm diameter tubes filled with gas with an anode in their centre. The position reconstruction is based on the drift time in the tube and a 80 μm resolution can be achieved with a single tube. The tubes are arranged in 2×4 monolayers of drift tubes for the inner station and 2×3 monolayers for the middle and outer stations which contribute to a resolution improvement.

In the inner part of the end-caps ($2.0 < |\eta| < 2.7$), MDT are replaced by Cathode Strip Chambers (CSC) with higher granularity due to their higher resistance to beam background, arranged in 2×4 layers.

RPC in the barrel and TGC in the end-cap provide information to make a trigger decision.

The expected resolution on the muon momentum measurement $\frac{\sigma(p_T)}{p_T}$ is around 3% for a $p_T = 100$ GeV muon and increases up to 10% at 1 TeV.

4.3 Data acquisition and trigger

At nominal design luminosity, the LHC will make bunches crossing every 25 ns. With the nominal luminosity of $10^{34} cm^{-2} s^{-1}$, this translates into a 1 GHz rate. This number takes into account the multiple interactions that happen simultaneously for each bunch crossing. Based on simulations about 23 simultaneous interactions are expected. This phenomenon is called in-time pileup.

However, the recording rate is limited by technology and storage capabilities to roughly 600 Hz. This is not a major constraint in term of physics because the dominant processes that happen at LHC are proton-proton scattering or jet production which are not the main targets for LHC physics analysis. A trigger system was thus developed in order for ATLAS to save first the events with interesting topologies.

ATLAS trigger is subdivided into three stages illustrated in Figure 4.11. The main features are described below:

- The level-1 trigger decreases the event rate to a maximum of ~ 100 kHz, making a decision on whether to accept or reject an event within 2.5 μs. It is based on hardware information only, from the calorimeters and muon chambers;

- The level-2 uses information from quick event reconstruction of the regions of interest identified at level-1. This step reduces the event rate by a factor of ~ 50. An offline reconstruction is then performed in the regions of interest (ROI) found during level-2 phase for all accepted events;

- Finally, the last stage, also called Event Filter (abbreviated in EF), is a software-based trigger that further reduces the rate to the required value of ~ 200 to 600 Hz. After the event is accepted by the EF, it is saved and ready to go to the full event reconstruction.
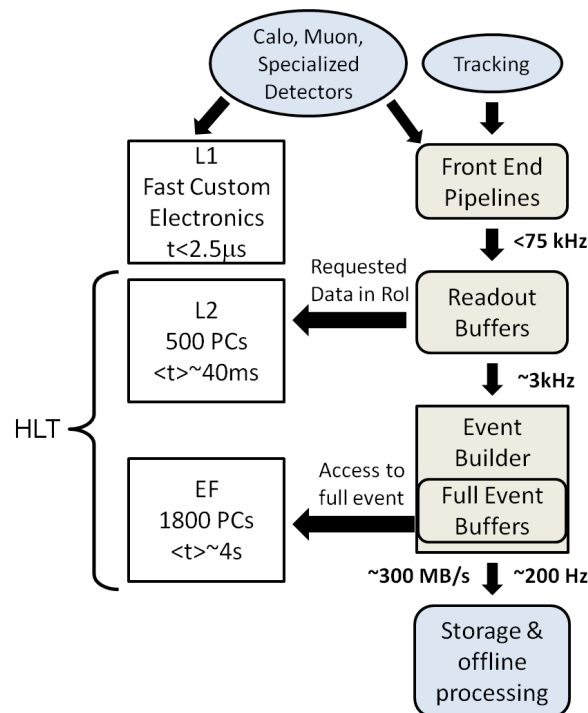
Figure 4.11: *Trigger chain [62].*

Several EF menus are optimized for different analyses. They can use criteria on the objects transverse momentum or reconstruction quality to make a decision.
Some of them would occupy too much bandwidth and a prescale factor is applied, meaning that only a fraction of the events normally passing the trigger are kept.

Data outgoing the detector are classified into several streams: the express stream contains a selection of events that is directly sent for processing. It is used for data quality assessment, before the whole data of a given run is processed.

4.4 Detector performances during Run I

LHC provided collisions in 2010, 2011 and 2012 at different centre of mass energies and different luminosities (see Chap. 3 for more details). The integrated luminosity recorded by ATLAS is shown in Figure 4.12(a) as a function of time. After removing periods with bad detector performances, 4.9 fb^{-1} in 2011 and 20.3 fb^{-1} in 2012 can be used for physics analyses.

(a) Integrated luminosity

(b) Mean number of interactions per bunch crossing
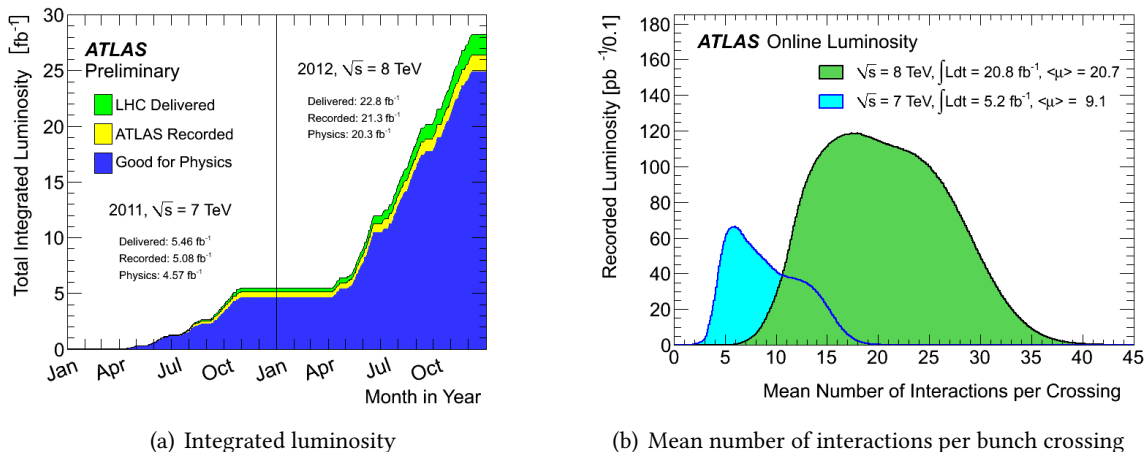
Figure 4.12: *(a): luminosity delivered and recorded in ATLAS. (b): mean number of interaction per bunch crossing in 2011 and 2012 data [54].*

The drawback of the high luminosity is the increased simultaneous number of collisions per bunch crossing, or pileup, as Figure 4.12(b) illustrates: the mean number of events per bunch crossing increases from 9.1 in 2011 to 20.3 in 2012. This gives rise to a higher number of jets per collision and requires that the variables used both in the reconstruction and in the analyses are pileup independent.

Despite the hard data-taking conditions, ATLAS managed to record a large fraction of the delivered luminosity. Among the recorded events, some have to be dropped for physics analysis due a defect in a sub-detector that may create fake E_T^{miss} for example. At the end, 95.5% of the events recorded in 2012 are used for physics analyses. The losses divided by sub-system are detailed in Figure 4.13.

ATLAS p-p run: April-December 2012										
Inner Tracker			Calorimeters		Muon Spectrometer				Magnets	
Pixel	SCT	TRT	LAr	Tile	MDT	RPC	CSC	TGC	Solenoid	Toroid
99.9	99.1	99.8	99.1	99.6	99.6	99.8	100.	99.6	99.8	99.5
All good for physics: 95.5%										
Luminosity weighted relative detector uptime and good quality data delivery during 2012 stable beams in pp collisions at √s=8 TeV between April 4th and December 6th (in %) − corresponding to 21.3 fb⁻¹ of recorded data.										

Figure 4.13: *Data good for physics [63].*

4.5 Reconstruction and calibration of the different objects

4.5.1 Simulation and reconstruction chains

An essential tool in all physics analyses is the simulation: usually, processes well described by simulation are well understood. Simulation of physics processes was outlined in Chapter 1 and more details will be given in the context of the Higgs boson in Chapter 8. But performances studies need to take into account detector effects and efficiency. This is performed with a precise simulation of the detector response simulated with the GEANT4 toolkit [64].

Figure 4.14 shows the different steps followed by simulated and real data before they are ready for analysis. For simulated data, events are first generated *via* Monte Carlo simulators such as `POWHEG` and/or `PYTHIA`. The outgoing particles are then passed through a simulation of the detector response to simulate the hits and energy deposits in the material of the detector. After this is done, the digitization steps transforms the induced particle flow to an electric signal, similar to the one induced by real data. All this truth information is stored in the event and can, afterwards, be compared to the reconstructed data to study the detector performances. After digitization of simulated data; both real and simulated data follow exactly the same path in the particle reconstruction.

For more accurate studies, pile-up also have to be taken into account in simulations since it can affects particle reconstruction and identification. It is added to the simulation at the digitization level from a list of Minimum Bias events generated with `PYTHIA`.
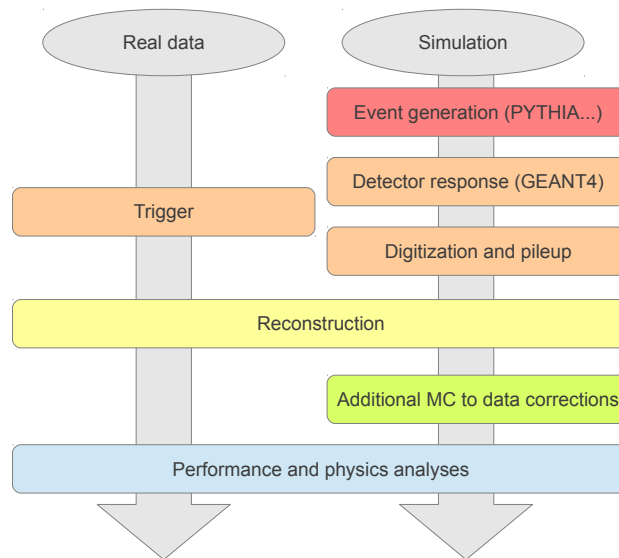
Figure 4.14: *Analysis flow comparison between real and simulated data.*

4.5.2 Tracks and vertex

Tracks are reconstructed from the combination of hits in the Inner Detector. Once tracks are known, a vertex finder algorithm is run with tracks as inputs. Tracks are then associated to the primary vertex based on their transverse (d_0) and longitudinal (z_0) distance of closest approach.

The reconstructed tracks are also used to identify electrons if they can be associated to an electromagnetic calorimeter cluster with energy consistent with the track momentum.

4.5.3 Electrons and photons

Electrons and photons are both characterized by an energetic cluster in the electromagnetic calorimeter. An additional track matched to the cluster is required to identify an electron. Photon identification takes into account conversions $\gamma \rightarrow e^+e^-$ happening in the matter in front of the electromagnetic calorimeter, which represents about 40% of the photons at energy considered in the $H \rightarrow \gamma\gamma$ analysis for example.

Reconstruction

For each part of the reconstruction based on the calorimeter information, the first step always consists in finding clusters of energetic cells. Clusters are formed by the sliding window algorithm [65] con-

sisting in moving a rectangular window of fixed η-ϕ expansion and adjust its position to maximize the total energy.

Inputs to the sliding window algorithm are electromagnetic towers. The different steps of cluster formation are then:

1. Creation of electromagnetic towers of size $\Delta\eta \times \Delta\phi = 0.025 \times 0.025$ adding the energies of all three layers of the electromagnetic calorimeter and the presampler informations. For cells belonging to several towers, energy is fractioned with respect to the fraction of surface of the cell in the tower.

2. Pre-cluster formation: sliding window of 3×5 towers in η-ϕ is used. Its position is computed using a 3×3 towers square to minimize the electronic noise;

3. Hypothesis on particle nature: a cluster-track matching is performed. If a track can be assigned to the pre-cluster, *i.e.* it lies within $\Delta\eta \times \Delta\phi = 0.05 \times 0.10$ of the cluster, it is labelled as electron (or converted photon), otherwise, it is considered to be an unconverted photon. The reconstruction of converted photon includes the reconstruction of the conversion vertices by the Inner Detector which are classified depending on the number of electron tracks assigned to them [66]. Single track conversions occur typically when one of the two produced electron tracks failed to be reconstructed or when this track does not have a hit in the b-layer. Double track conversions are well reconstructed at low values of the conversion radius, while at high radius one has more single track conversions [67]. Due to higher pile-up in 2012, very small modifications on the tracking, on the conversion vertex reconstruction and on the vertex-to-cluster matching changed the conversion reconstruction [68].

4. Final electromagnetic cluster: the final electromagnetic cluster size depends on the particle type and on the position in the electromagnetic calorimeter (barrel or end-caps). It has been optimized in order to minimize the lateral leakage of energy lost by the particle, without adding too much electronic noise to the cluster. Electron, or similarly, converted photon, clusters are basically larger than unconverted photons clusters in the ϕ direction due to the track bending in the magnetic field from the Inner Detector and bremsstrahlung radiations that makes the electrons clusters larger. There is no such argument in the end-caps where a fixed window size in used. The different final cluster sizes are summarized in Table 4.2 for barrel and end-caps and the nature of the particle. The reconstruction of the conversions was slightly changed for the analysis of 2012 data because of the harder pile-up conditions (see Section 2 of [68]).

Object	Barrel	End-cap
Electron	3×7	5×5
Converted photon	3×7	5×5
Unconverted photon	3×5	5×5

Table 4.2: *Cluster sizes as a function of the object and position in the electromagnetic calorimeter. The size in given in number of cells in the second sampling.*

At this stage, the reconstruction has created two containers: the electron one and the container of photons (converted and unconverted).

Calibration and resolution

Electron calibration is a three steps process:

1. It starts from the conversion of measured current in each cell to energy. The conversion factors are derived from regular calibration runs taken during the LHC operations in 2011 and 2012;

2. It is followed by a MC-based calibration where different effects are corrected.

3. Finally, an *in-situ* calibration is performed using to the $Z \rightarrow e^+e^-$ lineshape.

More about electrons calibration and extrapolation to photons will be described in the next chapter (Chap. 5).

4.5.4 Jets

Jets are the result of quarks and gluons hadronization that creates, at detector level, a bunch of particles inside a rough cone. The goal of all jet reconstruction algorithm is to group together the resulting objects and build a quadrivector that should reproduce the momentum of the initial parton. In the detector, jets create clusters in the calorimeters together will a lot of non-isolated tracks in the Inner Detector. A robust jet finding algorithm is necessary to recover them in each event.

Reconstruction

Several jet algorithms exist for jet reconstruction. The most basic ones are cone algorithms that consists in moving a fixed size cone on the calorimeter surface to find area with maximum energy. This technique's drawback is that it is not infrared safe [69, 70], meaning that if a soft gluon is emitted between two partons, the reconstructed jet will change.

ATLAS baseline choice for analyses is to use the soft and collinear safe anti-k_T algorithm [71] with distance parameter $R = 0.4$ or $R = 0.6$.

The anti-k_T algorithm starts from objects called proto-jets. It computes the distances d_{ij} between all the objects (Eq. 4.4) and $d_{iB} = \frac{1}{p_{T,i}^2}$ for all proto-jets.

$$d_{ij} = \frac{1}{max\left(p_{T,i}^2; p_{T,j}^2\right)} \frac{\Delta R_{ij}^2}{R^2} \tag{4.4}$$

The minimum of all d_{ij} and d_{iB} is selected. If d_{iB} is selected, a new jet is created from the proto-jet i and i is removed from the proto-jets list. In the other case, the two objects with the lower d_{ij} are grouped together and their quadrivectors combined to form a new proto-jet. This step is repeated as long as proto-jets remain.

The inputs to the anti-k_T algorithm can be:

- At truth level, stable hadron after hadronization.

- At reconstruction level, two kinds of objects built from the calorimeters energy deposits:

  - Towers: built in the same way than the sliding window for electrons;
  - Topoclusters [65]: they are formed with a *4-2-0* scheme: it starts from a seed having an energy greater than 4σ where σ denotes the mean electronic and pile-up noise in the electromagnetic calorimeter. Then, adjacent cells with $E > 2\sigma$ are added. Finally, all other neighbouring cells with $E > 0$ are considered without signal to noise ratio constraints. Topoclusters formed with this algorithm can have large spatial extansion and include several local maxima. A splitting algorithm is then used to create one cluster per local energy maximum.

In the following analyses, only jets reconstructed from topoclusters are used, hence called topojets.

Jet quality

Fake jets can be created by electronic noises in the calorimeters or by non collision background. Jets should then pass some quality criteria to reduce this contamination.

Pileup also creates jets that are not of particular interest for most of the analyses in ATLAS. Pileup can also affect the jet energy reconstruction since some particles from a pileup jet can end in the same cluster than the hard-scattered jet. The quantity used in that case to reject pileup jets is the Jet Vertex Fraction (JVF) defined as the fraction of the jet momentum coming from tracks associated to the primary vertex of the hard scattering in the event (Hard Primary Vertex in the next formula) [72]:

$$JVF = \frac{\sum\limits_{trk \in jet, HPV} p_T^{trk}}{\sum\limits_{trk \in jet} p_T^{trk}} \tag{4.5}$$
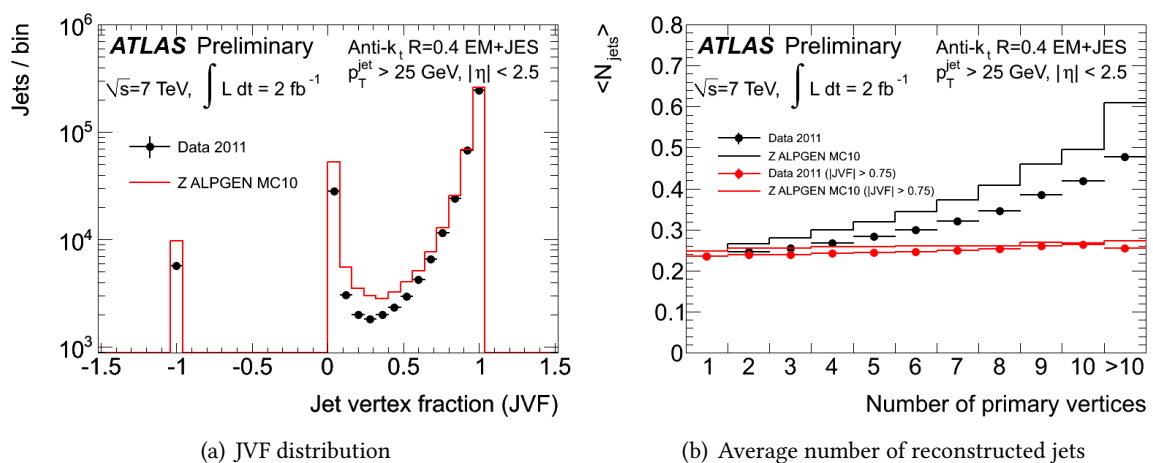
Figure 4.15: *Jet Vertex Fraction performance: (a) JVF distribution for data and Monte Carlo. JVF is set to -1 when no track is associated to the jet. $JVF = 0$ corresponds to jets with no track associated to the selected primary vertex in the event. (b) illustrates the impact of a $|JVF|$ cut at 0.75 on the reconstructed number of jets with respect to the number of primary vertices, representative of the pileup [73].*

Requiring a $|JVF|$ greater than typically 0.5 (for 2011 data) allows to limit the contamination from pile-up jets (Fig. 4.15).

Calibration and resolution

Jet energy scale, or hadronic scale, is accessible with difficulty. Indeed, a significant fraction of a jet energy is deposited as visible electromagnetic energy coming from electron, photon and π^0/η decays inside the jet. The remaining energy comes from charged secondary particles ($\pi^\pm$, ρ,...) that deposit ionization and excitation energy ($\sim 25\%$) and also from some energy induced by nuclear interactions, nuclear recoil, neutron capture... ($\sim 25\%$), which is not measurable by the calorimeters. The consequence is that a 10 GeV charged pion entering the calorimeter will leave less measurable energy than an electron or a photon with the same energy. The electromagnetic scale, defined to recover the true electron energy, is then not sufficient to reproduce the jets energy and corrections have to be applied.

The topoclusters calibration can follow two different paths [74, 75]:

- Electromagnetic (EM): topoclusters are calibrated at the electromagnetic scale;

- Local Cluster Weighting (LCW): it relies on the local pre-calibration of the initial topoclusters depending on their nature "electromagnetic", "hadronic" or "mixte" determined from the fraction of

energy in the electromagnetic calorimeter and in the hadronic calorimeter. This pre-calibration is derived from MC.

After this pre-calibration of topoclusters, corrections are applied to take into account the detector non-uniformity and pileup effect to lead to the final jet energy scale (JES). Finally, *in situ* calibration is applied using $Z + jet$ and $\gamma + jet$ events, as well as multijet events.

Flavor tagging

Identification of b jets is important for many B physics analyses but also for all analyses involving top quarks since the top decays leptonically to a bottom quark and a W boson $t \rightarrow Wb$. B mesons have a relatively long lifetime of 1.5 ps which allow them to travel a relatively long distance before decaying: 3 mm in the transverse plane at 50 GeV. This distance is long enough to form a secondary vertex, that can be disentangled from the primary vertex of the collision by the detector.

Several algorithms have been developed in ATLAS trying to identify b's using their specific properties: either they use the tracks impact parameters (d_0 and z_0 that tends to be larger for particles originating from a B decay, or they explicitly reconstruct the secondary displaced vertex. A last category of tagger takes advantage of the B direct decay to lepton ($\sim 20\%$ of the cases) and look for lepton inside jets.

Best performances are achieved with an algorithm combining the information form impact parameter and secondary vertex taggers in a neural network labelled as MV1 (MultiVariate) (Fig. 4.16).

Figure 4.16: *Light jet rejection as a function of the b identification efficiency for several b-tagger algorithm for $t\bar{t}$ simulated events [76].*

Finally, the MV1c tagger uses samples of c-quarks for the MVA training, resulting in a better discrimination between c and b. Typical working points correspond to a b-jet efficiency between 60 and 80%.

4.5.5 Muons

Reconstruction

Several reconstruction algorithms have been developed along the years. The simpler one consists in finding coherent track segments in the three layers of the muon spectrometer, then extrapolating this track down to the centre of the detector. Those muons are called standalone muons, taking into account the energy losses in the calorimeters. This technique has the advantage of higher pseudorapidity coverage compared to the Inner Detector (it goes up to $|\eta| = 2.7$ instead of 2.5). However, it suffers from some holes in the MS around $|\eta| = 0.0$ where the sensitive part is reduced to let enough place for cables, and in the transition region between barrel and end-cap around $|\eta| = 1.2$ where a muon candidate goes through only one chamber. Moreover, since there is no Inner Detector information, we cannot have access to impact parameter and it cannot discriminate a muon from direct production from a muon coming from a decay in a jet for example.

Combined muons are formed by the combination of an ID and a MS track reconstructed independently. Most of the muons used in the analyses are combined muons.

Two other methods exists, mainly to increase the reconstruction efficiency in the MS holes. The segment-tagged muons are reconstructed from a track in the ID, if this track can be associated to at least one segment in the muon spectrometer. Finally, the calorimeter-tagged muons come from an ID track associated to energy deposits in the calorimeter corresponding to minimum ionizing particles recover the acceptance in the $\eta = 0$ region (see Fig. 4.17).
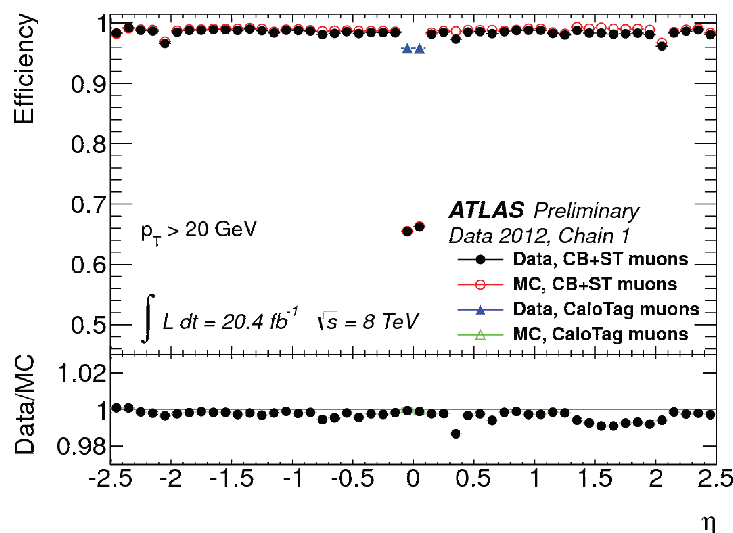
Figure 4.17: *Muon reconstruction efficiency in 2012 data [77].*

The efficiency is estimated by studying $Z \rightarrow \mu^+\mu^-$ process for muon with $p_T > 20$ GeV, below this value the process $J/\Psi \rightarrow \mu^+\mu^-$ is used.

Further quality criteria can be required on the muon track parameters (*e.g.* number of hits in the pixels, impact parameter) to define several muon qualities: looses, medium and tight from lower to higher reconstruction efficiency.

Calibration and resolution

Muon momentum reconstruction uses the track bending in the magnetic field provided by the Inner Detector solenoid and the toroid.

This prior measurement is then corrected using *in situ* $Z \rightarrow \mu^+\mu^-$ events (with tag-and-probe technique for efficiency measurement).

4.5.6 Missing transverse energy E_T^{miss}

Missing transverse energy is defined in such a way that the total energy, reconstructed or not, in the transverse plane is null:

$$\vec{E}_T^{miss} = -\sum \vec{E}_T^{visible} \tag{4.6}$$

We also define the projection of the $\vec{E}_T^{miss}$ on the x and y directions, labelled $E_{x,y}^{miss}$.

The total missing transverse energy is computed from the reconstructed objects in the event properly calibrated and selected in the following order:

$$E_{x,y}^{miss} = E_{x,y}^{miss,e} + E_{x,y}^{miss,\gamma} + E_{x,y}^{miss,\tau} + E_{x,y}^{miss,jets} + E_{x,y}^{miss,SoftTerm} + E_{x,y}^{miss,\mu} \tag{4.7}$$

τ jets are calibrated with the LCW method, with a correction to the Tau Energy Scale. Jets are topo-jets reconstructed with the anti-k_T algorithm with distance parameter $R = 0.4$, satisfying quality criteria especially in terms of $|JVF|$. They are calibrated with the LCW+JES scheme. Soft term designate the topoclusters and tracks that can not be associated to an energetic object in the final reconstruction.

The E_T^{miss} resolution is sensitive to pileup, increasing with the total energy deposited in the calorimeters, mainly through the soft term and the jet contributions. Some methods were thus derived to limit this pileup dependence, such as the Soft Term Vertex Fraction (STVF) [78]. In the STVF method, the soft term is scaled by the fraction of tracks entering the soft term computation that are associated to the the primary vertex of the event.

Figure 4.18 shows the E_T^{miss} distribution for $W \rightarrow e\nu$ events containing genuine E_T^{miss}. Figure 4.18(a) also shows the resolution improvement when applying a pileup suppression method.

(a) Monte Carlo   (b) Evolution with $\sum E_T$
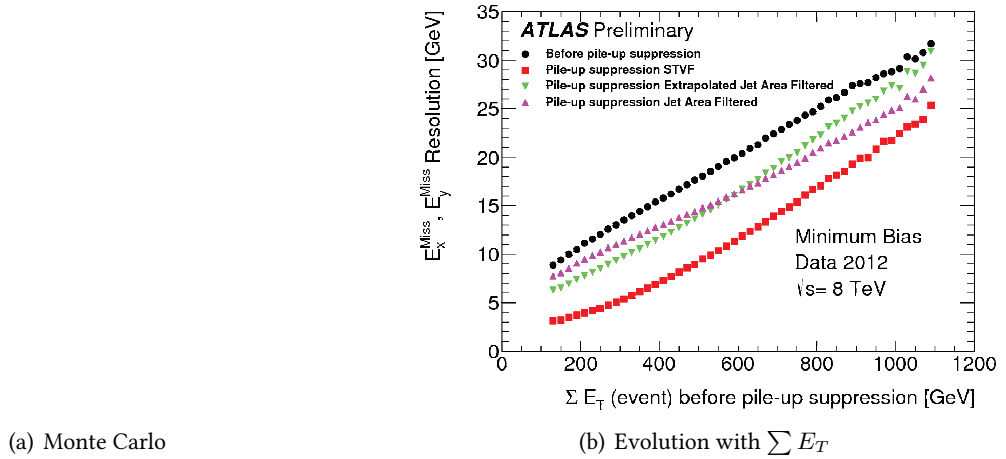
Figure 4.18: *E_T^{miss} resolution estimated in Monte Carlo (a) and evolution as a function of $\sum E_T$ in data and Monte Carlo (b) [78].*

4.6 Upgrade

Several improvements of the LHC are planned to increase the energy and/or the luminosity delivered to ATLAS and CMS [79]:

- The Long Shutdown 1 (LS1) in 2013 and 2014 is devoted to the main repairs in order to reach or approach the nominal energy of $\sqrt{s} \approx 14$ TeV. ATLAS should collect ~ 100 fb^{-1} of data before LS2.

- In 2018-2019 another long shut-down (LS2) is planned to install the LINAC4 in the injection chain, with the intention of achieving a luminosity of 2 to 3.10^{34} $cm^{-2}s^{-1}$ with a number of

interaction per bunch crossing from 55 to about 80. The total recorded luminosity recorded by each LHC experiment should be close to 300 fb^{-1}.

- The last functioning phase (HL-LHC) is expected with very high luminosity (5 to 7.10^{34} $cm^{-2}s^{-1}$ corresponding to $\mu \approx 150$). The total delivered luminosity is expected to be of the order of 3000 fb^{-1} in 2035-2040.

ATLAS will also benefit from these long shut-downs to adjust its subsystems to the higher expected luminosities. In the meantime, maintenance of existing detectors will be performed.

During LS1, an upgrade of the Inner Detector is performed, adding a new layer of pixel sensors closer to the beam pipe, the Insertable B-Layer (IBL, at $R = 33.4$ mm) [80]. This new layer will improve the tracking and vertexing performances because it is closer to the interaction point and will in principle add a new point per track closer to the vertex. The B-tagging will particularly benefit from this upgrade.

The main challenge coming from the increasing luminosity arises from the trigger, that has to provide a fast decision with high efficiency for interesting physics channels and high background rejection. Several actions will be taken to guarantee high performances of this part of the detector.

Conclusion

The 7000 tons of the ATLAS detector are installed in its final cavern since 2008. During LHC Run I, all its sub-systems have performed well in hard data taking conditions, with a very small data loss rate. Reconstruction performances in terms of particles identification and momentum or energy resolution have met the required performances for efficient physics analyses. The electromagnetic calorimeter is of primary importance for the $H \rightarrow \gamma\gamma$ channel and will be described with more details in next chapter.

❝ Any sufficiently advanced technology is indistinguishable from magic. ❞

CLARKE'S THIRD LAW

Chapter content

5.1 Principles of energy measurement with calorimeters

The electromagnetic calorimeter aims at measuring the energy of electromagnetic particles (electrons and photons). The detection of the latter, when they are not converted in an e^+e^- pair, rely only on this detector as they are not seen by the Inner Detector. The principles of calorimetry rely on particle interactions with matter. From this understanding, the structure and size of the calorimeter that best suit the experimental conditions can be decided.

5.1.1 Electromagnetic shower

Electrons and photons interact with matter in different ways depending on their energy. As shown in Figure 5.1, for energies larger than about 10 MeV, the dominant process responsible for energy losses in lead is pair creation for photons and bremsstrahlung for electrons. Diagrams for both these processes are illustrated in Figure 5.2. Below that energy threshold, the main mechanisms are ionization for electrons and Compton or photo-electric effect for photons, consisting in transferring part of the particle energy to an atomic electron.

| (a) Photons | (b) Electrons and positrons |
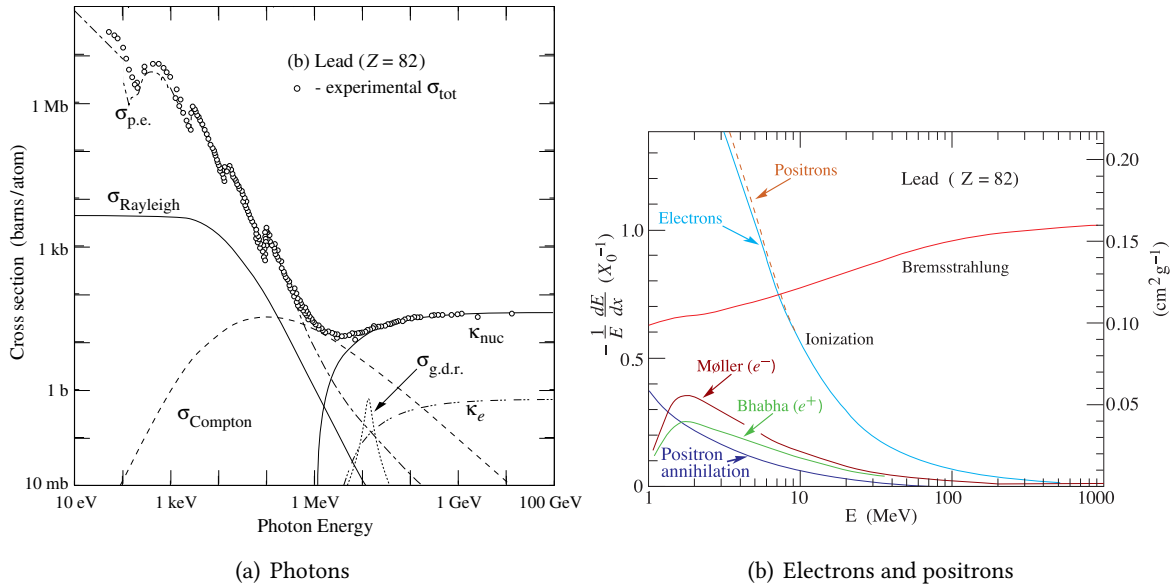
Figure 5.1: *Energy losses in matter (lead) as a function of the particle energy. For photons, the dominant processes are photoelectric effect ($\sigma_{p.e.}$) at low energy and pair production (κ) at energies higher than a few MeV (see [1] for more explanations about the notations).*
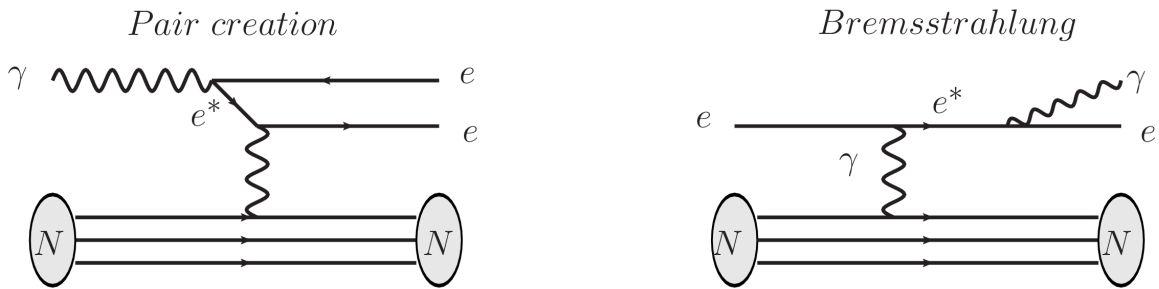
Figure 5.2: *Processes responsible for a shower development in an electromagnetic calorimeter. Presence of matter, denoted as N in this picture, is mandatory to ensure energy conservation.*

In a calorimeter, the incident particle is showered to lower energy particles and the resulting secondary particles are measured. Processes involved depends on the material properties and on the particle's nature and characteristics.

An electron or photon entering the calorimeter matter will radiate or convert through the process $\gamma \rightarrow ee$ or $e \rightarrow e\gamma$. If the secondary particles are energetic enough, the same reactions will occur and so on. This creates a cascade of particles, with lower and lower energy. The process stops when the secondary particles reach a critical energy, whose value depends on the material nature, where the dominant processes are no more bremsstrahlung and pair creation (see Fig. 5.3), but, for electrons, energy loss by ionization.

The energy lost by an electron in matter decreases exponentially with the distance x and its re-
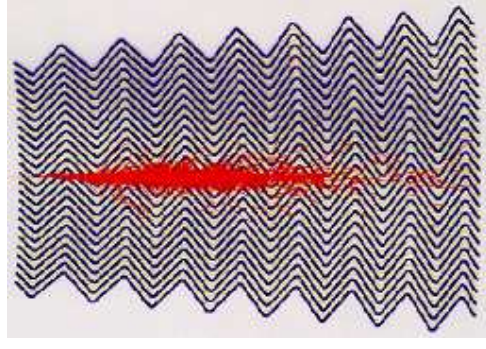
Figure 5.3: *Illustration of an electromagnetic shower development in the ATLAS electromagnetic calorimeter with accordion geometry. The incident particle is coming from the left of the figure [81].*

maining energy can be written $E(x) = E_0 e^{-\frac{x}{X_0}}$. X_0 is the radiation length and can be interpreted as the average distance over which an electron can travel before its energy is reduced to $\frac{1}{e} \approx 37\%$ of its original energy E_0. Similar relations exists for photons and it can be shown that their mean free path in matter is a simple function of the radiation length: $< l > = \frac{9}{7} X_0$.

Another important parameter to understand electromagnetic shower is the critical energy corresponding to the threshold energy below which the ionization is larger than the Bremsstrahlung for electrons and where the shower development is stopped due to the lack of energy of the secondary particles. It is defined, following [82], as the energy where the losses per radiation length is equal to the electron energy.

To a good approximation, the critical energy and the radiation length are expressed in Equations 5.1 and 5.2 as a function of the atomic number Z and mass A of the material [83]. The denser the material, the lower is the distance a particle can travel without loosing energy, characterized by $\frac{X_0}{\rho}$ where ρ is the material density. The critical energy depends on the number of electrons in the atomic cloud that are likely to be snatched from the atom by ionization: the higher is Z, the lower is the critical energy.

The lateral size of the shower, due for example to electrons multiple scatterings, is described by the Molière radius R_M (Eq. 5.3). On average, a cylinder of radius $1 R_M$ contains around 90% of the shower energy, and 99% of the energy is contained in $3.5 R_M$.

$$\text{Critical energy: } \epsilon[MeV] \approx \frac{a}{Z + b} \tag{5.1}$$

where a and b have different values depending on the matter state: for solids, $a = 610$ MeV and $b = 1.4$, while for gases $a = 710$ MeV and $b = 0.92$.

$$\text{Radiation length: } X_0[\text{g.cm}^{-2}] \approx \frac{716.4 \, A[\text{g.mol}^{-1}]}{Z(Z+1)ln\left(\frac{287}{\sqrt{Z}}\right)} \tag{5.2}$$

$$\text{Molière radius: } R_M[\text{cm}] \approx 21.2 \, \frac{X_0[cm]}{\epsilon[MeV]} \tag{5.3}$$

$$\tag{5.4}$$

Some numerical values for these parameters are given in Table 5.1 for the liquid argon and lead.

In the simple model where an electron radiates or a photon convert each X_0, the secondary particles have energy $E(n) \approx \frac{E_0}{2^n}$ where $n = \frac{x}{X_0}$ characterizes the distance inside the material. The shower will therefore stop at a depth x, reached when $E(n) = \epsilon$, *i.e.* when:

$$x_{max} = \frac{ln\left(\frac{E_0}{\epsilon}\right)}{ln(2)} X_0 \tag{5.5}$$

Material	Liquid Argon	Lead
Atomic number Z	18	82
Atomic mass number A	39.948	207.2
Density ρ [g.cm^{-3}]	1.40	11.4
Radiation Length X_0 [g.cm^{-2}]	19.55	6.37
Radiation Length X_0 [cm]	14.00	0.56
Critical energy ϵ [MeV]	32.84	7.43
Molière radius [cm]	9.04	1.60

Table 5.1: *Electromagnetic shower parameters numerical values in Liquid Argon and lead from [1].*

In practice, more realistic models are established thanks to Monte Carlo simulations.

Since energy and rate of particles are parameters given by the LHC accelerator, one can simulate the optimal parameters (calorimeter depth in X_0 and cells size) for the ATLAS electromagnetic calorimeter.

The energy loss ($\frac{dE}{dx}$) by the last low-energy electrons and positrons of the shower creates the signal (ionisation or scintillation) that can be measured. At this point, two choices can be made: either the whole calorimeter is made of an unique material, that acts both as active and passive material, which is the case for homogeneous calorimeters; or the detector is a sampling calorimeter with a passive dense material (the absorber) where the shower develops, and an active medium where the $\frac{dE}{dx}$ energy loss give rise to the measurable signal.

5.1.2 Application to the ATLAS calorimeter geometry

The ATLAS electromagnetic calorimeter is a sampling calorimeter in which the signal is produced by ionization of the liquid argon. It is made of a succession of lead absorber and liquid argon gaps with a readout electrode at its centre. It hence has to be operated at the liquid argon temperature, which requires a surrounding cryostat.The choice of liquid argon is dictated by its high resistance to radiations. Density is also the reason for using liquid state material instead of gas. The achieved radiation length and Molière radius are respectively $X_0 \approx 3.0$ cm and $R_M \approx 7.3$ cm at $\eta = 0$.

The absorbers and electrodes are shaped in an accordion geometry, that provides natural uniform coverage in the ϕ direction. Cells are projective with respect to the centre of the detector with a shape ensuring that particles go through the same amount of matter in each part of the detector (Fig. 5.4 and 5.5).

The total longitudinal expansion lies between $25X_0$ and about $42X_0$ (Fig. 5.5), corresponding to the full containment of electromagnetic particles up to a few TeV. The first layer of cells in the calorimeter is very finely segmented in η allowing to disentangle a single photon from the two collimated photons arising from a neutral pion decay. The second layer is where most of the energy is deposited with around $15X_0$ depth; the lateral size of the cells is dictated by the Molière radius of the shower in the electromagnetic calorimeter. Finally, the back layer collects the end of the showers, with coarser granularity.

More about cells characteristics can be found in the previous chapter (Section 4.2.4).
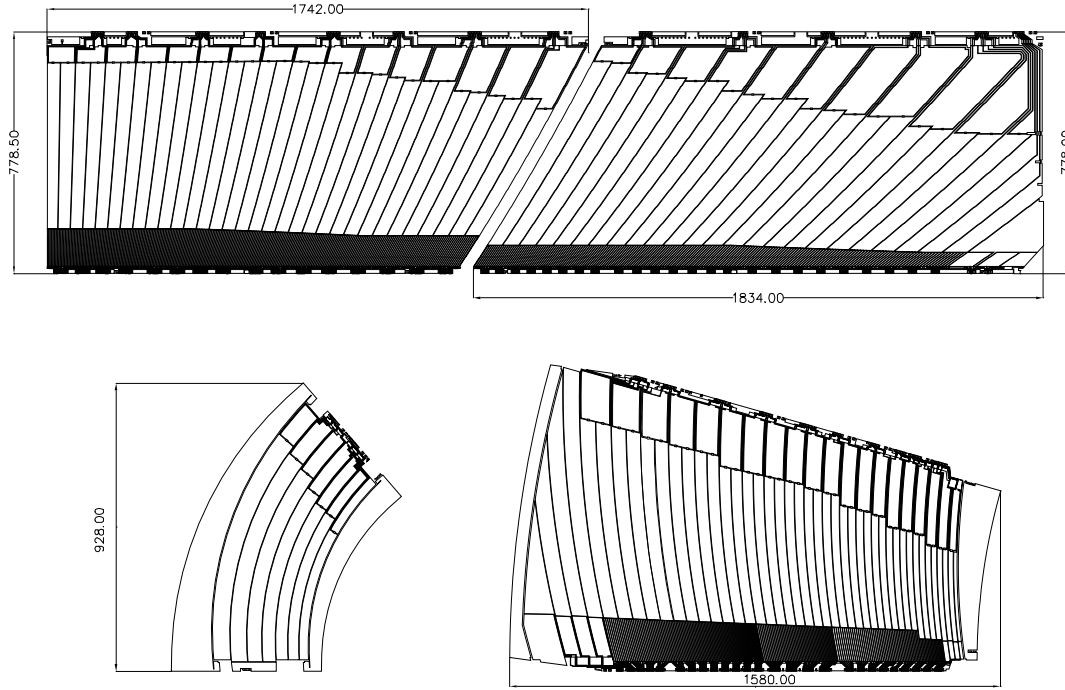
Figure 5.4: *Electrode geometry. Top: in the barrel. Bottom: for the two end-cap wheels [57].*
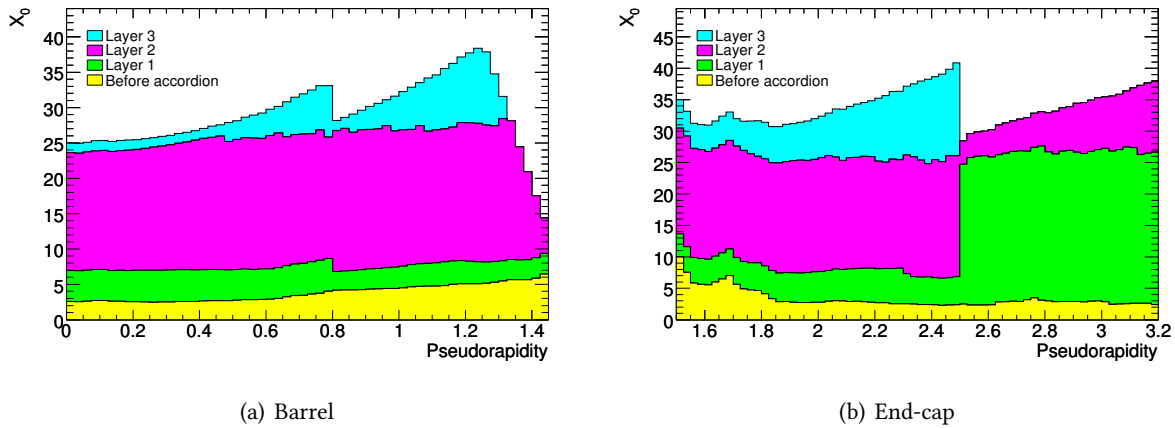
(a) Barrel

(b) End-cap

Figure 5.5: *Calorimeter depth in X_0 unit. The matter before the electromagnetic calorimeter and the detail of the three LAr layers are shown in the barrel and in the end-caps [57].*

5.1.3 Electronics and energy reconstruction

Some details about the electrodes are shown in Figure 5.6. A particle going through liquid argon produces the emission of ionization electrons. Thanks to the high voltage applied to the readout electrode, the ionization electrons drift toward it and create a measurable current. The signal shape is triangular as illustrated in Figure 5.7.

The current raises very fast and its amplitude is proportional to the initial particle energy ($A \sim 3\mu\text{A}/\text{GeV}$). The decrease is slower creating a triangular pulse shape. The duration of the triangular decrease is due to the drift time of ionization electrons towards the electrode.

The signal from the electrode is sent to the electronic readout sketched on Figure 5.8. It is separated into a Front-End system mounted directly on the cryostat, and a Back-End system set-up in an off-
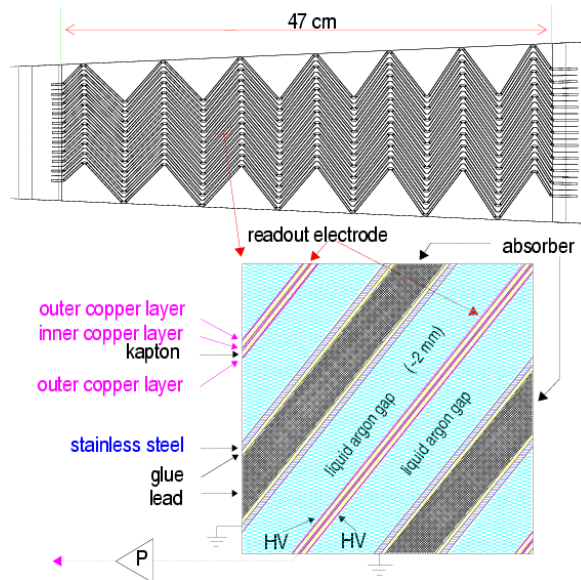
Figure 5.6: *Accordion structure of the barrel. The top figure is a view of a small sector of the barrel calorimeter in a plane transverse to the LHC beams. The bottom is a zoom on the electrode structure showing the liquid argon, lead absorber and copper electrode [84].*
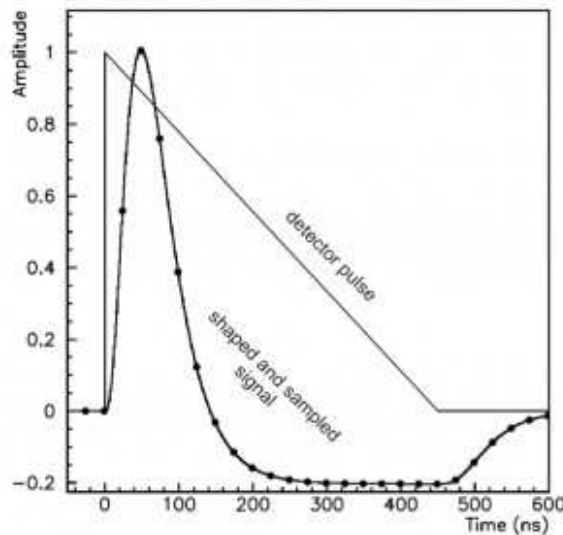
Figure 5.7: *Triangular signal shape going out of the electrode and pulse bipolar shape after the FEB [57].*

detector underground location. The Front-End Boards (FEBs) role is to shape, amplify and digitize the raw signal coming from the electrodes. It also contains trigger modules that contribute to the L1 trigger decision. The back-end system is based on the Digital Signal Processor (DSP) electronics that perform the optimal filtering calculation to reconstruct the cell energy.

In the Front-End Board (FEB) electronics, the signal is shaped to end-up with a bipolar pulse illustrated in Figure 5.7. This particular bipolar shape allows the signal to have a null integral, even in case of pileup, so no noise suppression has to be performed. The time constant is chosen in order to minimize the noise+pileup contribution for the nominal LHC luminosities.

The amplification uses three different gains to ensure a good precision on a wide energy range: low, medium and high corresponding to amplification factors of about 0.8, 8.4 and 82 respectively. The energy threshold between those gains are roughly 40 (high to medium) and 400 (medium to low) GeV in the second layer of the calorimeter.

The amplitude is then measured each 25 ns and sent to the DSP.
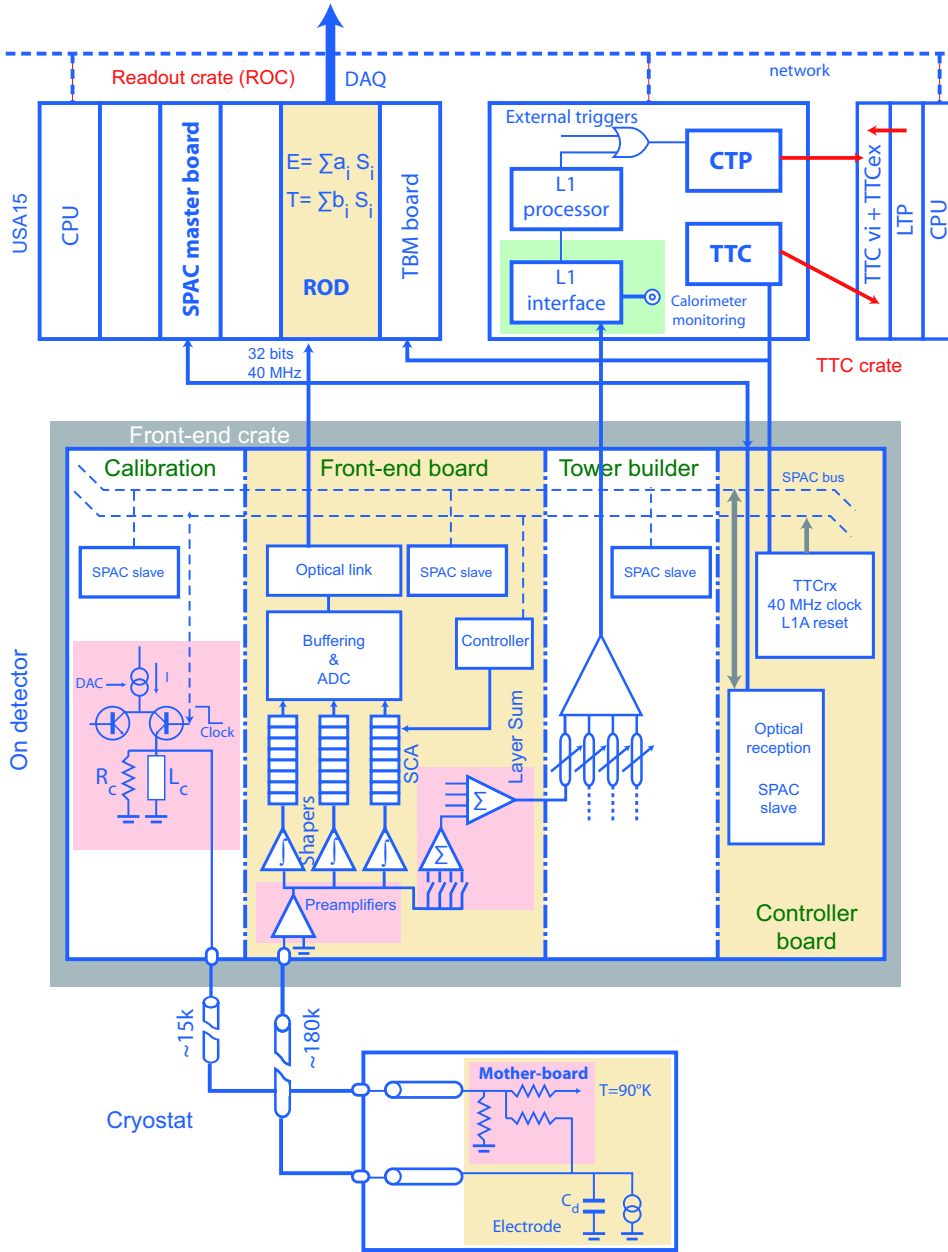
Figure 5.8: *The LAr calorimeter readout electronics. The different locations are shown; the electrode in the cryostat, the front-end crate on the detector and the read-out crate in the cavern [57].*

Each cell energy is first reconstructed by the online DSP system using the formula 5.6, whose coefficients are estimated from test beam measurements, Monte Carlo simulation and calibration runs. The calibration runs are taken regularly during the data-taking periods and consist in injecting a known signal into the full electronics chain and compare its reconstructed energy to the injected one.

$$E_{cell} = F_{\mu A \to MeV} \times \frac{M_{cal}}{M_{phys}} \times R \times \sum_i a_i (ADC_i - P) \tag{5.6}$$

where:

F is the current to energy conversion factor evaluated from test beam;

$\frac{M_{cal}}{M_{phys}}$ corrects for bias due to the different shapes between calibration and physics signals.

R is the electronic gain $(ADC \to \mu A)$.

a_i are the optimal filtering coefficients (OFC) used to estimate the pulse amplitude [85]. They are estimated together with R during the calibration runs. The OFCs are computed in order to reduce the noise (electronics and pile-up) contribution. Due to different pile-up conditions, these coefficients are different between 2011 and 2012 data.

P is the pedestal corresponding to the ADC response with zero current.

i is the index of the sample (usually 5 samples measured each 25 ns).

The DSP also computes, for each cell, a quality factor Q [86] quantifying the agreement between the expected shape of the physical signal and the observed one: the higher Q, the lower the cell quality.

5.1.4 Energy resolution

The energy resolution in a sampling calorimeter is approximated by the quadratic sum of three components as in Equation 5.7 (where the energy E is in GeV).

$$\frac{\sigma_E}{E} = \frac{a}{\sqrt{E}} \oplus \frac{b}{E} \oplus c \tag{5.7}$$

a is the stochastic term arising from the fluctuations due to the physical shower development in the calorimeter. The energy is proportional to the number of final particles in the shower N, hence the resolution goes like $\sqrt{N} \sim \sqrt{E}$. a is of the order of 10% in ATLAS.

b accounts for the degradation of low energy resolution due to electronic noise, including both the readout chain noise and the pileup. It characterized the fact that a high signal is easier to measure over the noise than a small amplitude signal, hence proportional to $\frac{1}{E}$. It is expected to be ~ 0.3 GeV.

c is the constant term gathering all the remaining uncertainties, coming, for example, from non-uniformity of the calorimeter or calibration stability. This term is the dominant one at high energy. The design is chosen to achieve a 0.7% constant term.

A better understanding of the detector allow to reduce the constant term and improve the energy resolution (see Section 5.3).

5.2 Data quality

Before being used for physics, data undergo a full set of tests to remove bad quality data, *i.e.* events for which at least one part of the detector was identified as behaving badly. For the electromagnetic calorimeter, the readout electronics suffers from several sources of noise, that need to be identified and controlled not to bias the physics analyses with fake signals. This section describes the main noise sources and the techniques developed during the last years to discard the affected events with the smaller possible luminosity losses. A full review can be found in [87] (see also [88]).

5.2.1 Prerequisites

Online data quality

Data in ATLAS are segmented in runs with a unique number. The basic units are not the events themselves but small constant time blocks of approximately constant integrated luminosities, the lumi-blocks (typically 60 s).

After data quality assessment from all ATLAS subsystems, a Good Run List (GRL) is provided to analysers containing the list of lumi-blocks where no critical defects were observed and can thus be used to produce physics results.

Data are first monitored online, from a fraction of events quickly processed, to ensure no data loss along the whole processing chain and stop the data-taking if a severe unrecoverable problem is detected (for example, if more than $\sim$ four FEBs lose connection with the data acquisition system). The spotted online defects are stored in a databased used for the final decision on whether or not to use the affected data.

Streams

The ATLAS trigger is divided into three stages, whose combination gives a trigger chain. Several chains are associated to form a trigger menu, and data associated to a given menu are called stream. Two categories of streams are defined, depending whether they are triggered on full or empty bunches. Indeed, the bunch structure of the LHC beams is such that some bunches do not contain protons. During a typical LHC run in 2012, beams are organized in a complicated and not constant structure but consisting in general of 35 filled bunches followed by 8 empty bunches.

The more important streams for data quality assessment in the LAr calorimeters are the following:

- The usual streams used for physics are triggered on filled bunches where real collisions happen, they are representative of the full dataset:

  - Express: the express stream is representative of the total dataset but contains only $\sim 3\%$ of the events;

  - LArCells: this stream is designed to increase the statistics that can be processed in a short amount of time by reducing the number of LAr cells, recording, for instance, only cells inside a region of interest. But it gives reliable information about most of the possible noises.

- To identify electronic noise, some events are triggered on the intentionally empty bunches, where no collision happen and any detected signal is the result of noise.

  - CosmicCalo is the main stream triggered on empty bunches.

  - LArCellsEmpty follows the same principle than the LArCells stream except that it is triggered on empty bunches.

Calibration loop

The data processing is made in two stages. During the first one (Express processing), a small fraction of the events is processed in order to identify the possible problems. The LADIeS[1] shift task is dedicated to the observation of this first processing in order to identify the bad quality data and take the appropriate action. This should be done within the 48 hours of the end of the run, during which the new calibration constants are computed. This period is hence called calibration loop. After this delay, the full (Bulk) processing of the run is launched, meaning that all possible defects should have been identified and corrected. After the full processing is finished, shifters have another chance to spot the remaining issues in the physics streams, that will be masked during the next full processing of the data.

5.2.2 Identification of defects

Several noises are known and can be identified in the data as described below. Some of them lead to defects that can be corrected at the reconstruction stage and the affected data is kept and labelled as recoverable. For the other intolerable defects, the affected lumi-blocks have to be dropped from the data to be used for physics analyses, unless more refined techniques exist to lower the data losses.

---

[1]LAr Data Inspection and Sign-off

High voltage trip

It happens that the High Voltage (HV) supplied to a set of readout electrodes suddenly goes down. This is detected quickly during the data-taking and an auto-recovery procedure is launched online. This is most often sufficient to recover the high voltage to its nominal value. Otherwise, an expert intervention is needed to further investigate the problem. In principle, all lumi-blocks where the high voltage is not at its nominal value should be dropped from the GRL. In practice, corrections can be applied at the reconstruction stage to take into account the non-nominal high voltage during the ramp-up. This relies on the checks that the distributions of variables sensitive to LAr problems such as the E_T^{miss} are not distorted for events in the ramp up lumi-blocks [87]. Thanks to this procedure, only the lumi-blocks corresponding to the ramp down are lost for physics (Fig. 5.9), corresponding to 0.46% of 2012 data.
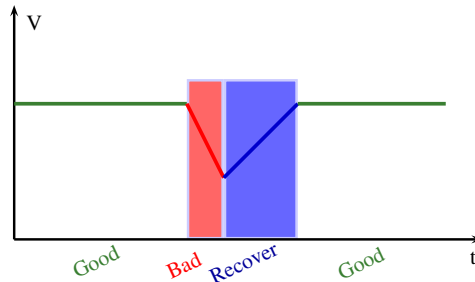
Figure 5.9: *HV trip illustration. The lumi-blocks affected by the trip are bad for physics. The lumi-blocks during an HV raise are recoverable offline and are hence kept.*

The source of HV trips is not yet understood. An empirical rule tends to show that they are not luminosity-dependent; their number increases only when the LHC operational conditions are not stable, similarly to a training procedure. This is encouraging for the next LHC runs where increased luminosities are expected.

5.2.2.1 Burst of coherent noise

Sometimes, for unknown reasons, large areas of the detector are affected by a burst of coherent noise, characterized by many cells giving large signals with distorted pulse shapes (bad quality factor) during a short period of time (Fig. 5.10).
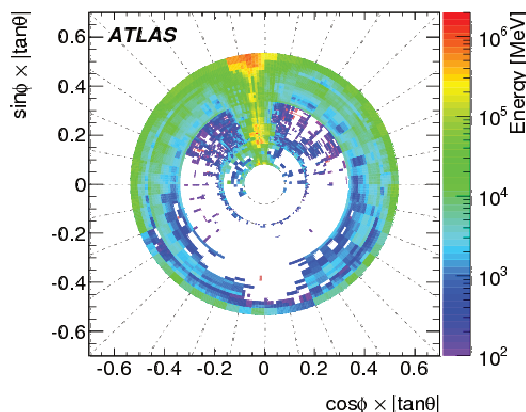
Figure 5.10: *Illustration of a noise burst in the LAr calorimeter. Some cells have abnormal measured energy ($\sim 10^5$ MeV) creating a hot spot in orange on this plot [87].*

Identifying the affected events is important in order not to mix them up with physics signals. An interesting variable to classify the noisy area is given by the fraction of cells with a signal greater than

three times the electronic noise, estimated from calibration runs, $Y_{3\sigma}$. The distribution of this variable for the electromagnetic end-caps measured in LHC empty bunches is shown in Figure 5.11 for 1.7 fb^{-1} of data. In case of Gaussian noise only, one would expect this variable to peak at around 0.13%[2], while large tails are observed.

Figure 5.11: $Y_{3\sigma}$ *in the end-caps [87].*

To reduce the impact of this noise, a two step procedure has been developed. First, a selection is performed based on the qua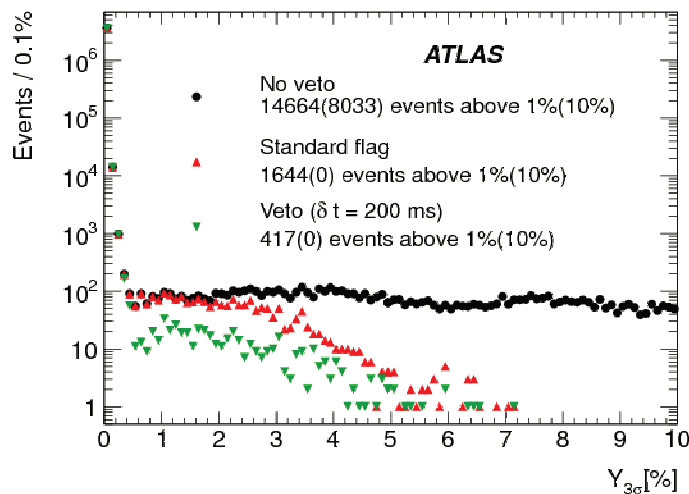lity factor Q: if there are more than five FEBs containing more than 30 channels with $Q > 4000$, the event is marked with a Standard flag and vetoed. Tails of the $Y_{3\sigma}$ are very much reduced with this procedure.

The remaining events could be discarded with a lumi-block masking procedure, which is the strategy applied in 2010 and early 2011 data. However, a more refined study of the burst structure allows to reduce the luminosity losses to a smaller time window. Indeed, the coherent noise burst duration was found to be shorter than a lumi-block duration of 60 s. The time window procedure is based on the identification of the most noisy event with the Standard flag. Events in a time window of $\pm\delta t \approx 50$ ms from it are vetoed (exact value depending on the year). The final distribution of $Y_{3\sigma}$ is shown in green on the Figure 5.11 where one can see the largely reduced tails. The bursts not flagged with this method are still discarded by masking the full affected lumi-blocks. The total amount of luminosity lost due to noise burst is about 0.2%, most of it correctly identified with the Standard flag + time window procedure.

Noise bursts number increases with luminosity, which may be problematic for the next LHC run. However, with the time window technique, the δt can be tuned to limit the impact of the burst on the data and limit the luminosity losses.

5.2.2.2 Sporadic noise

Some cells produce noise in a random way during a run and outside any burst of coherent noise, that creates hot spots (*i.e.* clusters with very high occupancy rate during a run). To avoid the reconstruction of fake particles, the guilty cells are masked, but to prevent calorimeter hole, the masking is done only for events in which the cell has a $Q > 4000$, except if it is very noisy and is masked for the whole run. For some very rare cases where a cell is identified as sporadically noisy during several consecutive runs, it can be masked permanently for the next runs.

Lots of efforts have been put in the automation of this task and shifters are helped by several tools, most of them being centralized in the Web Display Extractor (WDE)[3]. Based on the LArCellEmpty

---

[2]p-value corresponding to a significance of 3σ.

[3]https://atlas-larmon.cern.ch/WebDisplayExtractor/

stream, a flag is proposed to classify the cell as sporadicBurstNoise (masked when $Q > 4000$) or highNoiseHG (*i.e.* permanently masked, representing 0.06% of the total number of channels).

5.2.3 Beam background

Another source of observed noise in the calorimeters is not attributable to electronics but to beam-beam or beam-gas interactions inside the LHC beam pipes. Indeed, the beams can have large spreads due to non-homogeneous momentum of their constituting protons, creating a halo around the beam core. A cleaning system is part of the LHC structure, including collimators and absorbers to cut the unwanted halo. Nonetheless, some remnants produced by this beam halo can hit the ATLAS calorimeter, especially in the area close to the beam pipe were no protection is installed to leave enough room for the beams to circulate. These interactions can produce high energetic particles travelling in the direction parallel to the z direction, and leaving a large fraction of energy in the calorimeter.

On one hand, one does not want to mask the affected lumi-block or cells because this is a physical effect. On the other hand, this noise can hide some other pathologies such as hot spots. A strategy to mask this background for the data quality assessment is then developed [89]. More techniques are considered at the analysis stage to reject jets produced by beam background but they are not discussed here.

The CSC muon detector fully cover the LAr calorimeters in terms of pseudorapidity and is then usable to tag the beam background events. Beam background produced muons have different properties from collision muons. They are produced in a direction parallel to the beam pipe, characterized in Figure 5.12(a) by the quantity $|\theta_{pos} - \theta_{dir}|$ where θ_{pos} is measured with respect to the centre of the detector and θ_{dir} is given by the trajectory direction. For collision data, this quantity should be 0, which is not the case for non collision data where $\theta_{dir} \sim 0$. Another characteristics of beam background produced muons is their measured early time with respect to the collision one if interaction takes place in the first CSC crossed by the beam before the collision (Fig. 5.12(b)). Based on these observations, several techniques are derived to identify the beam-induced background with the CSC.
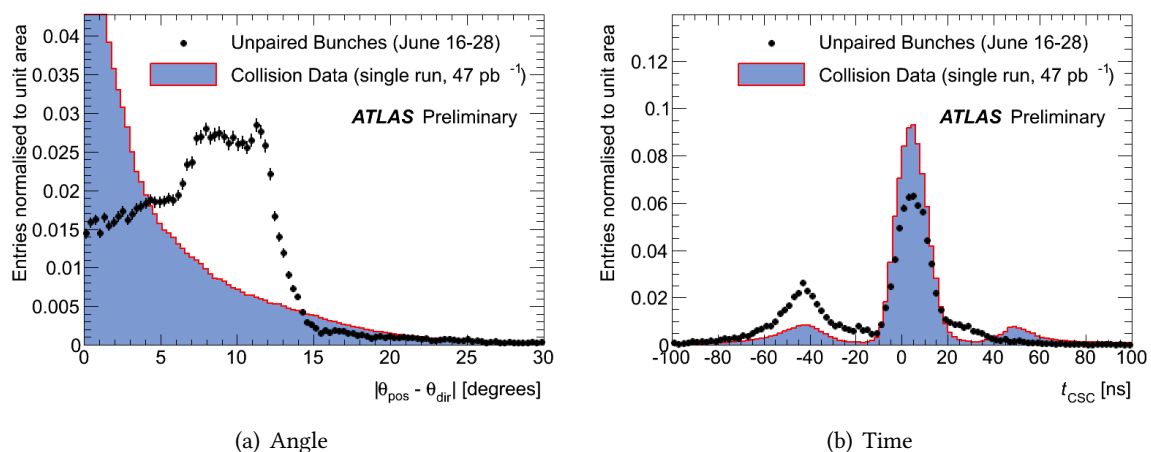

| (a) Angle | (b) Time |

Figure 5.12: *Discriminant variables used in the CSC veto technique [89]*

The beam background phenomenon appeared again in Summer 2012. The reason for its sudden re-apparition is not fully understood yet. The only change in the LHC conditions that took place approximately at the same moment is a magnet polarity flip in the ALICE experiment.

5.3   Offline calibration

The cell-level calibration described in Section 5.1.3 can be improved taking into consideration some known effects such as the energy losses outside the clusters. The standard historical calibration procedure is outlined below and is fully described in [90].

1. The full procedure starts with the energy reconstructed at cell level from Equation 5.6;

2. The particle identification algorithm is then run on these clusters as described in Section 4.5.3;

3. Then, an Monte Carlo-based calibration is performed to take into account out-of-cluster energy losses, depending on the particle nature (electron or (un)converted photon).

4. Finally, an *in-situ* correction is applied to data in order that the response from data and simulation to a given energy particle are the same. The correction on each electron energy is computed such that the Z peaks between data and Monte Carlo are aligned. The correction factor α is chosen as η dependant to take into account residual non-uniformities of the detector.

Since the final Run I analysis, this calibration uses a refined technique described in [91]. The Monte Carlo-based calibration has moved to an MultiVariate Approach (MVA) [92], whose improvements with respect to the standard calibration is visible in Figure 5.13.
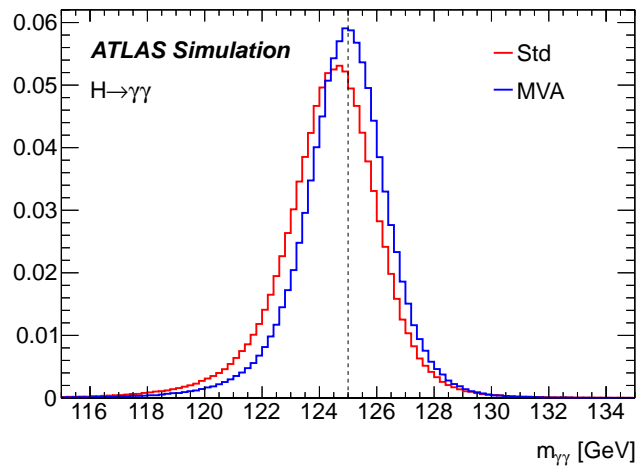
Figure 5.13: *New MVA calibration compared to the cut-based approach [91].*

After this Monte Carlo-based calibration, specific corrections for known identified effects are applied:

- In data, corrections are applied to correct for stability effect such non nominal high voltage settings;

- A specific procedure is deployed to calibrate separately the pre-sampler and the ratio $\frac{E_1}{E_2}$ of the energies measured in the first two samples of the accordion. The $\frac{E_1}{E_2}$ ratio is tuned thanks to muon response study in the calorimeter.

- A new dead material map (similar to Figure 4.6) is estimated from data and propagated to the GEANT4 detector simulation in the Monte Carlo samples.

Residual corrections from *in-situ* measurements are still needed. They are derived using mainly $Z \rightarrow e^+e^-$ events but also $J/\Psi \rightarrow e^+e^-$ and $W \rightarrow e\nu$ samples.
They correct especially for long range non uniformities in the calorimeter response.Thanks to the

precise knowledge of the Z boson mass from LEP, electron pairs from Z decays can be used in order to inter-calibrate different regions (in pseudo-rapidity) of the detector. The data electron energy in the region i is modified in the following way:

$$E^{measured} = (1 + \alpha_i)E^{true}$$

and the coefficients α_i are computed from a fit to the reconstructed Z boson mass, following the same method as the previous calibration [90]. They are illustrated in Figure 5.16(a). An estimation of the final constant term c is also performed quantifying the resolution $\sigma^{data} = \sigma^{MC} \oplus (c \times E)$. The constant term are shown in Figure 5.16(b).

Finally, Figure 5.15 shows the final data to Monte Carlo Z lineshape comparison after this full procedure.

(a) α correction
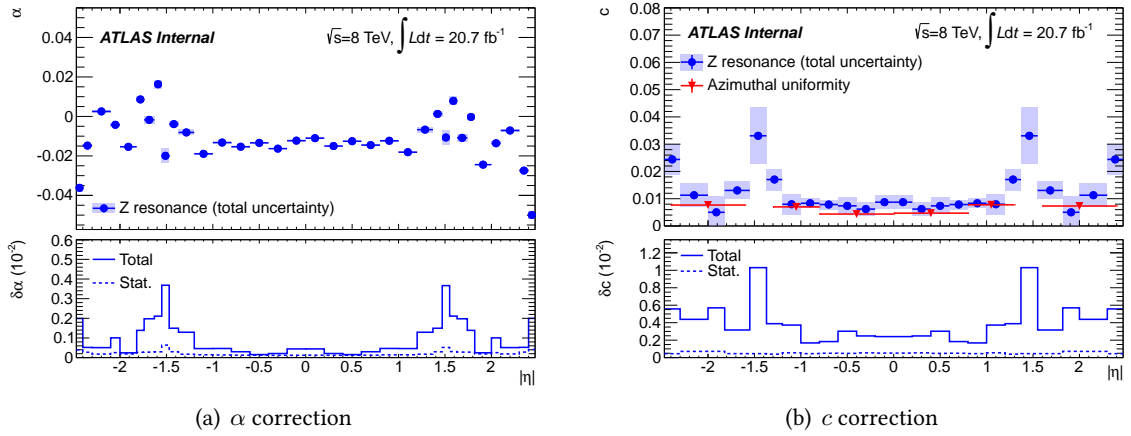
(b) c correction

Figure 5.14: *Final data to Monte Carlo corrections for 2012 data [91].*
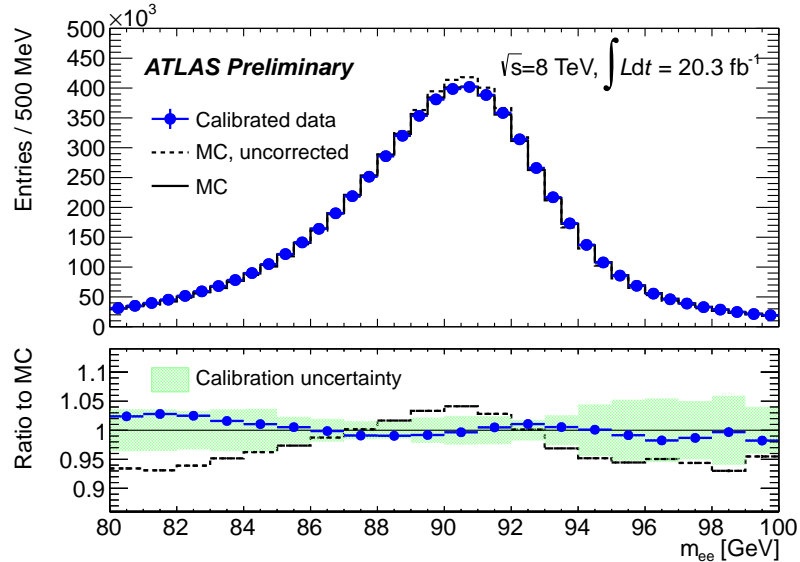
Figure 5.15: *Comparison between Monte Carlo and data after offline calibration for 2012 data [91].*

Figure 5.16 shows the same results than Figure 5.14 for 2011 data. One can see that the values are very similar, in particular in the barrel calorimeter. The relative energy response as a function of the number of collision per bunch crossings μ and as a function of time are presented in Figures 5.17 and show a stability at the level of 0.05%.

(a) α correction
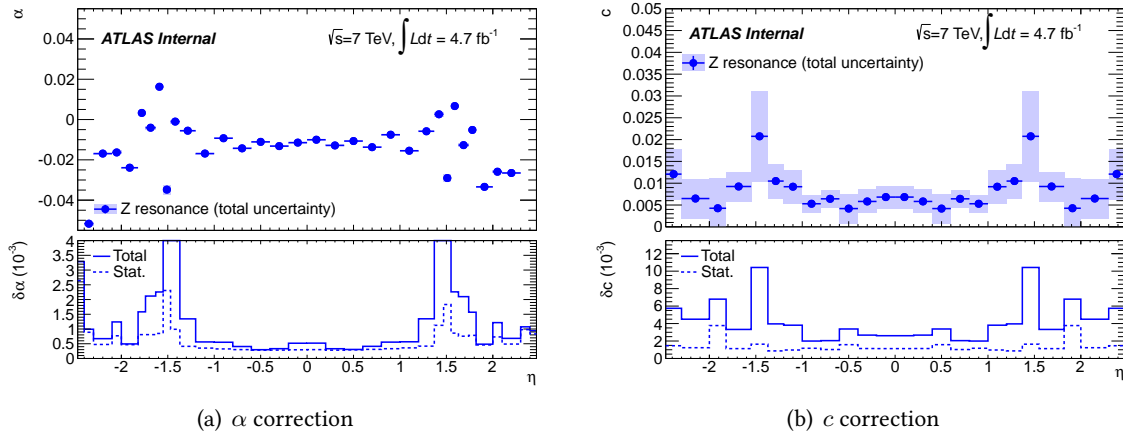
(b) c correction

Figure 5.16: *Final data to Monte Carlo corrections for 2011 data [91].*

(a) μ

(b) Time
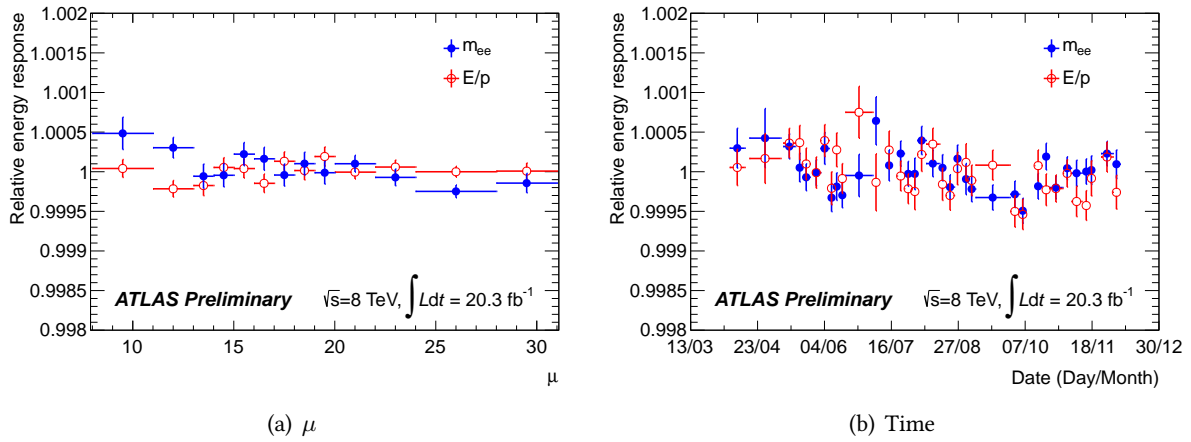
Figure 5.17: *Energy response as a function of μ and time, normalised to its average quantity for 2012 data [91].*

Figure 5.18 represents $\Delta\alpha$ *i.e.* the α computed from $J/\Psi \rightarrow e^+e^-$ and E_T-dependent $Z \rightarrow e^+e^-$ events, after the calibration procedure for 2012 data. They show a good agreement within the calibration uncertainties. Figure 5.19 shows similar plots for 2011 data, whose behaviour is similar to the 2012 data.

Figures 5.20 and 5.21 shows the $\Delta\alpha$ obtained after photon calibration from $Z \rightarrow \ell\ell\gamma$ events for 2012 and 2011 data. The agreement is good within the error bars.

Differences exist between 2011 and 2012 calibrations but they are minor: a change in the optimal filtering due to different pile-up conditions, a tiny pedestal shift, present in both years but slightly different between the two years [93, 94] and small differences in the photon and electron reconstructions. More informations about the 2011/2012 differences can be found in [95, 96].
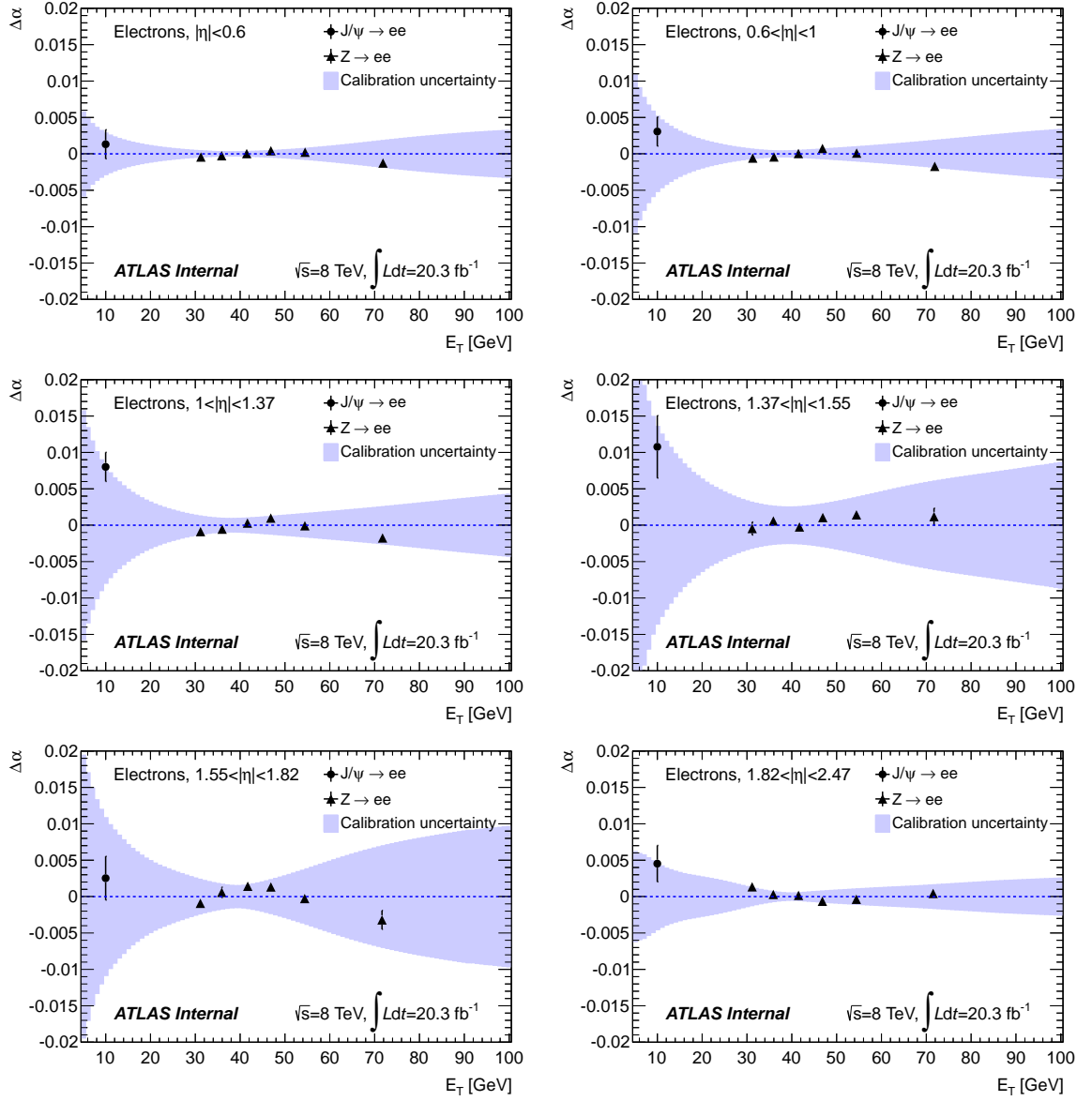
Figure 5.18: *Energy scale factors $\Delta\alpha$ for electrons. They represent the data/Monte Carlo difference after 2012 calibration [91].*
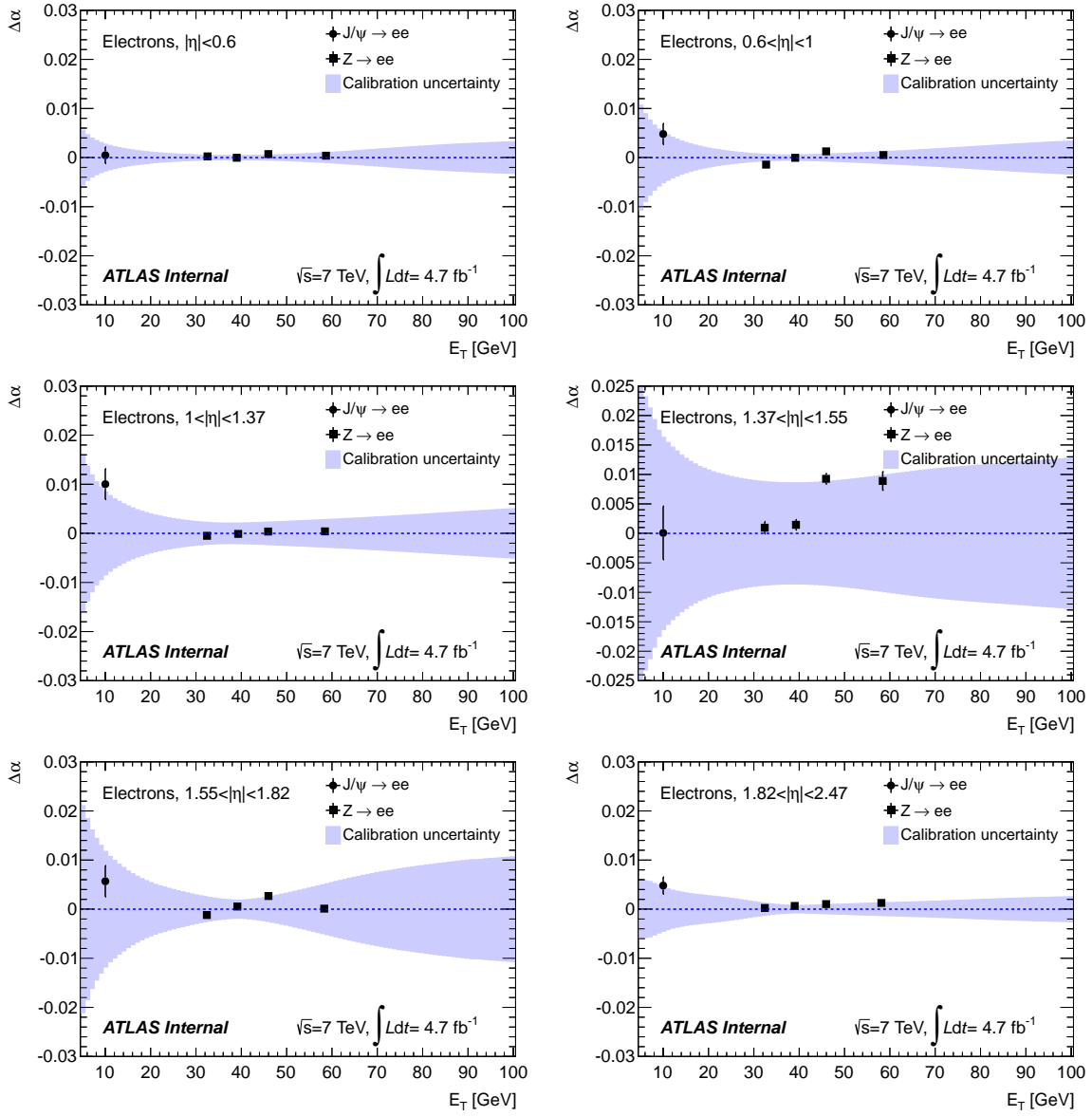
Figure 5.19: *Energy scale factors $\Delta\alpha$ for electrons. They represent the data/Monte Carlo difference after 2011 calibration [91].*
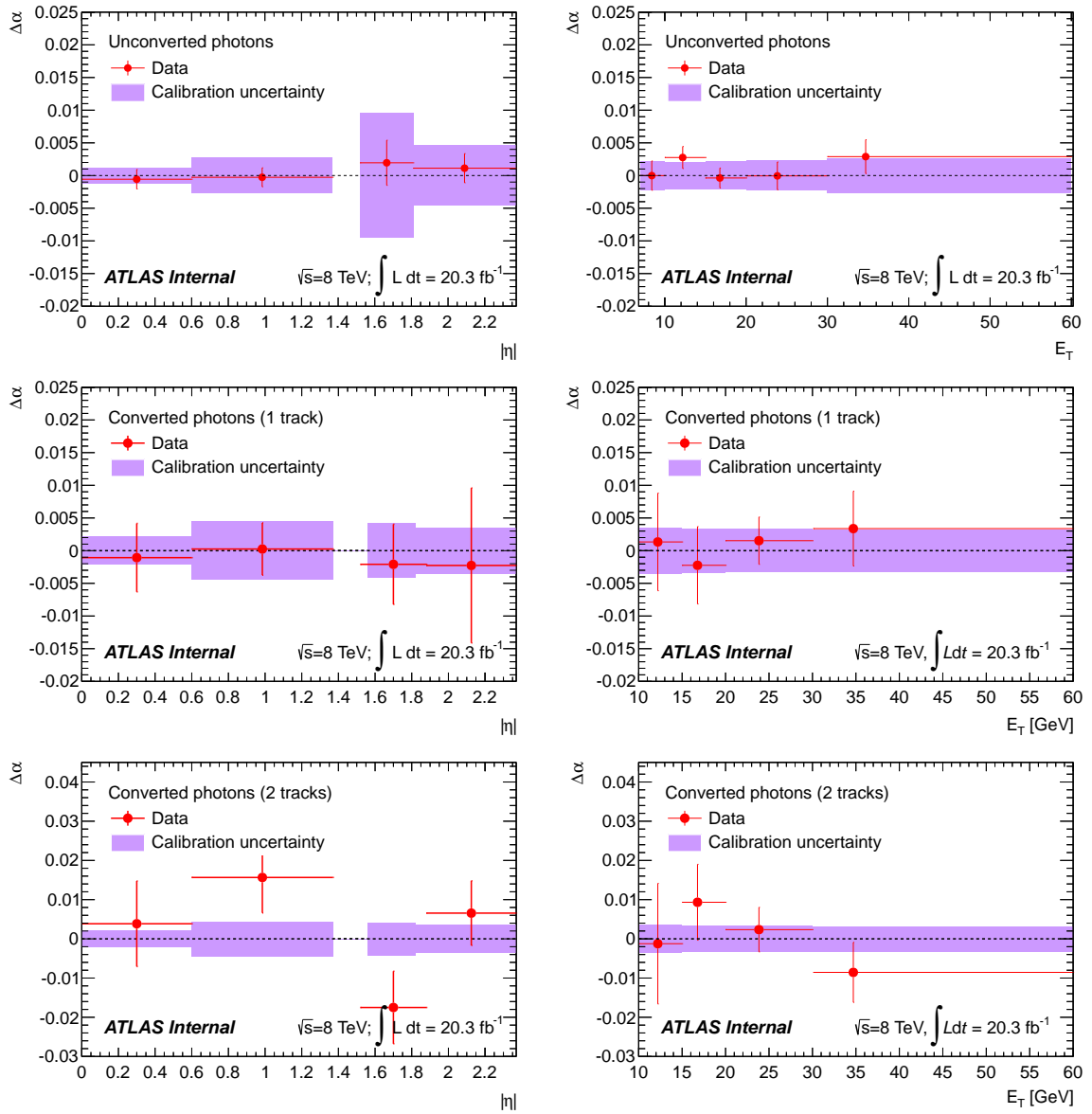
Figure 5.20: *Photon scale factors in 2012 as a function of $|\eta|$ (left) and E_T (right), for unconverted, one-track converted and two-track converted photons [91].*
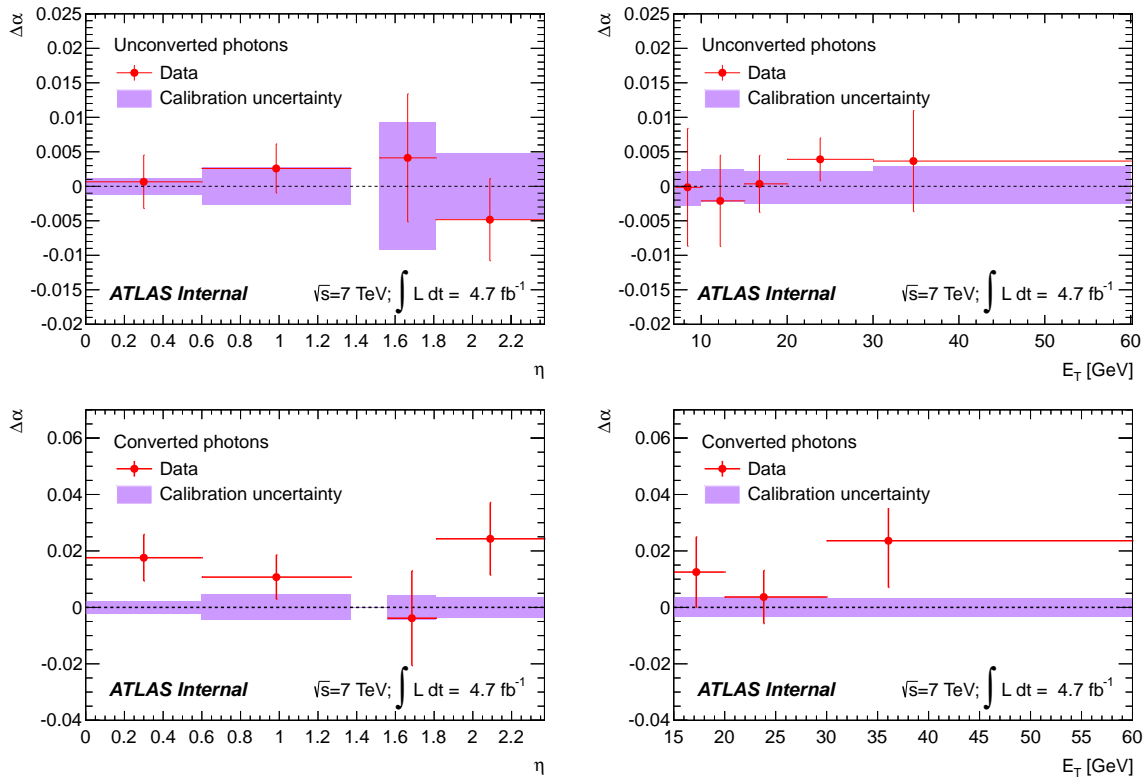
Figure 5.21: *Photon scale factors in 2011 as a function of $|\eta|$ (left) and E_T (right), for unconverted, one-track converted and two-track converted photons [91].*

5.4 The pointing method

Finding the photon's primary vertex is important in the context on the $H \rightarrow \gamma\gamma$ analysis since it is important for the mass resolution[4]. Indeed, the Higgs mass can be reconstructed from the photons transverse energy E_{Ti} and their polar angle θ_i (or pseudo-rapidity η_i) and azimuthal angle ϕ_i:

$$M_{\gamma_1\gamma_2} = \sqrt{2E_{T1}E_{T2}[ch(\eta_1 - \eta_2) - cos(\phi_1 - \phi_2)]}$$

The contribution to the resolution from the energy measurement is dominant, but the η resolution is not negligible. The precise knowledge of the pseudorapidity requires the measurement of the z of the primary vertex, *i.e.* the position of the Higgs decay on the z axis.

As a first approximation, one can consider that the interaction takes place at the centre of the detector $(0, 0, 0)$ with an uncertainty corresponding to the RMS of the interaction area: 56 mm in 2011 data and 48 mm in 2012. However, this is a crude approximation, which would degrade the $H \rightarrow \gamma\gamma$ mass resolution by a factor 1.4. The design of the electromagnetic calorimeter allows to get more precise determination of the z of the primary vertex.

The pointing [97] takes advantage of the longitudinal segmentation of the electromagnetic calorimeter to get the photon direction. The energy weighted barycentres of the photon shower in the first and second layer of the electromagnetic calorimeter are used to extrapolate its trajectory back to the interaction area (Fig.5.22).
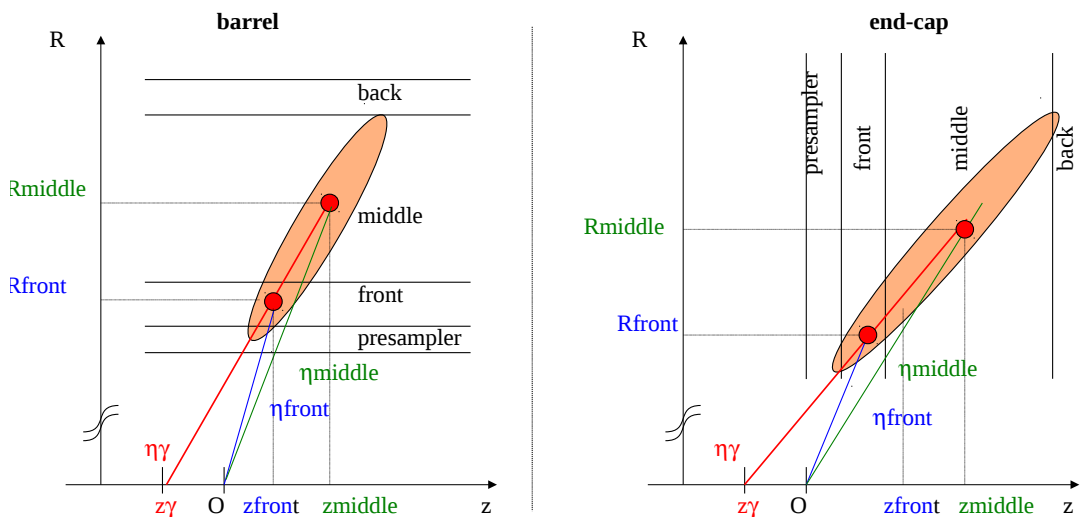

Figure 5.22: *Illustration of the pointing technique in the barrel (left) and in the end-caps (right) (adapted from [98]).*

For converted photons, it was shown [98] that a better precision can be achieved if the information from the tracker is also used. In this case, a derived pointing method is applied using the barycentre of the conversion electron in the electromagnetic calorimeter first layer and the conversion point from the tracker.

In practice, the extrapolation is not performed to the z axis, with coordinates $(x = 0, y = 0)$, but on the parallel axis of coordinates $(x = x_{BS}, y = y_{BS})$, which corresponds to the mean position of the interaction point in the transverse plane (Beam Spot).

From the z of each photon, the common vertex is determined with a weighted average of the

---

[4]As we shall see later, the determination of the primary vertex is important also for the track isolation.

individual z:

$$z_{common} = \frac{\frac{z_1}{\sigma_1^2} + \frac{z_2}{\sigma_2^2} + \frac{z_{BS}}{\sigma_{BS}^2}}{\frac{1}{\sigma_1^2} + \frac{1}{\sigma_2^2} + \frac{1}{\sigma_{BS}^2}}$$

where z_i and σ_i are the z coordinate and uncertainty of photon i. σ_{BS} value is 56 (or 48) mm and z_{BS} is close to 0. This formula gives a more important weight to the more precise measurement, precision that depends on the conversion status of the photon and its pseudorapidity (photons in the barrel have a better primary vertex resolution).

Thanks to the pointing technique, ATLAS can achieve a z resolution smaller than 20 mm, good enough not to degrade significantly the ≈ 4 GeV diphoton invariant mass FWHM.
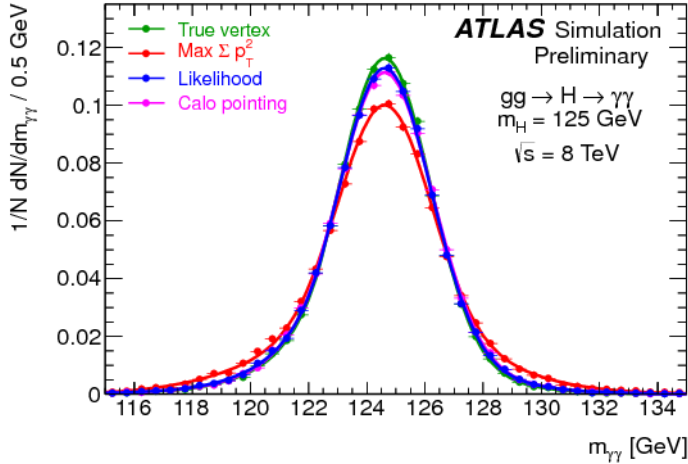
Figure 5.23: *Higgs mass resolution in the diphoton channel when the selected primary vertex is the highest $\sum p_T^2$ one or the vertex is selected with pointing. This last method considerably improved the resolution [99]. The likelihood method will be presented in Chapter 6.*

5.5 Oscillations

This study (described in the internal note [100]) was performed with a selection of single photon events in the first fb^{-1} of 2011 data. Monte Carlo samples used are $H \rightarrow \gamma\gamma$ samples[5] for photons and $Z \rightarrow e^+e^-$ samples for electrons. The calibration used at that time is described in [90].

Strange oscillations were identified for variables reconstructed from pointing, when compared to the Inner Detector information.

After defining the variables used in the analysis, oscillations will be shown before the different checks that were performed in order to determine the origin of the phenomenon. Finally, strategies to correct this effect are presented and the impact on the $H \rightarrow \gamma\gamma$ analysis is quantified.

5.5.1 Observable of interest

The selected photon should be tight (see § 6.2.2) with transverse momentum $p_T > 20$ GeV and outside the crack region $1.37 < |\eta_{s2}| < 1.52$.

Objects of interest are unconverted photons or photons converted in the TRT for which the track do not provide information about the primary vertex. They are then reconstructed by the pointing technique from the electromagnetic calorimeter first and second layers. The precision of the pointing is quantified by comparing the z determined from this method to the z of the primary vertex that is reconstructed from Inner Detector information only. To reduce the bias due to wrong primary vertex

---

[5]To increase the statistics in Monte Carlo, all Higgs masses were considered

identification, only events with a single primary vertex are used, which is made possible since this study uses only the first 2011 data with low pileup.

$$\Delta z = z_{pointing} - z_{PV} \tag{5.8}$$

Definition of the Δz variable that will be the benchmark used in the following is shown in Equation 5.8. Figure 5.24 shows its distribution in data for different areas of the detector.

(a) Barrel C

(b) Barrel A
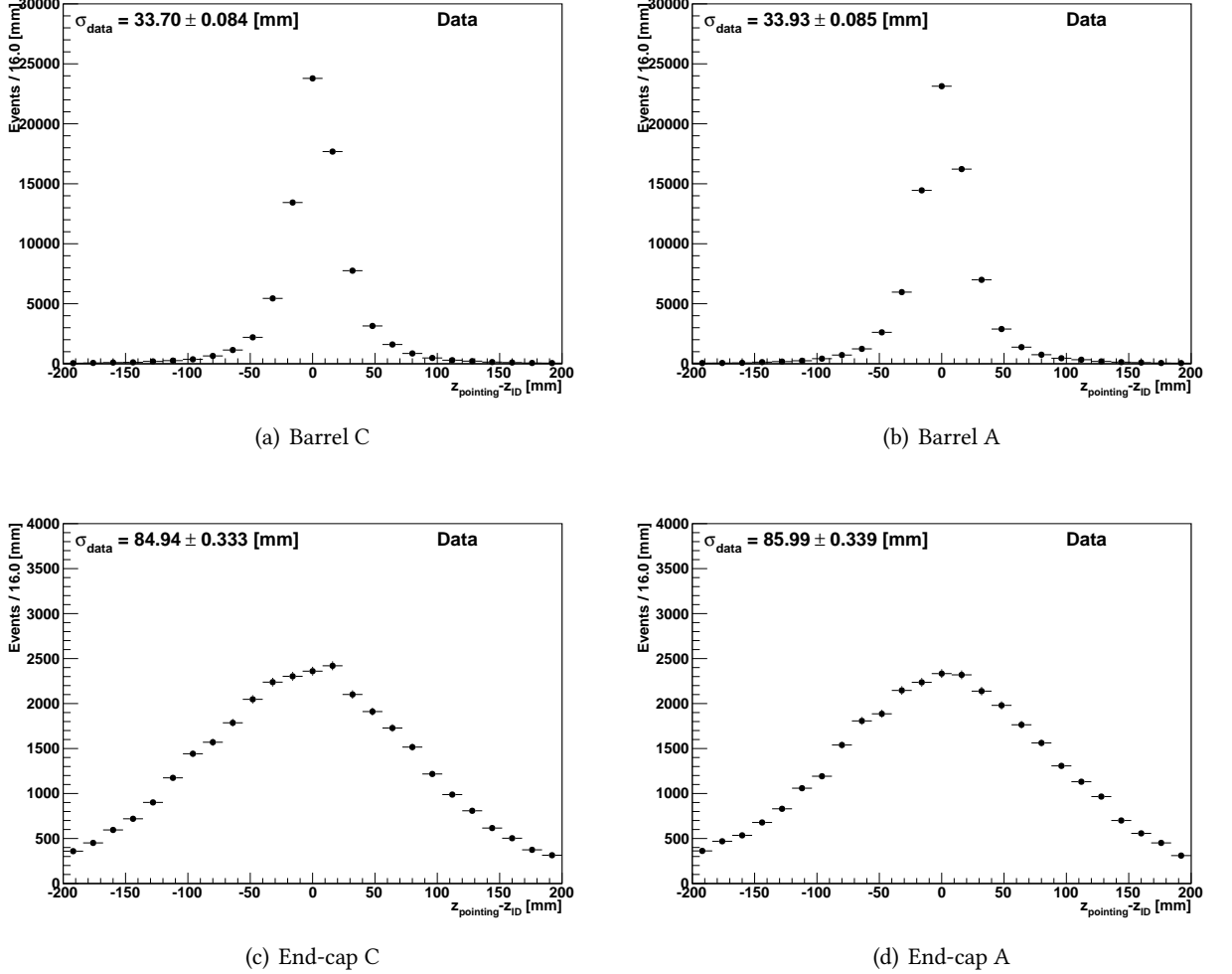
(c) End-cap C

(d) End-cap A

Figure 5.24: $\Delta z = z_{pointing} - z_{ID}$ *distribution in the different parts of the detector for data [100].*

A ($\eta > 0$) and C ($\eta > 0$) sides of the electromagnetic calorimeter are symmetric. However, the $\Delta z = z_{pointing} - z_{PV}$ distribution in the end-caps is much wider than in the barrel. This is expected because the incident angle of the particles on the end-caps is smaller and their position have to be projected on the horizontal axis. Moreover, the lever-arm is worse in the end-caps which are at a larger distance from the vertex.

The strange observation happens when looking at the pseudorapidity dependence of Δz, which is equivalent to scanning the electromagnetic calorimeter cells.

5.5.2 Presentation of the oscillations

We are interested in the profile of Δz as a function of η, *i.e.* the mean value of the distribution per η bin. Figures 5.25 and 5.26 show these profiles for data and simulation respectively, in the barrel and in the end-caps as a function of the pseudorapidity given by the cells in the second layers. For the

profiles, the single vertex requirement is removed because it was shown not to change the oscillation pattern and it allows to get more statistics.
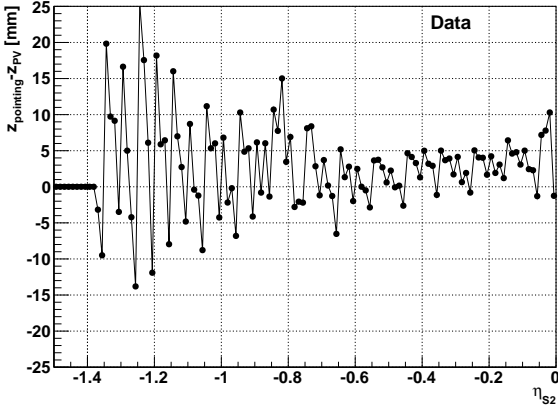
(a) Barrel C
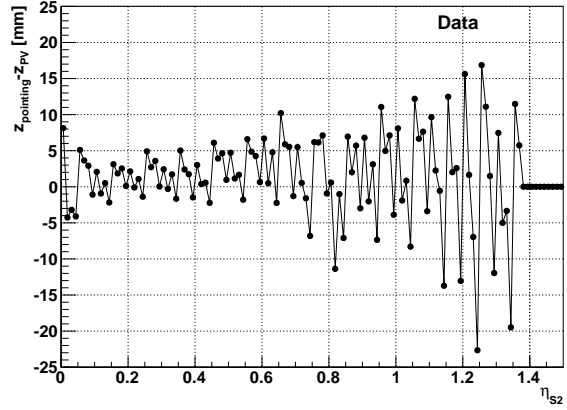
(b) Barrel A
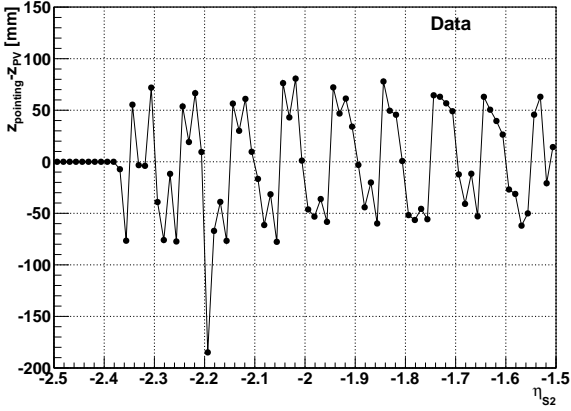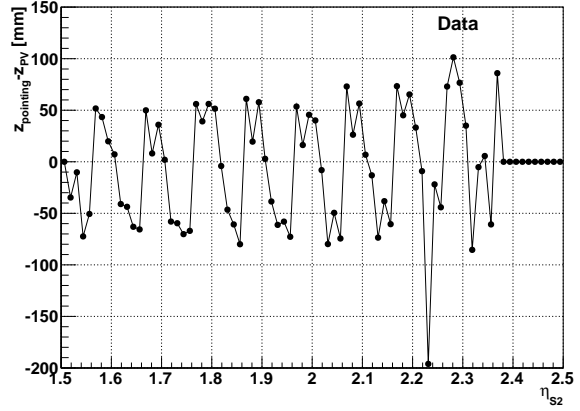
(c) End-cap C

(d) End-cap A

Figure 5.25: $\Delta z = z_{pointing} - z_{ID}$ profile as a function of the second layer pseudorapidity for data. A point corresponds to half a cell in the second layer $\Delta \eta = 0.025/2$ [100].

Oscillations are clearly visible in all the detector regions with different periods and amplitude. In the following, an interpretation attempt is presented for these different schemes, first concentrating on the end-caps where the effect is larger.

(a) Barrel C

(b) Barrel A
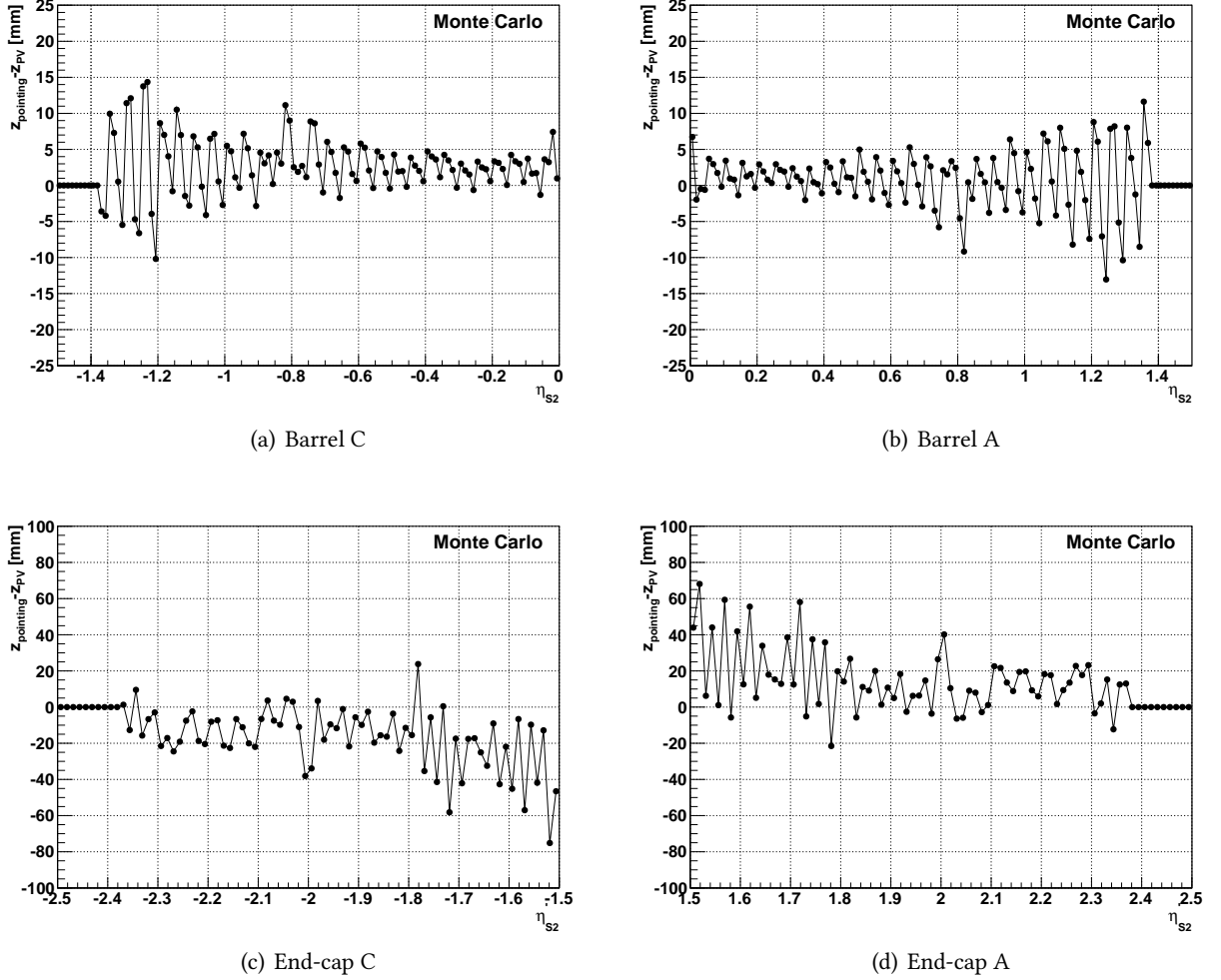
(c) End-cap C

(d) End-cap A

Figure 5.26: $\Delta z = z_{pointing} - z_{ID}$ profile as a function of the second layer pseudorapidity for Monte Carlo. A point corresponds to half a cell in the second layer $\Delta \eta = 0.025/2$ [100].

5.5.3   Oscillations in the end-caps

5.5.3.1 η shift

Oscillations in the end-caps have the particularity to have a 4-cell periodicity (in the second layer of the electromagnetic calorimeter) and are not reproduced by Monte Carlo simulations.

In order to better interpret the figures in terms of cells in the second layer, the pseudorapidity should take into account the few centimetres shift of the end-caps with respect to their initial design position. The consequence is the non-projectivity of the end-caps cells and a shift in the pseudorapidities measured with respect to the detector centre and the pseudorapidity dictated by the cells limits. Figure 5.27 illustrates this shift.

The variable η'_{S2} can be expressed as in Equation 5.9:

$$\eta'_{S2} = \eta_{S2} - \frac{shift}{Z_0} tanh(\eta_{S2}) \tag{5.9}$$

where the shift is taken to be 48.9 mm for A side and 55.1 mm for the C side. Z_0 is the expected position of the end-caps and η_{S2} is the pseudorapidity measured with respect to the centre of the detector.

Figure 5.28 is a comparison between the profiles with respect to the η_{S2} computed with the detector centre as origin (identical to Figures 5.25(c) and 5.25(d)), and the corrected η'_{S2} computed with respect
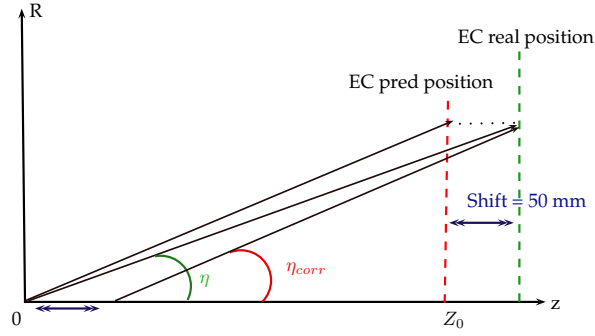
Figure 5.27: *Schematic view of the expected and effective end-cap positions in the (R, z) plane. The effect on the η_{S2} is also shown together with the $\eta'_{S2} \equiv \eta_{corr}$ definition [100].*

to a shifted centre. The oscillation pattern is also shifted and now better reproduces the geometry of the second layer cells: for example, the first two cells of the A end-cap side now have a negative fluctuations, the next two cells oscillate in the positive direction and so on.
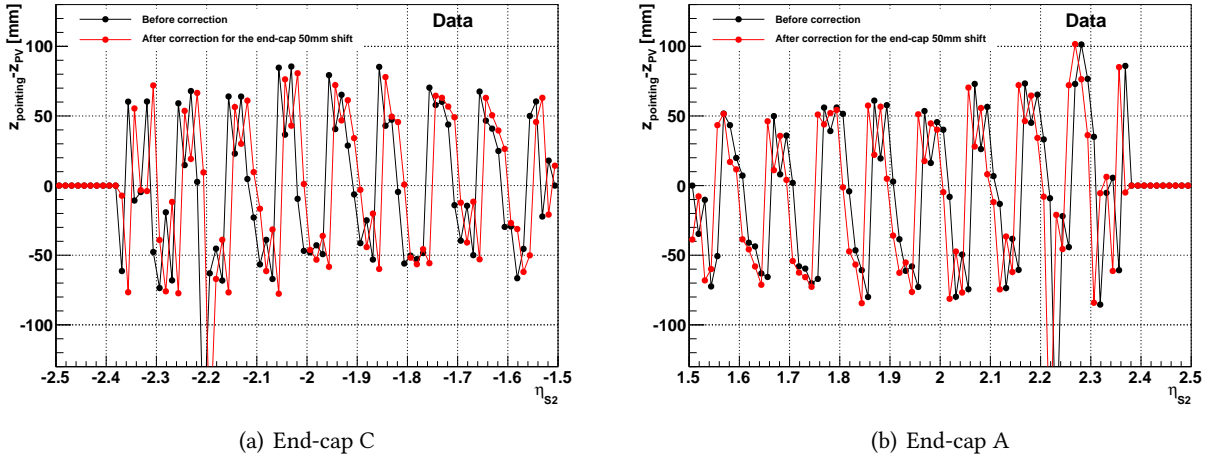
(a) End-cap C

(b) End-cap A

Figure 5.28: *Comparison of the Δz profiles obtained with respect to the pseudorapidity reconstructed form the centre of the detector η_{S2} and the corrected pseudorapidity taking into account the end-caps shift η'_{S2}. One point corresponds to half a cell in the second layer $\Delta\eta = 0.025/2$ [100].*

5.5.3.2 Attempt of interpretation

To try and explain this phenomena, a four-cell periodicity is looked for in the calorimeter, either in the electrode geometry or in the readout electronics.

The end-caps geometry, sketched in Figure 5.4, does not exhibit a particular η pattern. However, the readout electronics have an interesting particularity: four cells of the middle and two cells from the back are connected to the same electronic board. Consequently, the electric connection linking the two cells from the second layer in the middle of this block to the board are shorter than for the two cells at the extremities (Fig. 5.29).

If this effect would have such a big impact on the position determination, it should have measurable consequences on the energy measurement. To test this hypothesis, the idea is to look at the Z boson mass, when the Z decays to electron-positron and one of the decay products is in the end-cap. Figure 5.30 shows the profiles of m_Z with respect to η for the two end-cap sides. They do not
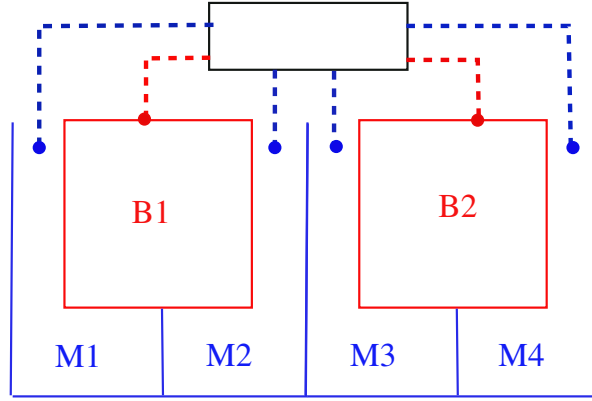
Figure 5.29: *Electronics layout in the end-cap: two back and four middle cells are connected to the same electronics card. Electric connections are longer for M1 and M4 middle cells than for M2 and M3. Scheme is not to scale. [100].*

present distinctive pattern, while one would expect the observed oscillations to induce a 5% mass variations [101].

(a) End-cap C

(b) End-cap A
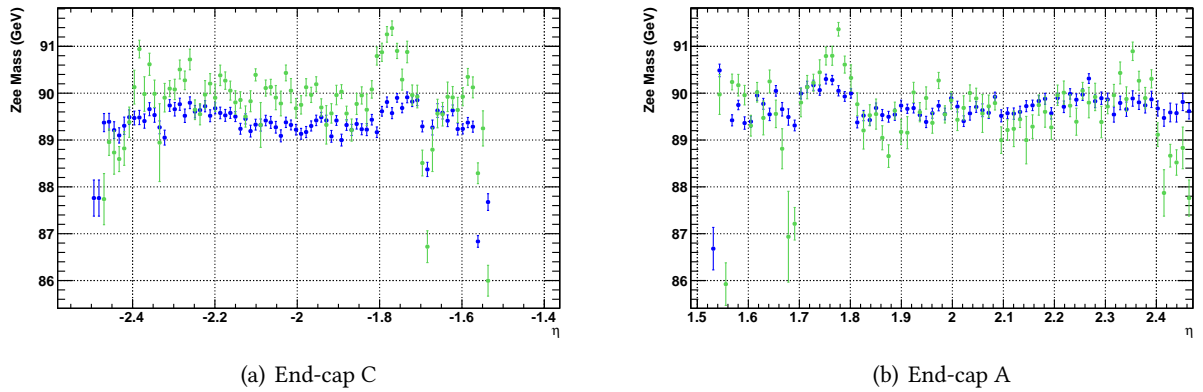
Figure 5.30: *Profiles of the Z mass when the Z decays to an electron pair as a function of the leading p_T electron pseudorapidity. One point corresponds to half a cell in the second layer $\Delta\eta = 0.025/2$. The blue points are from Monte Carlo while green markers represent data [100, 102].*

This indicates that the connection length is not responsible for the oscillation effect through the cell energy measurement.

Even though no convincing interpretation is found at this stage, a correction is derived in order to cancel these oscillations and their impact on the Higgs mass resolution in the diphoton channel is quantified.

5.5.3.3 Corrections

Two methods are tested to correct the oscillations. The first one relies on the $\Delta\eta = 0.1$ periodicity of the phenomenon, with an amplitude of the order of 50 mm. A second method consists in applying a bin-by-bin correction based on a fine profile.

Coarse correction

The observed oscillations have a fixed periodicity of 4 cells and an amplitude of the order of 50 mm. Following this observation, a correction with a simple crenel function is derived. Figure 5.31 shows the

profile before the correction, the applied crenel correction and the resulting profile after correction. The amplitude of the deformation is already greatly reduced and the pattern is more similar to the simulation.

(a) End-cap C

(b) End-cap A
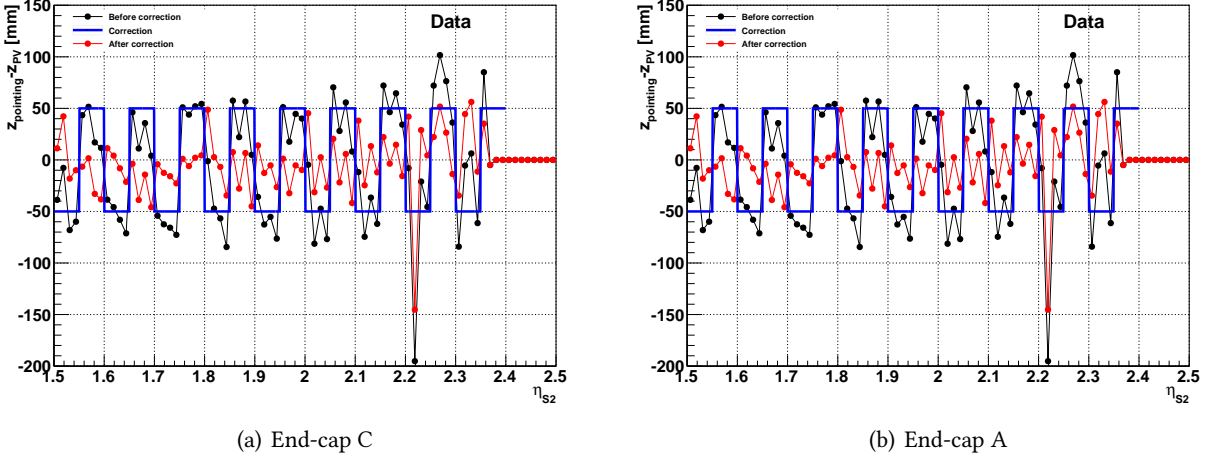
Figure 5.31: *Effect of the coarse correction on the η'_{S2} profiles for data. One point corresponds to half a cell in the second layer $\Delta\eta = 0.025/2$ [100].*

The improvement on the Δz width is visible in Figure 5.32 and is of the order of 8%.
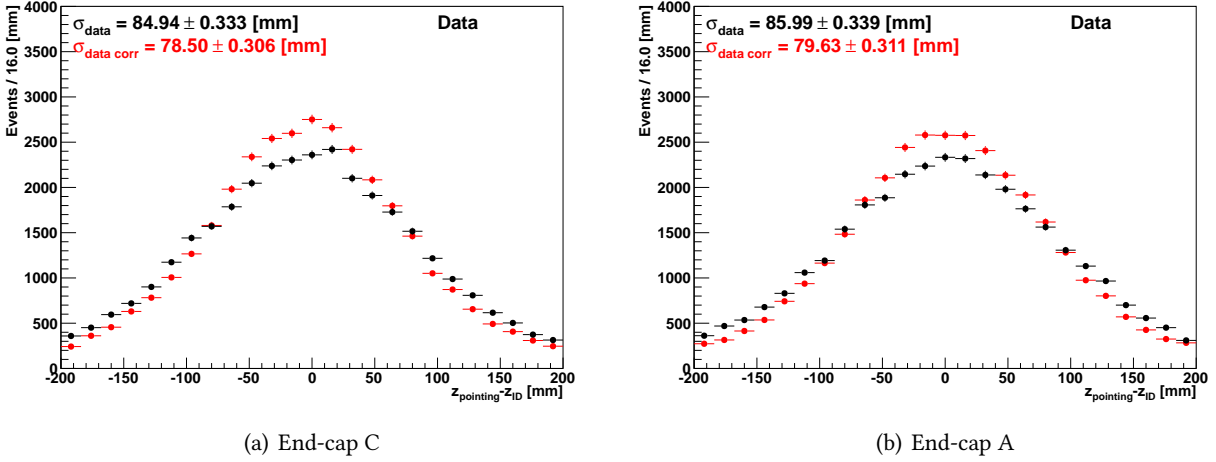
(a) End-cap C

(b) End-cap A

Figure 5.32: *Improvement on the Δz distribution from the crenel correction for data [100].*

Unconverted photons in the end-caps represent a small fraction of the photons coming from a Higgs decay. The impact of this correction on the Higgs mass resolution is thus expected to be small. To estimate it, only Monte Carlo samples can be considered. Since they do not show any oscillation nominally, the correction is applied to these samples in order to create the oscillations and reproduce the data. The effect of the correction on the simulation is shown in Figure 5.33: a four-cell oscillation appears. Applying the correction on the simulation, one then expects a degradation of the resolution since oscillations are magnified.

The mass resolution in this distorted sample is damaged by $\sim 0.5\%$. This is the order of the expected improvement of the m_H resolution in data when the oscillations are corrected.

(a) End-cap C

(b) End-cap A
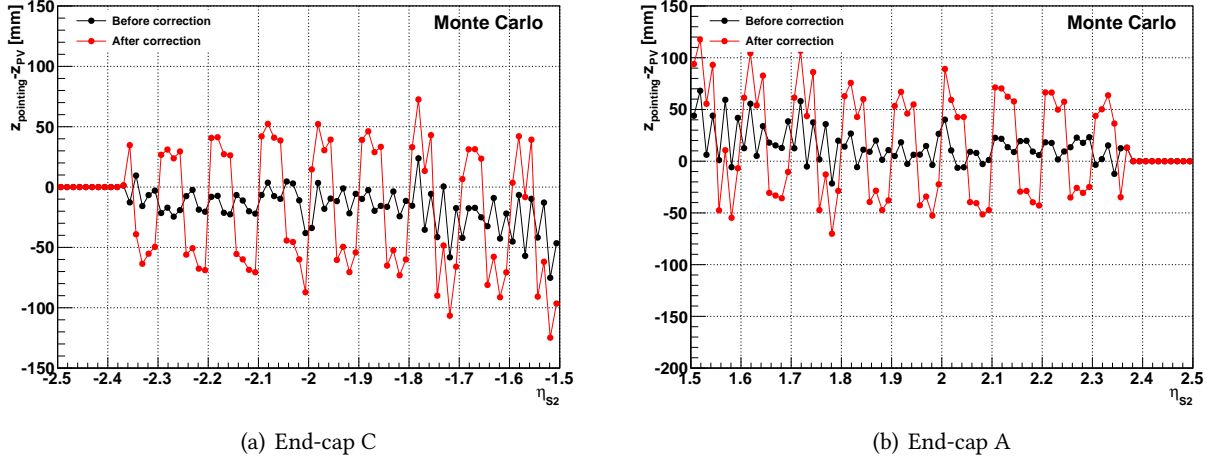
Figure 5.33: *Creation of oscillations with four-cell periodicity in the Monte Carlo by applying the crenel function shown in blue in Figure 5.32 [100].*

Bin-by-bin correction

A more accurate correction can be achieved by correcting the profiles on a bin-by-bin basis, each η bin being assigned a shift to apply to the Δz. More precisely, for each photon η, the shift to be applied to its reconstructed z comes from a linear interpolation between the Δz means in the two closest bins.

Profiles from which the correction is computed are created from the whole statistics available at that time, representing 5 fb^{-1}, with a fine binning. To further increase the statistics, the profiles are derived from a sample of electrons where the calorimeter pointing is computed in the same way than for unconverted photons. The effect of this correction for electrons is shown in Figure 5.34 that compared the pseudorapidities reconstructed from the pointing or from the electron track.

(a) No correction

(b) Bin-by-bin correction
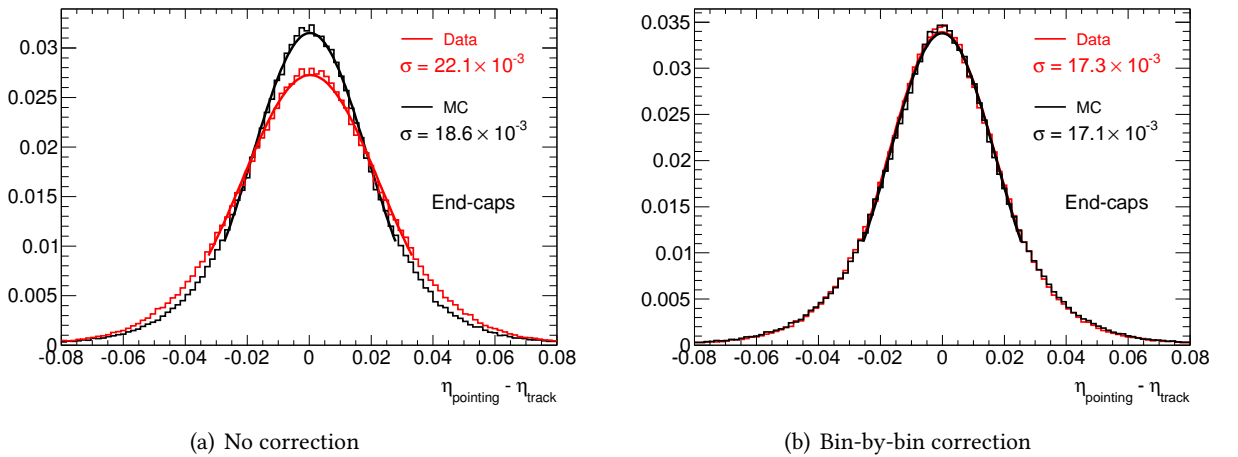
Figure 5.34: *Effect of the bin-by-bin correction on $\Delta\eta = \eta_{pointing} - \eta_{track}$ distribution for electrons in data and Monte Carlo [100].*

This correction is then applied to the photons of the previous 1 fb^{-1} dataset (Fig. 5.35). Remaining fluctuations are due to the limited statistics in the test sample.

Despite these fluctuations, an improvement in the Δz resolution for photons is observed: a 13% gain is achieved with respect to the uncorrected data (Fig. 5.36).

(a) End-cap C

(b) End-cap A
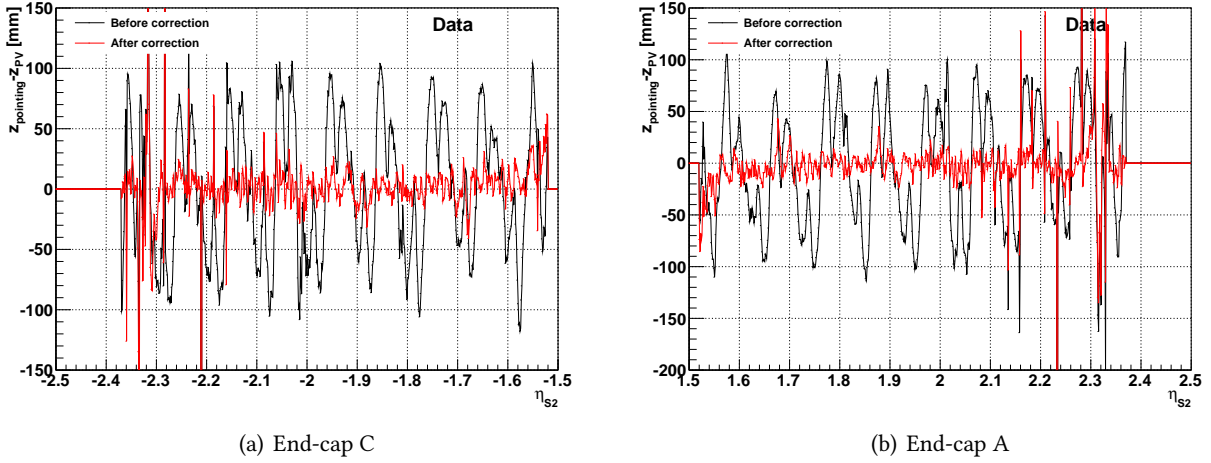
Figure 5.35: *Effect of the bin-by-bin correction on the photons profiles with respect to η_{S2} in data [100].*

(a) End-cap C

(b) End-cap A
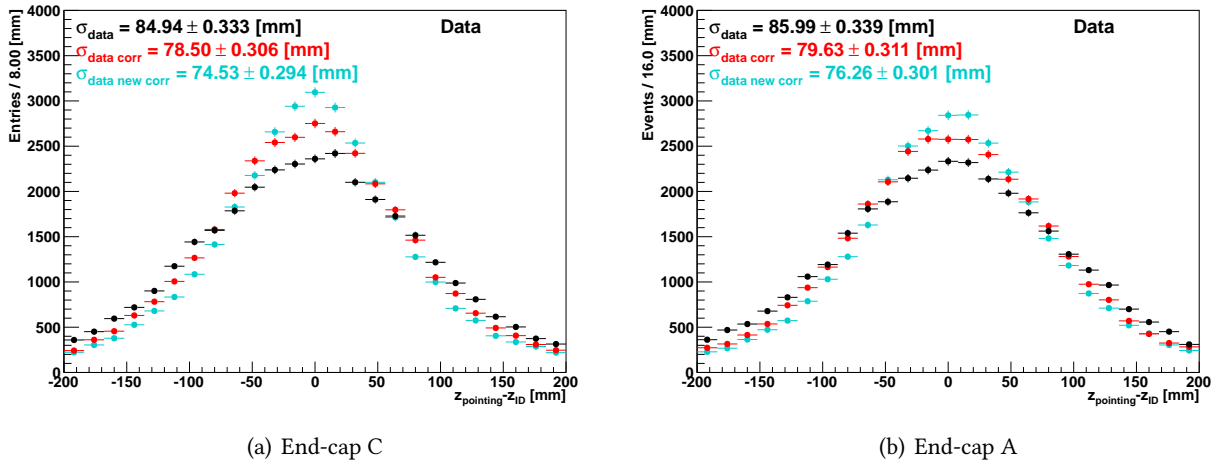
Figure 5.36: *Improvement of the Δz resolution due to the bin-by-bin correction in data. The new correction (blue) is compared to the previous one (red) and to the uncorrected data (black) [100].*

5.5.3.4 Comparison to Monte Carlo

The Δz distribution for the Monte Carlo is presented in Figure 5.26. Several differences are observed between data (Fig. 5.25) and Monte Carlo:

- The Δz distribution in data is wider than in the simulation, even after correction. Two possible reasons can explain this:

  1. Monte Carlo samples used are $H \to \gamma\gamma$ samples where the expected photon transverse momentum is large, while the selected single photons in data have $p_T > 20\ GeV$. The p_T distribution in both cases are then different.

  2. In data, even after selection, a large part of jet contamination remains, for which the pointing is not so efficient.

- The mean value of the oscillations in the end-caps is not constant at 0 but is shifted by a few mm in the Monte Carlo.

(a) End-cap C

(b) End-cap A
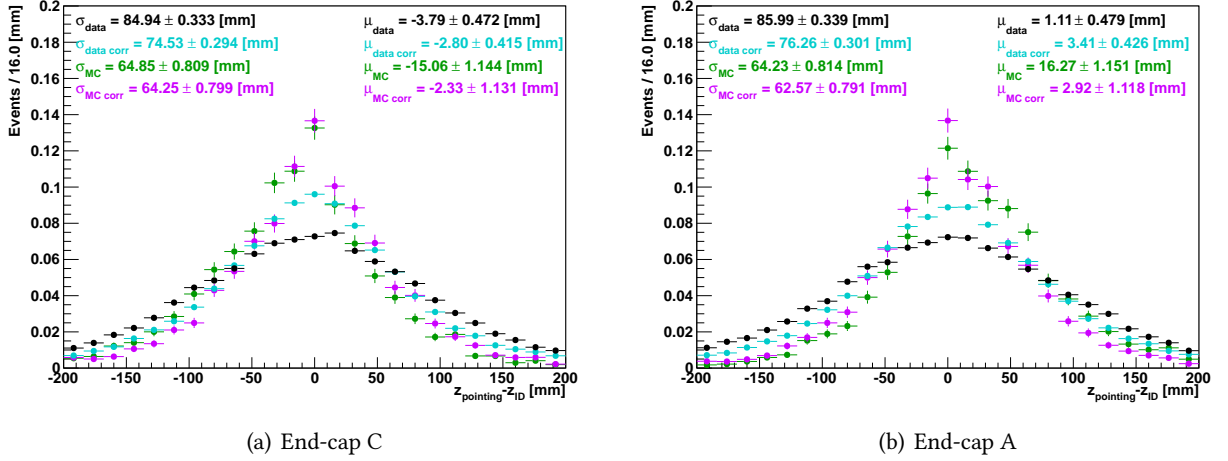
Figure 5.37: *Comparison of Δz distributions for data and Monte Carlo before correction and after applying a specific correction to each kind of samples.*

After the correction to data is applied, the question was whether the Monte Carlo should be corrected as well to get rid of the small oscillation pattern it presents. Tests were carried out from a $\Delta z = f(\eta_{S2})$ profile with a fine binning. A bin-by-bin correction is derived for the simulation. Figure 5.37 superimposes the Δz distributions before and after correction for data and Monte Carlo.

In terms of σ the Monte Carlo correction is not as efficient as the correction of data: the improvement is only $1-2\%$. However, the correction allows to get rid of the oscillation central value deviation and centres the profiles at 0. For this reason, a correction is also applied to the simulated samples for unconverted photons in the end-caps.

5.5.4 In the barrel

Data also present some oscillations in the electromagnetic calorimeter barrel region. They have a smaller amplitude and a two-cell periodicity.

5.5.4.1 Interpretation

Electrode geometry Oscillations in the barrel have a period in η_{S2} corresponding to two cells in the middle layer. This can be related to the electrode geometry illustrated in Figure 5.38.
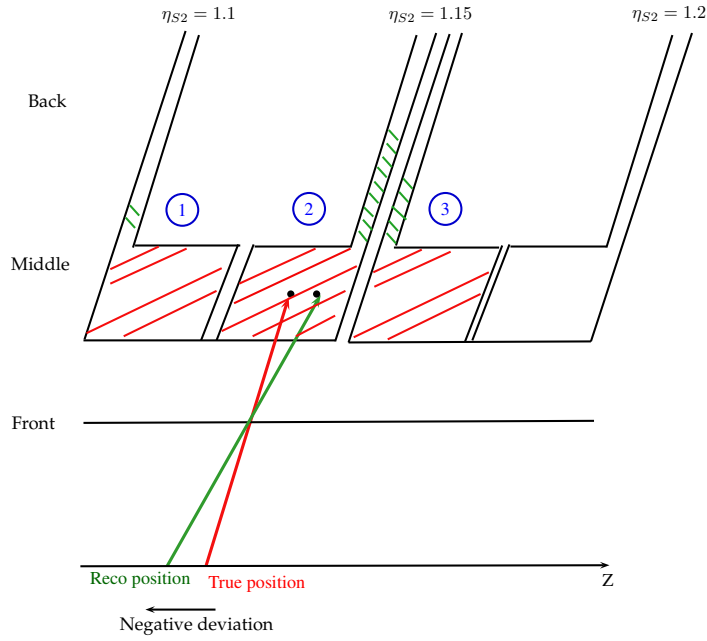
Figure 5.38: *Electrode geometry in the barrel. The red line corresponds to the real photon path, that would be properly reconstructed if one considers only red energy deposit. The green line is the reconstructed path, taking into account the energy deposited in the connection strips of middle cells. The deviation is reversed if the particle hits the cell number 1 or 3, which creates a 2-cell periodic oscillation [100].*

Similarities between barrel and end-caps: Looking at the barrel profiles with a finer binning, a four-cell oscillation also appears, with a smaller amplitude than the one observed in the end-caps (Fig. 5.39). Unlike the end-caps, the oscillation observed in the barrel is well described by the simulation (Fig. 5.40).

(a) Barrel C
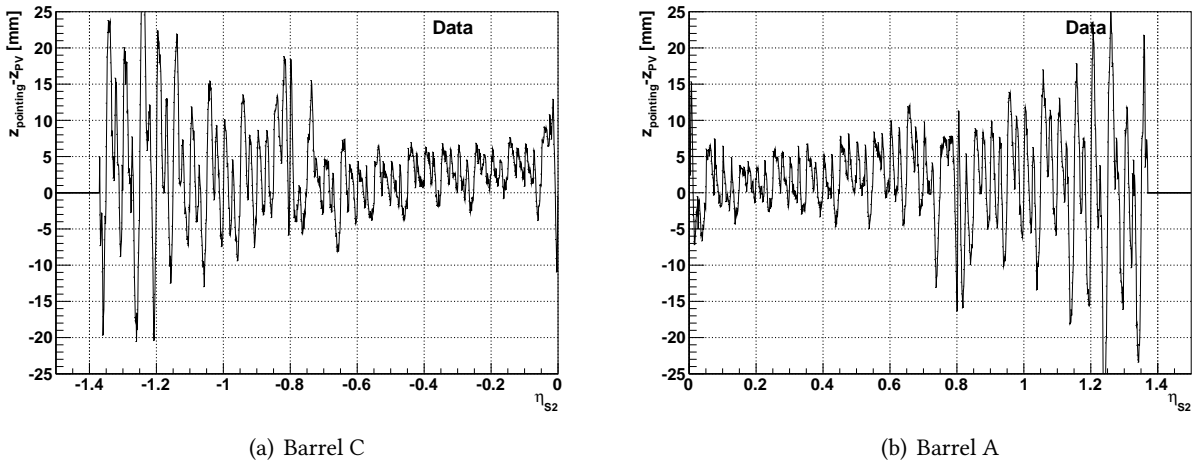
(b) Barrel A

Figure 5.39: *Δz profile as a function of the pseudorapidity in the barrel for data [100].*
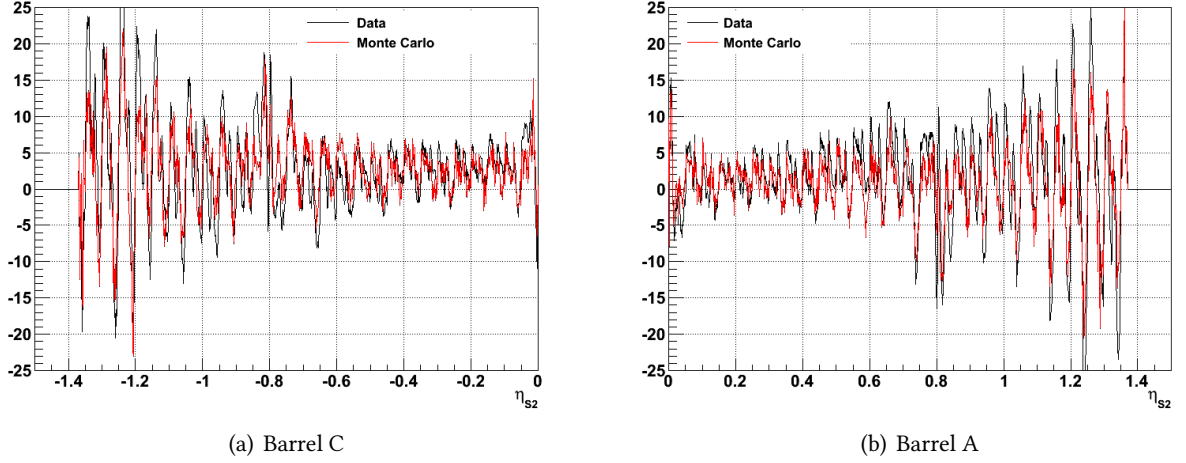
(a) Barrel C

(b) Barrel A

Figure 5.40: *Comparison of Δz profiles as a function of the pseudorapidity in the barrel for data (black) and Monte Carlo (red) [100].*

5.5.4.2 Correction

As for the end-caps, a correction is tested. Only the bin-by-bin correction is derived. The effect of this correction on the Δz distribution in data and Monte Carlo is shown in Figure 5.41.
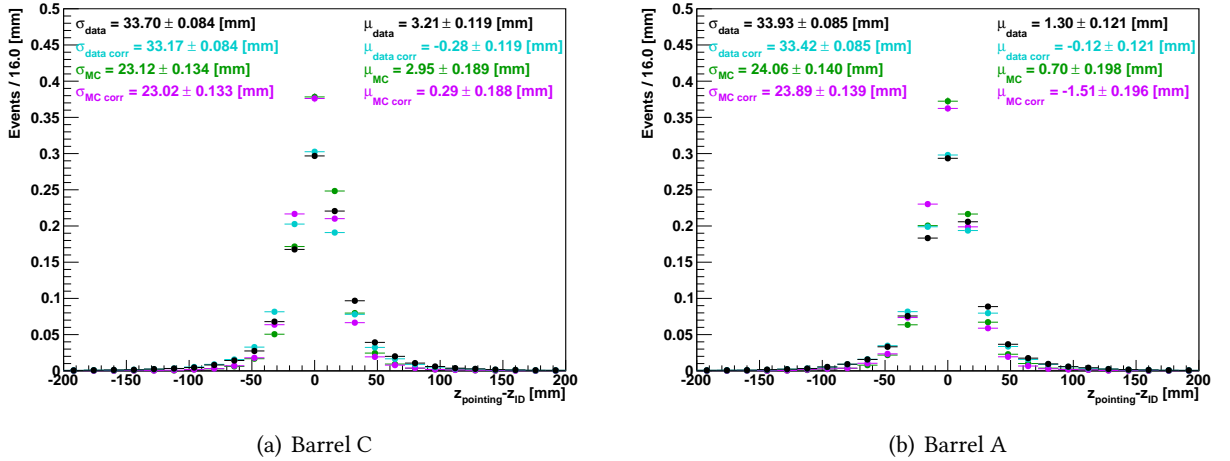
(a) Barrel C

(b) Barrel A

Figure 5.41: *Comparison to Monte Carlo and effect of the bin-by-bin correction in the barrel for data.*

The resulting improvement on the Δz RMS is below 1%. Even if the contribution to the Higgs mass resolution coming from photons in the barrel is larger than for the end-caps, the small improvement on the position resolution achieved in this way would not produce measurable improvement in the m_H resolution. For this reason, it is chosen not to apply any correction to photons falling in the barrel region.

Conclusion

The longitudinal segmentation of the calorimeter allows to use a pointing technique to reconstruct the photon direction, giving access to the Higgs primary vertex in the diphoton decay channel. The Higgs mass resolution is then improved. A still not fully understood oscillation pattern was observed in this pointing technique. An ad-hoc corrections limits its impact on the resolution. The $H \to \gamma\gamma$ analysis will be presented with more details in the next chapter.

Part III

Analysis

$H \rightarrow \gamma\gamma$ ANALYSIS

> ❝ *Once you eliminate the impossible, whatever remains, no matter how improbable, must be the truth.* ❞
>
> A. CONAN DOYLE

Chapter content

Despite a low branching ratio ($\approx 0.2\%$), the diphoton decay mode is an important channel for the Standard Model Higgs boson study in the low mass range. This channel was studied since the beginning of the perspective studies at the LHC, on Monte Carlo by C. Seez and J. Virdee in 1990 for CMS [103], and then in ATLAS [104]. A large fraction of the background can be rejected because of a good discriminating power fulfilled thanks to the good performances achieved by the detector. Photon performances include identification thanks to electromagnetic shower shape variables and the careful determination of the energy in the neighbourhood of the reconstructed particle, the isolation energy.

Optimized cuts on these quantities allow to reach a reasonable signal-to-noise ratio in the inclusive $\gamma\gamma$ channel.

Once the inclusively selected events are known, they are classified into several categories to enhance the signal-over-background ratio in some categories and therefore the sensitivity of the analysis (Chap. 2). These categories definition depends on the final goal of the analysis (discovery or some property measurement).

A large fraction of the results in this chapter are taken from the supporting documentation of the production measurements [105].

6.1 Analysis overview

6.1.1 Background

The diphoton final state suffers from different types of backgrounds:

- The reducible background is due to particles faking photons. It mostly comes from π^0 or η particles inside jets, decaying into two collimated photons, reconstructed as a single photon. Hence, γj and, to a lesser extent, the multijets (jj) events (Fig. 6.1 and 6.2) create a significant background to genuine diphoton events.

  Another source of reducible background is the Drell-Yan process ($Z^*/\gamma^* \to \gamma\gamma$), where both electrons are misidentified as photons.
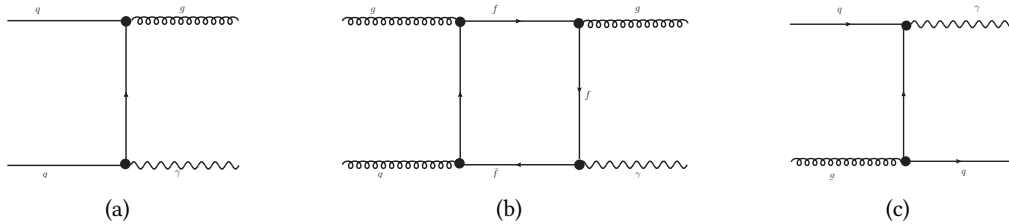
Figure 6.1: *Leading order diagrams for the γj production at the LHC forming part of the reducible background to the Higgs diphoton decay channel.*
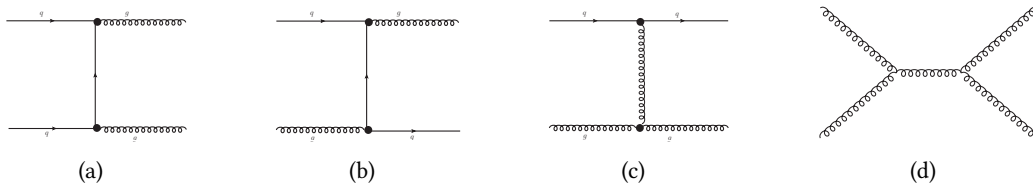
Figure 6.2: *Leading order diagrams for the jj production at the LHC forming part of the reducible background to the Higgs diphoton decay channel.*

- On the contrary, the irreducible background comes from processes involving two prompt photons in the final state. Three main processes contribute to this background:

  - The Born process (Fig. 6.3(a)), contribute at order α_{QED}^2 (at leading order);
  - The Box process (Fig. 6.3(b)) has a leading order contribution of order $\alpha_S^2 \alpha_{QED}^2$;
  - The Bremsstrahlung process (Fig. 6.3(c)), whose leading order is proportional to $\alpha_S \alpha_{QED}^2$.

  The higher order dependence of the box and bremsstrahlung processes is compensated by the large gluon density inside the colliding protons, in such a way that their cross-sections are of the

(a) Born · (b) Box · (c) Brem
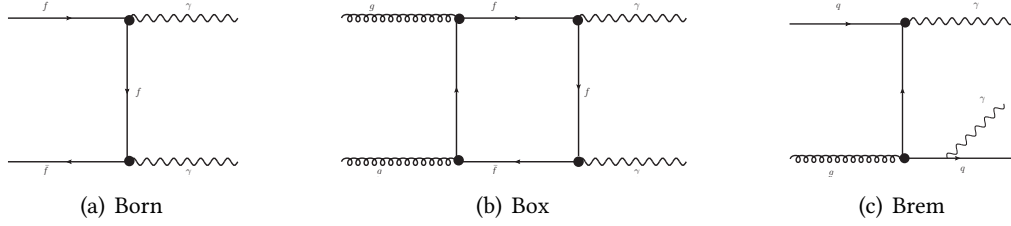
Figure 6.3: *Leading order diagrams for the direct diphoton production at the LHC forming the irreducible background to the Higgs diphoton decay channel.*

same order of magnitude than the box process.

This type of background can not be suppressed with a better photon identification but other kinematic variables can help in distinguishing the Higgs signal from these processes.

The production cross-sections of $\gamma\gamma$, γj and jj events are greater than the $H \to \gamma\gamma$ cross-section by several order of magnitude (Tab. 6.1).

	Process	σ [fb]
Signal	$H \to \gamma\gamma$	50
Background	$\gamma\gamma$	30.10^3
	γj	20.10^7
	jj	50.10^{10}

Table 6.1: *Approximate production cross-sections for the $H \to \gamma\gamma$ signal and its main backgrounds at the LHC.*

6.1.2 General analysis concepts

In order to select genuine diphoton events and reject the fakes (jets), the analysis follows several steps:

- At trigger level, events with two photons with p_T greater than a given threshold are recorded by the detector. In 2011, the trigger required two photons with p_T threshold of 20 GeV (`2g20_loose`). In 2012, the p_T thresholds had to be increased to 35 (25) GeV for the leading (subleading) photon (`g35_loose_g25_loose`) for the trigger rate to stay below the acceptable rate.

- The number of reconstructed vertices is required to be greater than one to reject non-projective background coming from cosmic events.

- A preselection is applied to select the photon objects, according to the following criteria:

  - First, further offline energy calibration corrections are applied;
  - Then, each photon transverse momentum must have a sufficiently high transverse momentum $p_T > 25$ GeV and loose quality criteria on the photon shower shape are applied;
  - Finally, the fiducial region is defined to be within $|\eta| < 2.37$ because it is the end of the fine longitudinal segmentation of the liquid Argon calorimeter. The transition region between barrel and end-cap (the crack: $1.37 < |\eta| < 1.52$) is also excluded (the crack was extended to $1.37 < |\eta| < 1.56$ in the final analysis due to the poor energy resolution in the region $1.52 < |\eta| < 1.56$).

All particles passing those criteria are labelled as photon candidates.

The diphoton pair is created from the leading and subleading photons *i.e.* the first and second photons in the p_T ordered list of candidate photons.

After this preselection, additional cuts are applied to the selected photons to enhance the signal over the background:

- Kinematics: a background study showed that the photons coming from the Higgs are harder than the one coming from background $\gamma\gamma$ events. A cut on each photon p_T is then used . More details are given in Section 6.2.1.

- Quality: in order to discard events with jet faking a photon, tight quality criteria on the electromagnetic shower shape of the objects are applied. The method is explained in Section 6.2.2.

- Isolation: in order to further reduce the fake photon background, an isolation criteria is imposed, limiting the allowed energy in the neighbourhood of the photon candidate cluster. See Section 6.2.3.

- Mass range: finally, the main analysis is restricted to the [100; 160] GeV diphoton invariant mass range, region where the Higgs branching ratio to a pair of photon is maximized in the Standard Model.

After this inclusive selection, events are classified into different categories to enhance the analysis sensitivity. These categories depends on the analysis target (*i.e.* discovery or property measurement).

6.1.3   Events categorization

Event categorization allows to increase the analysis significance. The categories depends on the analysis target. For discovery purposes, the categories must have different S/B. After the discovery, the aim of the analysis is to measure the particle properties, and the categorization is adapted on purpose.

The historical discovery targeted categorization makes use of the photon conversion status and pseudo-rapidity to form five categories with different sensitivities illustrated in Figure 6.4.
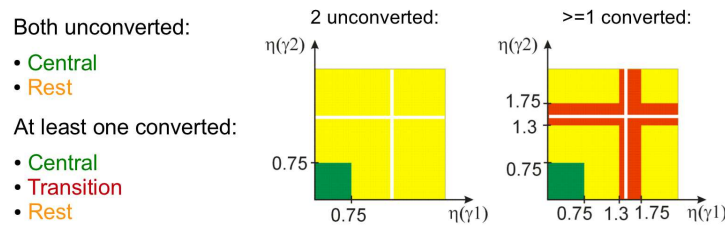
Figure 6.4: *Definition of the five conversion-η categories [].*

Another discriminating variable was found to be the diphoton p_{Tt} defined as a function of the single photons transverse momentum p_1 and p_2:

$$p_{Tt} = 2|p_{x1}.\hat{p}_{y,trust} - p_{y1}.\hat{p}_{x,trust}| \tag{6.1}$$

where the trust axis is defined by: $p_{xy,trust} = p_{xy,1} - p_{xy,2}$, and where the hat notation refers to normalized vectors (Fig. 6.5). The p_{Tt} distribution for the ggH and VBF signal processes and for the background is shown in Figure 6.6. The cut value p_{Tt}^{cut} is optimized to maximize the sensitivity, keeping enough statistics in the high p_{Tt} categories. It was first set to 60 GeV and increased to 70 GeV latter on.
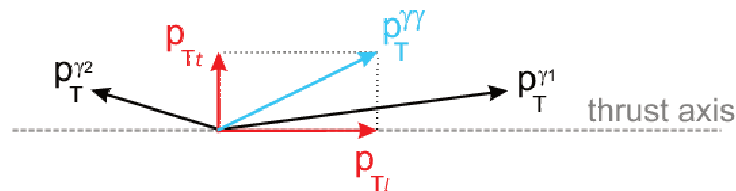
Figure 6.5: *Diphoton p_{Tt} definition [106].*

The resulting 9-category model, defined for the Council 2011 analysis [107], contains the following categories:

Figure 6.6: *Diphoton p_{Tt} distribution [99].*

1. **Unconverted central, low** p_{Tt} (Cat. 1): Both photon candidates are reconstructed as unconverted photons with $|\eta| < 0.75$ and the p_{Tt} of the diphoton system should be below the p_{Tt}^{cut}: $p_{Tt} < p_{Tt}^{cut}$.

2. **Unconverted central, high** p_{Tt} (Cat. 2): Both photon candidates are reconstructed as unconverted photons with $|\eta| < 0.75$, and $p_{Tt} > p_{Tt}^{cut}$.

3. **Unconverted rest, low** p_{Tt} (Cat. 3): Both photon candidates are reconstructed as unconverted photons and at least one candidate has $|\eta| > 0.75$, and $p_{Tt} < p_{Tt}^{cut}$.

4. **Unconverted rest, high** p_{Tt} (Cat. 4): Both photon candidates are reconstructed as unconverted photons and at least one candidate has $|\eta| > 0.75$, and $p_{Tt} > p_{Tt}^{cut}$.

5. **Converted central, low** p_{Tt} (Cat. 5): At least one photon candidate is reconstructed as converted photon and both photon candidates have $|\eta| < 0.75$, and $p_{Tt} < p_{Tt}^{cut}$.

6. **Converted central, high** p_{Tt} (Cat. 6): At least one photon candidate is reconstructed as converted photon and both photon candidates have $|\eta| < 0.75$, and $p_{Tt} > p_{Tt}^{cut}$.

7. **Converted rest, low** p_{Tt} (Cat. 7): At least one photon candidate is reconstructed as a converted photon and both photon candidates have $|\eta| < 1.3$ or $|\eta| > 1.75$, but at least one photon candidate has $|\eta| > 0.75$, and $p_{Tt} < p_{Tt}^{cut}$.

8. **Converted rest, high** p_{Tt} (Cat. 8): At least one photon candidate is reconstructed as a converted photon and both photon candidates have $|\eta| < 1.3$ or $|\eta| > 1.75$, but at least one photon candidate has $|\eta| > 0.75$, and $p_{Tt} > p_{Tt}^{cut}$.

9. **Converted transition** (Cat. 9): At least one photon candidate is reconstructed as a converted photon and at least one photon candidate is in the range $1.3 < |\eta| < 1.37$ or $1.52 < |\eta| < 1.75$.

Starting from this detector oriented categorization, new categories are introduced to discriminate each of the Higgs production modes in order to measure the couplings. For production modes other than ggH, some objects are produced in association with the Higgs (see Fig. 1.10):

- VBF: this process is characterized by the production of two forward jets with high invariant mass. These properties are used to define a VBF category, first defined with a cut-based approach and then improved with a selection based on a multivariate analysis (MVA) output.

- VH: the higgsstrahlung with W or Z can be identified thanks to the hadronic or leptonic decay of the weak gauge boson:

    - A hadronic category captures the hadronic decay of the W or Z ($V \to jj$) by selecting events with two jets with invariant mass close to the W and Z mass;

    - A E_T^{miss} (Missing E_T or MET) category selects events with large E_T^{miss}[1], corresponding to $W \to l\nu$ or $Z \to \nu\nu$ decay;

    - A leptonic selection concentrates on events with at least one lepton, corresponding to $W \to l\nu$ or $Z \to ll$ decay.

Each time, the remaining events are classified into the untagged nine conversion-η-p_{Tt} categories. In the selection order, the categories with the lower expected events are given the highest priority.

6.2 Event selection

6.2.1 Kinematics

Historically, the optimal cut on the photon candidates transverse momentum was found to be: $p_T^{leading} >$ 40 GeV and $p_T^{subleading} > 25$ GeV [103].

In 2012, trying to increase the analysis sensitivity, this cut was reinvestigated at $\sqrt{s} = 7$ TeV (instead of the 14 TeV initially planned). This was necessary because of the change in the trigger menus that happened during the year to face the increasing instantaneous luminosity. The p_T threshold for the diphoton trigger had to be increased from 20 (20) to 35 (25) GeV for the leading (subleading) photon. Since calibration is applied offline after trigger and can shift the momentum by up to a few GeV, keeping the 25 GeV cut is impossible for a good efficiency estimation.

This study was realized with 4.9fb^{-1} of 2011 data and the MC11C Monte Carlo production closer to the data taking condition in terms of pileup for example. The categorization used the historical nine categories with a p_{Tt} cut at 60 GeV.

The cut optimization strategy is to find the cuts maximizing the expected significance Z. The p_T distributions for the leading and the subleading photon after the preselection (*i.e.* loose photons with $p_T > 25$ GeV) are shown in Figures 6.11(a) and 6.11(b). Several configurations are considered presented in Figure 6.7. The hardest cut tested is 45 GeV not to cut into the core of the distribution for signal.
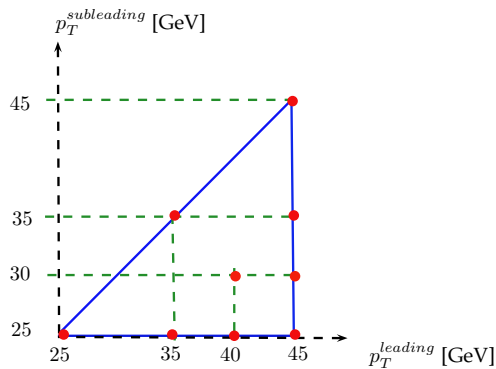
Figure 6.7: *p_T configurations considered for the kinematics cut optimization.*

At the time of this study, the technique to determine the background shape was not yet decided. For this reason, several models were tested:

expo : simple exponential $e^{s.m_{\gamma\gamma}}$ where s is the exponential slope.

---

[1]The real variable used in the E_T^{miss} significance whose definition is given in next chapter.

expo on reduced mass range : the function is the same as previously but the fit is performed on a reduced mass range: ± 40, ± 30 ou ± 25 GeV (with respect to the tested mass);

bern2 : order 2 Bernstein polynomials. Bernstein polynomials are preferred because they are positively defined, which is convenient for a probability density function.

bern3 : order 3 Bernstein polynomials.

Figure 6.8 shows the expected significance of the analysis for different p_T cut configuration and different models for background subtraction. Table 6.2 summarizes the results obtained at $m_H = 126$ GeV.

Cut p_T [GeV]	25-25	35-25	35-35	40-25	40-30	45-25	45-30	45-35	45-45
Exponential full range	1.360	1.378	1.415	1.394	1.408	1.401	1.418	1.427	1.400
Exponential reduced range 40	1.323	1.341	1.374	1.355	1.368	1.366	-	1.383	1.332
Exponential reduced range 30	1.286	1.303	1.333	1.315	1.327	-	1.333	1.340	1.282
Exponential reduced range 25	1.254	1.270	1.297	1.281	1.292	-	1.298	1.302	1.247
Bernstein 2nd order	1.292	1.308	1.338	1.322	-	1.331	-	1.345	1.283
Bernstein 3rd order	1.236	1.252	1.280	1.264	1.275	1.272	1.281	1.296	1.231

Table 6.2: *Expected significance for the 9-category model for different p_T cut configurations and background parametrization models at $m_H = 126$ GeV [108].*

Whatever background model is used, the best significance is achieved with the $(45 - 35)$ configuration. However, with this configuration, the invariant mass spectra can be distorted in the low mass region ($m_{\gamma\gamma} \sim 100 \, GeV$) (see Figures 6.9-6.10). The chosen configuration is then a compromise between the expected significance improvement, the data shape and the trigger threshold constraints. The $(40-30)$ configuration was chosen and used for the discovery analysis. It leads to an improvement in the expected significance of $\sim 1\%$ at $m_H = 126$ GeV.

(a) Expo full range

(b) Expo reduced range (40 GeV)

(c) Expo reduced range (30 GeV)

(d) Expo reduced range (25 GeV)

(e) Bern2

(f) Bern3
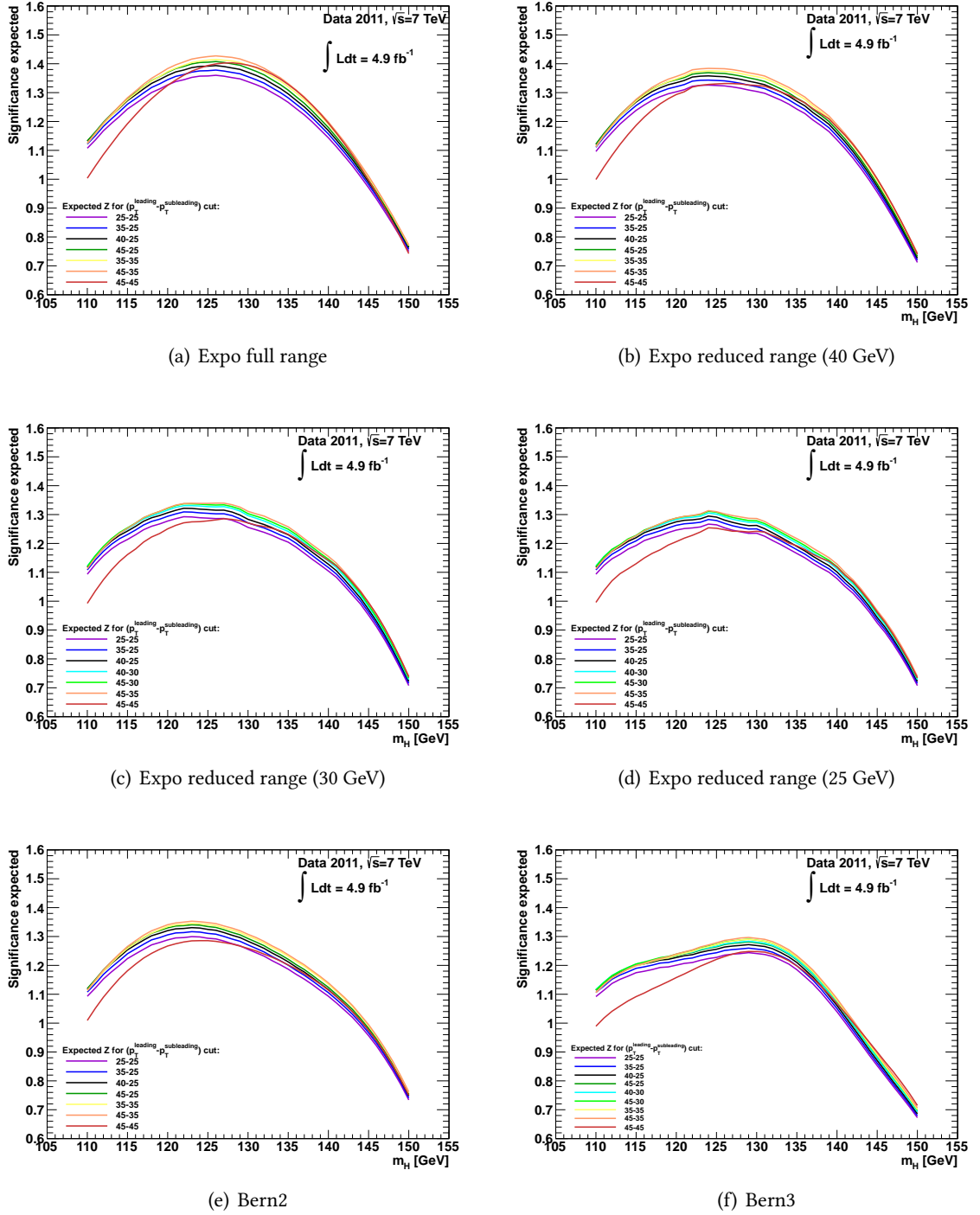
Figure 6.8: *Comparison of expected significance for different p_T cut configurations for a given background parametrization.*
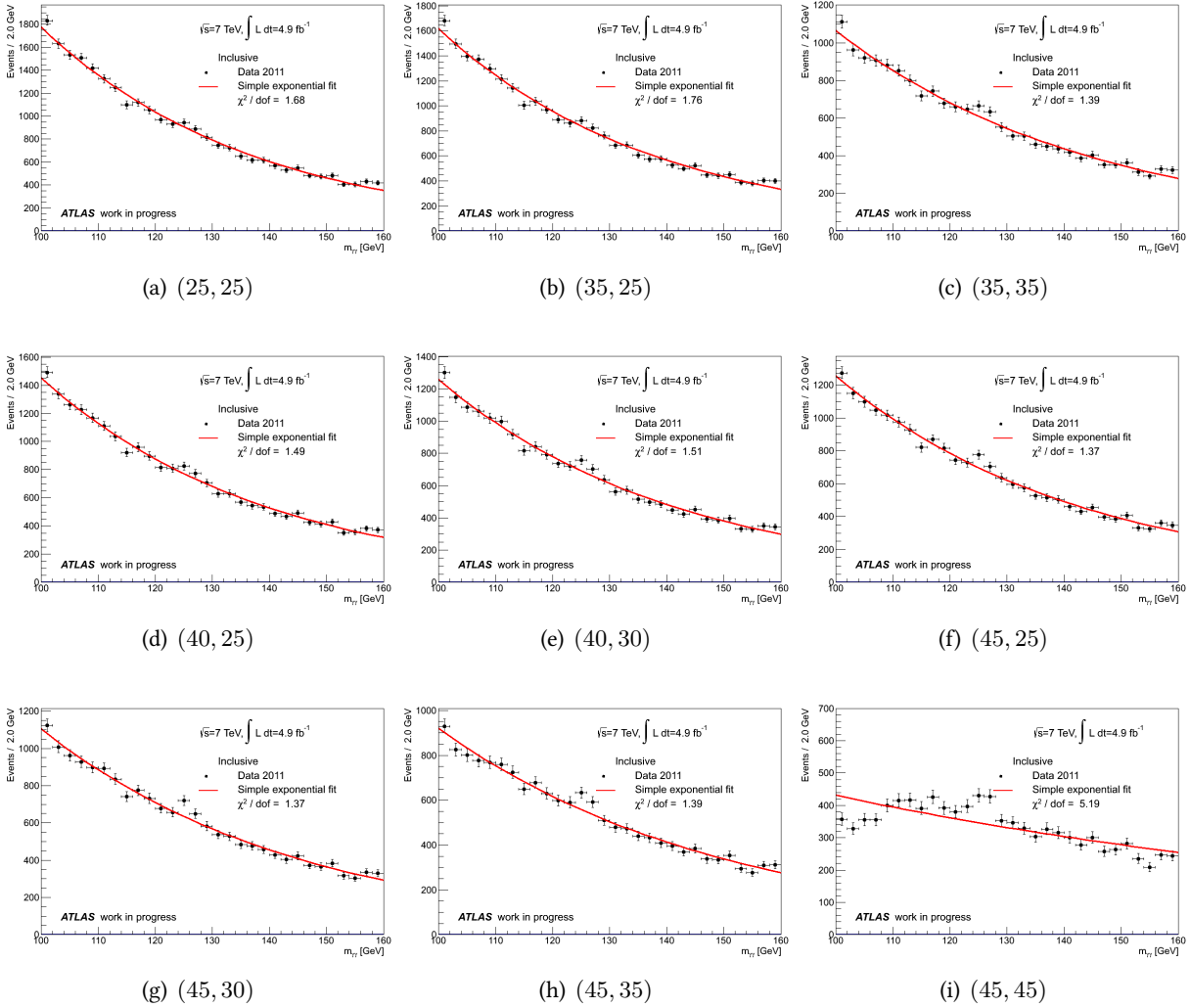
Figure 6.9: *Diphoton invariant mass distribution in data for different $(p_T^{leading}, p_T^{subleading})\,[GeV]$ cuts configurations. The result of an exponential fit of these data points on the whole mass range is superimposed [108].*
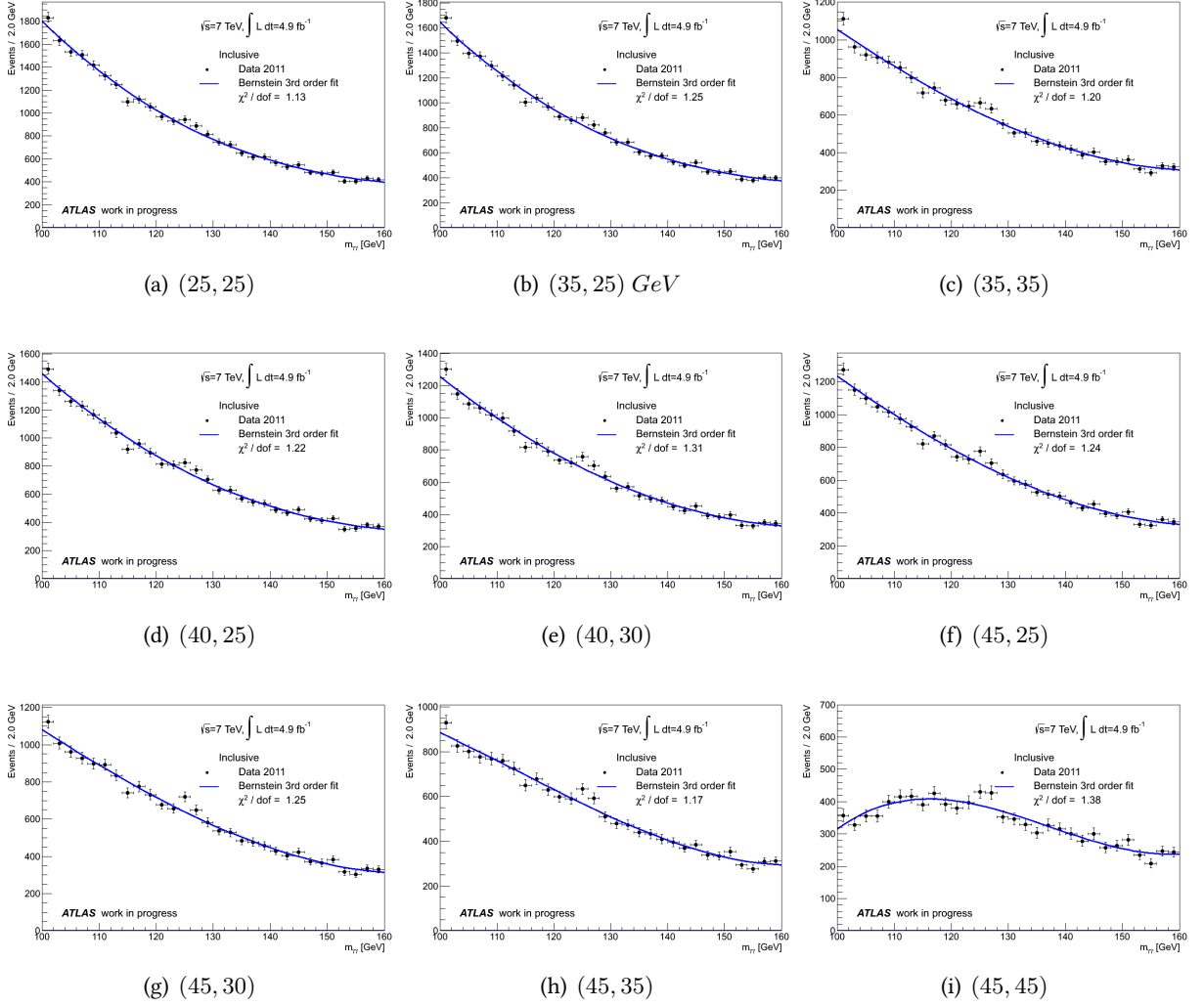
Figure 6.10: *Diphoton invariant mass distribution in data for different $(p_T^{leading}, p_T^{subleading})$ $[GeV]$ cuts configurations. The result of a fit of these data points with a 3rd order Bernstein polynomial on the whole mass range is superimposed [108].*

For the spin measurement that uses the Collins-Soper angle $|cos(\theta^*)|$ discriminating variable [109], it was shown that using a p_T cut depending on the diphoton invariant mass allows to decorrelate the two observables $m_{\gamma\gamma}$ and $|cos(\theta^*)|$ (see for instance [110]). The distribution of the variable $\frac{p_T}{m_{\gamma\gamma}}$ for the leading and the subleading photon are shown in Figures 6.11(c) and 6.11(d).

Studies were carried out to test the impact of this cut on the main analysis and no deterioration of the sensitivity was observed, which leads to the harmonization of the relative p_T cut among the $\gamma\gamma$ analyses for the final Run I publications. The chosen cuts values are $\frac{p_T^{leading}}{m_{\gamma\gamma}} > 0.35$ and $\frac{p_T^{subleading}}{m_{\gamma\gamma}} > 0.25$. For a diphoton invariant mass at the lower edge of the allowed range (100 GeV), that means that photons with p_T lower than 35 and 25 GeV are cut, which is too close to the trigger threshold. Since the Higgs was already discovered and found to be at a mass of around 126 GeV, it was chosen to restrain the studied mass range to the interval $[105; 160]$ GeV.

(a) $p_T^{leading}$

(b) $p_T^{subleading}$

(c) $\frac{p_T^{leading}}{m_{\gamma\gamma}}$

(d) $\frac{p_T^{subleading}}{m_{\gamma\gamma}}$
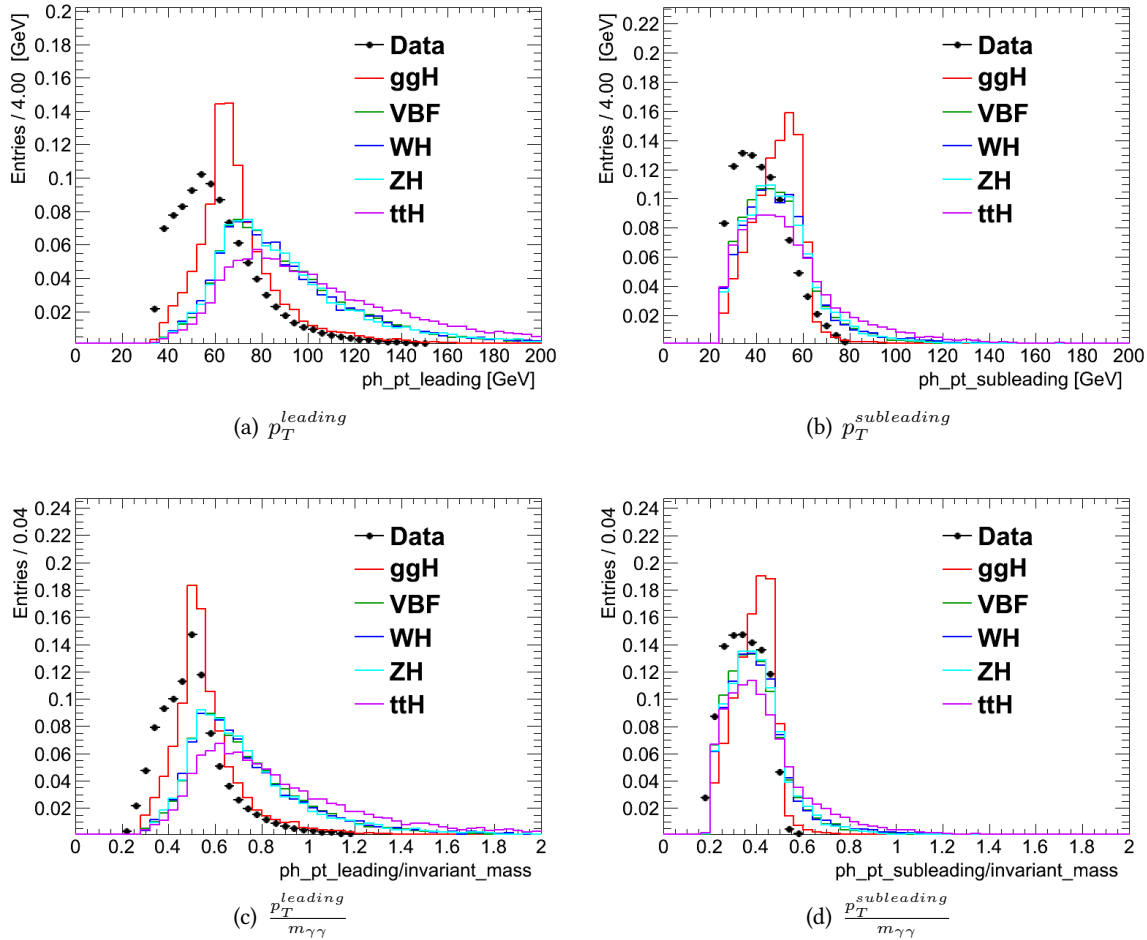
Figure 6.11: *p_T and $\frac{p_T}{m_{\gamma\gamma}}$ distributions after diphoton pair preselection for each of the production modes (Monte Carlo at $m_H = 125$ GeV and $\sqrt{s} = 8$ TeV) and for 2012 data.*

6.2.2 Photon quality

Electrons and photons are reconstructed from an electromagnetic cluster whose size is adapted depending on the particle nature hypothesis and its position (barrel or end-cap) in the detector. An electron is formed if a track can be matched to a cluster with spatial and energy conditions. A converted photon is created if a cluster is associated to a conversion vertex. Finally, all remaining clusters are labelled as unconverted photons (Section 4.5.3). For each photon or electron, several identification quality levels are defined: loose, medium (only for electrons) and tight [67]. They are based upon shower shape information and track properties (for electrons), to decide whether the shower looks like an expected electromagnetic object or jet shower in the calorimeter.

6.2.2.1 Shower shape

Cascades created by electromagnetic particles are usually narrower and have smaller longitudinal extension than the ones originating from a hadron. A typical example of a γ/π^0 candidates shower comparison from data is given in Figure 6.12. The lateral and longitudinal segmentation of the calorimeters can then be used to reject such particles faking a photon.

The ten discriminating variables defined for photon identification are listed below. Differences are observed when comparing the distributions of these discriminating variables between data and Monte Carlo. To account for this simulation effect, each variable is shifted in Monte Carlo in order

(a) Photon   (b) π^0
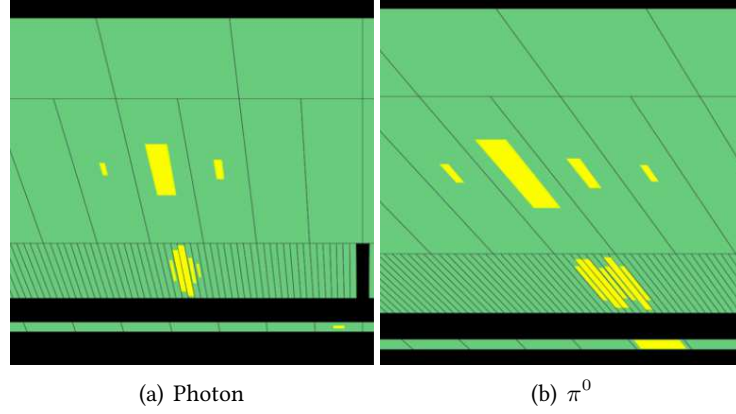
Figure 6.12: *Particle energy deposits in the pre-sampler and in the electromagnetic accordion for a photon (passing the tight identification criteria) and a π^0 candidate [111].*

to minimize the χ^2 between data and the shifted Monte Carlo distributions (fudge factors method). The remaining difference results in selection efficiency difference, that is corrected by weighting each selected photon with scale factors.

The Figures 6.13 to 6.15 represent their distribution for particles reconstructed as unconverted (left) and converted (right) photons. The truth photons Monte Carlo sample distribution is compared to a pure sample of photons from radiative Z events ($Z \rightarrow ll\gamma$) in data. It is confronted to a sample of simulated jets. The Monte Carlo samples are corrected by fudge factors in order that the mean of the distribution is consistent with the on observed in data. After the application of the fudge factors, differences remains in the shape of the shower shape distributions between data and Monte Carlo. This is corrected by the application of scale factors in the Monte Carlo, computed in such a way that the selection efficiencies in data and Monte Carlo are similar.

- Variables using the first layer (strips) information: (Fig. 6.13). They try to select showers with two close minima, characteristic of the two collimated photons originating from a π^0.

Front side energy ratio

$$F_{side} = \frac{E(\pm 3) - E(\pm 1)}{E(\pm 1)} \qquad (6.2)$$

estimates the containment of the shower in the electromagnetic calorimeter front layer. $E(\pm n)$ denotes the energy in the $\pm n$ strip(s) around the one containing the maximum of the energy.

Front lateral width (3 strips)

$$w_{\eta_1,3} = \sqrt{\frac{\sum E_i (i - i_{max})^2}{\sum E_i}} \qquad (6.3)$$

measures the shower width in the electromagnetic calorimeter front layer. i denotes the strip number and is varied by one unit around the strip with the maximum energy corresponding to i_{max}.

Front lateral width (total) $w_{\eta_1,tot}$ quantifies the shower width in a similar way than $w_{\eta_1,3}$ using 20 strips instead of 3.

Front second maximum difference

$$\Delta E = E^{S1}_{2^{nd}max} - E^{S1}_{min} \qquad (6.4)$$

is the difference between the energy of the strip with the second greatest energy and the energy in the strip cell with the least energy found between the greatest and the second greatest energy.

Ratio of two maxima

$$E_{ratio} = \frac{E_{max,1}^{S1} - E_{max,2}^{S1}}{E_{max,1}^{S1} + E_{max,2}^{S1}} \tag{6.5}$$

quantifies the energy separation between the first and second minima in the first layer of the accordion.

- Variables using the second layer (strips) information: (see Fig. 6.14 for their distribution). They characterize the longitudinal extension of the shower, usually larger for fakes.

Middle η energy ratio

$$R_\eta = \frac{E_{3\times7}^{S2}}{E_{7\times7}^{S2}} \tag{6.6}$$

measures the energy leakage out of the cluster in the η direction. It is defined as the ratio between the sum of the energies within 3×7 cells (in $\eta \times \phi$ cell of the electromagnetic calorimeter second layer units) and the energy sum contained in 7×7 cells, centred around the cluster seed.

Middle ϕ energy ratio

$$R_\phi = \frac{E_{3\times3}^{S2}}{E_{3\times7}^{S2}} \tag{6.7}$$

quantifies the energy leakage in the ϕ direction. It is the ratio between the sum of the energies within 3×3 cells (in $\eta \times \phi$) cells (in $\eta \times \phi$ cell of the electromagnetic calorimeter second layer units) and the sum of energies contained in 3×7 cells, centred around the cluster seed.
This variables behaves very differently for unconverted and converted photons, due to the electron and positron produced in the conversion process bent in opposite direction by the solenoidal magnetic field of the Inner Detector. Consequently, converted photons have larger values of R_ϕ than converted photons, as illustrated in Figure 6.14(c) and 6.14(d).

Middle lateral width

$$w_{\eta2} = \sqrt{\frac{\sum E_i \eta_i^2}{\sum E_i} - \left(\frac{\sum E_i \eta_i}{\sum E_i}\right)^2} \tag{6.8}$$

measures the shower lateral width in the electromagnetic calorimeter middle layer, using all cells in a window $\eta \times \phi = 3 \times 5$ measured in cell units.

- Variable using the hadronic leakage: (see Fig. 6.15 for their distribution). This variable take advantage of the typically larger energy deposited in the hadronic calorimeter by jets.

Normalized hadronic leakage

$$R_{had} = \frac{E_T^{had1}}{E_T} \tag{6.9}$$

is the transverse energy E_T^{had1} deposited in the first compartment of the hadronic calorimeter behind the electromagnetic cluster, normalized to the transverse energy E_T of the photon candidate, computed from the cluster energy E and the cluster pseudorapidity η_{S2} reconstructed in the second longitudinal sampling of the electromagnetic calorimeter ($E_T = E/\cosh(\eta_{S2})$).

(a) F_{side} unconverted

(b) F_{side} converted

(c) $w_{\eta_1,3}$ unconverted

(d) $w_{\eta_1,3}$ converted

(e) $w_{\eta_1,tot}$ unconverted

(f) $w_{\eta_1,tot}$ converted

(g) E_{ratio} unconverted

(h) E_{ratio} converted

(i) ΔE unconv
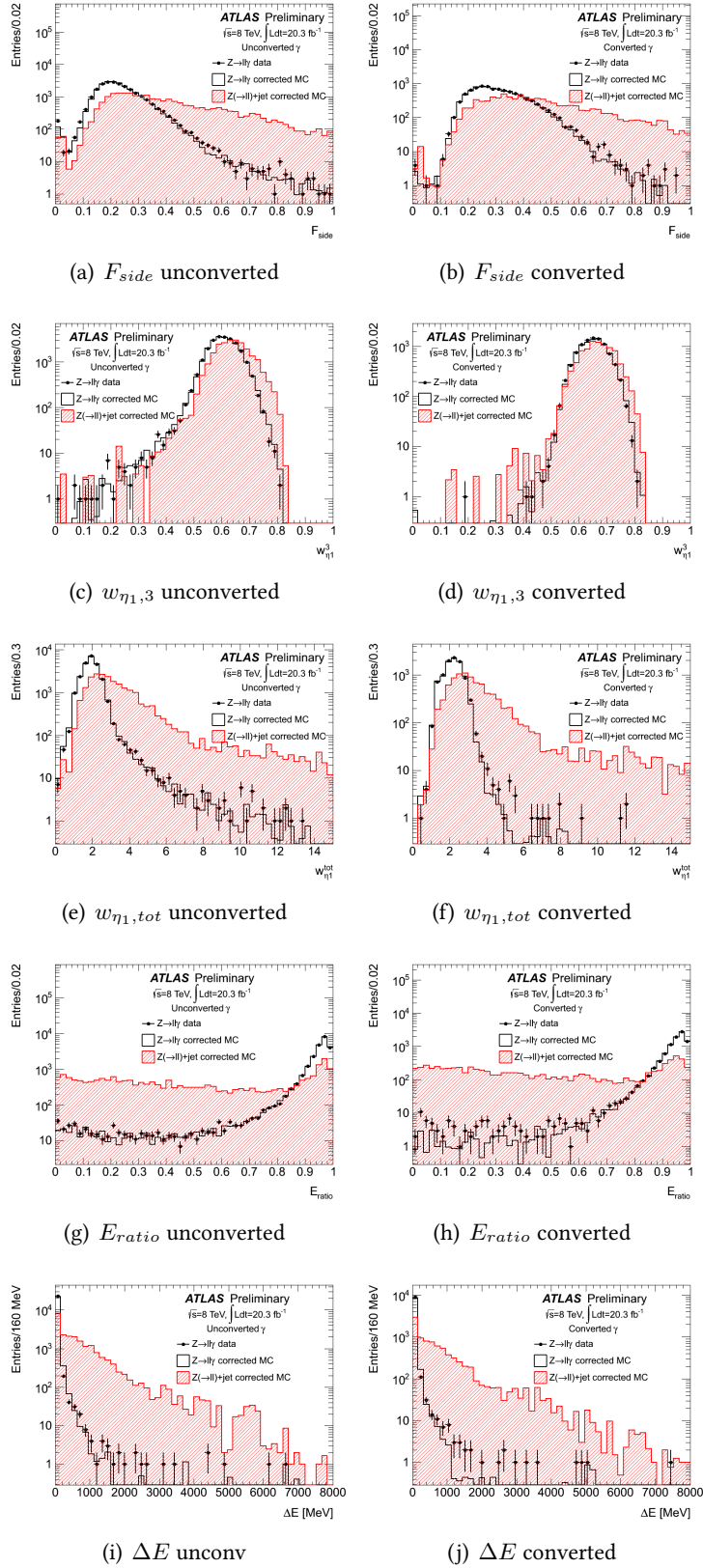
(j) ΔE converted

Figure 6.13: *Shower shape variables using the first layer for photon reconstructed as unconverted (left) and converted (right). The Monte Carlo is corrected with Fudge Factors to merge the mean of the distributions in data and Monte Carlo [112].*
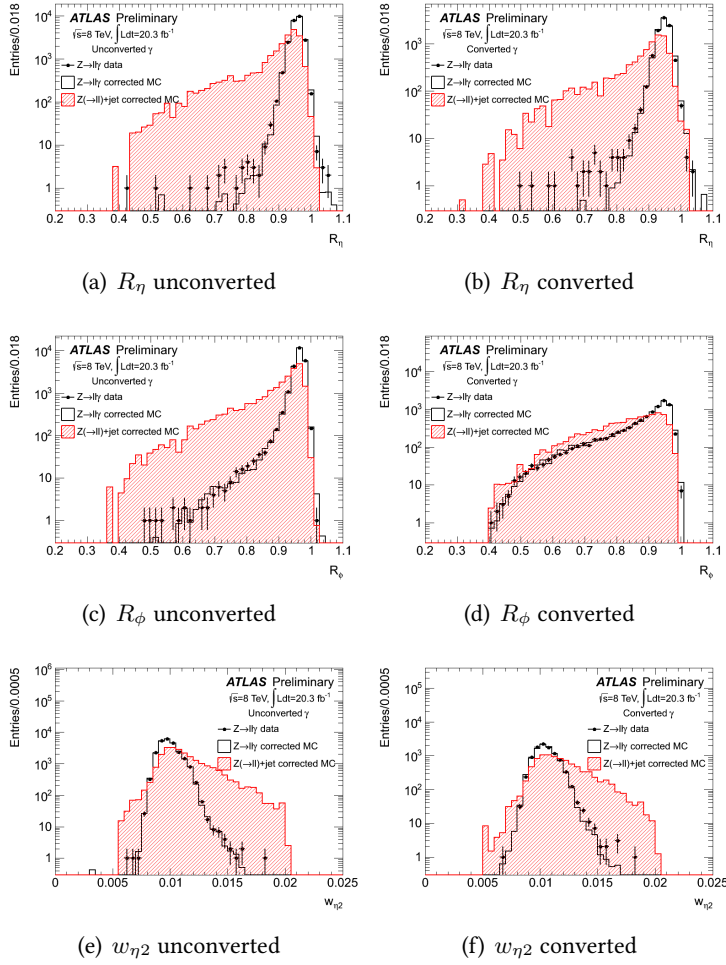
Figure 6.14: *Shower shape variables using the second layer for photon reconstructed as unconverted (left) and converted (right). The Monte Carlo is corrected with Fudge Factors to merge the mean of the distributions in data and Monte Carlo [112].*
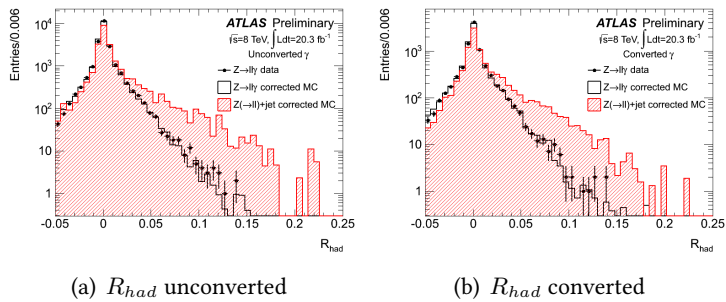
Figure 6.15: *Shower shape variables using the hadronic leakage for photon reconstructed as unconverted (left) and converted (right). The Monte Carlo is corrected with Fudge Factors to merge the mean of the distributions in data and Monte Carlo [112].*

6.2.2.2 Cut-based versus Neural Network approaches

Several sets of cuts are defined based on the shower shape information. Their optimization is done in bins of pseudorapidity in order to take into account the correlations of these variables with the electromagnetic calorimeter geometry and the varying amount of material with η.

The loose quality criteria are common to photons and electrons and is used for trigger decision.

For electrons, two more working points are used, medium and tight introducing tighter cuts on both the shower shapes variables and the track quality (number of hits in the pixels, *b*-layer, etc), with increasing electron purity and decreasing efficiency. For photons, only one additional set of cuts is produced, the tight quality.

Two approaches have been used to combine the information from each of these variables.

The historical approach is to use a cut-based method. Cuts on each variables are defined in order to achieve a good jet rejection. This method is used on the 8 TeV dataset. The cuts are derived separately for objects reconstructed as converted and unconverted photons, and depend on several $|\eta|$ bins. The cut optimization requires a final identification efficiency close to 85%, with maximized background rejection.

The identification efficiency can be estimated from Monte Carlo [67] or data-driven methods [113, 114]. Three data-driven methods are compared in Figure 6.16 for unconverted photons and in Figure 6.17 for converted photons:

- The radiative $Z \to ll\gamma$ decay allows to isolate a pure photon sample. It is useful in the low E_T region only.

- Another method uses a pure electron sample from $Z \to e^+e^-$ events. The shower shape variables distributions are then mapped to the distributions for photons with Smirnov transformations [115] derived from Monte Carlo. This method is quite straightforward for converted photons, whose shower is similar to the one created by electron. On the contrary, unconverted photons will suffer from more uncertainties.

- The matrix method uses the track isolation of the photon candidate before and after tight identification criteria.

For $E_T > 30$ GeV, the reconstruction efficiency is $\sim 75\%$ on average, and increases to more than 90% for $E_T \gtrsim 60$ GeV.

Another approach, neural network based [116], was developed for photons in the 2011 data. The inputs to the neural network algorithm are the same variables used in the cut-based approach with the addition of the particle pseudorapidity. The signal purity is increased, while the background rejection is sensibly constant. This leads to an increase in the expected significance of $\sim 5\%$.

6.2.3 Isolation

In spite of the caution taken to define the photon quality, a contamination from jets remains. Isolation allows to reduce even more this component. It consists in estimating the energy in a cone centred on the particle of interest: for a true photon, this energy is expected to be small, once the pile-up effects are subtracted. On the contrary, jets have very busy neighbourhood, meaning that they are surrounded by a lot of particles creating a large isolation energy. Requiring this energy to be below a given threshold hence allows to reduce the jet contamination.

6.2.3.1 Calorimetric

The calorimetric isolation used in the analysis is computed by summing the transverse energy of all calorimeter topo-clusters with positive energy, whose energy weighted barycentre belongs to the cone $\Delta R = 0.4$ around the considered particle. The region $\Delta\eta \times \Delta\phi = 5 \times 7$ cells around the seed is ignored to remove the energy of the particle itself (Fig. 6.18).

This raw computation is corrected for several effects:

- Leakage: photon energy leakage out of the central cluster is also taken into account. A correction is derived from Monte Carlo studies and a linear correction with the photon transverse momentum is applied.
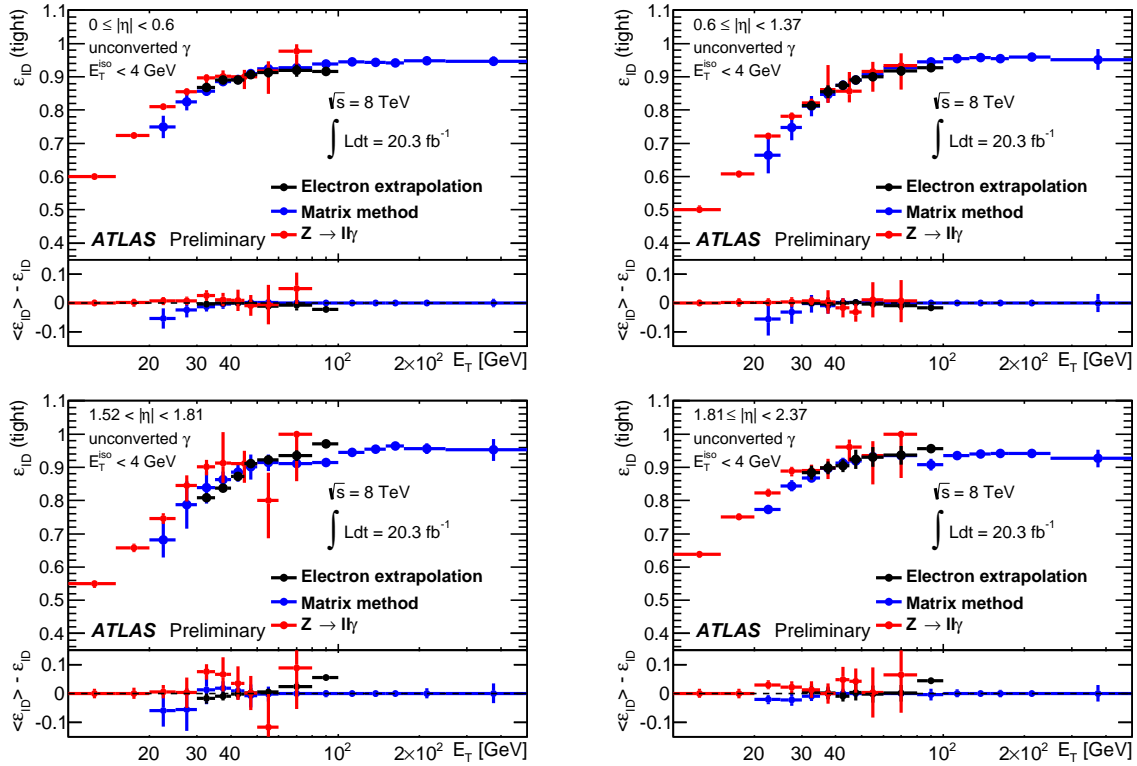
Figure 6.16: *Unconverted photon identification efficiency in 2012 data from data-driven techniques as a function of the photon E_T, in four η regions [114].*
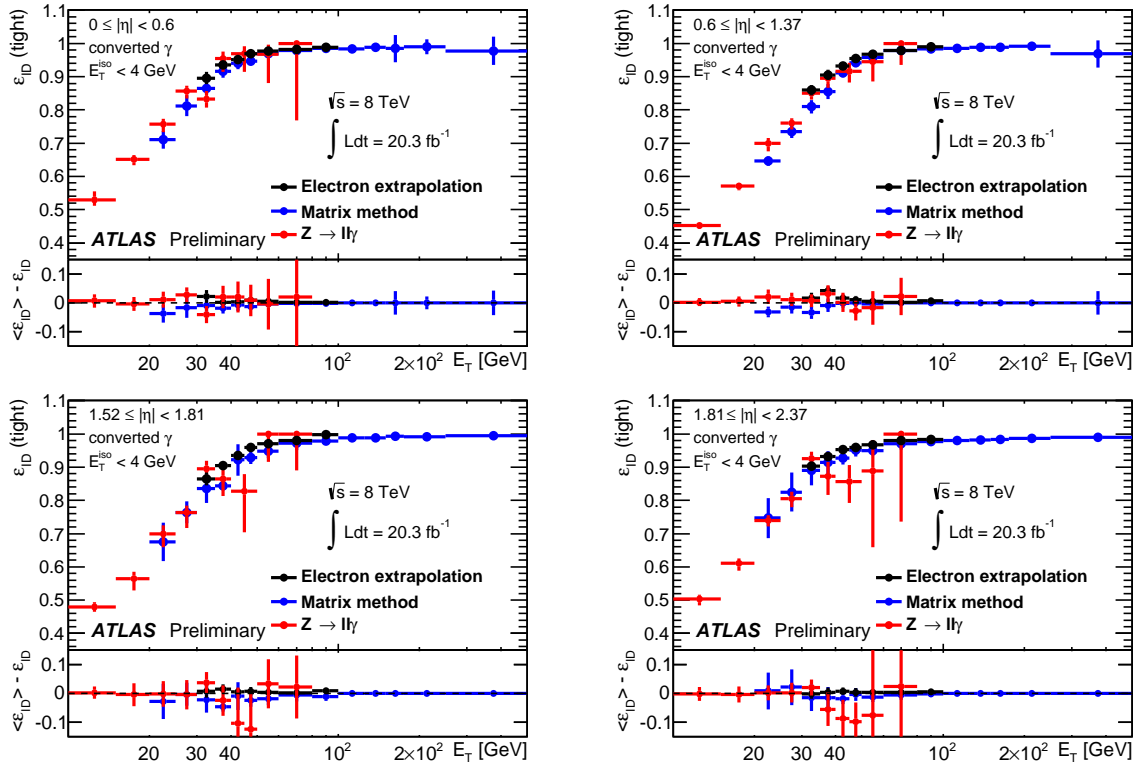
Figure 6.17: *Converted photon identification efficiency in 2012 data from data-driven techniques as a function of the photon E_T, in four η regions [114].*
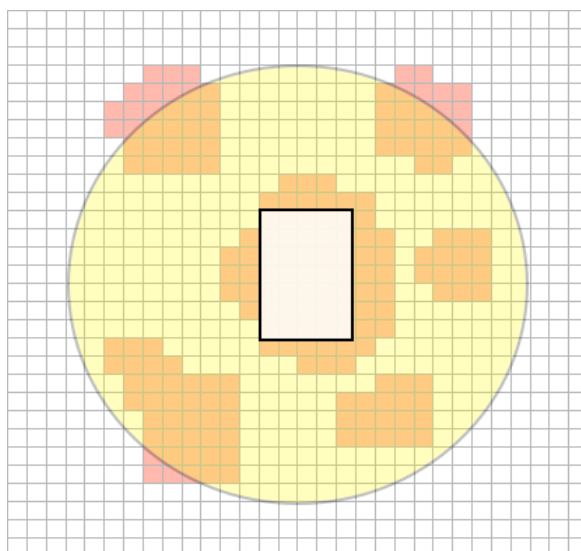
Figure 6.18: *Topo-isolation principle. All cells belonging to the depicted topo-clusters are considered [117].*

- Pile-up: an ambient energy from pileup is computed in an event-by-event basis using the jet-area technique [118, 119] and is removed from the raw energy. The stability versus pileup after this correction is illustrated in Figure 6.19. For 2012, an energy correction was applied for each event on a cell-by-cell basis (assuming a ϕ symmetry of the energy deposits), depending on the bunch crossing ID and lumi-block [120].

(a) Cell based isolation

(b) Topo-cluster isolation
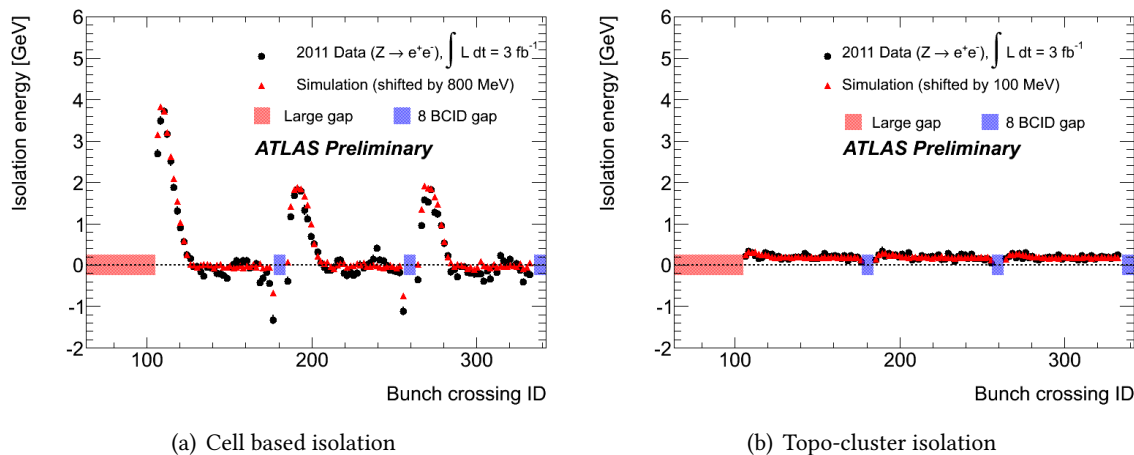
Figure 6.19: *Mean of the isolation energy as a function of the out of time pile up for 2011 data. The cell-based isolation sums up all cells within $\Delta R = 0.4$ while the topo-cluster isolation only use cells in topo-clusters whose barycentre lies within $\Delta R = 0.4$. The pile-up suppression for the topo-cluster isolation is shown to be efficient [121].*

Figure 6.20 shows the distribution of the final isolation variable for the leading and subleading photons, with loose and tight quality. The initial cut was 4 GeV but it was relaxed in favour of a more pile-up robust quantity, the track isolation.

6.2.3.2 Track

Starting from the Council 2012 analysis [123], a track isolation is added, which is a more robust quantity with respect to pile-up.

The track isolation transverse momentum is defined as the sum of the momentum of all tracks coming from the primary vertex within $\Delta R < 0.2$ with respect to the photon candidate cluster. For

(a) Leading photon

(b) Subleading photon
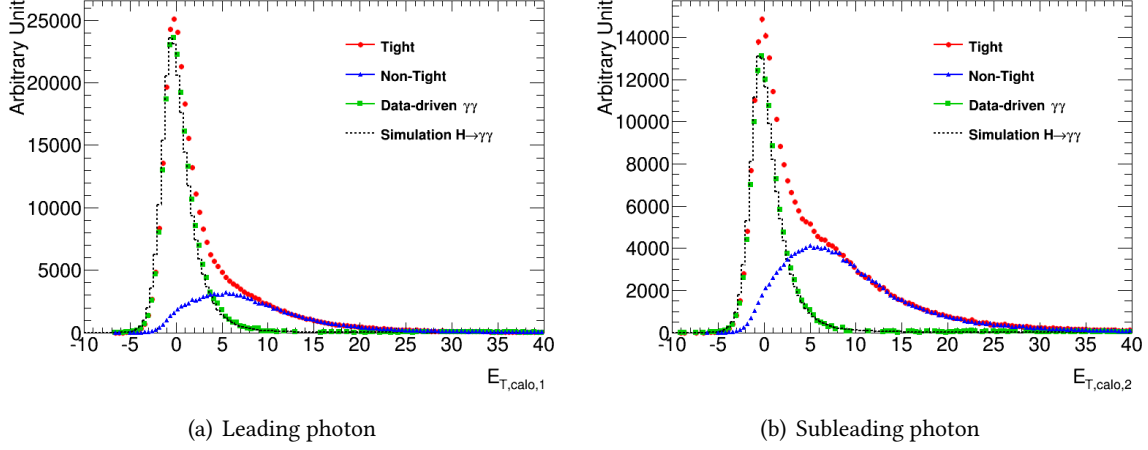
Figure 6.20: *Calorimetric isolation distributions for leading and subleading photons. The red histograms show the distribution for photons passing the tight quality criteria. The blue distribution is made from non-tight photons, normalized to the tail of the distribution for tight photons, where one does not expect prompt photons. The green is obtained by subtracting the blue contribution from the red. It is compared to a Monte Carlo $H \rightarrow \gamma\gamma$ signal sample [122].*

converted photons, the conversion tracks are removed. Track isolation distributions are illustrated in Figure 6.21.

(a) Leading photon

(b) Subleading photon
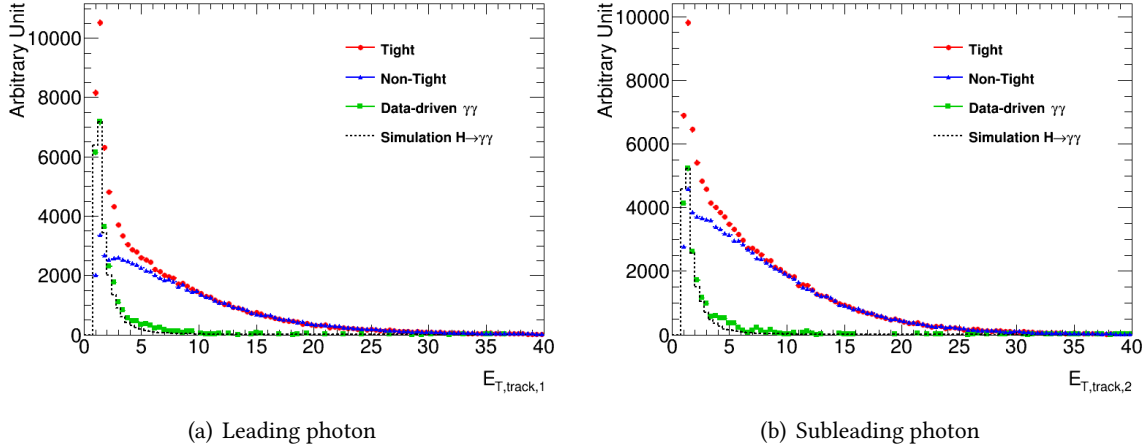
Figure 6.21: *Track isolation distributions for leading and subleading photons. The red histograms show the distribution for photons passing the tight quality criteria. The blue distribution is made from non-tight photons, normalized to the tail of the distribution for tight photons, where one does not expect prompt photons. The green is obtained by subtracting the blue contribution from the red. It is compared to a Monte Carlo $H \rightarrow \gamma\gamma$ signal sample [122].*

The cut optimization is driven by the will to maximize the number of expected signal events, while keeping constant the number of observed events in data. The chosen cuts for 7 and 8 TeV data are:

- 7 TeV: $\sum_{(topo-cluster \in \Delta R < 0.4)} E_T^{topo-cluster} < 5.5$ GeV and $\sum_{(trk \in PV \& \Delta R < 0.2)} p_T^{trk} < 2.2$ GeV;

- 8 TeV: $\sum_{(topo-cluster \in \Delta R < 0.4)} E_T^{topo-cluster} < 6.0$ GeV and $\sum_{(trk \in PV \& \Delta R < 0.2)} p_T^{trk} < 2.6$ GeV;

The results of the optimization are shown in Figure 6.22 for both 2011 and 2012 dataset.
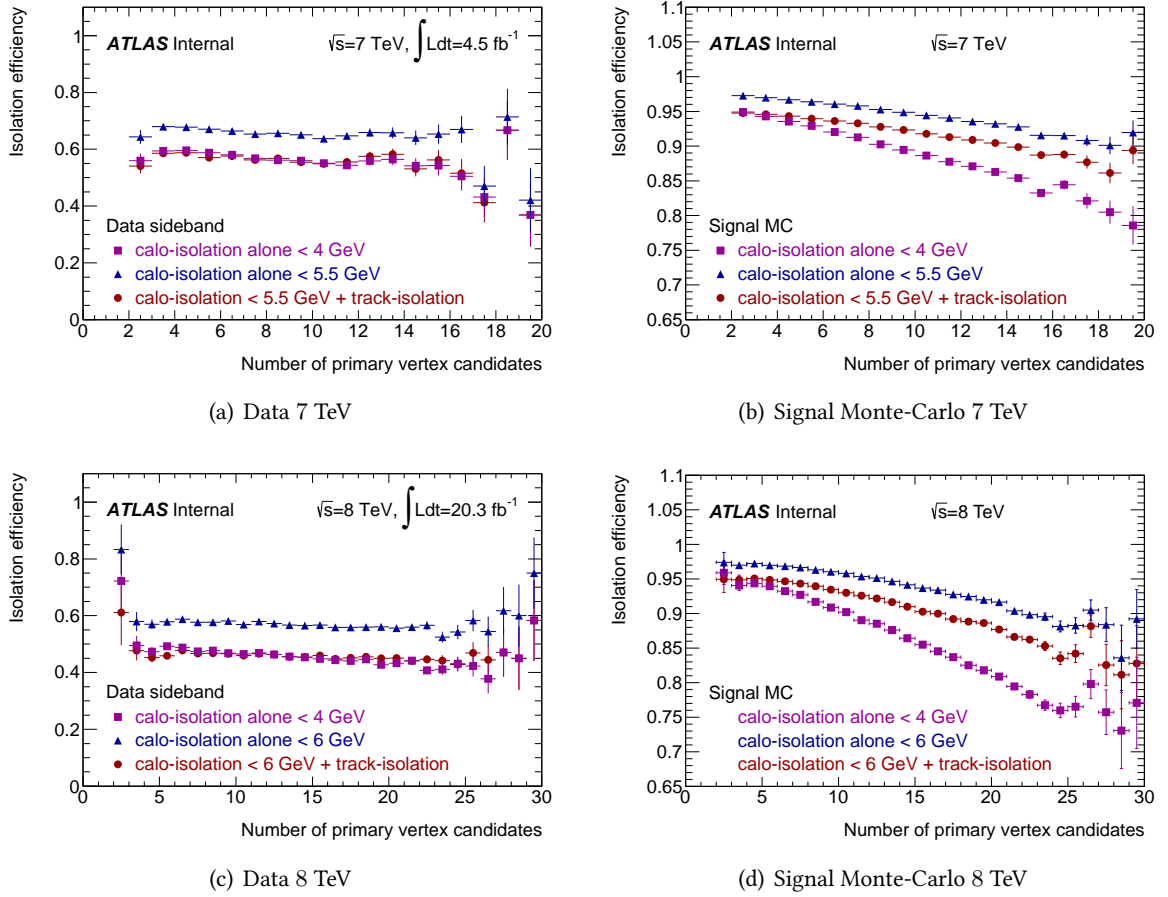
Figure 6.22: *Track isolation optimization for 7 and 8 TeV analyses [105].*

6.2.3.3 Primary vertex choice

The choice of the primary vertex is important for the mass resolution but also for the track isolation and for the jet vertex fraction determination (Sec. 4.5.4). The hard scattering primary vertex is usually chosen to be the primary vertex with the highest $\sum p_T^2$. This choice can be improved thanks to the pointing method, using the photon shower in the first two compartments of the electromagnetic calorimeter. For converted photons, the calorimeter pointing is extended to take into consideration information from the conversion electron tracks (more details can be found in Section 5.4).

The pointing technique is further improved with two methods:

- Likelihood: a likelihood method was used for the discovery analysis. It relies on several informations:

  - The direction of flight of the photons reconstructed from the pointing;

  - The $\sum p_T^2$ of all reconstructed vertices;

  - For 7 TeV, the conversion vertex for converted photons whose tracks have hits in the silicon detector (giving information on the z position).

The likelihood method allows to improve the $\gamma\gamma$ mass resolution and to increase the efficiency of finding the hard scattering vertex.

- Neural Network [124]: it is used in the analysis since Moriond 2013. The best performances were found to be achieved when combining the informations from four different sources:

- The result of the pointing method giving a position along the z axis;
- The $\sum p_T$ of all reconstructed vertices;
- The $\sum p_T^2$ of all reconstructed vertices;
- The difference in ϕ between the sum of all tracks originating from a vertex and the diphoton system;
- The z-pull from the calorimeter + conversion vertex pointing for converted photons $\frac{z_{vtx} - z_{pointing}}{\sigma_{pointing}}$

The neural network technique improves the probability of reconstructing a vertex within 3 mm from the true vertex by 6% [123]. Its evolution versus the number of reconstructed primary vertex is illustrated in Figure 6.23.
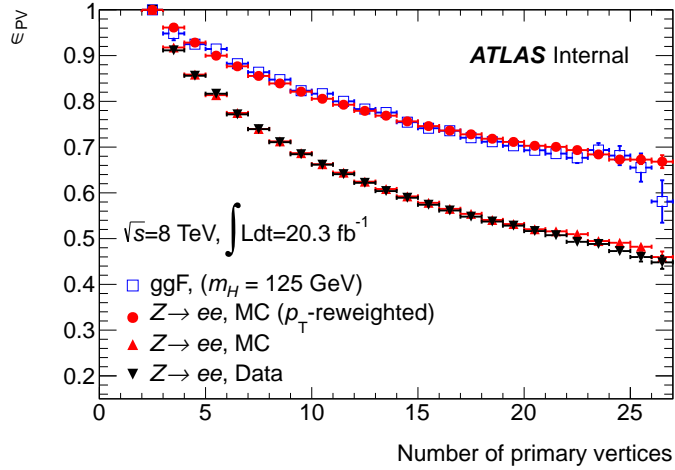
Figure 6.23: *Evolution of the primary vertex reconstruction efficiency (reconstructed vertex less than 3 mm away from the vertex reconstructed from the tracking information) as a function of the number of primary vertices in 2012 data [125].*

6.2.4   Summary

The work performed during this thesis was done at different stages of the analysis, with different selections and categorizations. Table 6.3 tries to wrap-up the evolution of the analysis selection and number of categories, throughout this thesis, for the 2012 data analysis. Track isolation was introduced since it is more stable with respect to pile-up. The determination of the primary vertex was improved, important issue for the track isolation and jet definition.

The analysis of 2011 data did not change up to the final analysis of Run I data, where the kinematics cuts were changed to relative p_T cuts and the track isolation was introduced.

	ICHEP 2012 [99, 126]	HCP/Council 2012 [123]	Moriond 2013 [127]	Final Run I (2014) [125]
Dataset [fb^{-1}]	6	13	20	20
Trigger		g35_loose_g25_loose		
Kinematics		$p_T > 40; 30$ GeV		$p_T/m_{\gamma\gamma} > 0.35; 0.25$
Quality	Tight cut-based	Tight cut-based	Tight cut-based	Tight cut-based
Isolation [GeV]	Topo < 4	Topo< 6 +Trk < 2.6	Topo< 6 +Trk < 2.6	Topo< 6 +Trk < 2.6
Primary vertex	Likelihood	Likelihood	Neural Network	Neural Network
# Categories	10	12	14	12
p_{Tt}^{cut}	60	60	60	70

Table 6.3: *Summary of the evolution of the analysis cuts for 8 TeV data. All analyses use in addition the 2011 dataset representing ~ 5 fb^{-1}.*

6.3 Monte Carlo corrections

The Monte Carlo samples are generated with (`POWHEG +`) `PYTHIA8` (depending on the signal process considered). They are then passed through a `GEANT4` simulation of the detector and digitized before being reconstructed and analysed with the same analysis chain than data. The properties of the simulations are usually chosen to match the observations, but some of them have to be tuned *a posteriori*.

All the corrections described here are applied at truth level before any selection. They act as an additional weights applied to each event.

z reweighting

The interaction area along the z axis in data is 56 mm in 2011 and 48 mm in 2012 and is not exactly centred at 0. The Monte Carlo samples use a larger z_{vertex} distribution. This is corrected by weighting the events in such a way that the weighted histogram matches the distribution observed in data (Fig. 6.24). The weight is then taken into account in the computation of the number of expected events (see Section 6.5.1).

(a) Before z reweighting

(b) After z reweighting
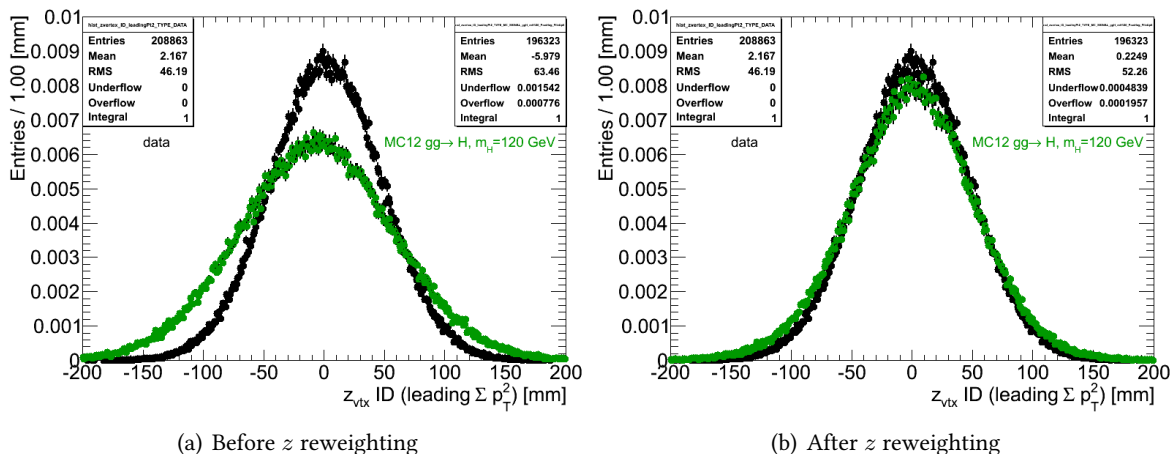
Figure 6.24: *z reweighting correction of the Monte Carlo.*

Pileup reweighting

The same reweighting technique is applied to the number of interactions per bunch crossing. The weights are derived from a high statistics ggH Monte Carlo sample at $m_H = 125$ GeV.

Since the most important quantity for the analysis is the number of primary vertex (for the primary vertex choice, see previous section), the weights are computed in such a way that the number of primary vertex is similar between data and Monte Carlo. Figure 6.25 illustrates the effect of the pile-up rescaling on the MC12A production, deliberately generated with a flat distribution because the data conditions were not established. The final (MC12C) Monte Carlo simulation of the 8 TeV data uses a distribution naturally closer to the data. A reweighting is applied to correct for small differences, but its effect is smaller.

p_T reweighting

The Higgs p_T is highly correlated to the p_{Tt} variable used to categorize the selected events. The modelling of this variable have an impact in the repartition of the events in the different categories and hence on the final measurement. A reweighting based on the Higgs transverse momentum is applied in order to match the last theoretical computations at NNLO+NNLL developed in programs

(a) Number of bunch crossings

(b) Number of primary vertex
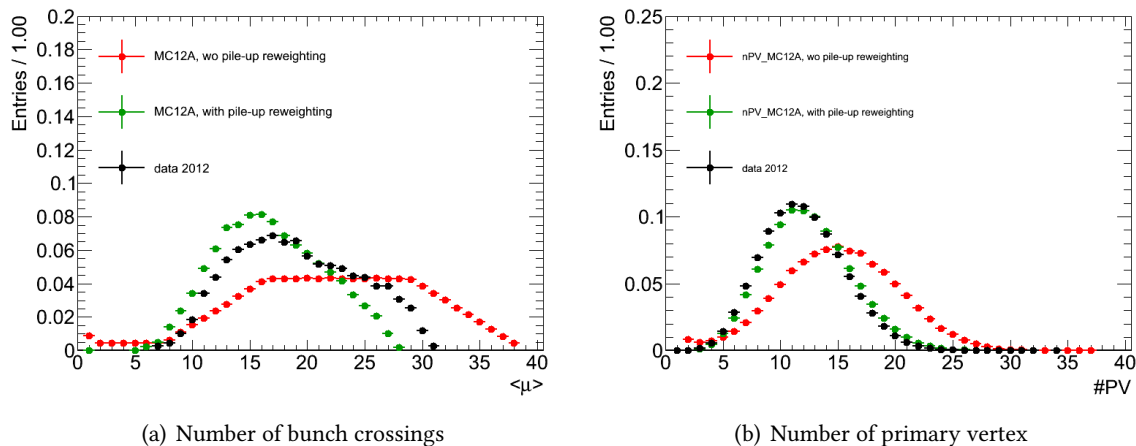
Figure 6.25: *Pileup reweighting correction of the Monte Carlo (MC12A).*

such as `HqT` and `HRes`. More explanations and the impact of the Higgs p_T modelling on the $H \to \gamma\gamma$ analysis are discussed in Chapter 9.

Interferences

Interferences between the $gg \to H \to \gamma\gamma$ signal production and the background continuum $gg \to \gamma\gamma$ reduces the signal yield by $\sim 0.9\%$. This effect is taken into account by applying a weight to the ggH Monte Carlo [128, 129] and results in the weights of Table 6.4.

Central low p_{Tt}	Central high p_{Tt}	Forward low p_{Tt}	Forward high p_{Tt}
-1.38	0.09	-1.36	0.04

Table 6.4: *Interference weight in the untagged categories for the final Run I couplings analysis.*

6.4 Background estimation

The QCD background is made of the processes shown in Figure 6.3 and of events where at least one jet is reconstructed as a photon, even after quality and isolation requirements. Another source of background is the Drell-Yan process ($Z^*/\gamma^* \to e^+e^-$), where the two electrons are reconstructed as photons. Even if very small compared to the dominant QCD background, Drell-Yan events can have an impact on the determination of the background shape with the spurious signal technique that make use of the expected background (see Section 6.5.2).

The results presented below are based on the 2012 partial dataset representing the first 13 fb^{-1}.

6.4.1 QCD

QCD background is made of *jet-jet*, γ-*jet* (or *jet-γ*) and $\gamma\gamma$ events.

Due to the large rejection factor achieved in the analysis, studies involving Monte Carlo simulations would require the processing of billions of events in order that a sufficient quantity pass the $H \to \gamma\gamma$ selection criteria. For this reason, we have given up Monte Carlo based studies in favour of real data side-bands, *i.e.* out of the signal region corresponding to about $[120; 130]$ GeV mass range. Several data driven methods are developed to get the background composition of the selected events (for a description of a simple case, see [130]).

- The baseline technique to estimate these contribution is the $2 \times 2D$ method [131]. Starting from an initial dataset formed by diphoton events where the photons must pass a relaxed quality cuts (close to the loose selection), it consists in classifying the events into several regions depending on the quality (tight or non-tight) of the two photons candidates and whether they pass the isolation cut or not. The signal region corresponds to the case where both photons are tight and isolated. All other cases constitute the fifteen control regions of this analysis. The number of expected background event can be extrapolated from the control region to the signal region, after the signal leakage out of the signal region has been estimated from $\gamma\gamma$ Monte Carlo (see Ref. [131] for more details). The results of this procedure for the first 13 fb^{-1} of 2012 data is shown in Figure 6.26.

Figure 6.26: *Composition of the reconstructed $\gamma\gamma$ events from the first 13 fb^{-1} of 2012 data samples in term of reducible and irreducible background [123].*

This results is cross-checked with three other procedures giving consistent results within the error bars.

- The $1 \times 2D$ technique is based on the measurement the $j \rightarrow \gamma$ fake rate in $W \rightarrow e\nu + jets$ events.

- The 4×4 matrix method consists in counting the number of events where the leading (first index) and subleading (second index) photons pass (P) or fail (F) the quality and isolations cuts. They are related to the number of truth $\gamma\gamma$ events through the Equation 6.10, where the coefficients of the matrix $\mathbf{E}$ are functions of the signal efficiencies and background fake rates, taking into account correlations between the isolation energies of the two photons.

$$\begin{pmatrix} N_{PP} \\ N_{PF} \\ N_{FP} \\ N_{FF} \end{pmatrix} = \mathbf{E} \begin{pmatrix} N_{\gamma\gamma} \\ N_{\gamma j} \\ N_{j\gamma} \\ N_{jj} \end{pmatrix} \tag{6.10}$$

- The template fit method use isolation distribution for $\gamma\gamma$, γj and jj events determined from data. A likelihood fit is then performed to the isolation distribution of events passing the tight and isolation requirements to find the fraction of each distribution that better match the observed spectrum.

The $\gamma\gamma$ purity with this method is found to be: $(76 \pm 3)\%$ in the 2012 dataset with cut-based tight photon identification and both calorimetric (topo-clusters) and track isolations [132].

6.4.2 Drell-Yan

6.4.2.1 Inclusive

The Drell-Yan process is made of $Z \to e^+e^-$ events. It is a background for the diphoton final state when both electrons are misidentified as photons.

It is estimated with data driven technique, measuring the $e \to \gamma$ fake rate for each of the photons. More precisely, several possibilities are envisaged to estimate the ee contamination, as illustrated in Figure 6.27.
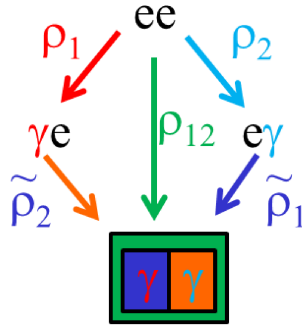
Figure 6.27: *Different paths to estimate the Drell-Yan background.*

From this figure, one can define the number of events wrongly reconstructed as diphoton events as

$$N_{\gamma\gamma} = \frac{1}{2} \left(\tilde{\rho_1} N_{e\gamma} + \tilde{\rho_2} N_{\gamma e} \right)$$
$$= \frac{1}{2} \alpha \left(\rho_1 N_{e\gamma} + \rho_2 N_{\gamma e} \right)$$

(6.11)

with the following definitions for ρ and α :

$$\rho_1 = \frac{N_{\gamma e}}{N_{ee}} \qquad\qquad \rho_2 = \frac{N_{e\gamma}}{N_{ee}} \qquad\qquad \rho_{12} = \alpha\rho_1\rho_2$$

ρ_1 and ρ_2 can be estimated from data, in the Z region, counting the number of events reconstructed as $e\gamma$ and γe events, with a mass consistent with the Z boson. The di-object distributions in data used to estimate these fake rates are displayed in Figure 6.28. Computing directly ρ_{12} from data is not possible due to the large $\gamma\gamma$ background in the Z region. However, this number is estimated from simulations to calculate the correlation coefficient α (see Fig. 6.28(b)).

Uncertainties: several sources of systematic uncertainties are considered and their impact on the previous determination quantified:

- p_T cut (symmetric/asymmetric): the $Z \to e^+e^-$ events are selected applying a symmetric p_T cut on the electrons. The effect of this different selection is taken as a systematic uncertainty;

- Fit range: the number of events are extracted by a sum of two gaussians (one for the core and another wider one for the background) fit to the selected events in the Z region. The effect of changing the fit range are estimated;

- Residual background, modelled with an exponential shape.

The number of expected Drell-Yan events from this method in the $[100; 160]$ GeV mass window is found to be:

$$N_{DY} = 382.8 \pm 6.1 \,(\text{stat}) \pm 64.63 \,(\text{syst})$$

for 13.0 fb^{-1} of data at $\sqrt{s} = 8$ TeV. Its distribution per bin of invariant mass is shown in Figure 6.29.
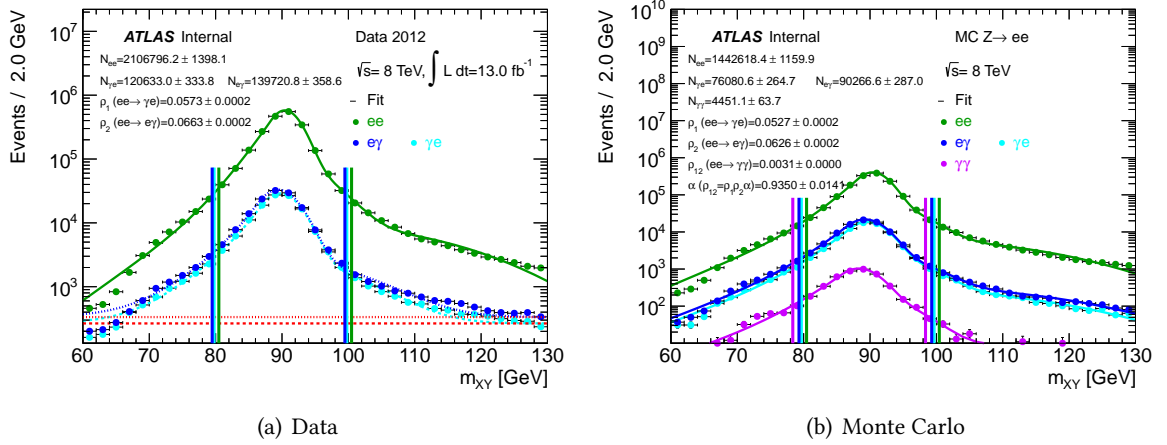
Figure 6.28: *Determination of the e → γ fake rate coefficients [133].*
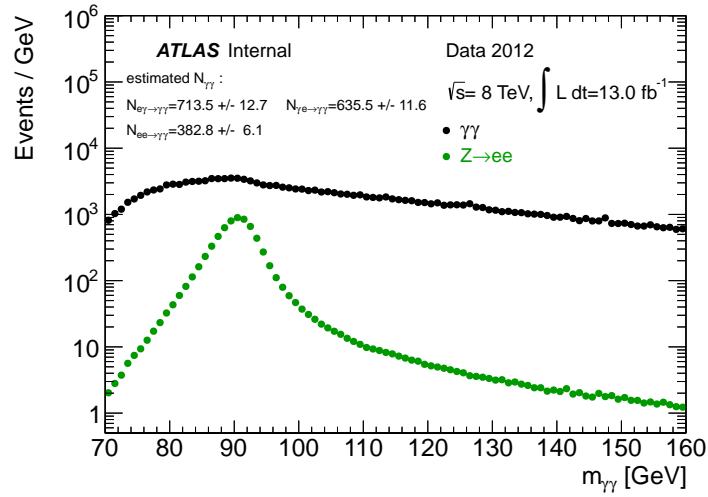
Figure 6.29: *Determination of the Drell-Yan background per invariant mass bin in the region of interest for 2012 data [132].*

6.4.2.2 Per category

The previous method works very well for the inclusive analysis, but its complexity increases quickly with the number of categories. Consequently, another solution is proposed, consisting in estimating the fraction of Drell-Yan events in each category from a $Z \to e^+e^-$ Monte Carlo sample. The inclusive Drell-Yan spectrum estimated from data is then weighted by this fraction of events to estimate this background per category i (see Eq. 6.12).

$$
\begin{aligned}
N_{\text{DY data}}^i &= \frac{N_{MC}^i}{N_{MC}^{incl}} \times N_{\text{DY data}}^{incl} \\
&\equiv \omega_{MC}^i \times N_{\text{DY data}}^{incl}
\end{aligned}
\tag{6.12}
$$

The results presented hereafter use a 12-category model, composed of the nine classical categories plus one VBF category (10), a VH-hadronic category (11) and a VH-leptonic category (12).

The procedure described above is applied for each of these categories and the resulting background decomposition per category is illustrated in Figure 6.30. As expected, the categories containing unconverted photons (number 2, 4 and 6, see Sec. 6.1.3) are found to have a negligible Drell-Yan contribution.

(a) Logarithmic scale

(b) Linear scale
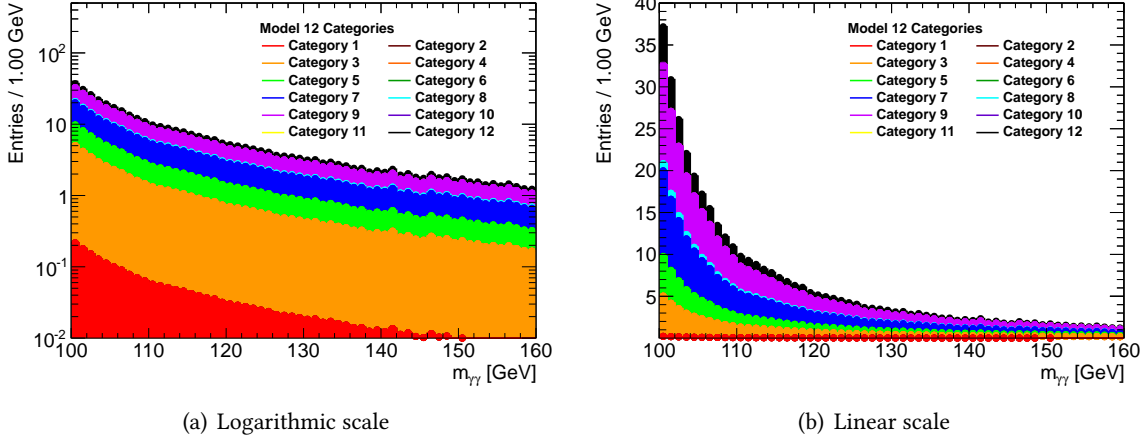
Figure 6.30: *Per category decomposition of the Drell-Yan background. The shape is common to all categories, only the normalization is adapted. The estimation yields 0 for the categories not appearing on these plots.*

Uncertainties : the statistical and systematics uncertainties from the inclusive Drell-Yan estimation are split into categories with the same weight that the inclusive number. An additonnal uncertainty arises from the low statistics of the Monte Carlo sample used to determine the weights. The uncertainty on ω_i is written:

$$\left(\sigma^i\right)^2 = \frac{\omega_{MC}^i \times \left(1 - \omega_{MC}^i\right)}{N_{MC}^{incl}} \tag{6.13}$$

that is propagated to the number of events in category i, $N_{DY\,data}^i$, through:

$$\sigma_{MC\,stat}^i = \sigma^i \times N_{DY\,data}^{incl} \tag{6.14}$$

To summarize, three sources of systematics uncertainties are estimated from the inclusive numbers as follows:

- Statistical uncertainty: $\omega_{MC}^i \times \sigma_{incl}^{stat}$

- Systematics uncertainty : $\omega_{MC}^i \times \sigma_{incl}^{syst}$

Those two parameters are computed in such a way that $\sum_i \sigma_i = \sigma_{incl}$, justified by the fact that the $N_{DY\,data}^i$ are fully correlated through the measurement of $N_{DY\,data}^{incl}$.

- Low statistics of the Monte Carlo sample : $\frac{\omega_{MC}^i \times \left(1 - \omega_{MC}^i\right)}{N_{MC}^{incl}} \times N_{DY\,data}^{incl}$

Table 6.5 details the number of expected Drell-Yan events per category and the associated uncertainties.

6.5 Statistical treatment

To perform a statistical analysis out of the selected data, one needs to define the signal shape and the expected yields from the Standard Model, the background shape (its normalization and parameter precise values are estimated by a fit to the data) and the systematics uncertainties impacting these quantities.

6.5.1 Signal model

The signal is characterized by a narrow resonance as shown in Figure 6.32. In order to measure the Higgs boson mass, the signal yield and shape parameters are parametrized as a function of the simulated Higgs mass.

Categ	Yield	Stat	MC Stat	Syst
1	2.2	0.0	2.3	0.5
2	0.0	0.0	0.0	0.0
3	49.4	0.8	10.3	10.2
4	0.0	0.0	0.0	0.0
5	48.5	0.8	10.3	10.0
6	0.4	0.0	1.0	0.1
7	105.1	1.7	13.8	21.6
8	8.8	0.1	4.6	1.8
9	121.3	1.9	14.4	24.9
10	0.0	0.0	0.0	0.0
11	0.0	0.0	0.0	0.0
12	47.0	0.7	10.1	9.7

Table 6.5: *Estimation of the Drell-Yan background for each of the 12 categories used for the HCP2012 analysis [123] with their associated uncertainties.*

6.5.1.1   Monte Carlo samples and cross-section predictions

The different Higgs production modes are simulated into different samples with their cross-section normalized to the latest estimations coming from the Yellow Report 3 [134], updating previous results from [27, 135]. Until the final Run I analysis presented here, the showering is made by PYTHIA6 [136] for the 7 TeV samples and PYTHIA8 [137] for 8 TeV. For the final Run I analysis, PYTHIA8 is used everywhere.

The ggH samples are generated at NLO by POWHEG [138, 139] and showered by PYTHIA. Its cross-section is normalized to the ones from [134]. Following earlier NLO computations [140–142], NNLO computations were done in the large top mass limit [143–145]. The cross-sections including NNLL resummation [146, 147] are used in [134]. They also include the effect of the charm quark, in addition to the more important contributions of top, bottom and their interferences (see Tab. 8.1 for numerical results), and two loops electroweak corrections [148–150] evaluated at NLO in [151]. The uncertainties on this cross-section will be rapidly discussed in Section 7.4.3.1.

The VBF production mode is also generated at NLO by POWHEG [152], showered by PYTHIA. The prediction comes from an approximate NNLO QCD computation [153] and with an NLO electro-weak correction computed with HAWK [154].

The Higgsstrahlung processes VH are simulated by PYTHIA, corresponding to a LO computation only. The W/ZH NLO predictions are normalized to cross sections calculated at NNLO [156, 157] (one can also see the original computation in [158]). This computation includes gg induced processes computed at NLO [159], non Drell-Yan-like contributions in the $q\bar{q}$ initiated channels at NNLO, where the Higgs boson is radiated by a top-quark loop [160].

Finally, the ttH process is generated by PYTHIA and normalized to the full NLO QCD corrections calculations [161–164].

After the first full Run I analysis (Sec. 6.6.2), several changes are made. All samples are regenerated with the same generator conditions between 7 and 8 TeV. They are all showered with PYTHIA8. The ttH samples are now generated by POWHEL[165, 166] + PYTHIA8 at NLO+PS. Moreover, two processes are added: bbH and tH.

6.5.1.2   Yield

The expected signal yield after the analysis selection is computed from the Higgs production cross-section σ_{SM}, the branching ratio of the $\gamma\gamma$ decay channel $\mathcal{B}r_{H\to\gamma\gamma,SM}$, the integrated recorded lumi-

nosity L and the analysis efficiency ϵ:

$$N_{selected} = \sigma_{SM} \times \mathcal{B}r_{H \to \gamma\gamma,SM} \times L \times \epsilon \tag{6.15}$$

The analysis efficiency is estimated from the simulation $\epsilon = \frac{W_{selected}}{W_{initial}}$, where W denotes the sum of the event weights. The initial sum of weight takes into account the pileup, z, p_T weights and the Monte Carlo weights for generators producing weighted events (such as MC@NLO). The final weight incorporate in addition the interference weight, which changes the overall normalization.

Dalitz events: When decaying the Higgs to two photons, the default configuration of PYTHIA8 takes into account the Dalitz process: $H \to \gamma\gamma^* \to \gamma f \bar{f}$. This increases the total cross-section by $\sim 6\%$ [167, 168]. Since the cross section of the Monte Carlo used in the following does not take into account the Dalitz decay, these events are not considered for the sum of event weight used in the sample normalization, while they are taken into account in the final selection, similarly to what happens in data. This 6% correction in 8 TeV Monte Carlo was forgotten for the Moriond 2013 [127] results and before, causing a small $\sim 6\%$) mistake on the signal strength μ.

The yield evolution with the mass is estimated from a fit to the expected yields obtained from Monte Carlo samples produced in the range of interest with 5 GeV step. It is parametrized with a 3rd order polynomial for each process and category in order to be able to vary the mass with smaller binning:

$$N_{proc}^{cat} = a0_{proc}^{cat} + a1_{proc}^{cat} \times (m_H - 125) + a2_{proc}^{cat} \times (m_H - 125)^2 + a3_{proc}^{cat} \times (m_H - 125)^3 \tag{6.16}$$

An example of such a parametrization of the yield as a function of the Higgs mass is illustrated in Figure 6.31.
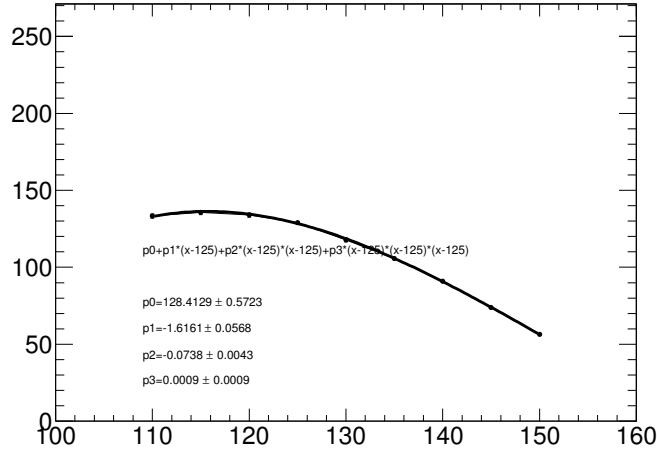
Figure 6.31: *Signal yield parametrization as a function of the Higgs mass (example of ggH in category central low p_{Tt} as defined in Section 7.3.7 [105].*

6.5.1.3 Shape

Each of the five production modes are shown to have similar shapes, and are hence grouped together in a global fit in order to increase the statistics and obtain a more robust result. The shape is modelled with a Crystal-Ball+Gaussian function and a combined fit including all processes is performed, for each category [169].

The Crystal-Ball shape is a Gaussian, with longer left tails modelled by an inverse power function:

$$CB(x) = N. \begin{cases} exp\left(-\frac{(x-\mu_{CB})^2}{2\sigma_{CB}^2}\right) & \text{if } x > \mu_{CB} - \alpha\sigma_{CB} \\ A.\left(B - \frac{(x-\mu_{CB})}{\sigma_{CB}}\right)^n & \text{if } x \le \mu_{CB} - \alpha\sigma_{CB} \end{cases} \tag{6.17}$$

where N is a normalization constant; A and B are determined in such a way that the function is continuous and depend only on the four CB parameters: μ_{CB}, σ_{CB}, α and n.

The chosen parametrization for the signal pdf is given in Equation 6.18. f_{CB} quantifies the fraction of Crystal-Ball.

$$f_S(m_{\gamma\gamma}) = f_{CB} \cdot F_{CB}(m_{\gamma\gamma}; \mu_{CB}, \sigma_{CB}, \alpha_{CB}) + (1 - f_{CB}) \cdot F_{Ga}(m_{\gamma\gamma}; \mu_{Ga}, \sigma_{GA}) \tag{6.18}$$

The CB parameters and the two Gauss parameters (the mean μ_{GA} and the width σ_{GA}) are parametrized as a function of the Higgs mass in the following way: (where m_H is expressed in GeV)

$$\begin{aligned} \mu_{CB}(m_H) &= \mu_{CB}(m_H = 125) + s_{\mu_{CB}}(m_H - 125) \\ \sigma_{CB}(m_H) &= \sigma_{CB}(m_H = 125) + s_{\sigma_{CB}}(m_H - 125) \\ \mu_{GA}(m_H) &= \mu_{GA}(m_H = 125) + s_{\mu_{GA}}(m_H - 125) \\ \sigma_{GA} &= \kappa.\sigma_{CB} \end{aligned} \tag{6.19}$$

To help the fit convergence, α is fixed to its fitted value at 125 GeV and n is fixed to 10 since it was shown to be the preferred value in most cases.

An illustration of the fit of all weighted processes at $m_H = 125$ GeV is shown in Figure 6.32.
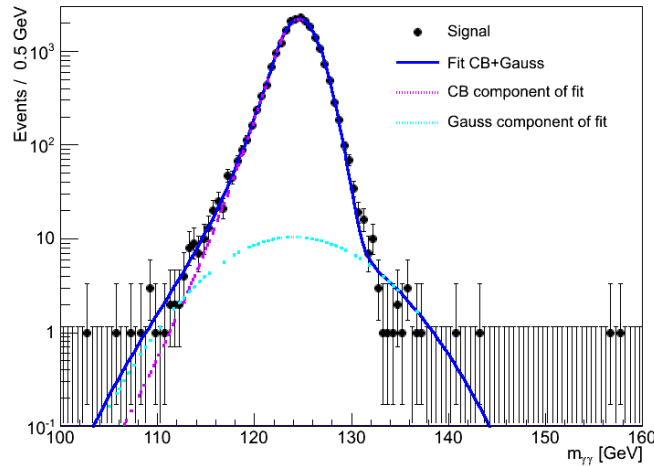
Figure 6.32: *Global fit of all signal processes (inclusive). The Gauss and Crystal-Ball components are shown with dashed lines. The selection is the one from the Moriond 2013 analysis.*

6.5.2 Background parametrization

The background subtraction in the fit does not come from simulation as is the case in most of the other similar analyses because the number of background events remaining after the selection is enough to apply a data-driven estimation of the contamination. The background is hence derived form a fit to the data. However, the parametrization has to be carefully chosen in order not to introduce a bias in the measured signal. This bias is estimated from high statistics Standard Model samples ($\gamma\gamma$, γj and jj). A signal+background fit is performed on this sample. The statistics is chosen to be sufficiently high in

order that the fitted signal is necessarily an artefact due to the background parametrization and not to the lack of statistics in the Monte Carlo.

The bias for a given parametrization is estimated by fitting the MC samples with a function combining the signal model from previous section and the tested background models (S+B fit), in the full mass range. A given parametrization is kept, if the number of signal events extracted from this fit, called the spurious signal N_{sp}, satisfies at least one of the two criteria:

- $N_{sp} < 10\% \, N_{S,exp}$

- $N_{sp} < 20\% \, \sigma_{bkg}$

where $N_{S,exp}$ is the expected number of signal passing the $H \rightarrow \gamma\gamma$ selection in the considered mass range ($[100; 160]$ GeV until the final Run I analysis where the lower bound was increased up to 105 GeV). σ_{bkg} is the statistical uncertainty on the number of background events, obtained from the $S + B$ fit of a pure background Asimov dataset.

An interpretation of the spurious signal is shown in Figure 6.33 showing the expected significance of the analysis as a function of the number of spurious signal events. The expected significance is computed with the full profile likelihood setup or using a simple formula in which the uncertainty on the background is written: $\sigma_B = \sqrt{B} \oplus n_{spurious} = \sqrt{(\sqrt{B})^2 + n_{spurious}^2}$, the significance hence becomes $Z = \frac{n_{signal}}{\sigma_B} = \frac{n_{signal}}{\sqrt{B+n_{spurious}^2}}$. The agreement between the approximated formula and the exact one is good enough, in the small spurious signal limit.
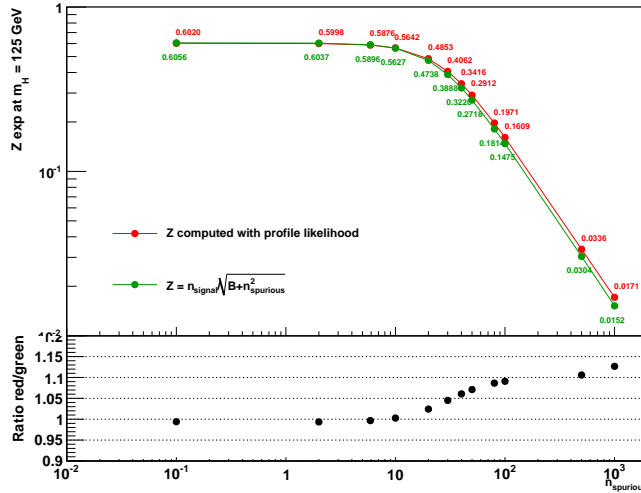
Figure 6.33: *An interpretation of spurious signal: expected significance computed with a profile likelihood compared to the significance obtained with the simple spurious signal interpretation, as a function of the number of spurious signal events.*

One can notice that, if $n_{spurious} \propto L \propto B$ (where L stands for the luminosity), then

$$\frac{n_{signal}}{\sqrt{B + n_{spurious}^2}} \xrightarrow[L \to \infty]{} \frac{n_{signal}}{n_{spurious}}$$

because the term $n_{spurious}^2 \propto L^2$ is dominant.

Consequently, $n_{signal}/n_{spurious}$ is the maximum significance one can obtain with the spurious term $n_{spurious}$.

6.5.3   Systematics uncertainties

Systematics are introduced into the model as multiplicative factors to the quantity which is uncertain generically labelled $\mathcal{P}$ in the following. It takes the form:

$$\mathcal{P} \to \mathcal{P} \times (1 + \delta\theta) \tag{6.20}$$

where δ is the value of the uncertainty determined from physical considerations and θ is the so-called nuisance parameter. Its initial value is 0, meaning that the value of the parameter $\mathcal{P}$ is strictly the one estimated from Monte Carlo studies. In order for the fit not to choose nuisance parameter values far from the one estimated by the experimentalists, these values are constrained by a Gaussian of width $\sigma_c = 1$.

In practice, systematics uncertainties are applied on the signal yield and signal shape parameters:

- Uncertainties due to the selection efficiency on the signal yield:

  - From theory: uncertainties on the inclusive cross-section and branching ratios;
  - From experiment: luminosity determination, trigger efficiency, photon identification and isolation.

- Uncertainties coming from the event categorization *i.e.* migrations of events between the categories. Since the categories are defined to have difference signal-to-noise ratio or different sensibility to a given production mode, migration of events between these categories changes the purity or the ratio S/B and have an impact on the measurement.

  - From theory: modelling of some discriminating variables such as the Higgs p_T can induce migrations among the categories whose definition uses the p_{Tt} (highly correlated to the Higgs transverse momentum).
  - From experiment: jets, E_T^{miss} and leptons energy scale and resolution.

- Uncertainties on the signal shape:

  - Peak position: the photon energy scale has an impact on the signal peak position, that is translated as an uncertainty on the mean of the Gauss and Crystal-Ball from the signal model;
  - Mass resolution: similarly the mass resolution is translated as an uncertainty on the Gauss and Crystal-Ball width.

The model in a given category can hence be written:

$$
\begin{aligned}
\mathcal{M}_{cat}(m_{\gamma\gamma}, \mu, \theta) =& \mu \times \sum_{proc} (N_{s,proc}^{cat}(\theta_{s,proc,yield})^{cat}) \times f_s^{cat}(m_{\gamma\gamma}, \theta_{s,shape}^{cat}) \\
&+ N_b^{cat} \times f_b^{cat}(m_{\gamma\gamma}, \theta_{b,shape}^{cat}) \\
&+ N_{spurious}^{cat} \times \theta_{spurious}^{cat} \times f_s^{cat}(m_{\gamma\gamma}, \theta_{s,shape}^{cat})
\end{aligned} \tag{6.21}
$$

μ is the parameter of interest quantifying the signal strength.

The signal f_S and background f_B probability density functions (pdf) are the one derived from studies detailed in the previous sections. The signal shape is fixed while the background shape and normalization are left free and adjusted on the observed data.

θ denotes the nuisance parameters, including the background shape and normalisation parameters and the systematics. Indeed, the model defined in Equation 6.21 is modified to add new parameters to account for the systematics uncertainties, allowing the expected signal to vary within limits dictated by the estimations of these parameters in previous subsections. They are divided into several contributions:

- $\theta_{s,proc,yield}$ are the nuisance parameters acting on the expected signal yield.

- $\theta_{s,shape}$ denotes the parameters acting on the signal shape, namely the peak position uncertainties and the mass resolution.

- $\theta_{b,shape}$ stands for the background parameters, adjusted on data (exponential slope and/or polynomial coefficients).

- $\theta_{spurious}^{cat}$ constrains the spurious signal in each category.

The constraints on the different nuisance parameters are also introduced in the final model. A Gaussian G_{np} of mean $\tilde{\theta} = 0$ and width $\sigma_c = 1$ is introduced once and only once for each of the nuisance parameter. The full model can be written:

$$\mathcal{M}(m_{\gamma\gamma}, \mu, \theta) = \prod_{cat} \mathcal{M}_{cat}(m_{\gamma\gamma}, \mu, \theta) \times \prod_{np} G_{np}(\tilde{\theta}_{np}, 1) \tag{6.22}$$

$\tilde{\theta}$ is called a global observable and is fixed to 0 in most of the cases, except when generating toy experiments.

6.6 Results and combination with other channels

Starting from the discovery in July 2012, whose main results are outlined below, the analysis of the $\gamma\gamma$ final state moved to a measurement era where Higgs mass, spin and couplings are tested. The first analysis of the full 2011+2012 dataset was shown at the Moriond 2013 conference and is summarized below. This analysis serves as a basis for the optimization that was done for the final analysis of Run I dataset, shown here [105].

On top of the results obtained from the diphoton channel only, this section also briefly describes the results of the combination with the other decay channels (mainly ZZ) within ATLAS. A brief comparison to the CMS results is also performed.

6.6.1 Discovery – July 2012

6.6.1.1 Diphoton channel

The discovery analysis [126] used a 10 category model made of the nine historical categories and completed by a VBF category tagging events with two jets produced in association with the Higgs. The final observed significance reaches 4.5σ for the combination of the full 2011 and 5.9 fb^{-1} of 2012 dataset, for the diphoton channel only (Fig. 6.34).

The measured signal strength, scale factor to the Standard Model signal, at a Higgs mass of 126.5 GeV was found to be:

$$\mu_{\gamma\gamma,ATLAS} = 1.8 \pm 0.5$$

A small excess of signal events with respect to the Standard Model expectations is found. However, it is not statistically significant and more data is needed to confirm this observation.

6.6.1.2 ATLAS combination

The combination of several Higgs decay channels studied by ATLAS was also performed at the same period. The statistical procedure is similar to the one used to combined several categories of a given channel, taking into account the correlations between the systematics sources. A brief description of the other channels entering this combination is given below.

(a) p_0 (b) Invariant mass distribution

Figure 6.34: *Discovery paper results from ATLAS for the $\gamma\gamma$ channel alone [126].*

- $H \to ZZ^* \to 4l$ channel: the $H \to ZZ$ channel has a large branching ratio on a large mass range ($m_H \in [110; 600]$ GeV), but it is balanced by the low branching fraction of the $Z \to l\bar{l}$ decay, where $l\bar{l}$ denotes either an electron or a muon pair. The analysis consists in selecting four leptons with decreasing p_T thresholds. Among those four reconstructed particles, the pair of opposite charge and same flavour leptons with the mass m_{12} closest to the Z mass is required to be consistent with a Z boson decay, *i.e.* $50 < m_{12} < 115$ GeV. The analysis is then divided into four independant channels, depending on the lepton flavours: $4e$, $2e2\mu$, $2\mu2e$ and 4μ. The background is estimated from a Monte Carlo for the $ZZ^{(*)}$ Standard Model background and uses control regions in data to arrive to an estimation of the $Z + jets$ and $t\bar{t}$ contamination. The results of this background estimation is displayed in Figure 6.35 as a function of the m_{4l} variable. It also illustrates the high signal to noise ratio of this channel.

Figure 6.35: *Invariant mass spectrum for the $H \to ZZ^* \to 4l$ channel in the low mass region. Backgrounds are shown in filled red and violet stacked histograms. The expected signal from Standard Model predictions is shown with the light blue filled area [126].*

- $H \to WW \to e\nu\mu\nu$ channel: it is characterized by the production of two isolated leptons with opposite charge. To further reduce the background, they are required to have opposite

flavour. Due to the presence of neutrinos, events with a low missing transverse energy are discarded. For this reason, the observable is not the WW invariant mass but the transverse invariant mass $m_T = \sqrt{(E_T^{ll} + E_T^{miss})^2 + |\mathbf{p}_T^{ll} + \mathbf{E}_T^{miss}|^2}$. The background decomposition depends on the number of jets in the event (Fig. 6.36(a)) and the inclusive dataset is hence divided into categories depending on the jets topology: 0 jet, 1 jet and ≥ 2 jets. The Standard Model WW and top background are estimated from Monte Carlo, but their normalization comes from data-driven analyses. Figure 6.36(b) shows the result of the background decomposition for the $0 + 1$ jet categories.

(a) Number of jets
(b) Transverse mass

Figure 6.36: *$4l$ invariant mass and WW transverse mass for the 0 and 1 jet channels [126].*

- $H \to \tau\tau$ and $H \to bb$ channels are also included even if not observing any signal at this time.

The result for the combination of these five channels is illustrated in Figure 6.37(a), where the contribution form each channel is decomposed. Figure 6.37(b) demonstrates that the large excess observed at $m_H \approx 125$ GeV is not reproduced at higher mass.

(a) Low mass region
(b) Whole mass range

Figure 6.37: *p_0 from the ATLAS discovery paper for the combination of $\gamma\gamma$, 4ℓ, WW, $\tau\tau$ and bb channels [126].*

When combined with the $H \to ZZ^* \to 4l$ and the WW decay channels, the significance of the excess observed around 125 GeV amounts to 6σ, meaning that the probability for the excess to be due to a statistical fluctuation of the background is below 10^{-9} (Fig. 6.37(b)). The measured signal strength, from a combination of all channels, was found to be:

$$\mu_{comb,ATLAS} = 1.4 \pm 0.3$$

in agreement with the Standard Model ($\mu = 1$) within the error bars.

An example of $H \rightarrow \gamma\gamma$ candidate event is illustrated in Figure 6.38.
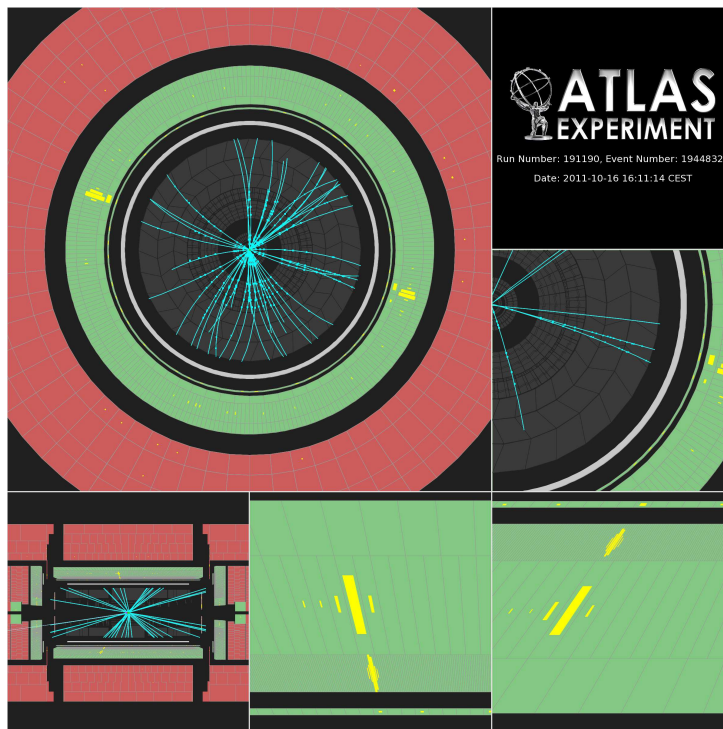
Figure 6.38: *Event display of a candidate diphoton event where the leading (subleading) photon candidate is unconverted (converted). The leading photon has $E_T = 66.8$ GeV and $\eta = -0.27$. The subleading photon has $E_T = 56.9$ GeV and $\eta = -0.67$. The measured diphoton mass is 125.8 GeV.* [170].

6.6.1.3 Results from CMS

This discovery is confirmed by the CMS experiment during a joint seminar with ATLAS on July 4th, 2012. Both the $H \rightarrow \gamma\gamma$ and combined results are in good agreement with the one observed by ATLAS. The CMS paper [171] details the results and the excess reaches a 5σ significance in favour of a signal, as illustrated in Figure 6.39.

The measured diphoton signal strength at a mass of 125.5 GeV is found to be:

$$\mu_{\gamma\gamma,CMS} = 1.6 \pm 0.4$$

and the CMS combination of all channels yields:

$$\mu_{comb,CMS} = 0.87 \pm 0.23$$

6.6.2 First analysis of the full Run I dataset (March 2013)

After this discovery, many efforts are carried out to measure the Higgs properties: its spin and parity state, expected to be $J^{PC} = 0^+$ in the Standard Model, its mass, not predicted by the standard theory, and its couplings to other Standard Model particles, that depend only on the boson mass.

We present here the main highlights of the Moriond 2013 analysis for the mass and coupling measurements [127], since this is the starting point for the optimization for the final Run I analysis. One should note that a small change was on the result came slightly after, for the publication of the
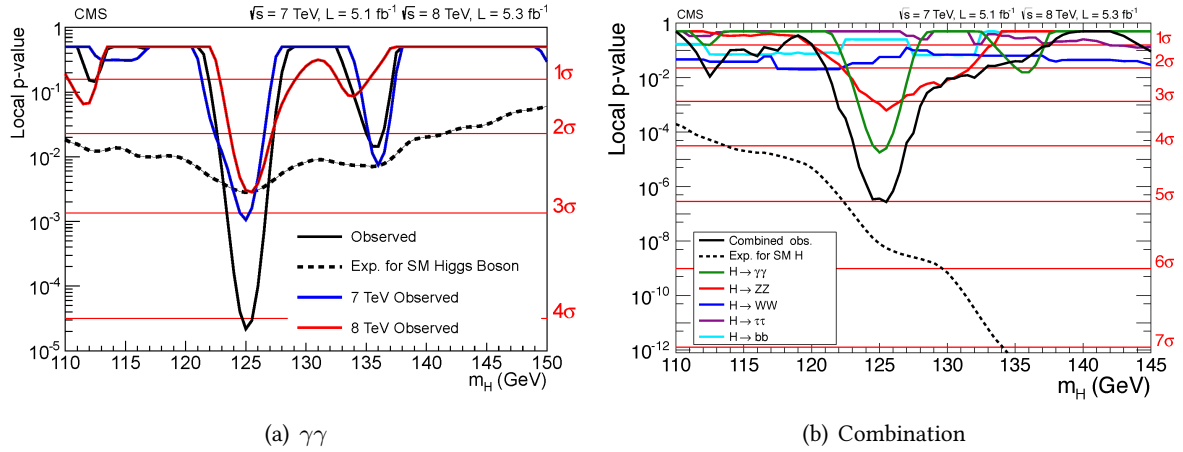
(a) $\gamma\gamma$

(b) Combination

Figure 6.39: *Discovery paper results from CMS [171].*

combined results [172], where the effect of the Dalitz events was corrected.An even minor change came later [173], due to a new measurement of the luminosity in 2012 (decreased from 20.7 to 20.3 fb^{-1}).

Both the mass and the couplings were measured using a 14-category model, starting from the historical nine category model and completed by five tagged categories:

- Two VBF categories, loose and tight. They are defined using a MutliVariate Analysis;

- One VH-hadronic category capturing the hadronic decay of the W and Z produced in association with the Higgs in the higgsstrahlung production;

- One VH-MET category cutting on the E_T^{miss} significance variable to select events with large genuine missing transverse energy, isolating $ZH \rightarrow \nu\nu H$ and $WH \rightarrow l\nu H$ processes;

- One VH-1lepton category requiring an additional electron or muon to separate the leptonic decay of the Z and W.

The full 2011+2012 dataset using this categorization allows to measure a 7σ significance for signal at around 126.5 GeV (Fig. 6.40).

(a) p_0

(b) Invariant mass distribution

Figure 6.40: *First analysis of the full 2011+2012 dataset from ATLAS in the $\gamma\gamma$ channel alone [127].*

6.6.2.1 Mass

The measured Higgs mass and the signal strength at the best mass fit value in the diphoton channel were found to be:

$$m_H = 126.8 \pm 0.2(\text{stat}) \pm 0.7(\text{syst})$$
$$\mu = 1.65 \pm 0.24(\text{stat}) \, ^{+0.25}_{-0.18}(\text{syst})$$

In the four-lepton channel, the mass was found to be lower and some tests and cross-checks were performed, but nothing worrying was observed. The statistical significance of the discrepancy was found to be 2.4σ [172, 174].

Figure 6.41: *Likelihood scan of the Higgs mass hypothesis [172, 175].*

6.6.2.2 Couplings

Thanks to the tagged categories, different couplings can be tested by separating the signal strength per production mode. Figure 6.42 illustrates the measured signal strength for the $ggH + ttH$, VBF and VH production modes.

The results of the combination of five channels in given in Figure 6.43. The larger tension with respect to the Standard Model is observed for the $\gamma\gamma$ channel but is not statistically significant and more data are needed to confirm/infirm this observation. When comparison the signal strength of the gg and qq initiated processes, observations are compatible with the Standard Model at a 2σ confidence level.

6.6.2.3 Spin and parity

The observation of a signal in the $\gamma\gamma$ channel forbids the observed resonance to have spin 1, according to the Landau-Yang theorem [177, 178]. The $\gamma\gamma$ channel is used to test the $J^P = 0^+$ hypothesis against $J^P = 2^+$. A $J^P = 2^+$ candidate is the graviton from extra-dimensions models for instance. The analysis is complicated by the fact that the two production modes for the 2^+ state (qq and gg) have very different distributions for the discriminating variables. Since the relative contribution is strongly dependent on the model, several combinations are tested.

Figure 6.42: *Production mode measurement in the diphoton channel for the Moriond 2013 conference [172].*

(a) Signal strength

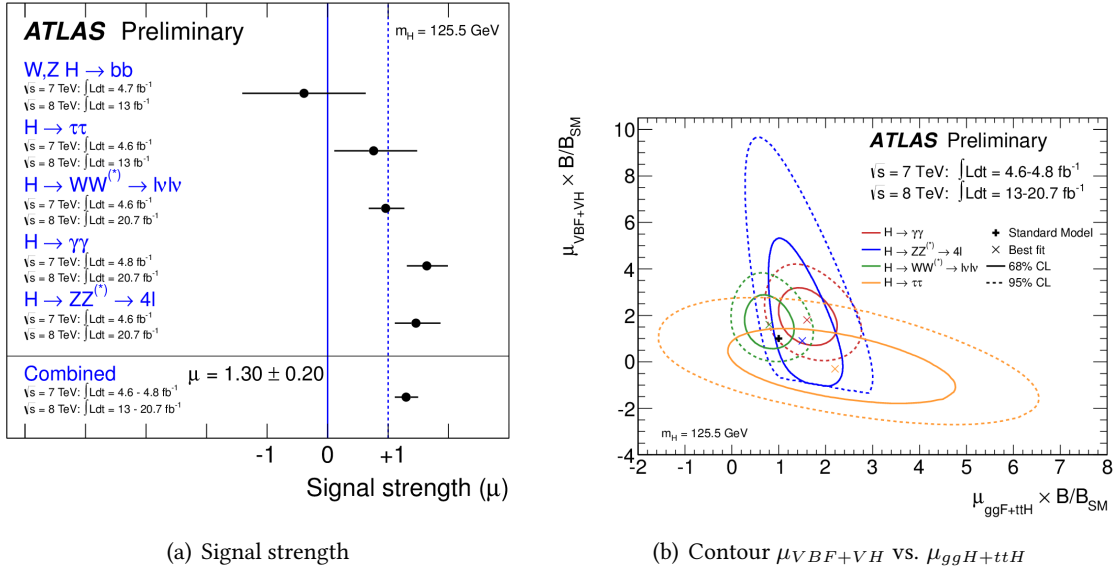(b) Contour μ_{VBF+VH} vs. $\mu_{ggH+ttH}$

**Figure 6.43:** *Couplings combination [176].*

On top of the $m_{\gamma\gamma}$ diphoton invariant mass helping to distinguish between signal and background, another discriminating variable is introduced to disentangle the spin-0 and spin-2 hypotheses. The θ^* in the Collins-Soper frame [109] is illustrated in Figure 6.44 and can be expressed as a function of the two photons kinematic variables:

$$\cos(\theta^*) = \frac{(E_1 + p_{z,1})(E_2 - p_{z,2}) - (E_1 - p_{z,1})(E_2 + p_{z,2})}{m_{\gamma\gamma} \cdot \sqrt{m_{\gamma\gamma}^2 + p_T^2}} \tag{6.23}$$

where $m_{\gamma\gamma}$ and p_T are the diphoton mass and transverse momentum and $E_i, p_{z,i}$ are the photon energies and longitudinal momenta.

The distribution of the $|\cos(\theta^*)|$ variable for a spin-0 particle, without kinematics cuts, is flat, as Figure 6.45 shows. When introducing acceptance and p_T cuts on the final photons, this distribution gets distorted.

The distribution obtained form 2012 dataset is illustrated in Figure 6.46(a) for each of the 10 $|\cos(\theta^*)|$ categories from the published spin analysis [180], following preliminary notes [123, 181, 182].
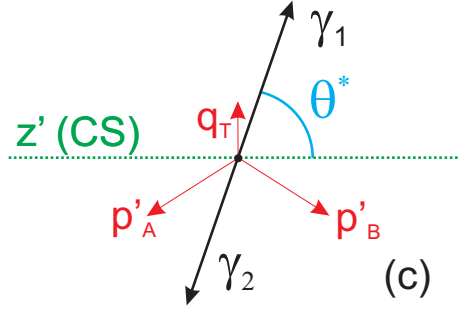
Figure 6.44: *Illustration of the sensitive angular variable in the resonance's rest frame, θ^*. It is calculated with respect to the z-axis in the Collins-Soper (CS) frame: p'_A is the momentum of the beam, and p'_B is the target momentum in the CS system, and then the z-axis of the CS coordinate system bisects the angle between p'_A and $-p'_B$, q_T is the unit vector of the direction opposite of $(p'_A + p'_B)_T$ [179].*
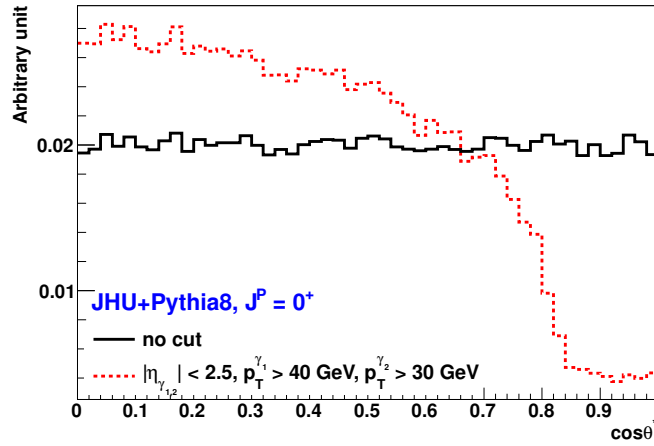
Figure 6.45: *The distribution of $|\cos(\theta^*)|$ for a scalar, without (black line) and with (red line) pT cuts on the photons. The kinematic cuts distort the flat shape [179].*

The test statistics chosen for the spin analysis differs from the usual LHC one (the profile likelihood ratio). Indeed, using the same test statistics requires to define a continuous parameter α characterizing the fraction of spin 0. Since the observed resonance is very unlikely to be a mixture of two spin states, the Tevatron-style test statistics is used instead:

$$q = log \frac{\mathcal{L}(J^P = 0^+, \hat{\hat{\mu}}_{0+}, \hat{\hat{\theta}}_{0+})}{\mathcal{L}(J^P = 2^+, \hat{\hat{\mu}}_{2+}, \hat{\hat{\theta}}_{2+})} \tag{6.24}$$

Figure 6.46(b) shows the distributions of this test statistics under the $J^P = 0^+$ and $J^P = 2^+$ (gg produced only) hypotheses.

When combined with the $H \to ZZ^* \to 4l$ and $H \to WW \to l\nu l\nu$ channel, several J^P hypotheses can be excluded [180]:

- $J^P = 0^-$: excluded at 97.8% CL.

- $J^P = 1^+$: excluded at 99.97% CL.

- $J^P = 1^-$: excluded at 99.7% CL.

- $J^P = 2^+$: excluded at 99.9% CL for all fractions of qq production with respect to gg.

(a) $|\cos(\theta^*)|$ in data

(b) Test statistics

Figure 6.46: *Main results from the $\gamma\gamma$ channel [180].*

6.6.3 Final Run I analysis

The final analysis of Run I data (2011+2012) is the first one to use the new calibration procedure and systematics for the photon energy scale described in Ref. [91].

Different categorizations are defined for the mass and couplings measurements. This is motivated by the will to distinguish each of the five Higgs production modes for the couplings analysis, keeping a reasonable number of categories for each analysis.

6.6.3.1 Mass

The mass categorization was carefully studied and the final choice, very close to the historical nine-category model, is made of ten categories depending on the photon pseudo-rapidity and conversion status of the photons and diphoton p_{Tt}. The two central categories contain events with both photons within $|\eta| < 0.75$. The transition categories are characterized by at least one photon close to the calorimeter crack ($1.3 < |\eta| < 1.75$). The rest categories contain the remaining events. Each of these three categories is split into converted (at least one photon is converted) and unconverted (both photons are unconverted) categories. The central and rest categories are then split into a low ($p_{Tt} < 70$ GeV) and high ($p_{Tt} > 70$ GeV) p_{Tt} categories.

Systematics uncertainties coming from the photon energy scale are evaluated and propagated in each category and amounts for an uncertainty up to 0.7% for the category with larger systematics uncertainties.

The final mass measurement in the diphoton channel using the mass categorization is:

$$m_H = 125.98 \pm 0.50 = 125.98 \pm 0.42(stat) \ \pm 0.28(syst) \text{ GeV}$$

Using the $H \to ZZ^* \to 4l$ information, the ATLAS combined mass becomes:

$$m_H = 125.36 \pm 0.37(stat) \ \pm 0.18(syst) \text{ GeV}$$

The difference between the $\gamma\gamma$ and $4l$ masses is illustrated in Figure 6.47. The discrepancy is estimated using the test statistics:

$$q(\Delta) = -2ln \left(\frac{\mathcal{L}_{\gamma\gamma}(\Delta, \hat{\hat{m}}_H, \hat{\hat{\theta}})}{\mathcal{L}_{\gamma\gamma}(\hat{\Delta}, \hat{m}_H, \hat{\theta})} \times \frac{\mathcal{L}_{4l}(\hat{m}_H, \hat{\hat{\theta}})}{\mathcal{L}_{4l}(\hat{m}_H, \hat{\theta})} \right) \tag{6.25}$$

where $\Delta = m_H^{\gamma\gamma} - m_H^{4l}$. The result of the fit is $\Delta = 1.47 \pm 0.72$ GeV, which corresponds to a 1.98σ deviation from the $\Delta = 0$ hypothesis, in the asymptotic approximation. This result is cross-checked with toy experiments and the significance of the difference is stable (1.97σ).
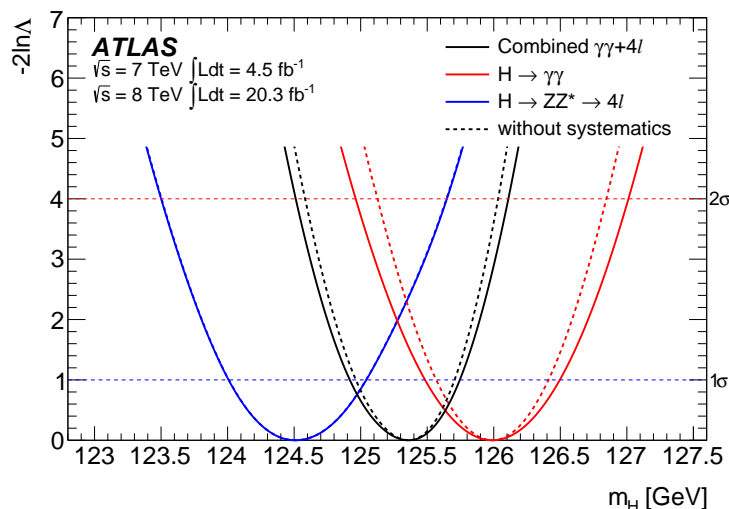

Figure 6.47: *Likelihood scan of the Higgs mass hypothesis [183].*

6.6.3.2 Couplings

The couplings analysis defines twelve categories: height tagged categories enriched in a given Higgs production mode, and four tagged categories. Their definition and the results of the analysis are detailed in the next chapter, together with the comparison to the mass analysis.

Conclusion

The $\gamma\gamma$ channel was an important channel for the Higgs boson discovery. Since then, analysis techniques have been improved to become more pile-up robust and improve the sensitivity to the different Higgs production modes. The categorization has also been adapted to fulfil the new analysis targets *i.e.* measurement of spin, mass and couplings. The first analysis of the 2011+2012 dataset allow to test the properties of this boson, without significant deviations from the Standard Model.

Next chapter details the couplings analysis strategy, optimization with respect to the one outlined here. The systematics uncertainties determination and the final results derived form the final analysis of the Run I dataset will also be discussed.

7

COUPLINGS MEASUREMENT

Chapter content

The analysis presented here is the final Run I data analysis which is described in details in the ATLAS internal note [105]. The full 2011 and 2012 datasets are used. The inclusive $\gamma\gamma$ selection was detailed in previous chapter.

The different categories are presented. Since they were added at different stage of the analysis, their optimization was not always done with the same dataset and setup. When possible, the plots presented in this chapter are updated with the full statistics, unless otherwise specified.

Unless otherwise specified, results are presented at the ATLAS combined mass of $m_H = 125.4$ GeV.

7.1 Analysis principle

7.1.1 General concepts

The couplings analysis relies on the strategy described in Ref. [134]. It is based on the assumption that the discovered resonance corresponds to as single particle state, similar to the Standard Model scalar Higgs boson.

The observed event rate in the $H \to ff$ final state, produced through the $ii \to H$ production mode is given by:

$$(\sigma \cdot \mathcal{B}r)(ii \to H \to ff) = \sigma_{ii \to H}\frac{\Gamma_{H \to ff}}{\Gamma_H} \tag{7.1}$$

where $\sigma_{ii \to H}$ is the production cross-section, $\Gamma_{H \to ff}$ is the Higgs width in the ff final state and Γ_H is the total Higgs width.

Any deviation of either of these quantities from the Standard Model is quantified by the coupling scale factors κ defined by:

$$\frac{\sigma_i}{\sigma_i^{SM}} = \kappa_i^2; \quad \frac{\Gamma_f}{\Gamma_f^{SM}} = \kappa_f^2 \tag{7.2}$$

Some assumptions need to be done to allow this parametrization. First, the observed signal is supposed to come from a single particle, whose couplings follow the same tensor structure than the Standard Model Higgs boson, especially it has to be a CP-even state ($J^P = 0^+$). It is also assumed this particle has a small width, approximated to zero on the whole mass range of interest for this analysis *i.e.* close to 125 GeV.

For example, the $gg \to H \to \gamma\gamma$ process is parametrized by:

$$(\sigma \cdot \mathcal{B}r)(gg \to H \to \gamma\gamma) = (\sigma \cdot \mathcal{B}r)_{SM}(gg \to H \to \gamma\gamma)\frac{\kappa_g^2 \kappa_\gamma^2}{\kappa_H^2} \tag{7.3}$$

where κ_H is defined as the ratio of the observed and expected total Higgs width.

Experimentally, the aim is then, for each decay channel, to try and disentangle each of the production modes to measure separately each

$$\mu_{ii \to H \to ff} = \frac{(\sigma \cdot \mathcal{B}r)}{(\sigma \cdot \mathcal{B}r)_{SM}}(ii \to H \to ff) \tag{7.4}$$

In Equation 7.3, the effective couplings to gluon (κ_g) and photons (κ_γ) were used. They can be expressed as a function of the true couplings, involving quarks and weak gauge boson in the loops. For example, the ggH production mode has both t and b quarks in the loop, the VBF production mode implies both couplings to W and Z bosons (Fig. 1.10) while the $\gamma\gamma$ decay channel mixes W and t couplings (Fig. 1.9).

Several simplified models can be used, for example using the same scale factor for all bosons $\kappa_V = \kappa_W = \kappa_Z$ and another scale factor for fermions $\kappa_F = \kappa_t = \kappa_b = \kappa_\tau = ...$ In this case, only the relative sign between κ_V and κ_F is physical. The interference between the top and W loops in the $\gamma\gamma$ decay channel can give some sensitivity on it.

This approach is applicable only to large deviations from the Standard Model and is sufficient for the level of precision expected from the first LHC data. For the next runs, it will have to be replaced by a more accurate method that will be discussed later on.

7.1.2   Applications in the $\gamma\gamma$ channel analysis

At the individual decay channel level, the aim is to test each of the production modes and measure $\mu_{ii\to H\to ff}$. For the diphoton channel, this notation is simplified into $\mu_{prod} = \frac{\sigma_{prod}}{\sigma_{prod}^{SM}}$ where only the information about the production mode is kept and the $\gamma\gamma$ decay is implicit.

The inclusive dataset is then classified into different categories, depending on the objects reconstructed in association with the diphoton pair and characteristic of a given production mode. This is summarized in Table 7.1.

#	Name	Tagged process
12	ttH leptonic	$t(\to Wb \to l\nu b)tH$
11	ttH hadronic	$t(\to Wb \to jjb)t(\to Wb \to jjb)H$
10	VH dilepton	$Z(\to ll)H$
9	VH one lepton	$W(\to l\nu)H$
8	VH E_T^{miss}	$Z(\to \nu\nu)H$
7	VH hadronic	$V(\to jj)H$
6	VBF loose	VBF
5	VBF tight	VBF
1-4	Untagged	$gg \to H$

Table 7.1: *Summary of the final categorization for the couplings measurement. V stands for both the W and Z bosons. The selection ordering follows the reverse category number: from category 12 down to 1.*

Events are classified according to Table 7.1. The selection order is illustrated in Figure 7.1.

In the following, the selection for the different categories introduced for the diphoton decay channel coupling analysis is discussed, starting from the definition of jets, leptons and E_T^{miss} objects used in the analysis.

7.2   Object definitions

The diphoton pair is selected from the algorithm presented in Chapter 6.

Jets and leptons are defined with the following cuts, based on performances groups recommendations and the will to keep as much statistics as possible in the tagged categories where the expected number of events can be quite low.

In the ATLAS reconstruction algorithm, some calorimeter clusters can be associated to different kind of particles. Not to consider the same energy deposit as being both a photon and an electron or a jet, an overlap removal procedure is applied. The highest priority is given to photons that are the first to be selected. Once the two leading photons are identified, the electron selection is addressed and electrons are required not to be close to photons. The next step is to consider the selected jets, are ignore jets close to either of the selected photons or to the good electrons. Finally, muons are selected such that they do not overlap with photons or jets.

7.2.1   Electrons

Electrons are reconstructed from electromagnetic clusters matched to an Inner Detector track. In 2012, the track momentum is corrected using a Gauss-Sum Filter (GSF) that better takes into account the bremsstrahlung energy losses [184]. The electron energy is computed from the cluster energy and track direction from the interaction point: $p_T = E^{cluster} \times cosh(\eta_{trk})$. This momentum is required
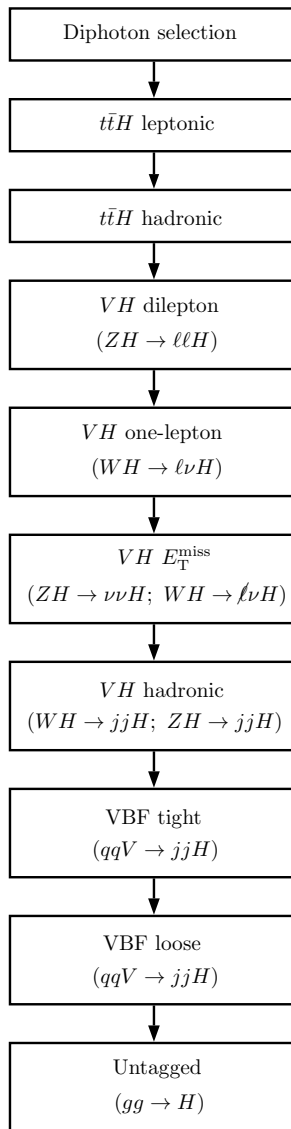
Figure 7.1: *Flowchart illustrating the 12 couplings categories and the order of the selection [125].*

to be greater than 15 GeV. Energy corrections are applied to both data and Monte Carlo: the data is calibrated based on the $Z \to e^+e^-$ peak position, while the Monte Carlo is smeared to match the observed m_{ee} resolution of the same peak.

Identification quality and isolation criteria are imposed. For 2012, the quality is defined with a likelihood approach and the Loose working point is chosen for this analysis, after having checked that it does not have a major impact on the results. For 2011 data, the medium++ cut-based working point is used. The isolation criteria depends on the particle energy and is defined as: $\sum_{topocluster \in \Delta R=0.4} E_T^{cluster} < 0.2 \cdot E_T^e$ and $\sum_{trk \in \Delta R=0.2} p_T^{trk} < 0.15 \cdot p_T^e$.

Electrons whose cluster lies within $\Delta R = 0.4$ of either of the selected photons are vetoed.

The electron identification efficiency is measured using tag-and-probe methods with events from leptonic decay of W or Z bosons or J/Ψ mesons. Precise descriptions can be found in [185, 186]. Corrections are derived from this method and applied to Monte Carlo in order that the selection efficiency is the same than the one measured in data.

7.2.2 Jets

Jets are defined by the anti-k_T algorithm with distance parameter $R = 0.4$ calibrated at EM scale. In order to further reduce the fake jets rate, a cut on the jet vertex fraction (Sec. 4.5.4) is applied for jets within the Inner Detector acceptance ($|\eta| < 2.4$): the fraction of the momentum from tracks associated to the jet and coming from the primary vertex should be greater than 0.5 for the 7 TeV data. Due to the increasing pile-up during the 8 TeV data-taking period, the minimum JVF threshold was reduced to 0.25. Additionally, the total jet momentum should pass some threshold, depending on the jet pseudorapidity: central jets ($|\eta| < 2.5$) should have $p_T^{jet} > 25$ GeV while more forward jets ($2.5 < |\eta| < 4.5$, region with high pileup jets occupancy) are required to have $p_T^{jet} > 30$ GeV. Jets with $|\eta| > 4.5$ are discarded due to the calorimeters coverage. Finally, the reconstructed jet too close to one of the two leading photons ($\Delta R = 0.4$) or one of the good electrons ($\Delta R = 0.2$) are vetoed.

7.2.3 Muons

Muons are reconstructed with the combined or segment-tagged muon algorithms within $|\eta| < 2.7$. They are required to have $p_T > 10$ GeV after Monte Carlo smearing. Additional quality requirement on the muon track with respect to the primary vertex and number of hits in the Inner Detector are applied. The isolation criteria is similar to the one applied on electrons: $\sum_{trk \in \Delta R = 0.2} p_T^{trk} < 0.15 \cdot p_T^\mu$ and $\sum_{topocluster \in \Delta R = 0.4} E_T^{cluster} < 0.2 \cdot p_T^\mu$. Finally, the reconstructed muon too close to one of the two leading photons ($\Delta R = 0.4$) or one of the good jets ($\Delta R = 0.4$) are vetoed.

7.2.4 E_T^{miss} and E_T^{miss} significance

The E_T^{miss} used in the diphoton analysis is derived from the RefFinal variable, using the best available calibration for each object:

$$E_{x(y)}^{\text{miss, RefFinal}} = -\left(\sum E_{x(y)}^\gamma + \sum E_{x(y)}^e + \sum E_{x\ (y)}^\tau + \sum E_{x(y)}^\mu + \sum E_{x(y)}^{\text{jets}} + \sum E_{x(y)}^{\text{soft jets}} + \sum E_{x(y)}^{\text{cell out}} \right) \tag{7.5}$$

Some modifications to the RefFinal algorithm are applied to adapt it to the analysis. First, in the selection priority is given to photons. As was described in the overlap removal procedure, it happens that a photon is also reconstructed as a jet or an electron. This is taken into account in the RefFinal algorithm where each object enters into the computation only once, starting from electrons followed by photons. For the $\gamma\gamma$ analysis, this selection is reversed to be sure that all photons are calibrated with their best available calibration. Contrarily to what is done in the official algorithm, the objects identification requirements were added to match the ones used in the analysis.

E_T^{miss} is a variable highly sensitive to pile-up. To further reduce this sensitivity, another discriminating variable can be used, the E_T^{miss} significance, denoted MET_{sig} in the following. It is defined by Equation 7.6 where $\sigma(E_T^{miss})$ denotes the E_T^{miss} resolution. Its square is proportional to the scalar sum of the measured momenta of the various objects in the event $\sigma(E_T^{miss}) \propto \sqrt{\sum E_T}$ [78, 187, 188].

$$MET_{sig} = \frac{E_T^{miss}}{\sigma(E_T^{miss})} \tag{7.6}$$

Figure 7.2 illustrates the discriminating power of the MET_{sig} variable.
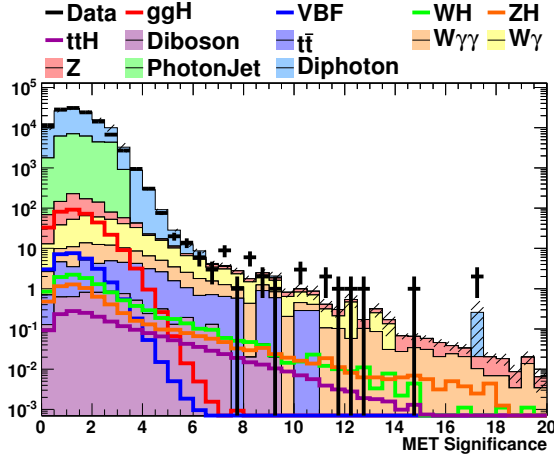
Figure 7.2: *E_T^{miss} significance distributions after diphoton selection for the different Higgs production modes and the full 2012 dataset (well reproduced by a Monte Carlo background estimation)* [188].

7.3 Category definition

More details about the category definition are given in the following subsections, trying to emphasize:

1. The targeted signal and the main expected background. Most of the categories are dominated by QCD background (untagged and 2-jets categories).

2. The variables used to discriminate between signal and background.

3. The strategy for the cuts optimization. Usually, the optimization is made trying to maximize the sensitivity (using extended significance formula [189]) and purity of the targeted production mode (N_0^{sig}):

$$\text{Significance} = \sqrt{2 \times \left(\sum_i N_i^{sig} + N_{bkg}\right) \times ln\left(1 + \frac{N_0^{sig}}{\sum_{i \neq 0} N_i^{sig} + N_{bkg}}\right) - N_0^{sig}} \qquad (7.7)$$

$$\text{Purity} = \frac{N_0^{sig}}{\sum_i N_i^{sig}} \qquad (7.8)$$

7.3.1 VBF

VBF categories are included since the discovery analysis. First using a single category defined with cut-based approach, it is now separated into a loose and a tight category based on a Boosted Decision Tree (BDT) output.

They aim at isolating the signal events produced *via* the VBF process. It is characterized by two forward jets with high invariant mass.

The selection then starts from the selection of two jets. Then, several discriminating variables are combined into a BDT to discriminate between the non-resonant background and reduce the contamination from other Higgs processes. These discriminating variables are listed below and illustrated in Figure 7.3 for the VBF signal, ggH process and non-resonant background.

- m_{jj} is the invariant mass of the leading two jets;

- $\Delta\eta_{jj}$ is the pseudorapidity separation between the leading two jets;

- $\Delta\phi_{\gamma\gamma,jj}$ is the azimuthal angle between the diphoton and dijet systems;

- $\Delta R_{\gamma,j}^{min}$ represents the minimum ΔR between leading/subleading photon and the leading/subleading jet;

- η^* is the Zeppenfeld variable [190] defined by $\eta_{\gamma\gamma} - \frac{\eta_{j1}+\eta_{j2}}{2}$;

- Finally, the diphoton p_{Tt} is also used as a discriminating variable.

(a) m_{jj}

(b) $\Delta\eta_{jj}$

(c) $\Delta\phi_{\gamma\gamma,jj}$

(d) $\Delta R_{\gamma,j}^{min}$

(e) η^*

(f) p_{Tt}
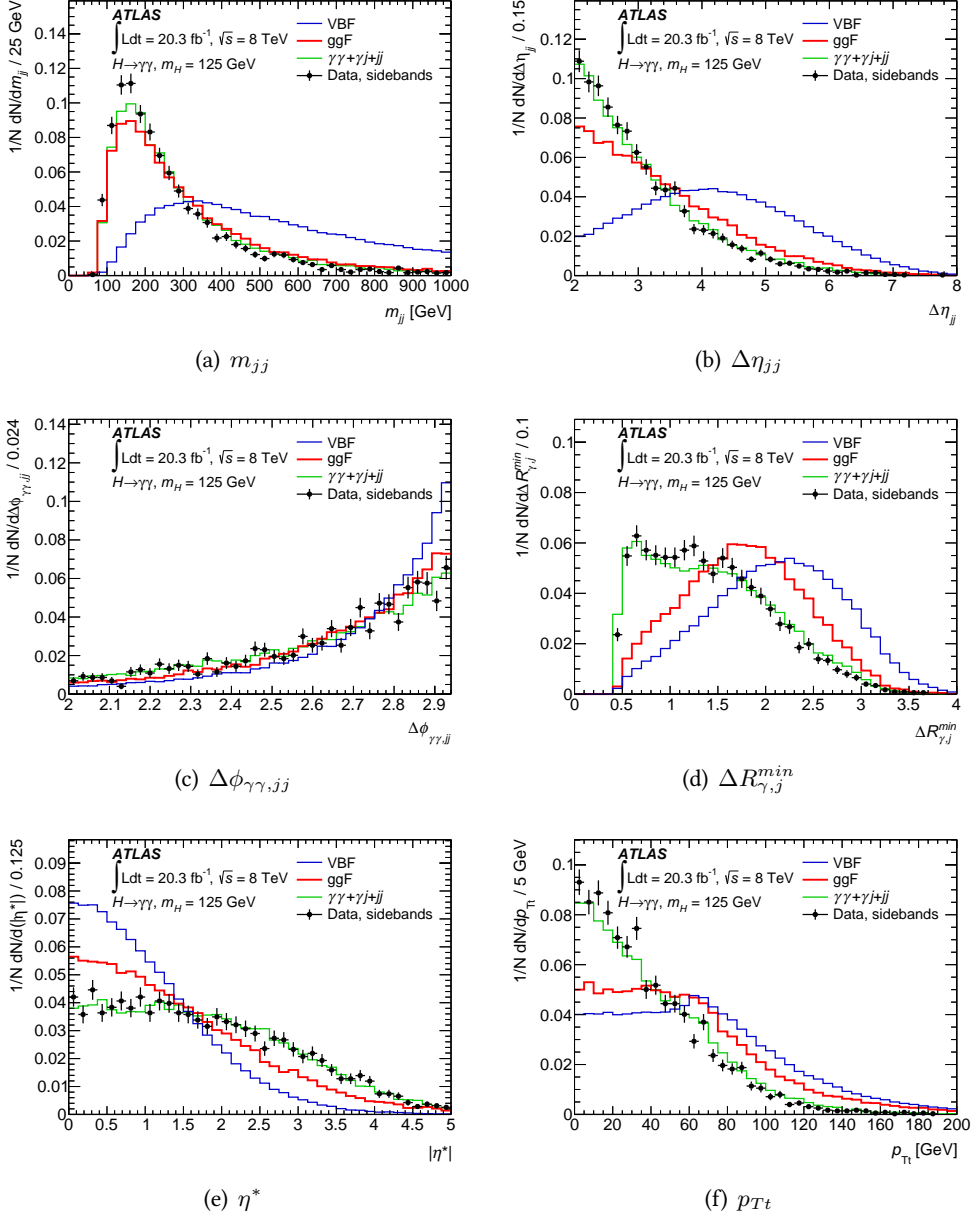
Figure 7.3: *Distributions of the six variables entering the BDT for the signal (VBF), resonant background (ggH) and non-background (from data sidebands), after diphoton and 2-jet selection [125].*

The BDT is trained with signal and background samples. The BDT output O_{BDT} after training is illustrated in Figure 7.4.
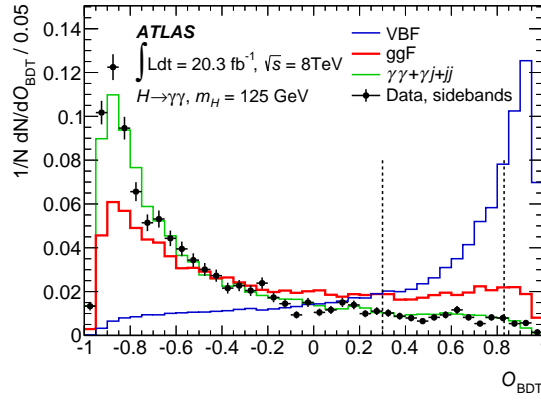
Figure 7.4: *BDT response for the VBF signal (red), ggH background (blue) and non-resonant QCD background (green). The two red lines indicate the BDT cuts that select loose and tight VBF categories [125].*

The cuts are applied on the BDT output. They are optimize on a VBF-significance basis, first choosing the lower limit for the tight category definition, in order to select events with $O_{BDT} > x_{tight}$. Figure 7.5(a) shows the evolution of the VBF significance as a function of x using the tight category only. The better expected results are achieved for $x = 0.83$. Once x is fixed, one can search for the best lower limit on the loose category $x' < O_{BDT} < x$. The significance of the loose category as a function of x' is illustrated in Figure 7.5(b) and is found to be optimal for $x' = 0.3$.
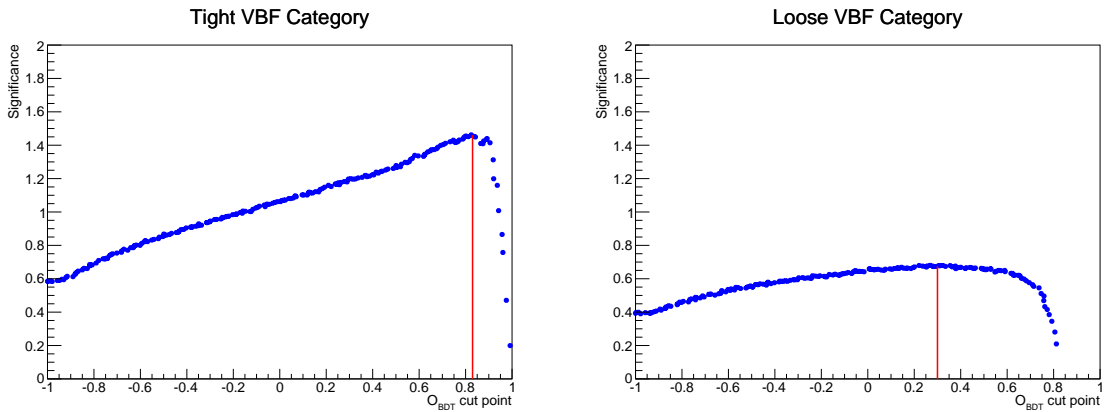
Figure 7.5: *Expected VBF significance in the tight and loose VBF categories as a function of the cut on the BDT output [105].*

7.3.2 VH-hadronic

The VH categories aim at selecting Higgs signal events produced *via* the Higgstrahlung process. They represent only about 5% of the expected events, so one expects low statistics categories.

The VH hadronic category tags the hadronic decay of W and Z. Similarly to the VBF categories, it is dominated by QCD background. Several discriminating variables are introduced to reduce this background:

- m_{jj} is the invariant mass of the leading two jets;

- $|\eta_{\gamma\gamma} - \eta_{jj}|$ is the pseudorapidity separation between the diphoton and the dijet systems;

- H_T is defined to be the scalar sum of the transverse momenta of the two leading photons and jets: $H_T = E_T^{\gamma 1} + E_T^{\gamma 2} + p_T^{j1} + p_T^{j}$;

- p_{Tt} of the diphoton system.

All of these variables are illustrated in Figure 7.6 for the VH signal, the resonant background made of signal events coming form other Higgs production modes and the non-resonant (QCD) background estimated from side-bands data or smeared Monte Carlo samples.

(a) m_{jj}

(b) $|\eta_{\gamma\gamma} - \eta_{jj}|$

(c) p_{Tt}
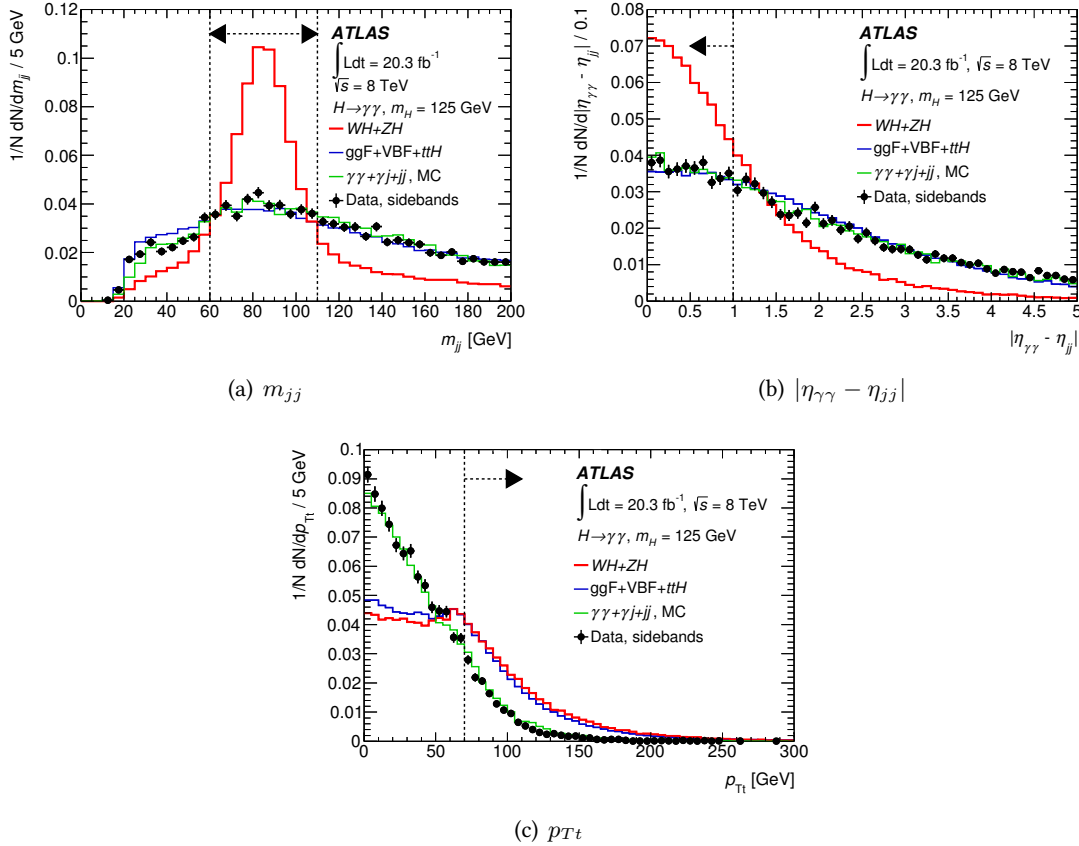
Figure 7.6: *Shape comparison of inputs variables for the VH categories for different Higgs production modes and side-bands data [125].*

The cut optimization was performed in a systematic way, moving the cuts on each of the five variables step by step. The best configuration leads to a 16% improvement on the expected significance, supposing all uncertainties will not change. However, this implies a cut on H_T that suffers from large theoretical uncertainties. For this reason, the final set of cuts does not use the H_T variable and is defined as:

- At least two jets;

- $60 < m_{jj} < 110$ GeV

- $p_{Tt} > 70$ GeV

- $|\eta_{\gamma\gamma} - \eta_{jj}| < 1$

As illustrated in Figure 7.7, the jet resolution does not allow to disentangle the $W \to jj$ process from $Z \to jj$ with the m_{jj} distribution.
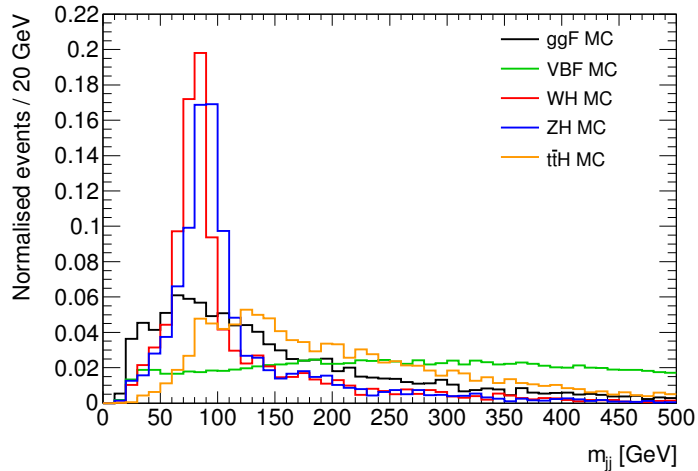

Figure 7.7: *m_{jj} distribution for different Higgs production modes for events with at least two reconstructed jets [191].*
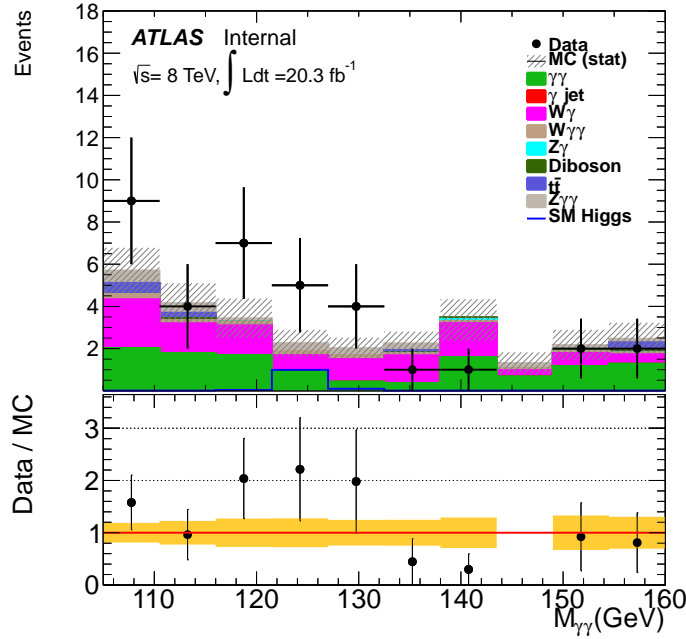
7.3.3 E_T^{miss} category

With the VH E_T^{miss} category, the analysis tries to isolate the decays of W and Z bosons implying neutrinos. The background is composed of Standard Model processes involving $Z/W + n\gamma$ but also $\gamma\gamma$ and γj events creating fake missing transverse energy.

As shown in Figure 7.2, the E_T^{miss} significance variable has a very high discriminating power and is the most important one in the definition of this category. It was shown that introducing an additional cut on the diphoton p_{Tt} can enhance the sensitivity of this category. The optimization of both cuts is shown in Figure 7.8. The MET_{sig} cut at 5 is chosen to maximize the sensitivity to the VH process. The optimal p_{Tt} cut is found to be close to 50 GeV, but the statistics of this category is drastically reduced. In order to keep enough events to estimate the background from a fit, conserving a high VH purity, the p_{Tt} requirement is relaxed to 20 GeV.

(a) MET_{sig}

(b) p_{Tt} with $MET_{sig} > 5$
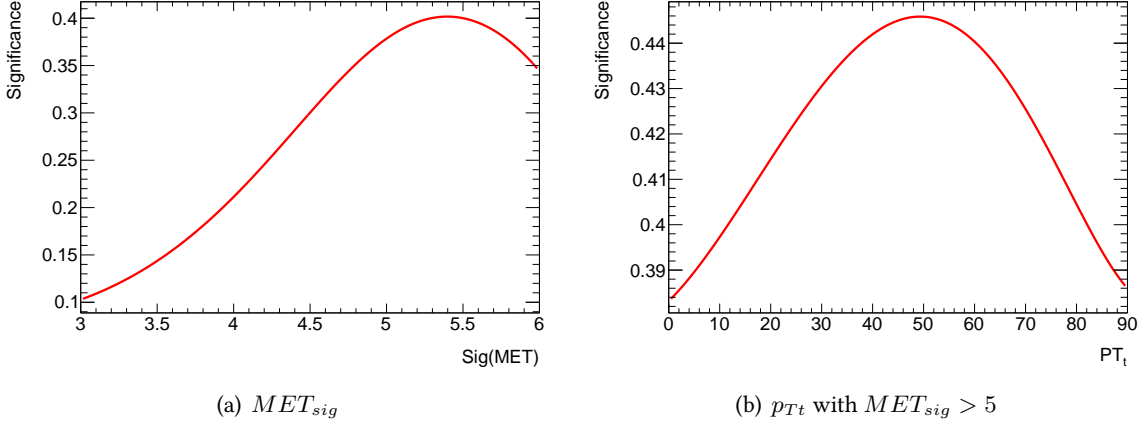
Figure 7.8: *The evaluated significance dependence on the E_T^{miss} significance cut and p_{Tt} variable in the VH E_T^{miss} category [105].*

Figure 7.9: *Background composition in the VH E_T^{miss} category from Monte Carlo [105].*

7.3.4 VH one lepton

The VH one lepton category is aimed at selecting exclusively the $WH \rightarrow l\nu H$ process, especially after the introduction of the VH dilepton category tagging $ZH \rightarrow llH$ events.

This channel suffers from backgrounds coming from $Z + \gamma$ Standard Model processes. To get rid of this background, where an electron would be misidentified as a photon, the invariant mass between the leading electron and each of the photons is computed. It either of these two mass is compatible with a Z boson, a veto is applied on the event (that remains in the inclusive selection though). The invariant mass between the leading electron and the leading and subleading photons are illustrated in Figure 7.10(a) and 7.10(b) respectively.

In addition, it was shown that the background rejection is increased if photons passing the electrons loose likelihood identification criteria are vetoed as well.

For the final analysis of Run I dataset, one of the analysis goal is to disentangle WH production

(a) Leading photon

(b) Subleading photon
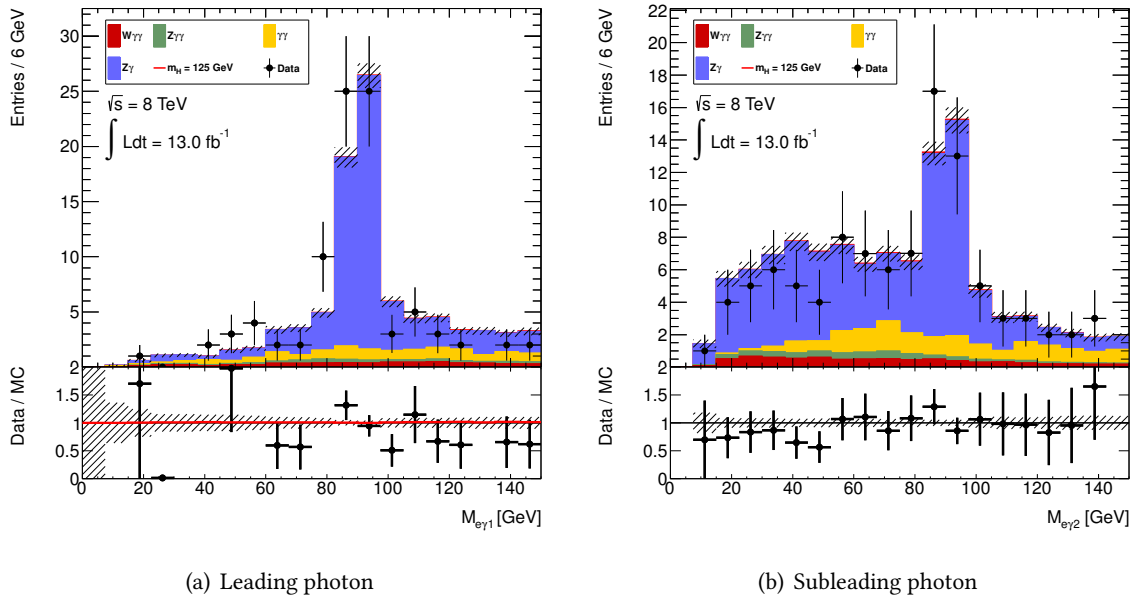
Figure 7.10: *Electron-photon invariant mass distribution for the leading and subleading photon for events having at least one lepton for background Monte Carlo samples and data [188].*

from ZH. To achieve this goal, an additional cut on MET_{sig} was introduced in this category. Its value is optimized on a WH significance basis and illustrated in Figure 7.11. The chosen requirement is $MET_{sig} > 1.5$.
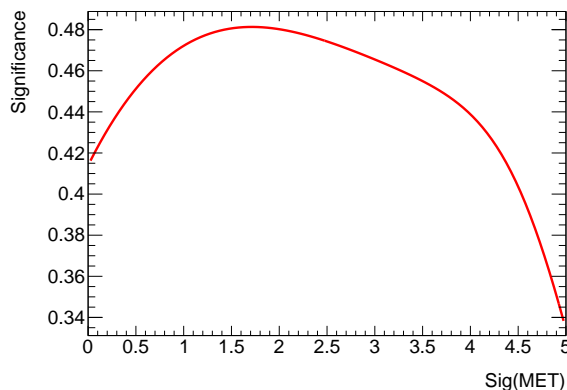
Figure 7.11: *The evaluated significance dependence on the MET significance cut in the one lepton category [105].*

Since the new analysis includes three categories before the one lepton selection (Tab. 7.1), two of them requiring leptons, their impact on the selection is tested. Starting from the 14 categories defined for the Moriond 2013 analysis (see § 6.6.2), the ttH and dilepton categories are successively included. As can be seen from Figure 7.12(a), this changes the composition of the one lepton category. Figure 7.12(b) shows the variation of the VH significance obtained by varying the MET_{sig} cut, considering only the one lepton category. The choice of the cut $MET_{sig} > 1.5$ is still justified when considering the ttH and dilepton categories.

The final number of observed events in data with the new selection and the expected background from Monte Carlo is shown in Figure 7.13. The main remaining backgrounds come from Standard Model processes involving truth leptons and photons.

(a) One lepton category composition

(b) Optimization of MET_{sig} cut
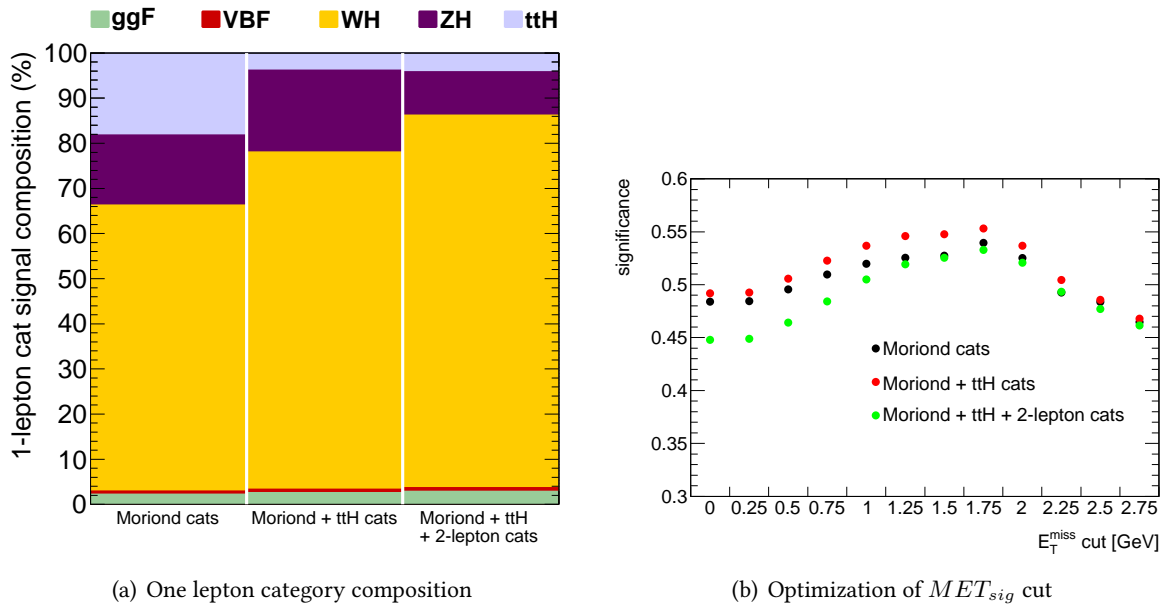
Figure 7.12: *(a) Signal composition for a Higgs boson with a mass of 125 GeV in the 1-lepton category with the default Moriond 2013 selection and when adding new categories before it in the selection order. (b) Expected VH significance in the 1-lepton category when adding a cut on the MET_{sig}, for different hypotheses of categories [105].*
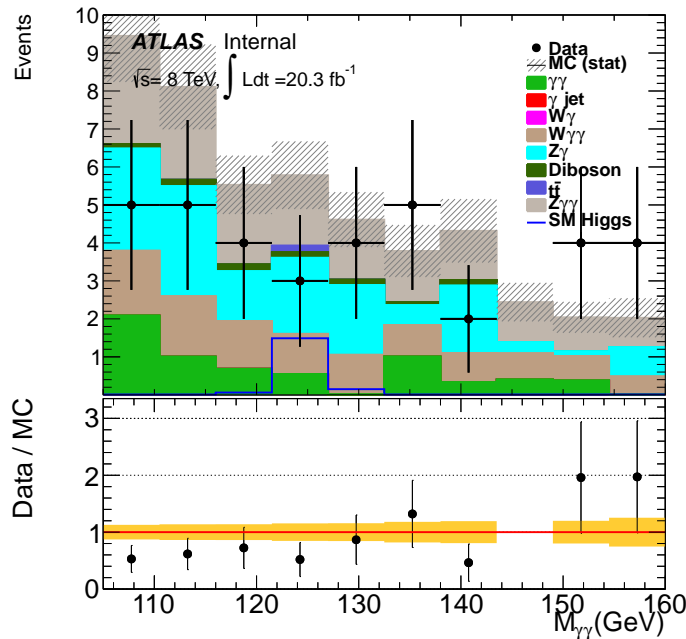
Figure 7.13: *Background composition in the VH-1lepton category from Monte Carlo [105].*

7.3.5 Dilepton

The study of the performances of adding a dilepton category was performed for the 2012 dataset only from the 14 Moriond 2013 categories, including a one-lepton (without cut on E_T^{miss} significance) and a E_T^{miss} significance category. It is aimed at selecting the $ZH \rightarrow ll\gamma\gamma$ final state, in order to decorrelate μ_{WH} and μ_{ZH}. The diphoton selection was also the one used for Moriond2013, whose main difference is the fixed p_T cuts on photons at 40 (30) GeV for the leading (subleading) photon. The study of this category is detailed with the old selection is Sections 7.3.5.1 and 7.3.5.2 while the updated results with the new selection are presented in Section 7.3.5.3.

7.3.5.1 Background estimation

The selection consists in choosing events with at least two leptons, two of them having the same flavour and opposite charge. A further requirement on the dilepton invariant mass is applied and m_{ll} is required to be between 70 and 110 GeV, quite loose since keeping some statistics is crucial for this analysis. Figure 7.14 illustrates the necessity of a cut on this variable to increase both the ZH purity versus the ttH contamination and the signal to noise ratio.

(a) ZH (b) ttH (c) $ll\gamma\gamma$
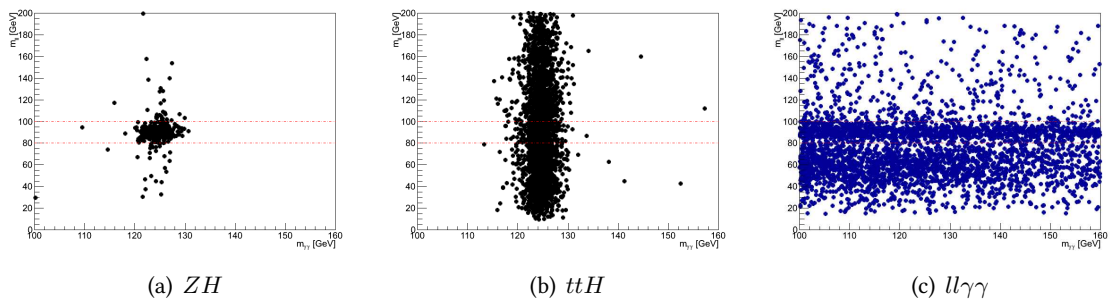
Figure 7.14: *Correlation between m_{ll} and $m_{\gamma\gamma}$ for ZH, ttH and background $ee\gamma\gamma$.*

Figure 7.15 shows the signal composition in this category before and after requiring $m_{ll} \in [70; 110]$ GeV. Note that, at the time these plots were made, no ttH categories were defined, that may increase the ttH contamination with respect to the final result.

(a) Without m_{ll} cut   (b) With m_{ll} cut

Figure 7.15: *Signal composition in the dilepton category with and without cut on the dilepton invariant mass.*

More investigations have been carried out to understand the background composition. The irreducible background is made of $ll\gamma\gamma$ events. Reducible background comes from $Z + jets$ events where at least one jet is misidentified as a photon.

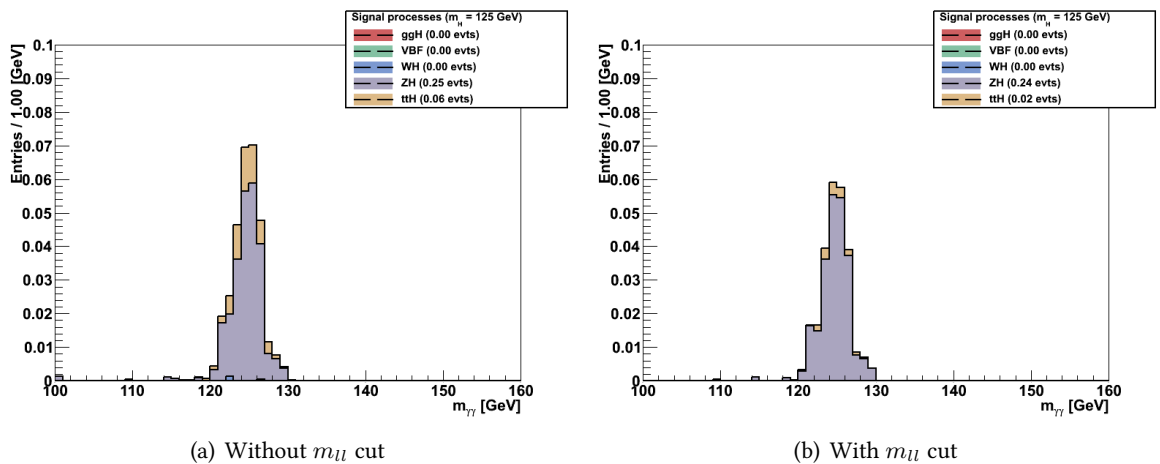The irreducible background is modelled by a matrix element generator, `SHERPA` [192], interfaced with `GEANT4`. Three diagrams contribute to the $ll\gamma\gamma$ matrix element. They are displayed in Figure 7.16. For diagram 7.16(a), the invariant mass between the two leptons m_{ll} should be close to the Z mass. In the case of the diagram 7.16(b), the Z mass is obtained with the three body invariant mass $m_{ll\gamma}$ while the four objects contribution is needed for the third diagram.

Dataset #	Generator	Process	$N_{initial}$	$\sigma[fb]$	$L[fb^{-1}]$	$N_{selected}\ ZH$
167476	Sherpa	$ee\gamma\gamma\ (p_T^\gamma > 25)$ + 3jets	200,000	9.29	$2.15\ 10^4$	1545
167477	Sherpa	$\mu\mu\gamma\gamma\ (p_T^\gamma > 25)$ + 3jets	200,000	9.30	$2.15\ 10^4$	1834
167478	Sherpa	$\tau\tau\gamma\gamma\ (p_T^\gamma > 25)$ + 3jets	200,000	9.25	$2.16\ 10^4$	1
147364	Sherpa	$ee\gamma\gamma\ (p_T^\gamma > 10)$ + 1jet	400,000	140	$2.9\ 10^3$	167
147365	Sherpa	$\mu\mu\gamma\gamma\ (p_T^\gamma > 10)$ + 1jet	400,000	140	$2.9\ 10^3$	211
147366	Sherpa	$\tau\tau\gamma\gamma\ (p_T^\gamma > 10)$ + 1jet	400,000	140	$2.9\ 10^3$	0
145161	Sherpa	$ee\gamma$+jets $(p_T^\gamma > 10)$ +3jets	3,200,000	$3.23\ 10^4$	99	0
145162	Sherpa	$\mu\mu\gamma$+jets $(p_T^\gamma > 10)$ +3jets	3,200,000	$3.23\ 10^4$	99	0
147770	Sherpa	$Z(ee) + 5jets$	10,000,000	$1.2074\ 10^6$	2.24	0
147771	Sherpa	$Z(\mu\mu) + 5jets$	10,000,000	$1.2074\ 10^6$	2.24	0

Table 7.2: *Monte Carlo samples used in the dilepton analysis. The number of generated events, the cross section and the filter efficiency are reported. The sample luminosity corresponds to $L = N_{initial}/\sigma$. $ll\gamma\gamma$ samples are produced with two different cuts on photons transverse momentum. See text to see explanations.*

| (a) | (b) | (c) |
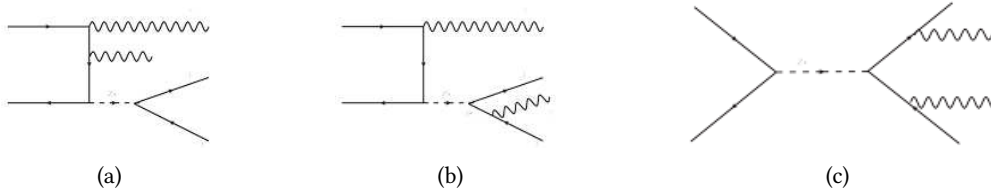
Figure 7.16: *Main background contributions to the dilepton category.*

Figure 7.17 is an illustration of the fact that the last diagram 7.16(c) does not contribute to the selected events due to the tight p_T cuts on the photons. Indeed, Figure 7.17(a) shows $m_{ll} : m_{ll\gamma}$ (with $x : y$ notations) for the $ee\gamma\gamma$ Monte Carlo sample with nominal cuts. Bottom and right pads represent the projection of m_{ll} and $m_{ll\gamma}$ respectively, the last bin containing the overflow. Events with $m_{ll} \sim m_Z$ come from the process 7.16(a). Similarly, events with low m_{ll} but $mll\gamma \sim m_Z$ come from 7.16(b). The middle plot in Figure 7.17 shows $m_{ll\gamma} : m_{ll\gamma\gamma}$: no events with $m_{ll\gamma\gamma} \sim m_Z$ are observed, showing that the diagram 7.16(c) does not contribute to the selected events. Figure 7.17(c) shows the $m_{ll\gamma} : m_{ll\gamma\gamma}$ distribution with relaxed cuts on the photon p_T, and the contribution from $Z \to ee\gamma\gamma$ is visible on central canvas.

| (a) $m_{ll} : m_{ll\gamma}$ | (b) $m_{ll\gamma} : m_{ll\gamma\gamma}$ | (c) $m_{ll\gamma} : m_{ll\gamma\gamma}$ relaxed cuts |
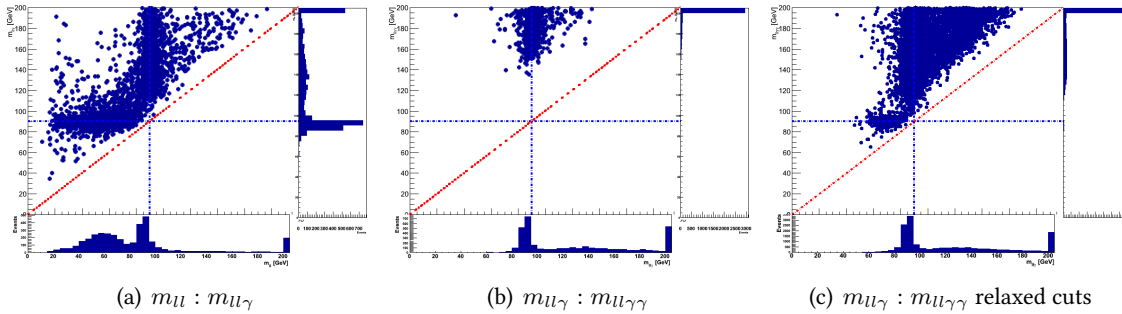
Figure 7.17: *Correlation between m_{ll}, $m_{ll\gamma\gamma}$ and $m_{ll\gamma\gamma}$ for the $ee\gamma\gamma$ background. $m_{ll\gamma}$ is the closest to the Z peak among the leading and subleading photon. See text.*

The reducible $Z + jets$ background can not be estimated directly form Monte Carlo due to the poor statistics surviving the kinematics and quality cuts on photons. The strategy proposed here is to relax the cuts on the photons p_T and quality to enrich the dataset with background. Two configurations were considered:

1. p_T cut on the photons reduced to 15 GeV;

2. Reduced p_T cut on the photons and quality requirement loosened (*i.e.* events with at least one photon loose but not tight).

In both these configurations, the Monte Carlo predictions are compared to the observations in data. Since the usual $\gamma\gamma$ stream used in the analysis requires tight p_T cuts on the photons and/or on electrons (see Table 7.3), the comparison to data is made using the $ee\gamma$ and $\mu\mu\gamma$ streams. The trigger requirement is also adapted and the usual diphoton trigger is combined with a single electron and a single muon trigger[1].

Stream	Photon(s)	Electron(s)	Muon(s)
	2 with $E_T > 20$ GeV	-	-
$\gamma\gamma$	1 with $E_T > 20$ GeV	1 with $E_T > 20$ GeV – medium	-
	-	2 with $E_T > 20$ GeV – medium	-
$ee\gamma$	1 with $p_T > 10$	2 with $p_T > 10$ GeV – loose++	-
$\mu\mu\gamma$	1 with $p_T > 10$	-	2 with $p_T > 10$ GeV – loose

Table 7.3: *Data streams and requirements on the different objects of interest for the dilepton analysis.*

Figures 7.18 and 7.19 show the dilepton invariant mass distribution obtained in each of these configurations for electrons and muons. The Monte Carlo samples use the relaxed p_T cuts on photons as well (datasets ID 14736x in Table 7.2). Due to the fact that these samples were generated with a lower number of jets in the matrix element, the cross-section is underestimated. The K-factor is estimated by generating a sample with the same SHERPA generator using the same configuration file and changing the maximum number of allowed jets. One can find [193]:

$$K = \frac{\sigma(ee\gamma\gamma, p_T^\gamma > 25, 3j)}{\sigma(ee\gamma\gamma, p_T^\gamma > 25, 1j)} = \frac{9.3023 \text{ fb}}{7.4534 \text{ fb}} = 1.248 \tag{7.9}$$

This K-factor is not applied on the plots below but may explain the remaining differences between data and Monte Carlo. Since some diagrams are common to the matrix elements of several samples, an overlap removal between the different samples is performed.

This study allows to conclude that the contribution from $Z + jets$ is sizeable when the photon quality is relaxed, as expected. When requiring tight photons, this contribution is reduced a lot. Considering that the photons purity increases with p_T, the contribution from $Z + jets$ in the nominal configuration is expected to be negligible.

The contribution from reducible background with jets faking a lepton is not addressed since the fake rate $j \to e/\mu$ is several order of magnitude below the $j \to \gamma$ fake rate.

The main background to the dilepton category hence comes from irreducible $ll\gamma\gamma$ processes. This conclusion justifies not to apply a $m_{e\gamma}$ cut similarly to the VH-one lepton category, since it was introduced to minimize the background coming from electrons misidentified as converted photons.

### 7.3.5.2 Statistical procedure

The introduction of a dilepton category allows to decorrelate μ_{WH} and μ_{ZH} as illustrated in Figure 7.20: their correlation with the 14 Moriond 2013 categories is 65% and is decreased down to 46% with the new dilepton category.

---

[1]Namely `EF_e24vhi_medium1` and `EF_mu24i_tight` trigger menu for the $ee\gamma$ and $\mu\mu\gamma$ streams respectively.

(a) Electrons – Configuration 1

(b) Electrons – Configuration 2
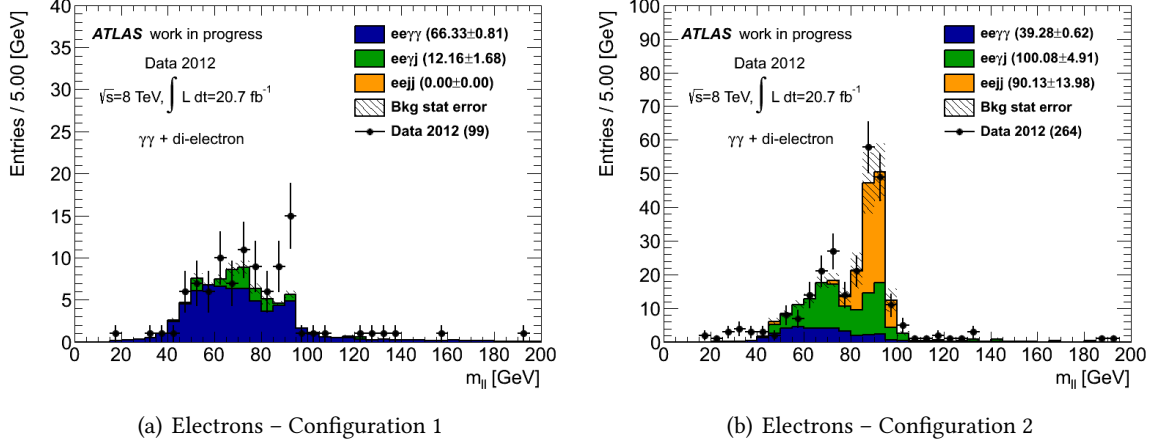
Figure 7.18: *Dielectron invariant mass distribution for relaxed cuts on photons. Numbers in parenthesis show the number of events normalized to the luminosity. Data are from the $ee\gamma$ stream. The $ee\gamma\gamma$ background contribution should be scaled up by about 25%. The $m_{ll} < 40$ GeV mass range should not be considered as a filter is applied at the Monte Carlo generation stage (for $Z + jets$ samples).*

(a) Muons – Configuration 1

(b) Muons – Configuration 2
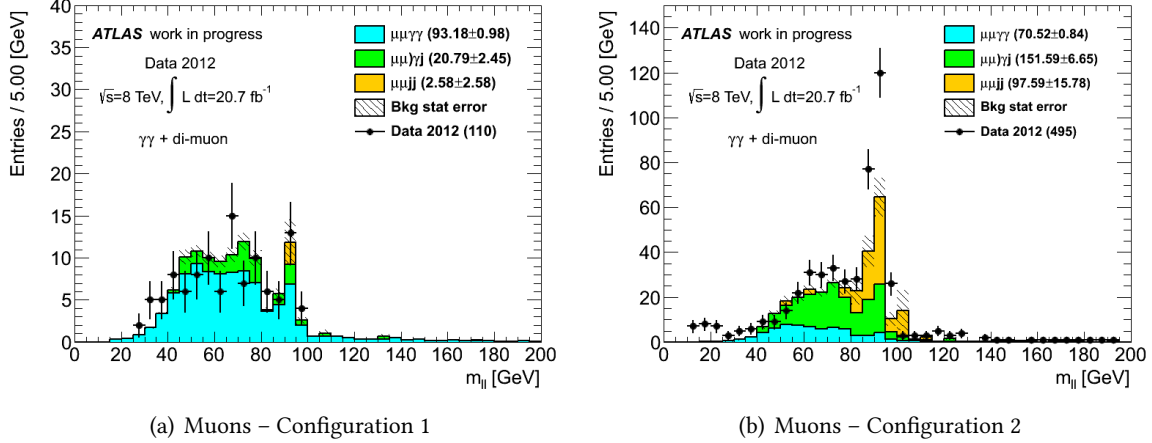
Figure 7.19: *Dimuon invariant mass distribution for relaxed cuts on photons. Numbers in parenthesis show the number of events normalized to the luminosity. Data are from the $\mu\mu\gamma$ stream. The $\mu\mu\gamma\gamma$ background contribution should be scaled up by about 25%. The $m_{ll} < 40$ GeV mass range should not be considered as a filter is applied at the Monte Carlo generation stage (for $Z + jets$ samples).*

With the Moriond 2013 selection, four events only are selected in this category in the whole 2012 dataset, none of them in the signal region $[120; 130]$ GeV. This make the usual statistical procedure consisting in determining the background shape from the data difficult. Several tests are performed to check the influence of the background parametrization on the results.

First of all, the classical technique of fitting the background with an exponential shape is performed. The choice of the exponential is confirmed with a spurious signal study. The Monte Carlo sample reproduces the main background, that previous paragraph showed to be made of $ll\gamma\gamma$ events. The $\tau\tau\gamma\gamma$ sample is also considered, even if having a small contribution. Figure 7.21 shows the results of an $S + B$ fit on this sample, for different B parametrizations. The bottom pad shows the number of fitted signal events, normalized to the luminosity. The criteria the spurious signal may fulfil are shown with dashed lines. The Monte Carlo sample statistics is not optimal, but the fits do not show any worrying deviations for choosing an exponential shape, and this is the choice made in the following.

The expected improvement on the μ_{ZH} measurements are quantified from an Asimov dataset.
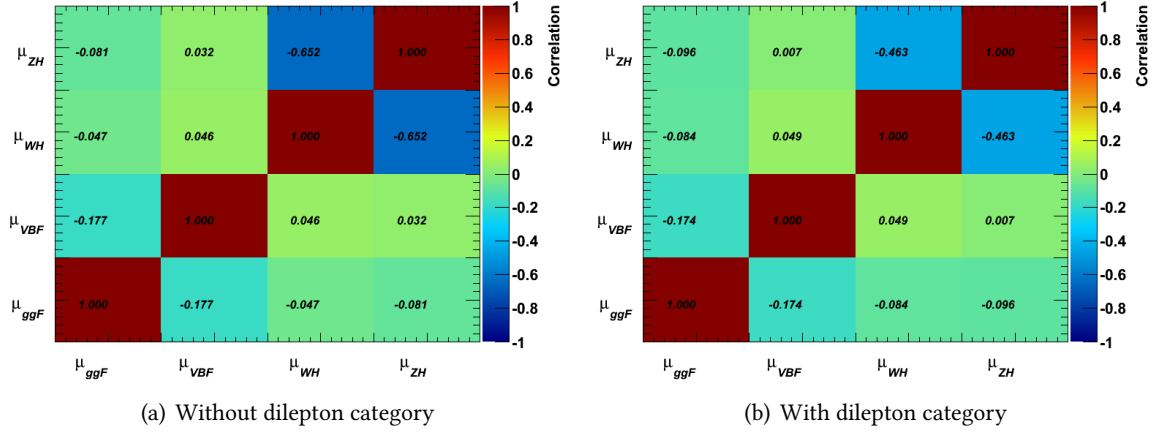
(a) Without dilepton category

(b) With dilepton category

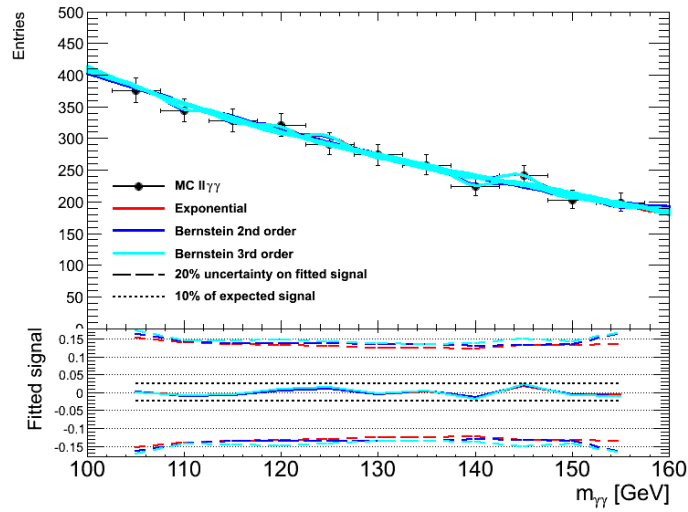**Figure 7.20:** *Correlation between the four parameters of interest.*

Figure 7.21: *Spurious signal study for the dilepton category with the Moriond 2013 selection.*

Table 7.4 shows the expected results if staying with the Moriond 2013 categorization, that will serve as baseline. It is compared with a configuration where the dilepton category is added, its background estimated from a fit to data with either an exponential or constant shape. The addition of the dilepton category improves the expected uncertainties on μ_{WH} and μ_{ZH}. When changing the background parametrization among reasonable functions, the result is not affected.

| Configuration | Without dilepton | | With dilepton | | | |
Bkg shape for dilepton	-		Exponential		Constant	
μ	err+	err -	err+	err -	err+	err -
ggH+ttH	0.46	-0.41	0.40	-0.37	0.40	-0.37
VBF	0.94	-0.79	0.84	-0.75	0.84	-0.75
WH	3.41	-3.07	2.32	-2.14	2.32	-2.15
ZH	6.35	-5.40	3.60	-2.29	3.62	-2.29

Table 7.4: *Expected uncertainties on μ_X from an Asimov dataset with $\mu = 1$ at $m_H = 126.5$ GeV. The baseline Moriond 2013 category configuration without dilepton category is compared to configuration adding a dilepton category. The impact of the background shape in the dilepton category is also tested.*

The improvements on μ_{VH} one one side, and μ_{WH} and μ_{ZH} on the other side are summarized in

Figure 7.22. A test was also performed to test the category ordering, starting the selection from the VH E_T^{miss} category instead of the dilepton category, but this was not conclusive.
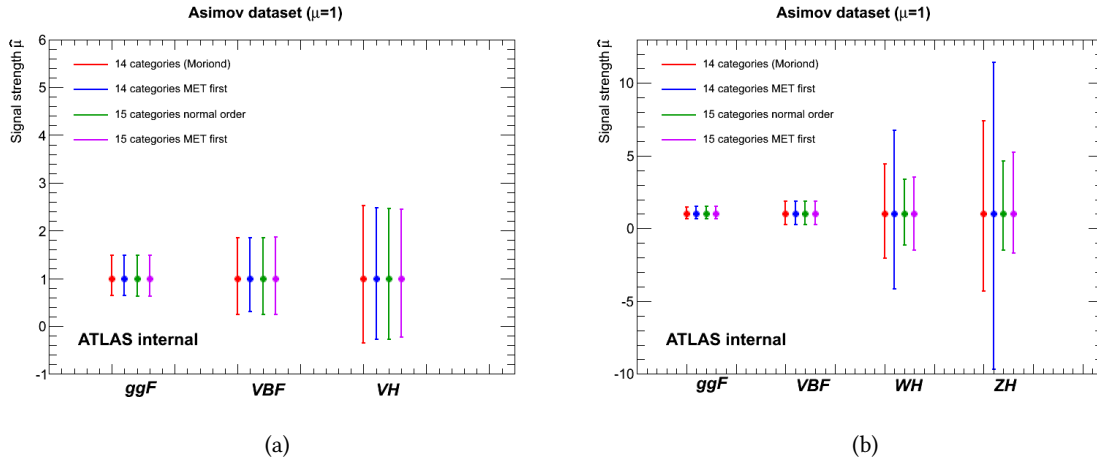

(a)   (b)

Figure 7.22: *Expected improvement on the signal strengths uncertainties. Comparing the red and green lines shows the improvement between the 14 Moriond 2013 categories and the 15-category model including a dilepton category.*

7.3.5.3   Final results

When introducing relative p_T cuts, only two data events survive the dilepton selection, as illustrated in Figure 7.23.
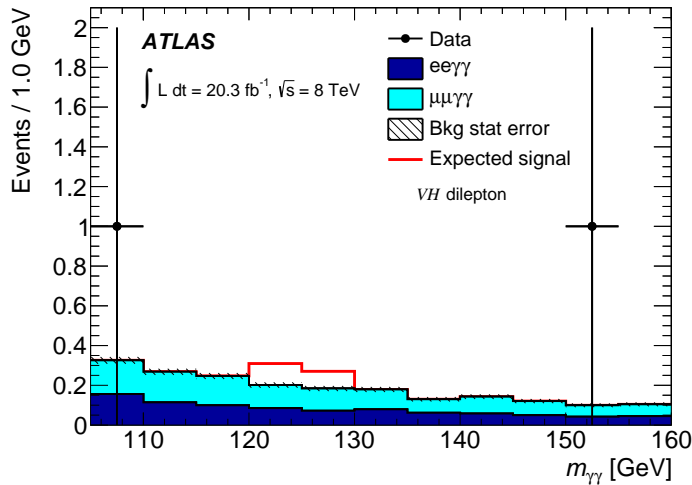

Figure 7.23: *Background composition in the VH-dilepton category from Monte Carlo [125].*

As described in Chapter 2, fitting such a low number of events, and especially with no event in the signal region requires the addition of ghosts events in the dataset to prevent the pdf to become negative.

7.3.6 $t\bar{t}H$

The analysis of the $t\bar{t}H$ production mode is a dedicated analysis taking advantage of several Higgs decay channels (see first analysis description in [194]). The analysis in the $\gamma\gamma$ channel defines two categories: the leptonic category selecting the leptonic decay of at least one top quark, and a hadronic

category selecting the full hadronic decay of the $t\bar{t}$ pair. The selection relies only on counting the number of jets, b-jets, leptons and quantify the E_T^{miss} reconstructed in the event.

The optimization of each category was done on a ttH limit basis, using statistical uncertainty only. The ggH contamination is minimized because it suffers from large theoretical uncertainties coming from c and and b quarks production. The analysis is described in detail in [195], [196] and [197].

Hadronic category

The hadronic category is defined by a logical OR between the following three configurations:

6j2b at least six jets, out of which at least two are b-tagged using the 80% MV1c tagger working point;

6j1b similar to previous configuration except that the p_T cut on jets is increased to 30 GeV and the requirement on the number of b jets is loosened to only one, with the 60% MV1c working point;

5j2b selects events with at least five jets, out of which at least two are classified as b-jets from the 70% MV1c tagger.

For each configuration, a lepton veto is applied to remove possible overlaps with the leptonic category.

Leptonic category

The leptonic category requires a reconstructed lepton, electron or muon. Two configurations are retained:

1b one b-tagged jet with the 80% MV1c tagger and $E_T^{miss} > 20$ GeV;

2b at least two b-jets from 80% of MV1c tagger. No E_T^{miss} requirement because the main background is found to come from $t\bar{t}$.

Similarly to the VH one lepton category, a veto is performed if the $m_{e\gamma}$ invariant mass between either electron and either photon is consistent with a Z boson.

7.3.7 Untagged

With the increasing number of categories, the historical nine untagged categories were reinvestigated in order to reduce their number, preserving a good expected significance. Several models were tested, and the final one is made of only four categories based on the photon pseudorapidities and diphoton p_{Tt} only.

The cut optimization is performed on a global signal significance basis and is illustrated in Figure 7.24 where the data side-bands and Monte Carlo are used to estimate the background. Both methods give consistent results and the chosen cuts are the following:

1. Central high p_{Tt}: $(|\eta_1| < 0.95$ and $|\eta_2| < 0.95)$ and $p_{Tt} > 70$ GeV

2. Central low p_{Tt}: $(|\eta_1| < 0.95$ and $|\eta_2| < 0.95)$ and $p_{Tt} < 70$ GeV

3. Forward high p_{Tt}: $(|\eta_1| > 0.95$ or $|\eta_2| > 0.95)$ and $p_{Tt} > 70$ GeV

4. Forward low p_{Tt}: $(|\eta_1| > 0.95$ or $|\eta_2| > 0.95)$ and $p_{Tt} < 70$ GeV

Figure 7.25 shows the p_{Tt} distribution in the forward and central categories, justifying the use the same cut for both categories.
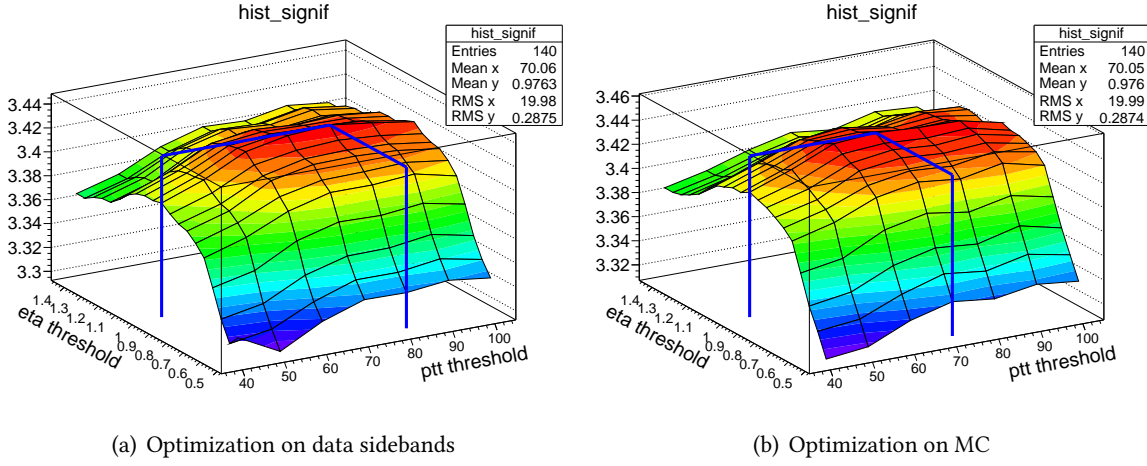
(a) Optimization on data sidebands

(b) Optimization on MC

Figure 7.24: *Significance as a function of the cut on p_{Tt} (10 GeV step) and η (0.05 step) for the p_{Tt}-η model [105].*
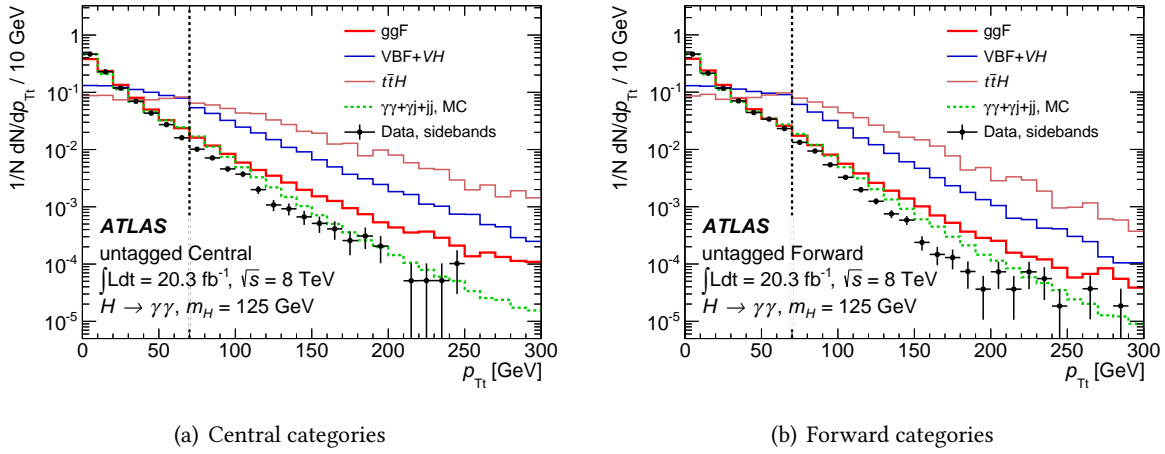

(a) Central categories

(b) Forward categories

Figure 7.25: *p_{Tt} distributions in the untagged categories [125].*

7.4 Statistical model

7.4.1 Signal model

As usual, the signal is parametrized by a Crystal-Ball+Gaussian shape with a global fit to all signal processes. The shape parameters and the yields are parametrized as a function of the Higgs mass with polynomials as described in Section 6.5.1.3.

Two more signal processes are taken into account:

bbH it was noticed that the bbH production mode (Fig. 7.26) was not considered so far while its contribution is not negligible compared to the ttH one [28, 198–200]. However, its impact on our analysis is expected to be small since its cross section decreases quickly as the b-jet p_T increases.

Fully simulated samples are not yet produced for this process and the usual technique can not be used. It is accounted for in the signal model according to the following prescription: its yield at $m_H = 125.5$ GeV is taken to be 1.1% of the ggH cross-section; its mass dependence is similar to the ttH process (Fig. 1.12).This results in the $N_{bbH}(m_H)$ dependence:

$$N_{bbH}(m_H) = \frac{N_{ttH}(m_H)}{N_{ttH}(125.5)} \times \frac{N_{ggH}(125.5)}{\sigma_{ggH}(125.5)} \times \sigma_{bbH}(125.5) \tag{7.10}$$

(a) 4 flavours scheme   (b) 5 flavours scheme
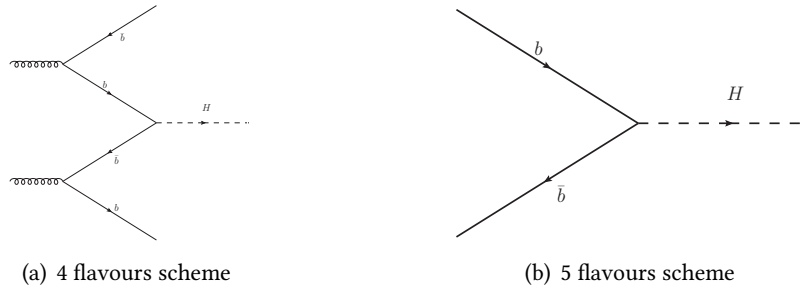
Figure 7.26: *bbH process in the four flavours parton density containing only u,d,c,s and g contributions and for the five flavours scheme adding the contribution from b quark.*

where we have $\frac{\sigma_{bbH}(125.5)}{\sigma_{ggH}(125.5)} = 1.1\%$.

tH The tH process is taken into account since it represents up to 5% of the total signal in the ttH categories (Tab 7.5). Two kinds of Monte Carlo samples need to be produced to fully describe the tH process: tHj (Fig. 7.27) and WtH (Fig. 7.28). The diagrams $q\bar{q}' \to W^* \to tbH$ (s-channel) are neglected. However, only the first one is available, only for $m_H = 125$ GeV, at that time, its prediction are then scaled up by a factor 1.3 to account for the total tH process. The impact of having ~ 400 MeV mass difference on acceptance is checked to be negligible and a flat mass dependence of the acceptance is then used. The mass dependence of the cross section is taken into account.

	7 TeV	8 TeV
σ_{tHj} [pb]	0.00891	0.0138
K_{tHj}	1.19	1.23
σ_{ttH} [pb]	0.08632	0.1293

Table 7.5: *tH cross section and K-factors at $\sqrt{s} = 7$ and 8 TeV compared to the ttH cross section, at $m_H = 125$ GeV.*

(a)   (b)

Figure 7.27: *Example of diagrams for the tH production in the tHj channel (see [201] for a complete description).*

(a)   (b)
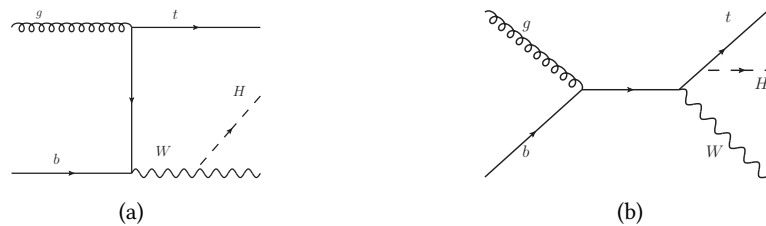
Figure 7.28: *Example of diagrams contributing to the tH production in association with a W boson (see [201] for a complete description).*

The result in terms of category composition is shown in Figure 7.29. It is very similar between 7 and 8 TeV. A small difference appears in the VH E_T^{miss} category because the 7 TeV analysis uses a looser photon identification based on a Neural Network (Sec. 6.2.2.2); therefore, in the E_T^{miss} computation, more jets are wrongly calibrated as photons [202].

(a) 7 TeV

(b) 8 TeV
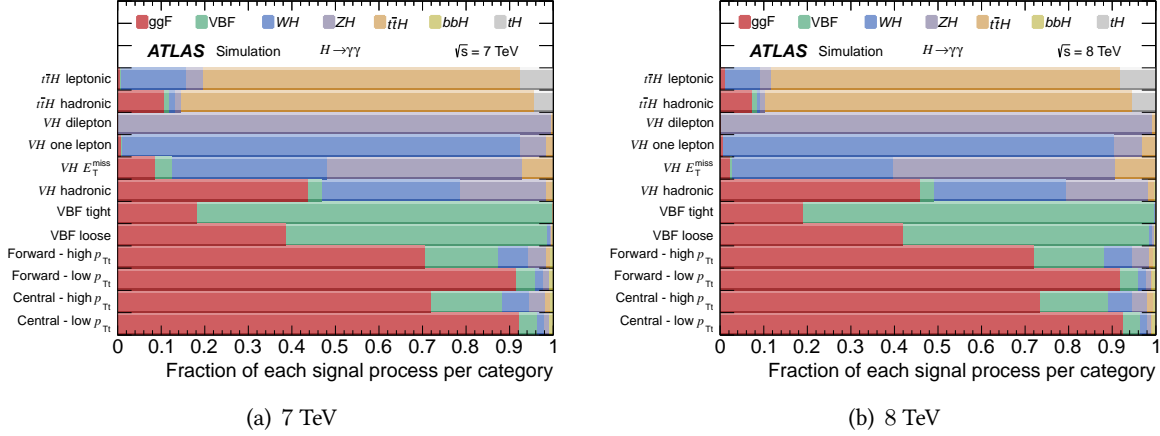
Figure 7.29: *Category composition in terms of signal processes for the* 7 *and* 8 *TeV Standard Model predictions [125].*

The number of expected events and resolution in each category are given in Tables 7.6 and 7.7 for 7 TeV and 8 TeV respectively. The number of background events in the signal region is estimated by a fit to the data side-bands in order to derive the signal-to-noise ratios.

Category #	Category name	n_{signal}	$\sigma_{68\%}$	$\sigma_{90\%}$	n_{bkg} in $\sigma_{90\%}$	$s/b\,(\sigma_{90\%})$	$s/\sqrt{b}\,(\sigma_{90\%})$
1	Central low p_{Tt}	26.01	1.36	2.32	402.50	0.06	1.15
2	Central high p_{Tt}	1.99	1.21	2.05	10.86	0.16	0.54
3	Forward low p_{Tt}	39.52	1.69	3.03	1386.41	0.03	0.95
4	Forward high p_{Tt}	2.87	1.49	2.59	46.83	0.06	0.38
5	VBF loose	1.62	1.43	2.53	6.65	0.22	0.57
6	VBF tight	0.95	1.37	2.40	0.48	1.79	1.24
7	VH hadronic	0.57	1.36	2.33	2.78	0.18	0.31
8	VH E_T^{miss}	0.45	1.33	2.36	1.54	0.26	0.33
9	VH one lepton	0.34	1.48	2.56	0.33	0.92	0.53
10	VH dilepton	0.05	1.45	2.59	0.00	-	-
11	ttH hadronic	0.07	1.38	2.37	0.21	0.28	0.13
12	ttH leptonic	0.10	1.42	2.44	0.11	0.82	0.27

Table 7.6: *Signal model parameters and expected background (from fit) for 2011 7 TeV datasets. $\sigma_{X\%}$ is the size of the window (in GeV) containing $X\%$ of the signal. No event is observed in category 10 (VH-dilepton).*

7.4.2 Background parametrization

The background is modelled by a fit to the data. The function parametrization is chosen with a spurious signal study whose principles are described in Section 6.5.2. The following only shows the results of the study for this particular analysis.
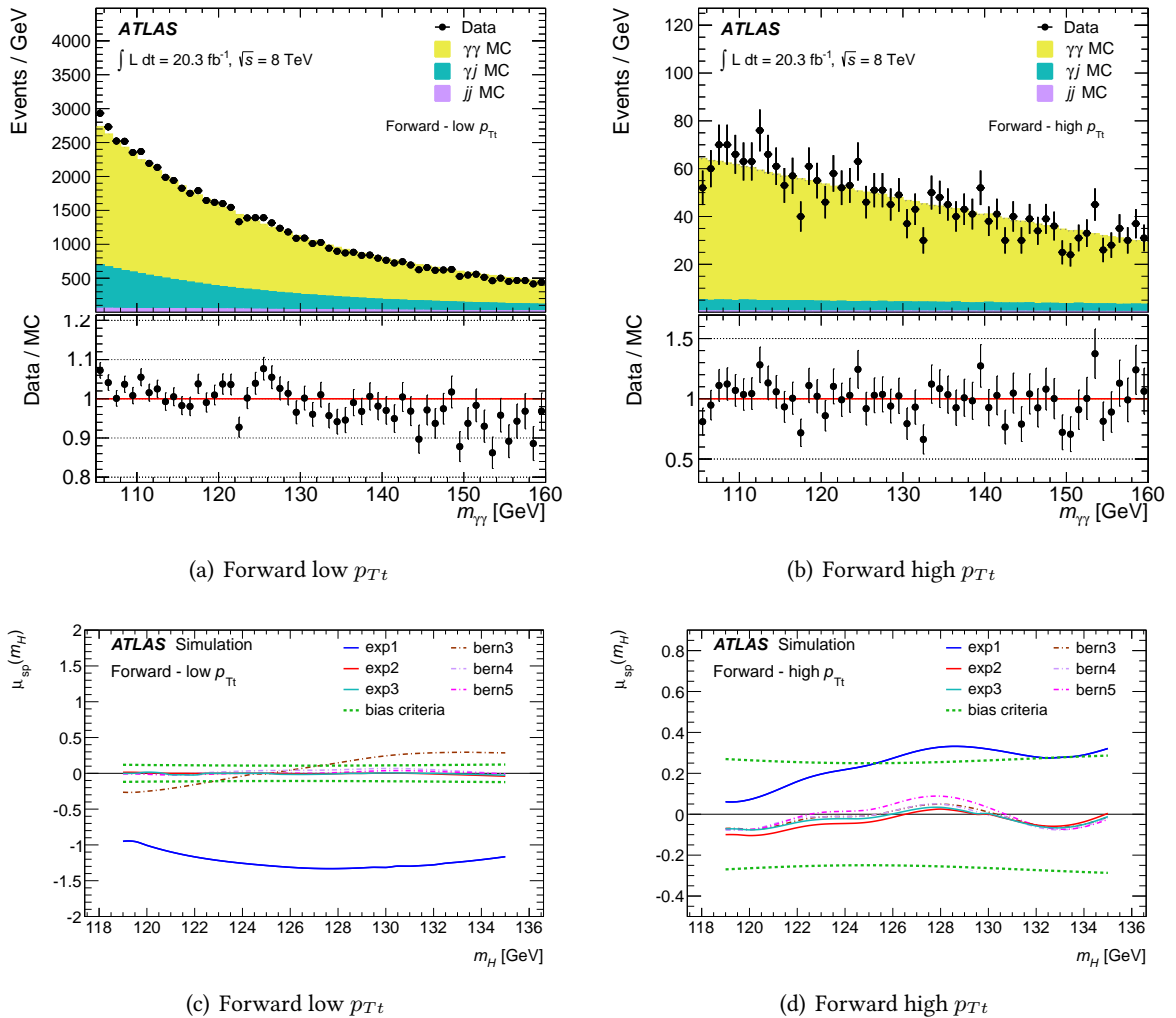
The smeared Monte Carlo is a mixture of jj, γj and $\gamma\gamma$ events with a composition compatible with purity studies coming form the data driven QCD background estimation. Figure 7.30 shows the distribution of this Monte Carlo sample compared to the data for two categories.

The tested shapes are Bernstein polynomials of order 2, 3 and 4 and exponential of polynomials: $exp(\sum_{n=1}^{N} a_n(m_{\gamma\gamma} - 100)^n)$ with N=1,2 or 3.

The 7 TeV dataset needs some special treatment because the smeared Monte Carlo are not produced. For the high statistics categories, a reweighting is derived to take into account the change of

Category #	Category name	n_{signal}	$\sigma_{68\%}$	$\sigma_{90\%}$	n_{bkg} in $\sigma_{90\%}$	s/b ($\sigma_{90\%}$)	$s/\sqrt{b}$ ($\sigma_{90\%}$)
1	Central low p_{Tt}	138.41	1.47	2.49	2376.42	0.05	2.53
2	Central high p_{Tt}	11.44	1.31	2.22	68.33	0.15	1.23
3	Forward low p_{Tt}	212.52	1.86	3.30	8538.51	0.02	2.05
4	Forward high p_{Tt}	16.48	1.64	2.89	282.67	0.05	0.88
5	VBF loose	9.26	1.57	2.78	44.42	0.19	1.25
6	VBF tight	5.88	1.46	2.62	6.67	0.79	2.05
7	VH hadronic	3.27	1.43	2.57	18.30	0.16	0.69
8	VH E_T^{miss}	1.14	1.58	2.73	3.21	0.32	0.57
9	VH one lepton	1.67	1.60	2.80	4.39	0.36	0.76
10	VH dilepton	0.26	1.59	2.80	0.27	0.86	0.45
11	ttH hadronic	0.49	1.52	2.61	1.74	0.26	0.34
12	ttH leptonic	0.62	1.57	2.68	0.53	0.96	0.70

Table 7.7: *Signal model parameters and expected background (from fit) for 2012 8 TeV datasets. $\sigma_{X\%}$ is the size of the window (in GeV) containing $X\%$ of the signal.*

(a) Forward low p_{Tt}

(b) Forward high p_{Tt}

(c) Forward low p_{Tt}

(d) Forward high p_{Tt}

Figure 7.30: *Top: smeared Monte Carlo shape and comparison to data at 8 TeV. Bottom: $\mu_{SS} = \frac{N_{spurious}}{N_{signal}^{expected}}$ [125].*

the parton density functions between 7 and 8 TeV. The spurious signal study is repeated with these reweighted smeared Monte Carlo samples. For the low statistics categories (both ttH categories, VH-dilepton, VH-one lepton and VH E_T^{miss}), it was chosen to correlate the background shapes between

both years. In this case, the spurious signal at 7 TeV is obtained by scaling the one computed at 8 TeV to the number of expected signal events.

The chosen parametrization for each of the twelve categories and the associated spurious signals are reviewed in Table 7.8.

#	Category Name	Background model	N_{spur} (7 TeV)	N_{spur} (8 TeV)
1	Central - low p_{Tt}	Exp. pol. 2nd order	1.11	6.74
2	Central - high p_{Tt}	Simple exponential	0.07	0.41
3	Forward - low p_{Tt}	Exp. pol. 2nd order	1.17	6.99
4	Forward - high p_{Tt}	Exp. pol. 2nd order	0.25	1.18
5	VBF loose	Simple exponential	0.17	1.30
6	VBF tight	Simple exponential	0.03	0.31
7	VH hadronic	Simple exponential	0.08	0.45
8	VH E_T^{miss}	Simple exponential	0.05	0.12
9	VH one lepton	Simple exponential	0.03	0.11
10	VH dilepton	Simple exponential	0.004	0.02
11	ttH hadronic	Simple exponential	0.06	0.33
12	ttH leptonic	Simple exponential	0.03	0.17

Table 7.8: *List of the functions chosen to model the invariant mass distributions of the backgrounds and the associated spurious signal term N_{spur} for the 12 categories and for the 7 and 8 TeV datasets.*

7.4.3 Systematics uncertainties

Several sources of systematics uncertainties are identified and their effect on the analysis quantified. The uncertainties impact different parts of the model:

- Analysis efficiency can be affected by changes in the cut definition and/or variable modelling. This is translated into an uncertainty on the expected signal yield. Two kinds of uncertainties on the signal yield can be defined:

    - Efficiencies: change the overall number of selected events. The most important quantity is the difference between data and Monte Carlo efficiency, which is quantified with the use of scale factors. These uncertainties are common to all analyses using the same inclusive event selection.

    - Migrations: impact only the distribution of the selected events into the different categories. Since categories are defined with different signal-to-noise ratios, this can change the final measurement.

    For each of them, theory and experimental sources are identified. The experimental uncertainties are computed using the difference of efficiency between data and Monte Carlo.

- Photon energy scale induces uncertainties on the peak position, propagated to systematics on the mean of the Crystal-Ball and Gaussian coming from the signal model (see Section 6.5.1).

- Mass resolution is also an uncertain quantity impacting the resolution of the Crystal-Ball and Gaussian in the signal model.

- Finally, the background modelling is also a source of uncertainty. It is accounted for in the analysis by adding a signal bias corresponding to the spurious signal.

The next sections detail the different sources of uncertainty that have been considered for the $\gamma\gamma$ couplings analysis.

7.4.3.1 Signal efficiency

The theory uncertainties on the inclusive signal efficiency come from:

Inclusive cross-sections
 The predicted inclusive cross sections for each process suffer from theory uncertainties due to QCD scale dependence (*i.e.* missing higher order corrections) and Parton Density Functions of the proton. Values used in this analysis are provided by the LHC Higgs cross section working group [134]. Their values are summarized in Table 7.9 for 8 TeV data. One should note that there is a discussion in [203, 204] of possible underestimation of these uncertainties. Some approximate N^{3}LO ggH computations have been carried out recently [205–208], which are not included in this computation.

	7 TeV			8 TeV		
Process	Central value	Scale	PDF+α_S	Central value	Scale	PDF+α_S
ggH	18.82	+7.2 / -7.8	+7.5 / -6.9	14.77	+7.1 / -7.8	+7.6 / -7.1
VBF	1.558	+0.2 / -0.2	+2.6 / -2.7	1.206	+0.3 / -0.3	+2.5 / -2.1
WH	0.6767	+1.0 / -1.0	+2.3 / -2.3	0.5555	+1.0 / -1.0	+2.5 / -2.5
ZH	0.4000	+3.2 / -3.2	+2.5 / -2.5	0.3227	+2.9 / -2.9	+2.6 / -2.6
ttH	0.1247	+3.8 / -9.3	+8.1 / -8.1	0.0833	+3.2 / -9.3	+8.4 / -8.4
bbH	0.1498	+13 / -23	+6.4 / -6.4	0.1953	+13 / -22	+6.4 / -6.4

Table 7.9: *Standard Model Higgs cross sections* [pb] *and theory uncertainties* [%] *at* $m_H = 126.5$ *GeV following Higgs cross section working group prescriptions* [134].

 The scale uncertainties are treated as uncorrelated among the five production modes: ggH, VBF, VH, ttH and bbH. For the PDF, only two nuisance parameters are introduced, depending on the gg (ggH, ttH) or qq (VH, VBF) nature of the process.

Branching ratio
 An uncertainty of 4.8% of the signal yield is added, due to the Higgs branching ratio to $\gamma\gamma$ uncertainty [134].

ttH modelling
 Some uncertainties are added in the ttH categories only:

- Additional uncertainties on the cross-section normalization due to scale variation and scale choice amounts for up to 2% uncertainty on the ttH signal yield.
- Extra uncertainties on the ggH and WH processes are also included;
- An additional uncertainty of 100% is taken into account, due to the heavy flavour modelling in the contributions from ggH, VBF and WH processes. Even it very large, the fraction of events from these processes in the ttH categories is very low so its impact on the final measurement is expected to be small;

Some experimental sources are also identified to have an impact on the signal efficiency. They are summarized in Table 7.10 and detailed below.

Luminosity
 The luminosity is determined from Van der Meer scans carried out several times during the 2011

Uncertainty source	7 TeV	8 TeV
Luminosity	1.8	2.8
Trigger	0.5	0.5
Photon ID	8.4	1.0
Isolation	0.6	0.3

Table 7.10: *Relative systematic uncertainties on the inclusive yields* [%] *for the 7 TeV and 8 TeV datasets.*

and 2012 runs. The uncertainties on this determinations, coming from both the individual scans and the difference observed in their repetitions, are evaluated using the techniques described in Ref. [209]. It is found to be 2.8% for 2012 and 1.8% in 2011. This uncertainty is considered as uncorrelated between 2011 and 2012.

Trigger

The trigger efficiency and its related uncertainty are evaluated using data-driven methods. The `g35_loose_g25_loose` trigger efficiency is evaluated for relative p_T cuts on the photons. The measured efficiency is 99.04% with a total uncertainty of 0.53%. The 2011 `2g20_loose` has comparable efficiency and the same uncertainty, correlated with 2012.

Photon identification

The photon identification efficiency is measured from a combination of three data driven methods. The resulting uncertainties for the 8 TeV analysis, where correlations between photons are taken into account, is found to be 1% on the inclusive signal yield. The systematics for 2011 uncertainties amounts to 8.4% of the inclusive signal yield. Both uncertainties are uncorrelated between 2011 and 2012.

Photon isolation

Two methods exist for the photon isolation systematics determination. A first method uses electrons from $Z \rightarrow e^+e^-$. The influence of using electrons is quantified by changing the electron quality requirement and leads to quite high uncertainties. It is applied for the 2011 dataset. For 2012 data, another method is derived using directly tight photons from $Z \rightarrow ll\gamma$ process. The dependence with the number of primary vertex, pseudo-rapidity and transverse energy is checked and found to be negligible. This new method allows to decrease the isolation uncertainty in 2012 from 1.2% to 0.3%.

The photon identification and isolation are expected to be less efficient in the hard jet environment required by the ttH selection. The related uncertainties are then increased in these two categories to 9.3% (2011) and 4.1% (2012) for the photon identification and to 3.1% (2011) and 3.0% (2012) for the photon isolation [210].

Photon energy scale

The impact of the photon energy scale on the inclusive signal yield is tested by varying the photon p_T by δp_T according to the uncertainty on the energy δE where $p_T = E/ch(\eta)$. The impact on the acceptance is found to be negligible.

Monte Carlo statistics The limited statistics in the Monte Carlo samples gives rise to an uncertainty on the number of selected signal events. It is estimated for each of the five production modes whose full simulation samples are available, and for each category (Tab. 7.11). In principle, one should use $5 \times 12 = 60$ nuisance parameters per year, one per production mode and per category. However, given the size of the uncertainty, it is expected to be negligible for most of the measurements. A systematic study showed that only four of these nuisance parameters have an impact greater than 0.1% on the final systematics uncertainty on the μ_X:

- The ZH yield in category 10 (dilepton) for 2011;

- The ZH and WH yields in category 10 (dilepton) for 2012;
- The ttH yield in category 12 (ttH leptonic) for 2012.

2011	ggH	VBF	ttH	WH	ZH
CP1	0.19	0.37	1.01	0.55	0.53
CP2	0.65	0.64	1.14	1.01	0.99
CP3	0.15	0.29	0.90	0.40	0.39
CP4	0.55	0.53	1.12	0.78	0.78
CP5	1.12	0.38	4.27	3.51	3.51
CP6	2.15	0.42	9.21	10.37	9.76
CP7	1.72	2.68	2.07	0.81	0.79
CP8	2.16	2.12	1.20	1.00	0.71
CP9	12.60	10.00	2.08	0.64	1.79
CP10	0.00	0.00	9.90	57.74	**1.24**
CP11	11.62	12.91	0.77	12.13	8.84
CP12	30.15	30.15	0.64	2.86	4.12

2012	ggH	VBF	ttH	WH	ZH
CP1	0.19	0.37	1.08	0.57	0.54
CP2	0.64	0.64	1.20	1.01	0.98
CP3	0.16	0.30	0.95	0.41	0.40
CP4	0.54	0.53	1.15	0.78	0.77
CP5	1.09	0.39	4.43	3.31	3.21
CP6	2.05	0.42	8.01	8.30	8.91
CP7	1.70	2.74	2.14	0.82	0.80
CP8	10.72	10.91	1.38	1.25	0.82
CP9	13.48	12.91	1.89	0.66	1.91
CP10	0.00	0.00	9.45	**100.**	**1.25**
CP11	12.13	13.61	0.70	14.00	8.28
CP12	33.33	25.00	**0.65**	4.10	5.63

Table 7.11: *Uncertainties coming from the statistical limitation of the 7 TeV (left) and 8 TeV (right) Monte Carlo samples [%] [105].*

Four nuisance parameters acting on the signal yields with gaussian constraint are then added to the model.

7.4.3.2 Migrations

Migrations uncertainties take into account different events repartition in the categories. In principle, $\sum_{cat} \sigma_{cat}^{mig} N_{cat}$ should be zero, hence a positive sign uncertainty should always be compensated by a negative uncertainty in another category. In practice, the number of affected events can be so small that the number of events moving out of low statistics category is not negligible, but the corresponding events entering the high statistics category are negligible. This explains why some migration systematics are defined only in some categories, and sometimes have always the same sign.

Higgs p_T modelling

The Higgs p_T is highly correlated to the diphoton p_{Tt}. Uncertainties on the Higgs p_T spectrum then induces migrations among the untagged categories using a p_{Tt} cut. The determination of this uncertainty is discussed in Chapter 9. The final results are recalled in Table 9.3. The inclusive scale uncertainty should be set to zero in the high p_{Tt} categories because the $\sim 20\%$ p_T uncertainty already covers it.

	ctrl-low-p_{Tt}	ctrl-high-p_{Tt}	fwd-low-p_{Tt}	fwd-high-p_{Tt}
Scale, 7 TeV	7.8	0	7.8	0
p_t^H mig, 7 TeV	-1.4	24.1	-1.4	23.8
Scale, 8 TeV	7.8	0	7.8	0
p_T^H mig, 8 TeV	-1.5	24.2	-1.5	23.9

Table 7.12: *Migration uncertainties in percent on the ggH cross section in the high and low p_{Tt} categories from* `HRes2.0`*.*

The impact of PDF variations on the Higgs p_T shape were also checked and found to be significantly smaller than the QCD scale uncertainties hence neglected is this analysis. More details about the Higgs p_T and its uncertainties are given in Chapter 9.

N$_{jets}$ cross section

This systematics comes from the exclusive N_{jets} cross-section uncertainty that is translated into migrations of events out of the 2-jets categories. It is estimated using the `MCFM` pure NLO generator. Details about this method can be found in Section 8.3 of Yellow Report 3 [134].

The increase in ggH scale uncertainty when the BDT applies criteria on this variable is found to be 25% and 52% and is summarized in Table 7.13.

Category	VBF loose	VBF tight	VH had
≥ 2 jets uncertainty	20.4%	20.4%	20.4%
≥ 3 jets uncertainty	25%	52%	0

Table 7.13: *Systematics due to the modelling of ggH +jets in the two-jet categories* [%].

$\Delta\phi$ and η^* modelling

The VBF selection uses angular variables $\Delta\phi_{\gamma\gamma-jj}$ and η^* as BDT inputs. The uncertainty on the modelling of these two quantities for the ggH process in the Monte Carlo are estimated looking at the difference in signal yield between the nominal POWHEG+PYTHIA8 sample, in which the second jet is always generated by the parton shower, and the MINLO HJJ [211] which models the second jet in gluon fusion up to NLO. The VBF process does not have this problem since it is generated at NLO with POWHEG, hence both jets are already generated at NLO accuracy.

The weights from the ggH samples are derived independently for $\Delta\phi_{jj}$ and η^*, as the ratio between the nominal and the MINLO HJJ sample after each dataset have been normalized to the same cross-section. They are then applied to the nominal sample and this weighted sample passes through the BDT. The effect of the reweighting on the BDT output is shown in Figure 7.31. The migrations systematics are shown in Table 7.14 for categories in which it is not negligible.

(a) $\Delta\phi_{\gamma\gamma-jj}$ (b) η^*
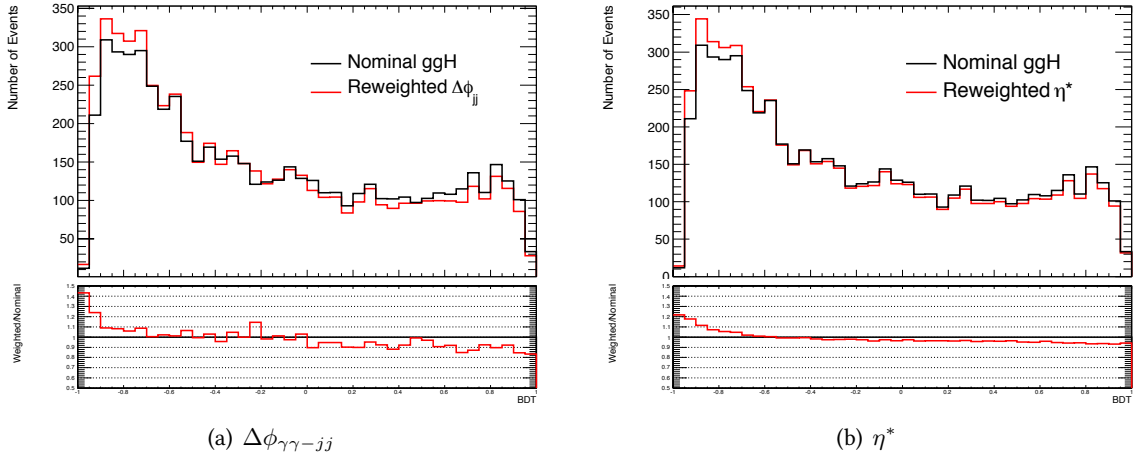
Figure 7.31: *The resulting POWHEG BDT distributions with (red) and without (black) reweighting to MINLO HJJ* [105].

Reweighted Sample	Tight VBF	Loose VBF
HJJ $\Delta\phi$	-11.18	-8.93
HJJ $\eta*$	-6.60	-4.82

Table 7.14: *Changes in gluon fusion event yields after reweighting with MINLO HJJ for the loose and tight VBF categories* [%].

Underlying event

The underlying event, or Multi parton interaction (MPI), modelling can change the number of jets in the events. Its impact on the ggH and VBF repartition is estimated by comparing the nominal POWHEG+PYTHIA8 samples to a sample with underlying event turned off in PYTHIA8.

For ggH, MPI will add additional jets and hence move events into the jet categories (VBF, VHhad and ttH had, categories 5-7 and 11). The fullsim samples generated with MPI turned off only had

300k events each. The statistical precision on the expected number of events in each category was too poor to obtain a statistically significant estimate of the change in yield relative to the nominal sample. The only category that gives a statistically significant shift is the ttH category, for which the yield ratio is 0.4 ± 0.16, i.e. a 60% drop in yield is observed when the UE is turned off. It hence seems the MPI greatly increase the migration of ggH into this category (that requires at least 5 jets). This is the only uncertainty that is taken directly from the fullsim yield. For the other categories the nominal sample is reweighted based on a fit to the "no-MPI"/"with-MPI" ratio as a function of $\Delta\phi_{\gamma\gamma-jj}$ calculated from the particle level jets. This variable was found to be particularly sensitive to the MPI, probably as the MPI tend to add a dijet system that is (more) uncorrelated with the Higgs, while the di-jet system produced in direct association with the Higgs will tend to be back-to-back with the Higgs (see Yellow Report 3, Section 8.3 [134]). This prescription was followed both for ggH and VBF and the results are summarized in Figure 7.32 and Table 7.15.
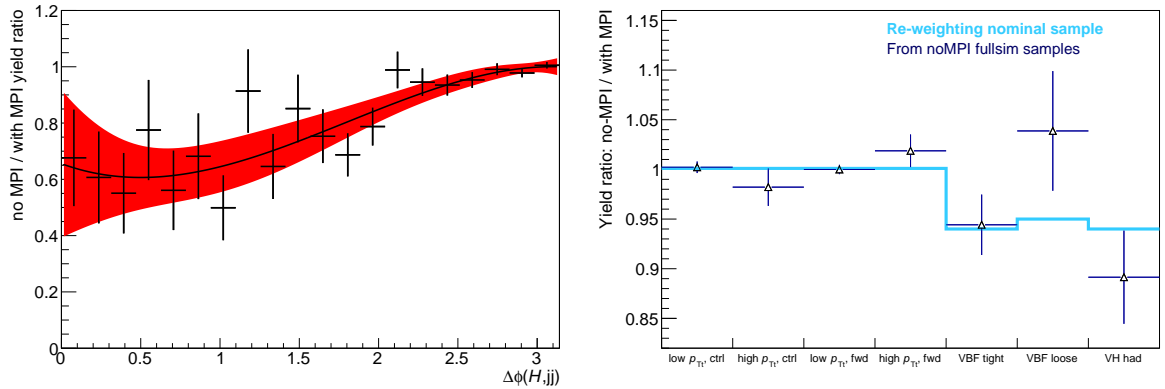
Figure 7.32: *Left: Reweighing function used to propagate the the effect of the UE modelling uncertainty to the events. Right: Impact of turning the modelling of UE off, using the fullsim sample (points) and by re-weighing the nominal sample (light blue line). The reweighting gives more stable results that are consistent within statistics with the (low-stats) fullsim results [105].*

Category	1	2	3	4	5	6	7	8	9	10	11	12
ggH UE uncert.	+0.1%	+0.1%	+0.1%	+0.1%	−6%	−5%	−6%	-	-	-	−60%	−5%
VBF UE uncert.	+1.2%	+1.2%	+1.2%	+1.2%	−2.6%	−1.7%	−2.8%	−2.2%	−1.7%	-	−4%	−4%

Table 7.15: *Migration systematics due to the modelling of the underlying event* [%]. *Turning off the underlying reduces the number of jets in the events, making them migrate migrate towards the untagged categories [105].*

The results in this section was derived with 8 TeV samples. The same procedure was applied to 7 TeV samples and it was found to give consistent results within the statistical precision. The same relative uncertainties are hence assigned also to 7 TeV Monte Carlo.

Material in front of the calorimeter

The material description used to be accounted for in the systematics uncertainties since it can change the fraction of converted photons versus unconverted ones. However, the new categorization for the couplings analysis do not use any more the photon conversion status. Its impact on the signal yield is nonetheless quantified, comparing the signal yields from a Monte Carlo sample with nominal geometry, and a sample simulated with a distorted geometry introducing 5% more material in front of the calorimeter. The impact is found to be negligible.

Jet Energy Scale (JES) and Resolution (JER), JVF and MET

Jets and MET suffer from many systematics uncertainties.

The impact of each of these parameters on the analysis is estimated for each category and each

production mode. Then, a simplification procedure is applied to keep only the parameters giving an uncertainty sizeable with respect to the statistical uncertainty.

The same simplification procedure is applied for all JET and MET uncertainties:

- First, the production modes where uncertainty has the same order of magnitude and where we do expect the same behaviour for these processes (*e.g.* MET impact on ggH and VBF is expected to be small) are merged. It has the advantage of limiting the statistically-induced variations.

- Eventually merge categories for the same reasons;

- Choice of systematics sources leading to an uncertainty at least equal to the statistical uncertainty;

- Finally, the up and down uncertainties are symmetrized: the up and down absolute values are averaged and the sign of the up variation is assigned to the final uncertainty.

The above procedure results in keeping ten nuisance parameters coming from the use of jets in the analysis. Four additional uncertainties related to the soft term scale and resolution in the E_T^{miss} definition are also considered. Tables 7.16 and 7.17 give an order of magnitude of these uncertainties after quadratic sum of all nuisance parameters.

Category	ggH	VBF	ttH	$WH + ZH$
Central+Forward - low p_{Tt}	0.1	3.0	4.4	0.1
Central+Forward - high p_{Tt}	1.0	4.7	4.0	1.4
VBF loose	13	4.0	7.3	13
VBF tight	14	8.7	8.0	12
VH hadronic	3.5	3.4	7.1	2.3
VH E_T^{miss}	0.1	0.3	2.0	0.2
VH one lepton	2.4	3.5	4.0	0.6
VH dilepton	0	0	5.6	1.0
ttH hadronic	18	22	6.8	17
ttH leptonic	15	11	0.5	6.3

Table 7.16: *Size of the uncertainties induced by jet energy scale, resolution and jet vertex fraction systematic on the signal yield in each category and production process in 2012. The numbers are relative % variations obtained by summing in quadrature the contribution of each uncertainty component neglecting the sign of the migration. They are of the same order of magnitude for 2011 and 2012 [125].*

Category	$ggH + VBF$	ttH	WH	ZH
Untagged	0.0	0.2	0.1	0.3
VBF loose	0.0	1.7	0.3	0.2
VBF tight	0.0	2.2	1.1	0.8
VH hadronic	0.0	0.3	0.0	0.1
VH E_T^{miss}	35	1.0	1.2	0.8
VH one lepton	5.1	0.4	0.4	4.0
VH dilepton	0.0	1.0	0.0	0.1
ttH hadronic	0.0	0.0	0.0	0.0
ttH leptonic	2.7	0.1	0.6	2.7

Table 7.17: *Size of the uncertainties induced by the E_T^{miss} energy scale and resolution systematic on the signal yield in each category and production process. The numbers are relative % variations obtained by summing in quadrature the contribution of each uncertainty component neglecting the sign of the migration. They are of the same order of magnitude for 2011 and 2012 [125].*

Lepton scale factors

Differences in selection efficiency for electrons and muons between data and Monte Carlo can also change the repartition of the events in the categories involving leptons (VH-one lepton, VH-dilepton, ttH-leptonic). See Table 7.18 for the detailed value of the systematics applied on the signal yield.

	Category	Electrons					Muons				
		ggH	VBF	ttH	WH	ZH	ggH	VBF	ttH	WH	ZH
2012	VH one lepton	0.53	1.03	0.40	0.43	0.42	0.30	0.16	0.23	0.21	0.25
	VH dilepton	-	-	-	-	-	0.00	0.00	0.29	0.00	0.41
	ttH leptonic	1.62	0.86	0.41	0.40	0.48	0.08	0.15	0.21	0.22	0.20
2011	VH one lepton	1.17	1.63	0.45	0.56	0.56	0.23	0.13	0.21	0.19	0.22
	VH dilepton	-	-	-	-	-	0.0	0.0	0.14	0.05	0.35
	ttH leptonic	2.51	0.94	0.56	0.56	0.63	0.23	0.06	0.18	0.18	0.19

Table 7.18: *Leptons scale factor uncertainties* [%].

b-tagging

Uncertainties on the b-tagging algorithm, used for classifying the events in the ttH categories are summarized in Table 7.19 for 2012. The nuisance parameters are classified according to their impact on the μ_{ttH} measurement and only the first ten are kept (Fig. 7.33). Other nuisance parameters are considered for 2011 dataset (Tab. 7.20).

	mistag48	btag14	btag23	btag24	ctag23	btag19	mistag32	ctag24	btag20	mistag47
					Hadronic category					
ggH	1.200	0.158	0.202	0.012	0.439	8.530	1.540	14.200	1.090	2.270
VBF	0.452	0.366	0.053	0.499	0.807	2.000	1.920	0.109	1.440	3.750
WH	0.294	0.385	0.151	0.556	0.529	2.120	1.840	0.041	1.610	3.760
ZH	0.847	0.131	0.284	0.253	0.204	0.649	0.180	0.069	0.901	1.600
ttH	0.743	0.493	0.246	0.882	0.675	0.281	0.032	0.008	0.216	0.471
					Leptonic category					
ggH	0.375	0.147	0.864	0.033	0.362	7.140	0.408	9.540	0.466	2.480
VBF	0.684	0.383	0.180	0.614	0.466	4.540	4.340	4.560	1.750	4.920
WH	0.047	0.030	0.080	0.065	0.056	0.800	0.637	0.012	0.597	5.380
ZH	0.276	0.153	0.276	0.196	0.302	1.560	4.680	0.031	0.736	3.100
ttH	0.440	0.266	0.180	0.425	0.420	0.104	0.047	0.004	0.076	0.212

Table 7.19: *Flavor tagging systematics in the ttH categories for 2012 data* [%]

	Leptonic category			Hadronic category		
	Btag	CTag	MisTag	Btag	CTag	MisTag
ggH	0.00	0.00	0.00	0.61	15.53	14.48
VBF	0.00	0.00	0.00	0.00	29.03	10.25
WH	0.74	3.40	6.63	0.00	7.82	16.55
ZH	0.80	5.20	4.40	3.98	10.60	3.13
ttH	1.13	0.37	0.27	1.93	1.98	1.54
tHj	2.25	0.32	0.35	1.93	1.98	1.54
WtH	1.66	1.85	0.99	4.03	1.04	1.79

Table 7.20: *Flavor tagging systematics in the ttH categories for 2011 data* [%]
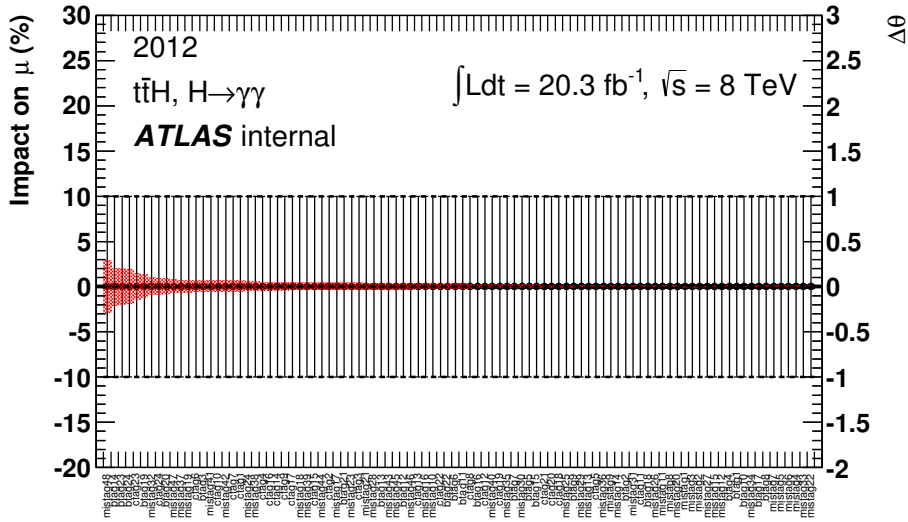
Figure 7.33: *b-tagging nuisance parameters effect on the μ uncertainty using only the ttH categories (red area). Only the first ten are kept in the analysis [195].*

7.4.3.3 Mass systematics

Systematics uncertainties on the signal peak position (ESS for Energy Scale Systematics) and on the signal mass resolution are propagated to the couplings categories with the same method and correlation model than for the mass analysis.

The ESS is accounted for by including 29 new nuisance parameters acting on the Gauss and Crystal-Ball means, following the physics described in [91]. Their values are reported in Tables 7.21 and 7.22. The background modelling is also found to have an impact on the peak position and twelve additional nuisance parameters (one per category) are introduced to account for this uncertainty (Table 7.23).

Four nuisance parameters are added to account for mass resolution systematics [212] whose values per category are reported in Tables 7.24 and 7.25. The four contributions to the resolution corresponds to the asymptotic resolution at high energy (the constant term), the intrinsic fluctuations of the calorimeter, the effect of passive material in front of the calorimeter and the electronic and pileup noise.

7.4.3.4 Background modelling

The fitted signal on a background-only sample, called spurious signal, corresponds to the bias introduced by choosing a given parametrization for the background. It is propagated to the statistical model by adding an additional term:

$$N_{spurious} \cdot f_S \cdot \theta_{spurious} \tag{7.11}$$

where f_S is the signal probability function. $\theta_{spurious}$ is a nuisance parameter, constrained by a unit Gaussian to vary within ± 5. One nuisance parameter is introduced for each category, but it is correlated between the years since the same parametrization is used. The number of spurious signal events to be added in each category is summarized in Table 7.8.

Cat.	1	2	3	4	5	6	7	8	9	10	11	12
Zee	0.03	0.03	0.07	0.09	0.05	0.05	0.05	0.04	0.06	0.03	0.05	0.05
L2Gain	-0.10	-0.18	-0.11	-0.21	-0.15	-0.19	-0.22	-0.23	-0.16	-0.17	-0.18	-0.18
LateralLeakageUC	0.04	0.02	0.04	0.05	0.04	0.05	0.04	0.01	0.03	0.02	0.04	0.03
LateralLeakageCV	0.04	0.03	0.08	0.09	0.06	0.06	0.06	0.06	0.06	0.03	0.06	0.06
ConvInefficiency	0.02	0.00	0.02	0.03	0.02	0.02	0.01	0.00	0.02	-0.01	0.02	0.01
ConvFakeRate	0.01	0.00	0.01	0.03	0.01	0.01	0.00	-0.01	0.01	-0.02	0.01	0.01
Geant4	0.01	0.01	0.01	0.01	0.02	0.01	0.02	-0.01	0.02	-0.02	0.01	0.01
Pedestal	-0.01	-0.03	-0.01	0.00	-0.02	-0.01	-0.02	-0.05	-0.01	-0.03	-0.02	-0.03
ConvRadius	-0.01	-0.01	-0.02	0.00	-0.01	0.00	0.00	-0.03	-0.02	-0.04	-0.01	-0.02
L1Gain	0.00	-0.01	0.05	0.05	0.02	0.02	0.02	0.03	0.03	0.00	0.03	0.01
LArCalib_Barr	-0.10	-0.14	-0.05	-0.06	-0.08	-0.10	-0.09	-0.11	-0.08	-0.12	-0.09	-0.09
LArCalib_EC	0.00	0.00	-0.03	-0.03	-0.01	-0.02	-0.02	-0.01	-0.02	-0.03	-0.01	-0.02
LArUnconvCalib_Barr	0.02	0.02	0.02	0.04	0.03	0.03	0.03	-0.01	0.02	-0.01	0.02	0.02
LArUnconvCalib_EC	0.00	0.00	0.00	0.00	0.00	0.00	0.00	0.00	0.00	0.00	0.00	-0.01
LArElecUnconv_Barr	-0.05	-0.06	-0.09	-0.10	-0.08	-0.08	-0.09	-0.10	-0.08	-0.10	-0.08	-0.08
LArElecUnconv_EC	0.00	0.00	-0.06	-0.06	-0.03	-0.03	-0.04	-0.05	-0.04	-0.04	-0.03	-0.03
LArCalibElec	0.00	-0.01	0.01	0.02	0.01	0.01	0.00	0.00	0.00	-0.02	0.01	-0.02
MatID1	0.07	0.07	0.05	0.05	0.06	0.07	0.05	0.05	0.06	0.04	0.07	0.06
MatID2	0.00	0.00	0.03	0.04	0.02	0.02	0.02	0.00	0.02	0.00	0.02	0.01
MatID3	0.00	0.00	0.02	0.02	0.01	0.00	0.01	0.00	0.01	0.00	0.00	0.00
MatID4	0.00	0.00	0.01	0.01	0.00	0.00	0.00	0.00	0.01	0.00	0.00	0.00
Presampler_Barr	0.04	0.04	0.03	0.02	0.03	0.03	0.03	0.04	0.04	0.03	0.03	0.03
Presampler_EC	0.00	0.00	0.02	0.02	0.01	0.02	0.01	0.02	0.01	0.01	0.01	0.01
S12_Barr	0.02	0.03	0.01	0.01	0.01	0.02	0.02	0.03	0.01	0.03	0.02	0.02
S12_EC	0.00	0.00	0.01	0.01	0.01	0.00	0.01	0.01	0.01	0.02	0.00	0.00
MatCalo_Barr	0.02	0.02	0.02	0.02	0.02	0.02	0.02	0.02	0.02	0.01	0.02	0.02
MatCalo_EC	0.00	0.00	0.00	0.01	0.00	0.00	0.01	0.01	0.00	0.00	0.00	0.00
MatCryo_Barr	0.02	0.02	0.01	0.02	0.02	0.02	0.02	0.02	0.01	0.02	0.02	0.02
MatCryo_EC	0.00	0.00	0.04	0.04	0.02	0.01	0.02	0.03	0.02	0.02	0.01	0.01

Table 7.21: *Photon energy scale systematics impact on the peak position μ_{CB} and $\mu_{Gaussian}$ for 2012 dataset* [%].

Cat.	1	2	3	4	5	6	7	8	9	10	11	12
Zee	0.04	0.05	0.08	0.07	0.06	0.06	0.05	0.07	0.07	0.06	0.06	0.06
L2Gain	-0.10	-0.17	-0.11	-0.22	-0.16	-0.18	-0.23	-0.21	-0.16	-0.15	-0.17	-0.16
LateralLeakageUC	0.03	0.04	0.04	0.04	0.04	0.04	0.02	0.03	0.04	0.05	0.04	0.05
LateralLeakageCV	0.04	0.04	0.09	0.09	0.07	0.07	0.06	0.08	0.08	0.07	0.08	0.08
ConvInefficiency	0.02	0.01	0.02	0.01	0.01	0.02	0.00	0.02	0.02	0.00	0.01	0.03
ConvFakeRate	0.01	0.01	0.02	0.01	0.02	0.03	0.01	0.01	0.02	0.00	0.01	0.02
Geant4	0.01	0.02	0.01	0.01	0.01	0.02	0.01	0.00	0.02	0.00	0.01	0.02
Pedestal	-0.02	-0.02	-0.01	-0.02	-0.02	-0.01	-0.03	-0.01	0.00	-0.03	-0.02	-0.01
ConvRadius	-0.01	-0.02	-0.03	-0.03	-0.02	-0.01	-0.01	-0.02	-0.01	-0.02	-0.02	0.00
L1Gain	0.00	0.00	0.04	0.03	0.02	0.02	0.02	0.02	0.04	0.01	0.02	0.03
LArCalib_Barr	-0.09	-0.10	-0.05	-0.07	-0.08	-0.08	-0.09	-0.09	-0.06	-0.06	-0.08	-0.07
LArCalib_EC	0.00	0.00	-0.03	-0.03	-0.01	-0.01	-0.02	-0.02	-0.02	-0.01	-0.01	-0.01
LArUnconvCalib_Barr	0.02	0.02	0.03	0.02	0.02	0.04	0.02	0.02	0.04	0.03	0.03	0.04
LArUnconvCalib_EC	0.00	0.00	0.00	-0.01	0.00	0.00	-0.01	0.00	0.00	-0.01	0.00	0.00
LArElecUnconv_Barr	-0.05	-0.06	-0.09	-0.11	-0.08	-0.08	-0.10	-0.09	-0.07	-0.07	-0.08	-0.08
LArElecUnconv_EC	0.00	0.00	-0.05	-0.05	-0.02	-0.02	-0.03	-0.03	-0.03	-0.03	-0.02	-0.02
LArCalibElec	0.00	0.00	0.01	0.00	0.00	0.01	0.00	0.01	0.01	0.01	0.00	0.01
MatID1	0.07	0.06	0.05	0.04	0.05	0.06	0.05	0.05	0.06	0.07	0.06	0.07
MatID2	0.00	0.00	0.03	0.04	0.02	0.02	0.02	0.02	0.02	0.03	0.02	0.02
MatID3	0.00	0.00	0.01	0.02	0.01	0.01	0.01	0.01	0.01	0.00	0.01	0.01
MatID4	0.00	0.00	0.01	0.00	0.00	0.00	0.00	0.01	0.00	0.00	0.00	0.00
Presampler_Barr	0.03	0.04	0.03	0.03	0.03	0.03	0.04	0.03	0.03	0.03	0.03	0.03
Presampler_EC	0.00	0.00	0.04	0.04	0.02	0.01	0.03	0.02	0.02	0.02	0.02	0.02
S12_Barr	0.02	0.02	0.01	0.01	0.02	0.02	0.02	0.02	0.01	0.02	0.02	0.02
S12_EC	0.00	0.00	0.01	0.01	0.01	0.00	0.01	0.01	0.01	0.01	0.00	0.00
MatCalo_Barr	0.02	0.02	0.01	0.02	0.01	0.02	0.01	0.01	0.02	0.02	0.02	0.02
MatCalo_EC	0.00	0.00	0.00	0.00	0.00	0.00	0.00	0.00	0.00	0.01	0.00	0.00
MatCryo_Barr	0.02	0.02	0.01	0.01	0.01	0.02	0.01	0.02	0.02	0.02	0.02	0.02
MatCryo_EC	0.00	0.00	0.04	0.04	0.02	0.02	0.02	0.03	0.03	0.02	0.02	0.02

Table 7.22: *Photon energy scale systematics on the peak position μ_{CB} and $\mu_{Gaussian}$ for 2011 dataset* [%].

#	Category	2011	2012
1	Central - low p_{Tt}		0.1
2	Central - high p_{Tt}		0.08
3	Forward - low p_{Tt}		0.08
4	Forward - high p_{Tt}		0.1
5	VBF loose		0.1
6	VBF tight		0.1
7	VH hadronic		0.18
8	VH E_T^{miss}		0.06
9	VH one lepton		0.02
10	VH dilepton		0.2
11	ttH hadronic		
12	ttH leptonic		

Table 7.23: *Background modelling uncertainty on the peak position.*

#	Category	Constant	Intrinsic	Material	Noise
1	Central - low p_{Tt}	7.5	2.6	4.9	2.6
2	Central - high p_{Tt}	9.6	5.6	6.2	1.7
3	Forward - low p_{Tt}	9.9	1.3	6.0	2.1
4	Forward - high p_{Tt}	12	2.8	7.8	1.9
5	VBF loose	9.4	2.6	6.0	2.1
6	VBF tight	10	3.8	6.5	2.1
7	VH hadronic	11	4.0	7.2	1.6
8	VH E_T^{miss}	11	3.6	7.4	1.7
9	VH one lepton	9.8	2.8	6.3	2.1
10	VH dilepton	9.5	2.7	6.2	2.1
11	ttH hadronic	9.6	3.6	6.3	1.9
12	ttH leptonic	9.5	3.4	6.2	2.1

Table 7.24: *Systematic uncertainties on the diphoton mass resolution for the 8 TeV data [%] due to the four contributions described in the text. For each category, the uncertainty is estimated with the simulation of the Higgs boson production process making the largest contribution to the signal yield.*

#	Category	Constant	Intrinsic	Material	Noise
1	Central - low p_{Tt}	7.57	2.64	4.87	0.89
2	Central - high p_{Tt}	9.29	4.93	6.16	1.36
3	Forward - low p_{Tt}	9.60	1.35	6.04	0.63
4	Forward - high p_{Tt}	10.90	2.66	7.16	0.94
5	VBF loose	8.92	2.69	5.78	0.93
6	VBF tight	9.56	3.64	6.20	0.98
7	VH hadronic	10.38	3.63	6.48	1.08
8	VH E_T^{miss}	10.03	3.61	6.98	1.12
9	VH one lepton	9.31	2.67	6.20	0.83
10	VH dilepton	9.07	2.55	5.64	0.57
11	ttH hadronic	9.38	3.46	5.97	1.07
12	ttH leptonic	9.56	3.45	6.21	1.06

Table 7.25: *Systematic uncertainties on the diphoton mass resolution for the 7 TeV data [%] due to the four contributions described in the text. For each category, the uncertainty is estimated with the simulation of the Higgs boson production process making the largest contribution to the signal yield.*

7.4.3.5 Summary

Table 7.26 summarizes the uncertainty sources and the number of nuisance parameters introduced into the model. To these nuisance parameters, one should add the 24 unconstrained parameters for the background normalization (one per category per year) and the background shape parameters.

	Syst. source	# NP	Prefix	Implementation	Comment
Theory	Scales	5	QCDScale_	$N_s^{proc} \times (1 + \delta_i^{proc}\theta_i)$	WH and ZH correlated
	PDF+α_S	2	pdf_	$N_s^{proc} \times (1 + \delta_i^{proc}\theta_i)$	gg or qq initiated
	BR	1	ATLAS_BR_gg	$N_s^{tot} \times (1 + \delta_i^{tot}\theta_i)$	
	Jet-bin	1	QCDscale_3jets	$N_s^{ggH} \times e^{(\sqrt{ln(1+\delta_i^2)})\theta_i}$	
	ttH modelling	2	MOD_Scale	$N_s^{ttH} \times e^{(\sqrt{ln(1+\delta_i^2)})\theta_i}$	
	Extra scale unc.ttH	2	Scale_	$N_s^{proc} \times e^{(\sqrt{ln(1+\delta_i^2)})\theta_i}$	On ggH and WH yields
	HF	1	HF_	$N_s^{proc} \times e^{(\sqrt{ln(1+\delta_i^2)})\theta_i}$	
Exp. incl.	Luminosity	2	ATLAS_LUMI_201x	$N_s^{tot} \times e^{(\sqrt{ln(1+\delta_i^2)})\theta_i}$	Uncorrelated 2011/2012
	Trigger	1	ATLAS_Hgg_Trigger	$N_s^{tot} \times e^{(\sqrt{ln(1+\delta_i^2)})\theta_i}$	
	Photon ID	2	ATLAS_PH_ID	$N_s^{tot} \times e^{(\sqrt{ln(1+\delta_i^2)})\theta_i}$	Uncorrelated 2011/2012
	Isolation	2	ATLAS_PH_ISO	$N_s^{tot} \times e^{(\sqrt{ln(1+\delta_i^2)})\theta_i}$	Uncorrelated 2011/2012
Stat	Limited MC stat	4	ATLAS_stat_	$N_s^{proc} \times (1 + \delta_i^{proc}\theta_i)$	Pruning is used
Migrations	JES	17	ATLAS_JES_	$N_s^{proc} \times (1 + \delta_i^{proc}\theta_i)$	
			ATLAS_JER_	$N_s^{proc} \times (1 + \delta_i^{proc}\theta_i)$	
			ATLAS_JVF_	$N_s^{proc} \times (1 + \delta_i^{proc}\theta_i)$	
	MET	4	ATLAS_MET_	$N_s^{proc} \times (1 + \delta_i^{proc}\theta_i)$	
	Lepton SF	2		$N_s^{proc} \times (1 + \delta_i^{proc}\theta_i)$	
	B tagging	10	ATLAS_BTag_	$N_s^{proc} \times (1 + \delta_i^{proc}\theta_i)$	
	$\Delta\phi_{jj}$	1		$N_s^{ggH} \times (1 + \delta_i^{proc}\theta_i)$	
	η^*	1		$N_s^{ggH} \times (1 + \delta_i^{proc}\theta_i)$	
	UE+PS	1	ATLAS_UEPS	$N_s^{proc} \times (1 + \delta_i^{proc}\theta_i)$	
	Higgs p_T	1	ATLAS_Hgg_Pt_MOD	$N_s^{ggH} \times (1 + \delta_i^{proc}\theta_i)$	
Mass	Mass energy scale	43	ATLAS_MSS_	$\mu_{CB} \times (1 + \delta_i^{tot}\theta_i)$	All correlated 2011/2012
				$\mu_{Gauss} \times (1 + \delta_i^{proc}\theta_i)$	except Pedestal
	Mass resolution	4	ATLAS_Hgg_mass_Res_	$\sigma_{CB} \times e^{(\sqrt{ln(1+\delta_i^2)})\theta_i}$	
				$\sigma_{Gauss} \times e^{(\sqrt{ln(1+\delta_i^2)})\theta_i}$	
Bkg	Spurious signal	12	ATLAS_Hgg_BIAS_Cat	$N_{spurious}^{cat} \times f_s^{cat} \times \theta_{spurious}^{cat}$	Correlated 2011/2012

Table 7.26: *Summary of nuisance parameters. When acting on N_s^{tot}, the uncertainty value is the same for all processes, contrarily to the case denoted N_s^{proc} where the uncertainty has a different value depending on the signal process.*

7.4.3.6 Uncertainty breakdown

To quantify the impact of the uncertainties on the measurement, they are grouped into several categories:

- The statistical uncertainty is always present and contained in particular into the background shape and normalization parameters;

- Theoretical systematics uncertainties.

- Experimental systematics uncertainties.

The statistical uncertainty only is obtained by fixing all the systematics nuisance parameters to 0. We then recompute the error on the parameter of interest and subtract in quadrature from the total error. The impact of each group of systematics is computed in a similar way, fixing to 0 all nuisance parameter except the ones belonging to the group of interest, and subtracting the statistical error from the fit result in these conditions.

7.4.4 Expected improvements

A test is performed with an Asimov dataset at $\mu = 1$. Table 7.27 shows the expected improvement on the uncertainties on $\mu_{ggH+ttH}$, μ_{VBF} and $\mu_{WH+ZH} \equiv \mu_{VH}$, only measured parameters for the Moriond 2013 analysis. Up to 38% improvements is expected for the μ_{VH} uncertainty.

	Moriond 2013		New analysis		Improvement [%]
	Err+	Err-	Err+	Err-	
μ	0.265	0.302	0.241	0.263	12
$\mu_{ggH+ttH}$	0.354	0.403	0.329	0.356	10
μ_{VBF}	0.728	0.844	0.657	0.750	12
μ_{VH}	1.276	1.465	0.889	1.114	38

Table 7.27: *Expected uncertainties from an Asimov dataset at $\mu = 1$ and fixed mass. The improvement is estimated averaging the up and down expected uncertainty.*

7.5 Results for $\gamma\gamma$

The different results of this analysis are presented in this section. After presenting the observed number of events and invariant mass spectra, a global μ fit is performed and the results compared to the previous analysis of the same dataset (Moriond 2013) and to the mass analysis, using different categorization. The results of the fit to the individual signal strength μ_X are presented in a second time.

7.5.1 Invariant mass distributions in data

Following the selection described above, the number of events observed in 2011 and 2012 datasets are summarized in Table 7.28. No event is observed in the VH-dilepton category in 2011, that will bring constraints on the μ_{ZH} measurements as we shall see later.

The $m_{\gamma\gamma}$ distributions is illustrated in Figure 7.34, where the events are weighted by the signal-to-noise ratios of their category, according to Table 7.6 or 7.7.

Cat.	Incl.	1	2	3	4	5	6	7	8	9	10	11	12
2011	17225	4400	141	12131	429	58	7	34	14	5	0	3	3
2012	94566	24080	806	66394	2528	411	67	185	35	38	2	15	5

Table 7.28: *Repartition of the selected events among the 12 categories for data. The first column is the inclusive number of events [105].*

The detailed invariant mass spectra per category and per year are displayed in the Appendix A. The VBF and ttH categories both contain candidate signal event(s). This is not the case of the VH-dilepton category in which the two observed events in the combined 2011+2012 dataset are at the edge of the $m_{\gamma\gamma}$ spectrum.

Figure 7.35 shows the S/B weighted $m_{\gamma\gamma}$ spectra for each group of categories for the combination of the 2011 and 2012 dataset (S/B ratios for each categories are taken from Tables 7.6 and 7.7).
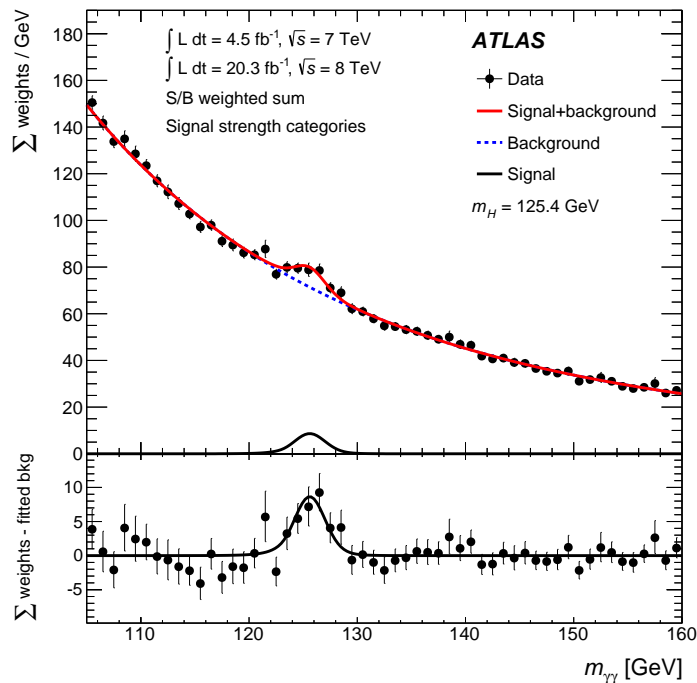
Figure 7.34: *Diphoton invariant mass spectra observed in combined 2011+2012 dataset. The events are weighted by the signal-to-noise ratio of each category [125].*

(a) Untagged

(b) VBF

(c) VH

(d) ttH
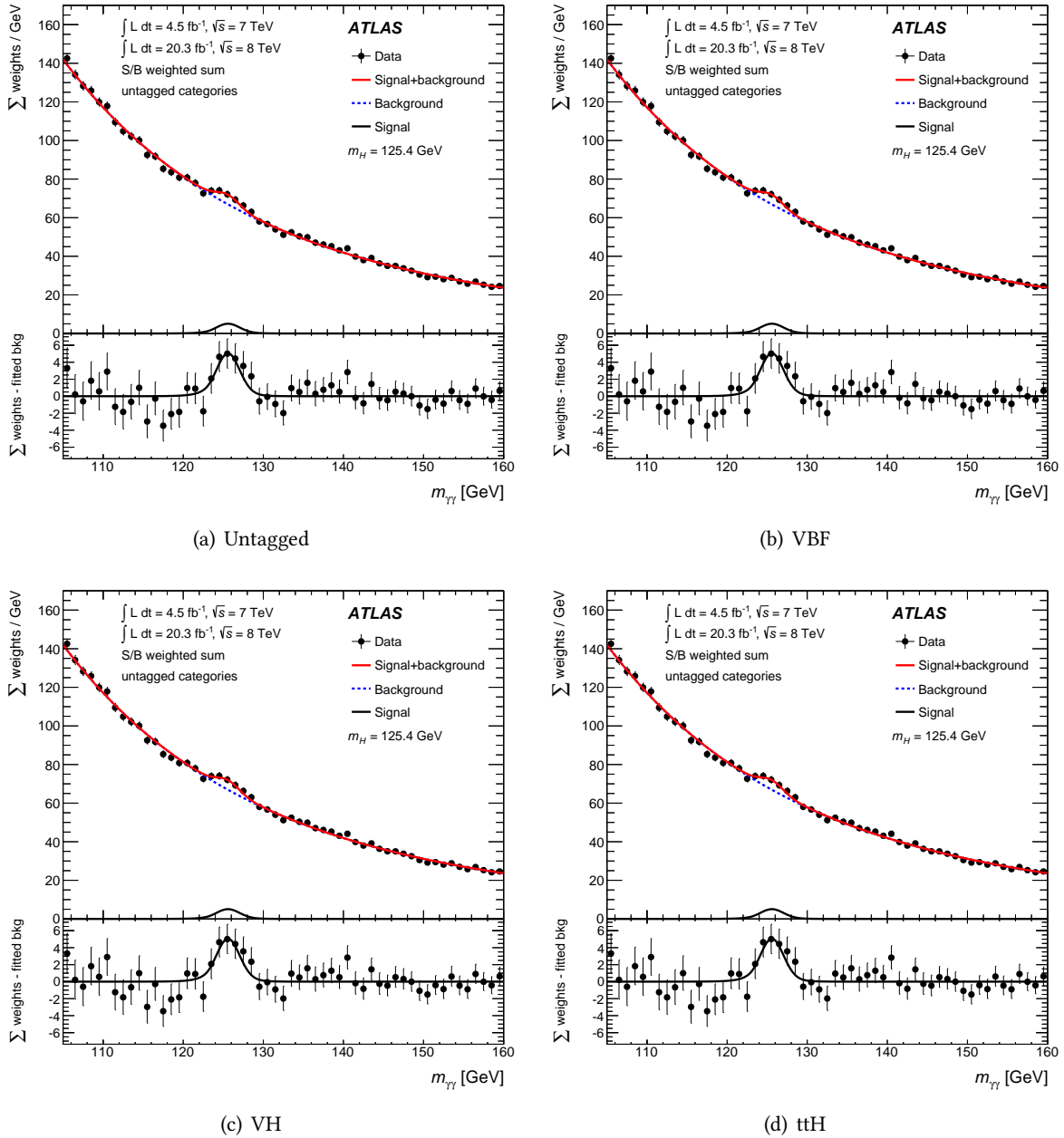
Figure 7.35: *Diphoton invariant mass spectra observed in combined dataset for the different groups of categories. The events are weighted by the signal-to-noise ratio of each category [125].*

7.5.2 Mass and inclusive signal strength

7.5.2.1 Couplings categories result

For the first time for the final analysis of Run I dataset, the mass and couplings analyses use different categorization. The mass analysis is detailed in Ref. [213] and the main results were shown in Section 6.6.3.1 of this document.

With the couplings categories, the local significance of the excess is found to be 5.2σ (4.7σ expected).

The best fit signal strength at the ATLAS combined mass ($m_H = 125.4$ GeV) is found to be:

$$\mu = 1.17^{+0.23}_{-0.23} \text{ (stat) } ^{+0.10}_{-0.08} \text{ (syst) } ^{+0.12}_{-0.08} \text{ (theory)}$$

The observed improvement on the μ uncertainty with respect to the previous Moriond 2013 analysis [127] is of the order of $\frac{0.35}{0.28} = 25\%$. The systematics uncertainty is dominated by the signal mass resolution (0.08), the luminosity (0.03) and the remaining experimental uncertainties (0.03).

The details of the results for the fit of the 2011 and 2012 datasets separately, compared with the results from the mass categorization, are given in Table 7.29.

Dataset	Analysis	Mass [GeV]	μ
7 TeV	M	$124.49^{+0.55}_{-0.57}$ (stat) $^{+0.28}_{-0.31}$ (syst)	$1.63^{+0.62}_{-0.60}$ (stat) $^{+0.30}_{-0.19}$ (syst)
	C	$123.86^{+0.63}_{-0.69}$	$1.66^{+0.57}_{-0.56}$ (stat) $^{+0.23}_{-0.12}$ (syst) $^{+0.21}_{-0.10}$ (theory)
8 TeV	M	$126.30^{+0.36}_{-0.37}$ (stat) $^{+0.29}_{-0.30}$ (syst)	1.33 ± 0.27 (stat) $^{+0.19}_{-0.12}$ (syst)
	C	$126.46^{+0.44}_{-0.44}$	$1.29^{+0.25}_{-0.25}$ (stat) $^{+0.10}_{-0.07}$ (syst) $^{+0.13}_{-0.09}$ (theory)
Combined	M	125.98 ± 0.42 (stat) $^{+0.28}_{-0.27}$ (syst)	1.29 ± 0.25 (stat) $^{+0.19}_{-0.13}$ (syst)
	C	$126.24^{+0.37}_{-0.38}$ (stat) $^{+0.31}_{-0.30}$ (syst)	$1.17^{+0.23}_{-0.23}$ (stat) $^{+0.10}_{-0.08}$ (syst) $^{+0.12}_{-0.08}$ (theory)

Table 7.29: *Comparison of the results on μ and mass combined fit for different datasets between the mass (M) and couplings (C) analyses [105].*

Several discrepancies are observed and investigated further in the following:

- The combined signal strength in the couplings analysis is smaller than the one obtained with the mass categories. This can be related to the larger mass difference. Indeed, the μ dependence with the mass is illustrated in Figure 7.36 with all the systematics and with the mass energy scale systematics, allowing the peak to move, fixed to 0 (Fig. 7.36(a)). In the later case, the fitted μ decreases quickly when the mass get away from the best fit mass for each year. The combined μ is the (weighted) average between the two years. Since the mass two peaks are shifted, the combined μ at the combined mass is lower than the fitted μ in each dataset, at the corresponding best fit mass. When the mass scale systematics are taken into account, the fitted μ is flatter close to the peak. At a mass $m_H \approx 125$ GeV, *i.e.* between the 2011 and 2012 peaks, the systematics can push towards the peak when considering only one year. When both years are considered and since the peak position systematics are correlated between both years, this can not happen and the fitted combined μ is lower than the average of the two years.

- The fitted mass in the couplings analysis is different by 2.6 GeV between 2011 and 2012. A compatibility study is presented in Section 7.5.2.2 about this mass difference.

(a) No mass sytematics [105]

(b) Full systematics [105]

(c) Combined result [125]
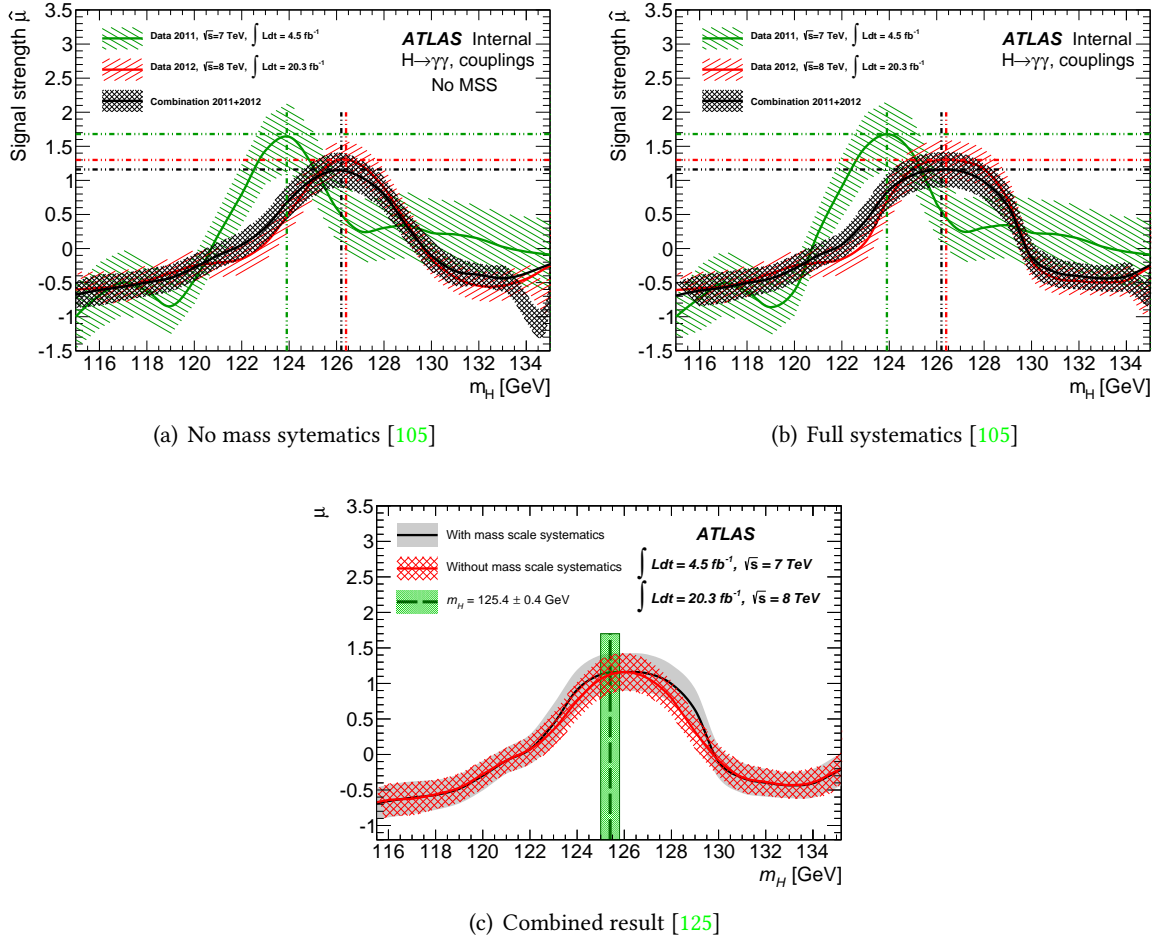
Figure 7.36: *Fitted signal strength as a function of the fixed Higgs mass for data with and without the mass scale systematics.*

7.5.2.2 Compatiblity between 2011 and 2012 masses in the couplings analysis

In order to test the compatibility of the two masses measured with the 2011 and 2012 datasets, several checks were performed.

The first checks consists in measuring an independent mass in each category by fitting a Δ_i parameter representing a shift with respect to the combined mass m_H, similarly to the method used to quantify the compatibility between the $\gamma\gamma$ and $4l$ masses. The profile likelihood for category i is expressed in Equation 7.12, in which the common signal strength among the categories belongs to the nuisance parameters θ.

$$q(\Delta_i) = -2ln\left(\frac{\mathcal{L}_i(\Delta_i, \hat{\hat{m}}_H, \hat{\hat{\theta}})}{\mathcal{L}_i(\hat{\Delta}_i, \hat{m}_H, \hat{\theta})} \times \frac{\prod_{j\neq i}\mathcal{L}_j(\hat{\hat{m}}_H, \hat{\hat{\theta}})}{\prod_{j\neq i}\mathcal{L}_j(\hat{m}_H, \hat{\theta})}\right) \tag{7.12}$$

The compatibility corresponds to the evaluation of the test statistics 7.12 at $\Delta_i = 0$ and is translated into a number of (two-sided) standard deviations with the formula:

$$\sigma_i = \sqrt{q(\Delta_i = 0)} \tag{7.13}$$

in the asymptotic approximation.

This procedure is first applied to the 2011 and 2012 datasets separately, for each of the 12 categories. The signal strength is chosen to be the same in all categories. The ZH category where there is obviously no signal is ignored for this test. The results are summarized in Figure 7.37.

(a) 2011 (b) 2012
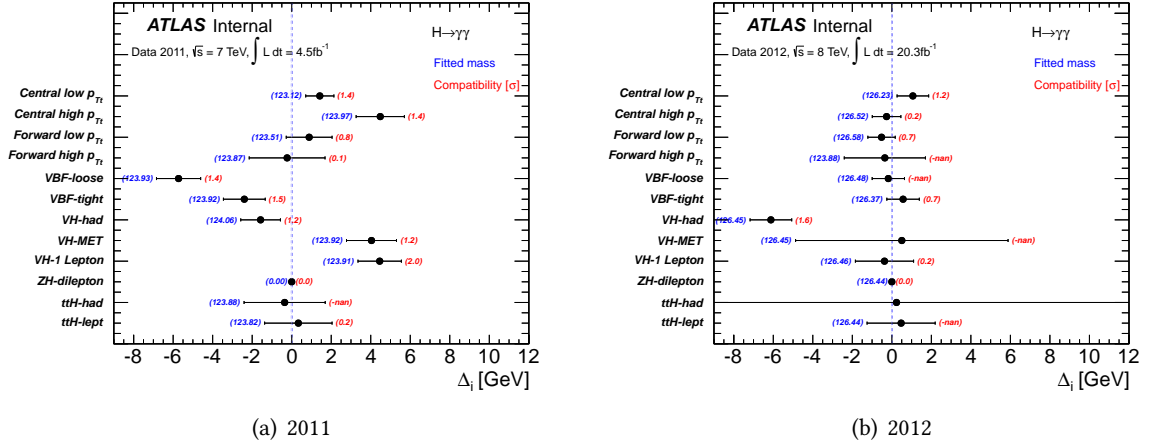
Figure 7.37: *Compatibility among categories for 2011 and 2012 separately. The results for the ZH category are arbitrarily set to 0. The blue numbers are the fitted combined mass in each case. The red numbers are the compatibility with the blue combined mass from Equation 7.13 with two-sided asymptotic approximation [105].*

The compatibility of the results among the categories is rather good for the 2012 dataset. For the 2011 dataset, larger discrepancies are observed. However, this has to be contrasted with the effect illustrated on Figure 7.38, due to the non-asymptoticity of the model. The likelihood scan of the Δ_{Cat5_2011} (corresponding to VBF-loose) clearly shows that the absolute minimum of the likelihood is obtained for a mass farer from the peak. This also explains the values of the compatibilities on Figure 7.37, that sometimes seem to be small compared to the error bars.
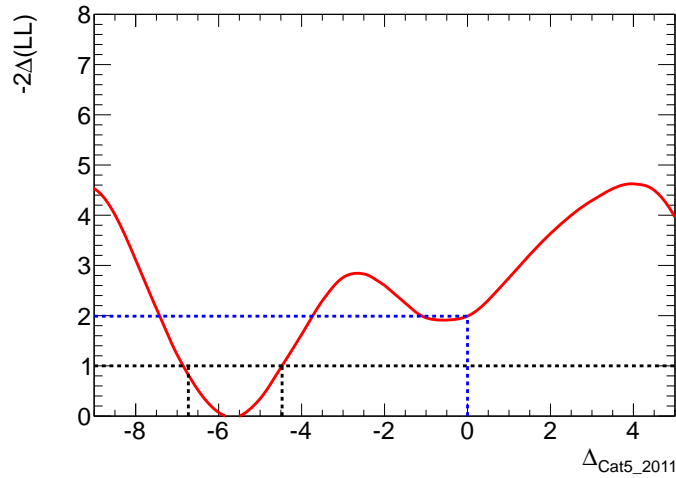
Figure 7.38: *Likelihood scan for the VBF-loose category in 2011 (Cat5) [105].*

The second check consists in assessing the compatibility of the mass measured in 2011 and 2012. The signal strength for 2011 and 2012 are constrained to be equal. The likelihood scan of $\Delta_{2011} = m_H^{2011} - m_H^{2012}$ is illustrated in Figure 7.39. The compatibility between the two measured masses reaches 3.4σ with the asymptotic approximation.

This result is checked with toys, making no assumption on the asymptoticity, as illustrated in Figure 7.40 that shows the $q(\Delta = 0)$ distribution, where $q(\Delta = 0)$ is computed for each toy. The vertical black line represents the $q(\Delta = 0)$ value measured for real data. The p-value is computed as the ratio of the number of toys having $q(\Delta = 0) > q(\Delta = 0)_{data}$ to the total number of toys. Using toy data, the compatibility of the measured mass between 2011 and 2012 is 3.1σ, which is the retained
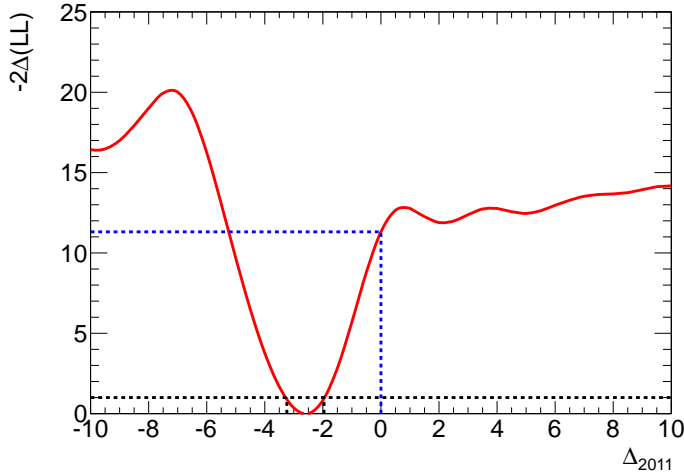
Figure 7.39: *Likelihood scan of the Δ_{2011} parameter of interest [105].*

number. Another approach (Fig. 7.41) consists in fitting the $\hat{\Delta}$ distribution in each toy with a Gaussian. The fitted standard deviation is found to be $\sigma = 0.77$ GeV. The measured Δ in data is 2.6 GeV, *i.e.* 3.4σ away from $\Delta = 0$.
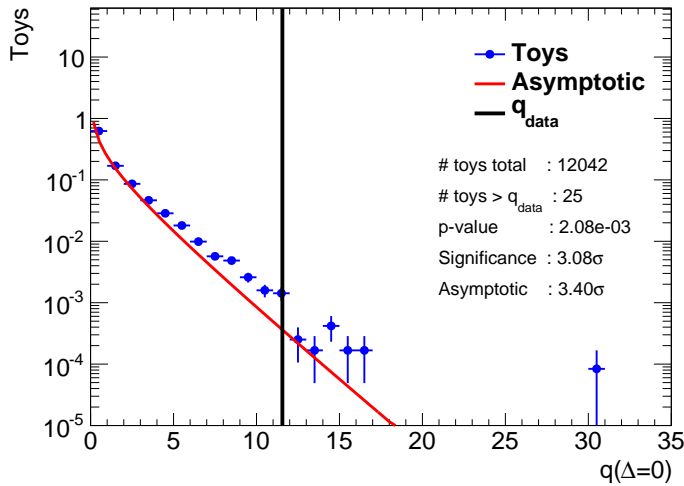
Figure 7.40: $q(\Delta = 0)$ *distribution in toys compared to asymptotic expectations [105].*

The low mass measured in the 2011 dataset is further investigated by looking at the fitted mass in the tagged/untagged categories. Figure 7.42 shows the mass difference between tagged and untagged categories, in 2011 and 2012 datasets. There is a large difference between the tagged categories of 2011 and 2012 datasets, which mainly explains why the mass difference between the 2011 and 2012 datasets is smaller for the mass analysis than for the couplings categorization (Tab. 7.29).

This mass difference between 2011 and 2012 datasets cannot be explained by the photons calibration that was tested for both years and where no worrying difference was observed (see Sec. 5.3).

(a) $\hat{\Delta}$ distribution in toys and Gaussian fit of the core of the distribution

(b) $q(\Delta = 0)$ VS $\hat{\Delta}$
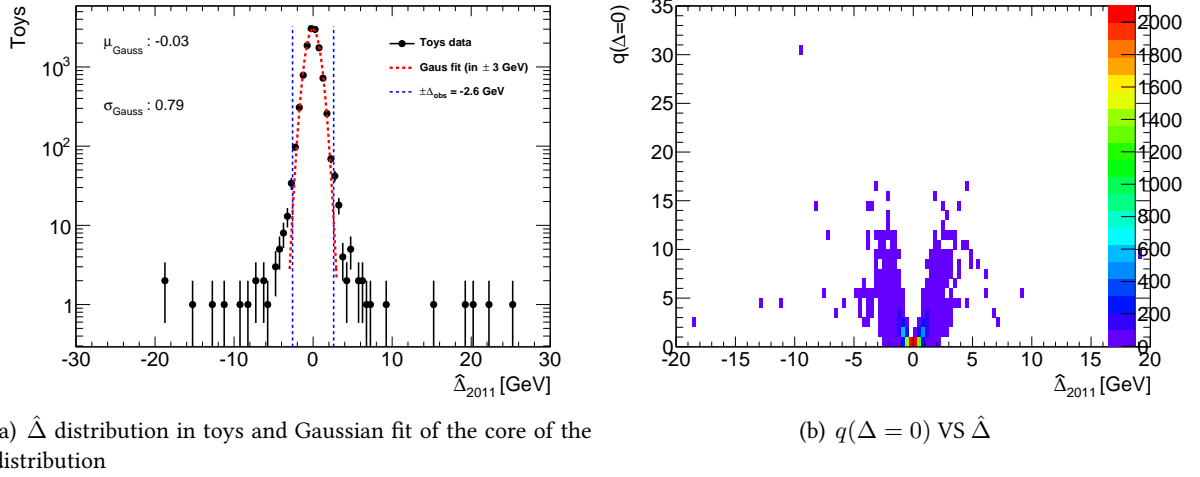
Figure 7.41: *Cross-checks on the toys for the compatibility between 2011 and 2012 measured mass with the couplings categories [105].*
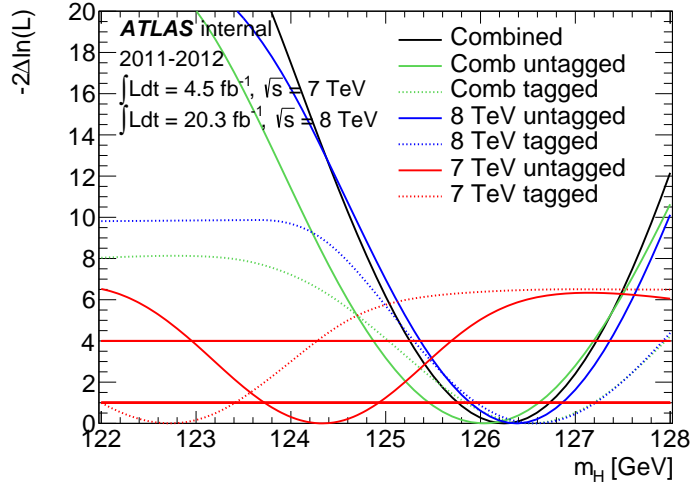
Figure 7.42: *Likelihood scan of m_H in the tagged and untagged categories in 2011, 2012 dataset and the combination [105].*

7.5.2.3 Compatibility with Moriond 2013 result

The new couplings analysis using the selection and categorization described in this document (the "new" analysis) yields slightly different results than the analysis of the same dataset performed for the Moriond 2013 conference (the "old" analysis). The goal of the jackknife technique [214, 215] is to quantify the probability that $\Delta\mu = \mu^{old} - \mu^{new}$ and $\Delta m_H = m_H^{old} - m_H^{new}$ deviate from 0.

The jackknife procedure is the following:

1. Generate a pseudo-dataset j by removing d events from the observed dataset. Each event can be removed once and only once, meaning that $g = N/d$ pseudo-datasets can be created from a dataset containing N events. The dependence of the results with the size of the sample of removed events , d, is also tested.

2. For each pseudo-dataset j, evaluate the estimator θ_i. In our case, θ is the signal strength or the mass.

3. The variance of θ can then be evaluated using the following formula:

$$V(\theta) = \frac{g-1}{g} \sum_{j=1}^{g} (\bar{\theta} - \theta_{(j)})^2; \quad \text{with } \bar{\theta} = 1/g \sum_{j=1}^{g} \theta_{(j)} \tag{7.14}$$

4. A correlation coefficient can be extracted from formula 7.15.

$$\rho = \frac{\text{cov}(\theta_{old}, \theta_{new})}{\sqrt{\text{V}(\theta_{old})\text{V}(\theta_{new})}} \tag{7.15}$$

The jackknife technique is used to quantify the agreement between the old μ (Tab. 7.30) and m_H (Tab. 7.31) measurements and the new ones, for the 2011, 2012 datasets separately and the combination of both datasets. For an estimator θ, $\Delta\theta$ is the observed difference between old and new measurements. $\delta(\Delta\theta)$ is the RMS of the distribution of $\Delta\theta$ from the g pseudo-datasets obtained with the jackknife technique. The compatibility is computed as $\Delta\theta/\delta(\Delta\theta)$.

For the mass measurement, the compatibility is computed from the hypothesis $\Delta m_H = 0$. However, due to the change of calibration, the mass shift is expected to be 0.45 GeV. The compatibility of the difference with respect to this hypothesis is also quantified.

For the mass, the larger incompatibility is obtained for the 2011 dataset, as expected from the larger mass difference (2.39 GeV), but all numbers are below 3σ. For the signal strength measurement, the larger difference is achieved for the combined dataset, related to the mass difference.

Year	$\Delta\mu$	$\delta(\Delta\mu)$	ρ [%]	σ ($\Delta\mu = 0$)
2011 (d=20)	1.03	0.60	60.0	1.7
2012 (d=100)	0.25	0.18	74.2	1.4
2011+2012 (d=100)	0.40	0.18	70.4	2.2

Table 7.30: *Results of the jackknife method applied on the μ difference between old and new analysis for 2011, 2012 and 2011+2012 datasets at fixed $m_H = 125.4$ GeV [105].*

Year	Δm_H	$\delta(\Delta m_H)$	ρ [%]	σ ($\Delta m_H = 0$)	σ ($\Delta m_H = 0.45$)
2011	2.39	0.71	15.8	3.3	2.7
2012	0.47	0.35	52.3	1.4	0.1
2011+2012	0.59	0.40	47.5	1.5	0.35

Table 7.31: *Results of the jackknife method applied on the m_H difference between old and new analysis for 2011, 2012 and 2011+2012 datasets. The compatibility is given for the hypothesis of no mass deviation between the two analyses, and a deviation of 0.45 GeV due to the new calibration [105].*

The impact of varying d on the combined dataset with μ as estimator is also checked. The results are shown in Table 7.32.

d	$\delta(\Delta\mu)$	ρ [%]	σ ($\Delta\mu = 0$)
20	0.15	74.2	2.7
50	0.18	72.9	2.3
100	0.18	70.4	2.2
200	0.17	73.0	2.4
300	0.17	72.2	2.4
400	0.16	73.4	2.6
500	0.15	73.2	2.7

Table 7.32: *The impact of varying d on combined dataset with μ as estimator [105].*

7.5.2.4 Comparison to the mass analysis

Table 7.29 shows that the measured mass with the couplings categories is lower than the one obtained from the mass categories. It is related to the lower measured mass in the tagged categories, as can be seen from Figure 7.42.

Figure 7.43 shows the S/B weighted spectra from the mass and couplings categories. The slightly lower measured mass with respect to the mass analysis is visible, especially in 2011 dataset.

(a) 2011   (b) 2012
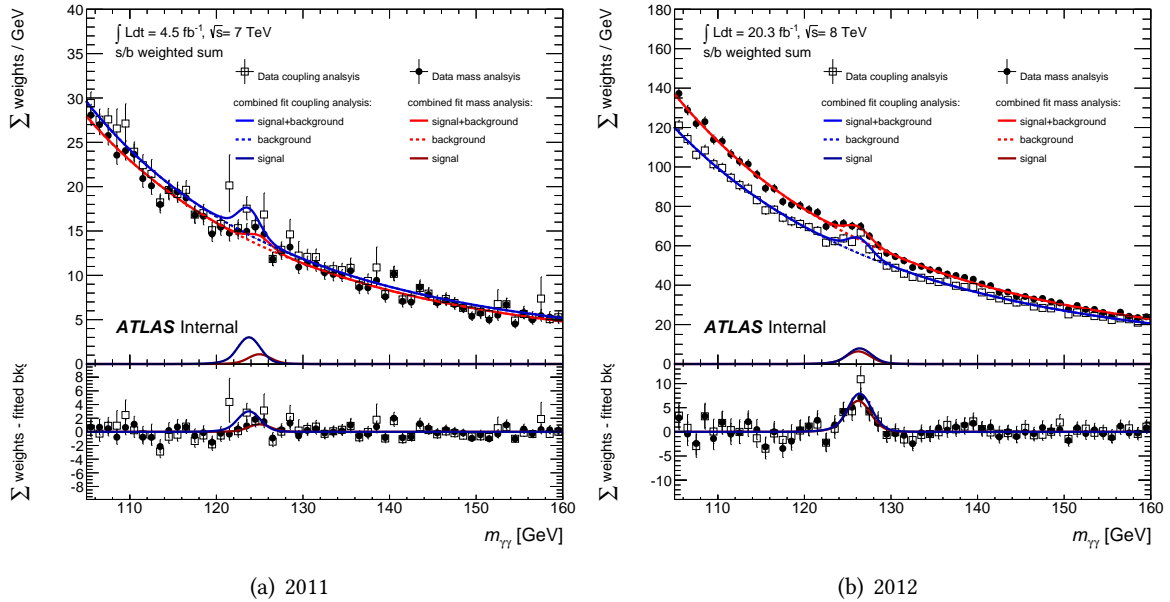
Figure 7.43: *Comparison of the weighted mass spectra for the mass and couplings categories of the final Run I analysis [105].*

The compatibility of the measured signal strength with both categorizations are estimated with the jackknife technique, and the compatibility are found to be below 1σ for the 2011, 2012 and combined datasets.

7.5.3 Individual signal strengths

In the previous section, all signal processes were scaled by the same factor $\mu = \frac{N_{ggH}^{obs}}{N_{ggH}^{SM}} = \frac{N_{VBF}^{obs}}{N_{VBF}^{SM}} = ...$ In the following, each production mode is scaled by its own factor, except bbH and tH which are fixed to its Standard Model expectation, *i.e.* $\mu_{bbH} \equiv \mu_{tH} \equiv 1$.

7.5.3.1 Comparison to Moriond 2013 result

In the Moriond 2013 analysis, only $\mu_{ggH+ttH}$, μ_{VBF} and $\mu_{VH} \equiv \mu_{WH+ZH}$ were measured. This measurement is repeated for the new selection and categorization. Table 7.33 shows the results of both measurements. It has to be compared to Table 7.27 showing the expected improvement from an Asimov dataset.

Table 7.34 presents the compatibility between both analyses, estimated using the jackknife technique.

Even if μ_{VBF} has been divided by a factor of 2, the uncertainty on this measurement is very large and the compatibility with the previous result is 1.5σ.

Figure 7.44 shows the μ_{VBF} versus μ_{ggH} contour plot. Contrarily to the strategy adopted for the Moriond 2013 result, for the left plot, μ_{VH} and μ_{ttH} are profiled. The agreement with the Standard Model is increased from 2σ at the time of Moriond 2013 to less than 1σ for the new analysis.

	Old		New		Improvement [%]
μ	Central	Unc.	Central	Unc.	
ggH	1.47	0.34	1.30	0.29	+17
VBF	1.80	0.80	0.78	0.68	+18
VH	1.62	1.32	0.74	0.89	+48

Table 7.33: *Measured value for the different μ_X at $m_H = 125.4$ GeV and comparison to the previous analysis. Uncertainties are approximated with symmetric errors.*

Year	μ_{old}	μ_{new}	$\Delta\mu$	$\delta(\Delta\mu)$	ρ [%]	$\sigma(\Delta\mu = 0)$
$\mu_{ggH+ttH}$	1.47	1.30	0.18	0.24	71.6	0.8
μ_{VBF}	1.79	0.78	1.02	0.69	60.5	1.5
μ_{VH}	1.63	0.74	0.89	1.20	54.1	0.7

Table 7.34: *Results of the jackknife method to quantify the agreement between the previous and new measurements of $\mu_{ggH+ttH}$, μ_{VBF} and μ_{VH}. m_H fixed to 125.4 GeV [105].*
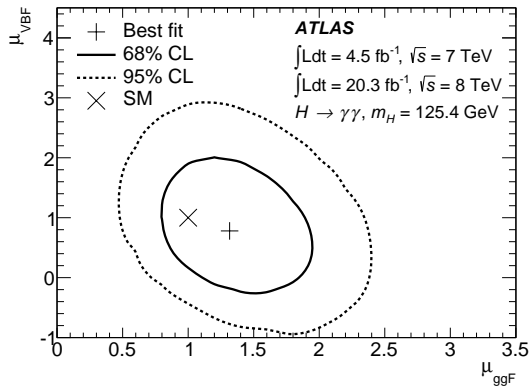
(a) Moriond 2013 [127]   (b) New analysis [125]

Figure 7.44: *μ_{VBF}-μ_{ggH} contour from $\gamma\gamma$ channel only. For the new analysis, μ_{bbH} is fixed to the Standard Model expectations and the other processes are profiled.*

7.5.3.2 Separation of the five production modes

Finally, each of the five production modes signal strength is now allowed to vary independently. The fit result is illustrated on Figure 7.45 for the 2011+2012 combination. The dashed vertical line on this plot for μ_{ZH} illustrates the cut-off introduced, constraining the pdf to be positive on the full mass range.
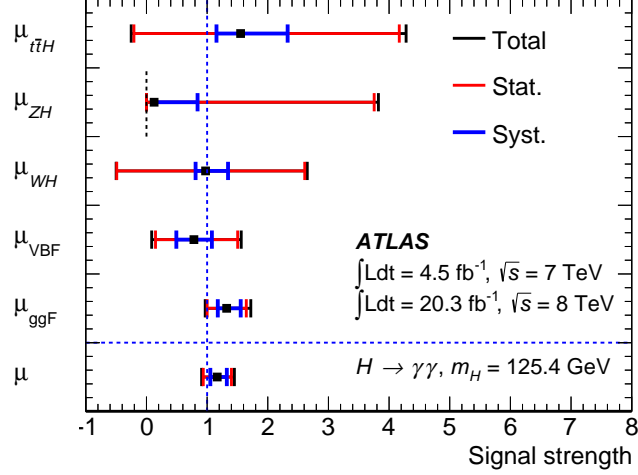
Figure 7.45: *Summary of the individual signal strength fit [125].*

The final result including the uncertainty breakdown is:

$$\mu_{ggH} = 1.32^{+0.32}_{-0.32}(stat.) \, ^{+0.23}_{-0.15}(syst.)$$
$$\mu_{VBF} = 0.78^{+0.72}_{-0.63}(stat.) \, ^{+0.30}_{-0.29}(syst.)$$
$$\mu_{WH} = 0.97^{+1.64}_{-1.46}(stat.) \, ^{+0.36}_{-0.17}(syst.)$$
$$\mu_{ZH} = 0.13^{+3.62}_{-0.13}(stat.) \, ^{+0.64}_{-0.00}(syst.)$$
$$\mu_{ttH} = 1.55^{+2.62}_{-1.75}(stat.) \, ^{+0.79}_{-0.36}(syst.)$$

A cut-off in the likelihood scan of μ_{ZH} is observed, due to the fact that no events are selected in the signal region, and to prevent the pdf in this category to become negative. This is also the reason why the negative uncertainties are null.

7.5.3.3 Ratios to ggH

The ratios of coupling strength of VBF, VH and $t\bar{t}H$ to ggH are studied. They allow to reduce the systematics uncertainties common to all processes (for instance the luminosity).

The likelihood scans of those parameters of interest can be found in Figure 7.46. The numeric results are:

$$\mu_{VBF}/\mu_{ggH} = 0.59^{+0.77}_{-0.53} \text{ This gives } 1.2\sigma \text{ evidence of VBF production}$$
$$\mu_{VH}/\mu_{ggH} = 0.56^{+1.06}_{-0.56} \text{ This gives } 0.7\sigma \text{ evidence of VH production.}$$
$$\mu_{t\bar{t}H}/\mu_{ggH} = 1.18^{+2.18}_{-1.37} \text{ This gives } 0.8\sigma \text{ evidence of ttH production.}$$

(a) μ_{VBF}/μ_{ggH}

(b) μ_{VH}/μ_{ggH}

(c) $\mu_{t\bar{t}H}/\mu_{ggH}$
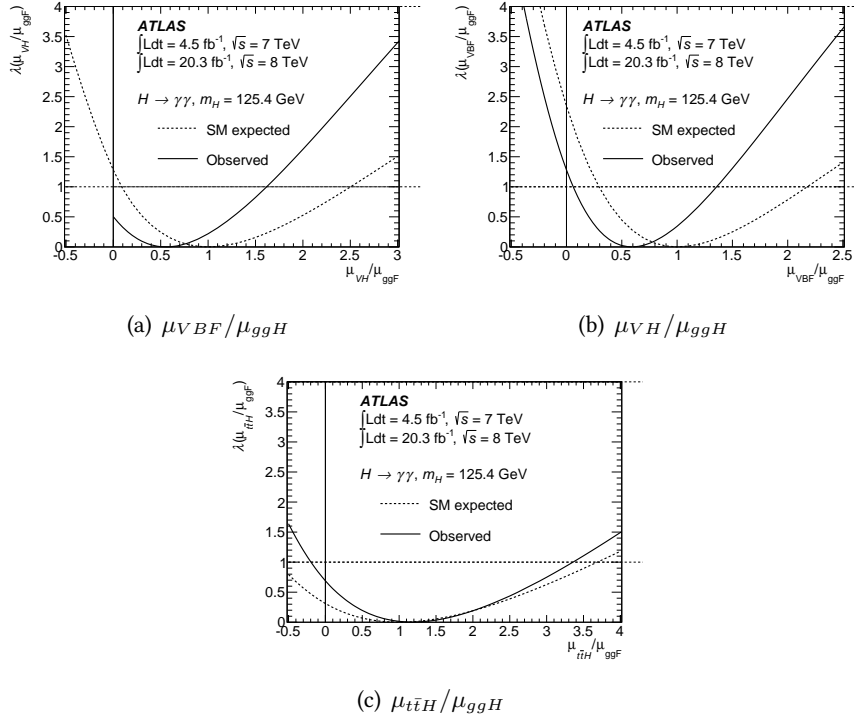
Figure 7.46: *Likelihood scan for μ_X/μ_{ggH}* [125].

7.5.3.4 $\kappa_F-\kappa_V$ contour

A parametrization of the different signal strength μ_X allows to measure κ_V and κ_F, the couplings to bosons and fermions scale factors.

The $\kappa_F-\kappa_V$ contour obtained from the $H \rightarrow \gamma\gamma$ analysis only is presented in Figure 7.47. The observations agree with the Standard Model within 1σ.
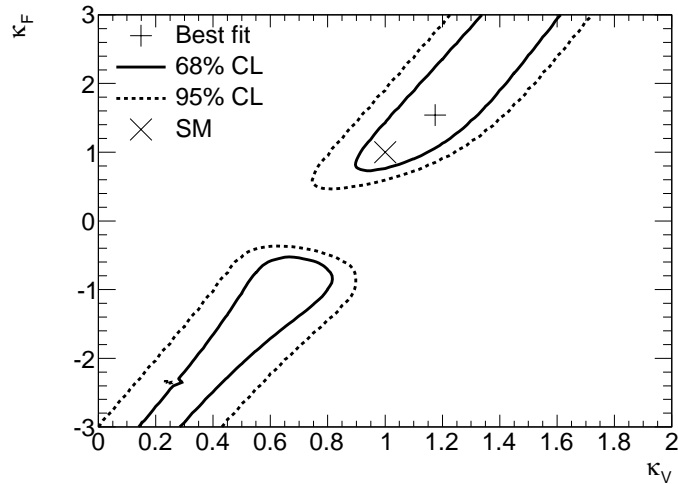
Figure 7.47: *κ_V-κ_F contour from $\gamma\gamma$ channel only* [125].

7.5.4 Comparison with CMS

Very recently, CMS has published its final results [216] on the $H \to \gamma\gamma$ channel. The results are very similar to the one obtained by ATLAS.

The observed (expected) significance of the excess is 5.7σ (5.2σ).

The mass measured in the $\gamma\gamma$ final state is $124.70 \pm 0.31(stat) \pm 0.15(syst)$ GeV in agreement with the ATLAS value of 125.98 ± 0.50 GeV (2.1σ difference with a naive error combination).

Finally, the signal strength in CMS is found to be (at the $\gamma\gamma$ best fit mass):

$$\mu = 1.14^{+0.26}_{-0.23} = 1.14 \pm 0.21 \text{ (stat) } ^{+0.09}_{-0.05} \text{ (syst) } ^{+0.13}_{-0.09} \text{ (theory)}$$

in very good agreement with the ATLAS measurement.

Conclusion

The optimized analysis of the 2011+2012 dataset provide an improved measurement of the Higgs production modes. Even if different from the previous measurement performed on the same dataset, using different calibration, inclusive selection and event categorization, all compatibility checks performed do not show any worrying discrepancy.

The new categorization allows to test the WH and ZH production separately and the Higgs couplings to the top quark with the isolation of the ttH production mode.

Part IV

Higgs p_T

8

MONTE CARLO TOOLS

❝ We are not to tell nature what she's gotta be. She's always got better imagination than we have. ❞

SIR DOUGLAS ROBB

Chapter content

Monte Carlo generators are essential to prepare any physics analysis and interpret its results. At the LHC, the processes of interest are governed by QCD but at the hadron energies involved, this theory is non-perturbative, making any prediction difficult. Hopefully, the short and long distance effects can be treated separately thanks to the QCD factorization theorem. It can be applied on a large variety of phenomena, both for inclusive and differential variables such as the Higgs inclusive cross-section or its transverse momentum p_T^H spectrum predictions in its dominant gluon fusion production mode.

8.1 QCD factorization theorem

The cross section of the process $A + B \rightarrow X$, where A and B are hadrons, can be computed starting from the QCD factorization theorem [217]:

$$\sigma_{AB} = \sum_{a \in A, b \in B} \int_0^1 dx_1 dx_2 f_{a/A}(x_1, \mu_F^2) f_{b/B}(x_2, \mu_F^2) \hat{\sigma}_{a,b}(x_1 p_1, x_2 p_2, \alpha_S(\mu_R^2), \mu_F^2) \tag{8.1}$$

with the following notations:

σ_{AB} is the total cross section at hadron level. It depends on the hadron momenta;

a,b denotes partons inside the hadron;

$f_{a/A(x)}$ is the probability density function (PDF) to find parton a (quark or gluon) inside hadron A, carrying a fraction x of the total hadron momentum.

$\hat{\sigma}_{a,b}$ is the partonic cross section of partons a and b.

The sum runs over each of the parton constituting the hadron and is integrated over the full momentum phase-space. A visual representation of this formula can be found in Figure 8.1.
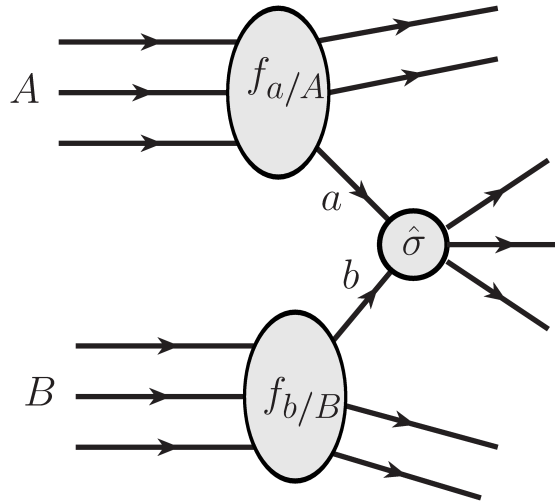
Figure 8.1: *Illustration of the short and long distance effect in the QCD factorization theorem.*

Same formula can be applied using differential cross-sections with respect to the transverse momentum or rapidity of the particle X.

In Equation 8.1, two arbitrary scales have been introduced:

- μ_R is the standard renormalization scale entering into the running of the strong coupling α_S.

- μ_F is the factorization scale, characterizing the frontier between the hadron and the parton scales.

They are usually chosen close to the scale of the hard-process (the Higgs mass in the gluon fusion process for instance). The variation of these scales in a reasonable range is a source of uncertainty for all QCD predictions.

Thanks to the factorization theorem, two independent computations are needed to access the full hadronic Higgs cross section:

- The PDF of parton in the hadron at large distances, non-perturbative effect evaluated thanks to fits to experimental data. It has the advantage to be universal. It can hence be computed from a specific process and dataset and be applied to a large variety of processes.

- The partonic cross sections at short distances: they involve relatively high energies and are thus computable in the perturbative QCD framework.

8.1.1 Parton Density Functions (PDF)

The proton PDF can be accessed by experiments probing its structure such as Deep Inelastic Scattering (DIS, Fig. 8.2) experiments and data from the HERA ep collider.

For instance, a simple model of DIS shows that the differential cross-section can be expressed as:

$$\frac{d^2\sigma}{dxdy} = \frac{2\pi\alpha^2 s}{Q^4}\left(1 + (1-y)^2\right)F_2(x) + \mathcal{O}(\alpha_S) \tag{8.2}$$
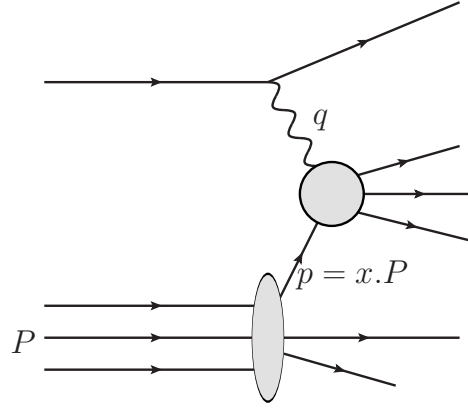
Figure 8.2: *Deep inelastic scattering of an electron on a proton or neutron. P is the initial nucleon momentum.*

where $x = \frac{Q^2}{2.p.q}$ is the Bjorken variable quantifying the longitudinal momentum of the interacting parton, Q^2 is the exchanged momentum defined by $Q^2 = -q^2 > 0$ and $y = \frac{Q^2}{s.x}$ (where $\sqrt{s}$ is the centre of mass energy).

$F_2(x)$ can be written as a function of the parton density functions:

$$F_2(x) = x \cdot \sum_q e_q^2 f_q(x) \tag{8.3}$$

e_q are the quark electric charges and f_q their parton density functions. In particular, for electron scattering on proton, $F_2^p(x) = x\left(\frac{4}{9}u_p(x) + \frac{1}{9}d_p(x)\right)$. For electrons scattering on a neutron, this function becomes: $F_2^n(x) = x\left(\frac{4}{9}u_n(x) + \frac{1}{9}d_n(x)\right) \simeq x\left(\frac{4}{9}d_p(x) + \frac{1}{9}u_p(x)\right)$ due to the isospin symmetry. The knowledge of F_2^p and F_2^n then allows to determine u_p and d_p.

More accurate models have been developed to take into account higher orders and spin correlations between partons.

The evolution of σ with Q^2 is given by the DGLAP evolution equations [218–220] at different orders. The x dependence having non-perturbative origin, needs to be measured. To do so, it is parametrized as a function of x at fixed $Q \equiv Q_0$ and the free parameters are determined from a fit to experimental data.

Different sets of PDF exist, depending on the parametrization of the structure functions with x, the datasets used to perform the fit and the order of the DGLAP evolution equations. Two of them are commonly used for the LHC data predictions: MSTW 2008 at NLO and NNLO [221] and CTEQ10 at NLO [222] or NNLO [223]. The result of the fit is illustrated in Figure 8.3 for MSTW2008.

MSTW 2008 NLO PDFs (68% C.L.)
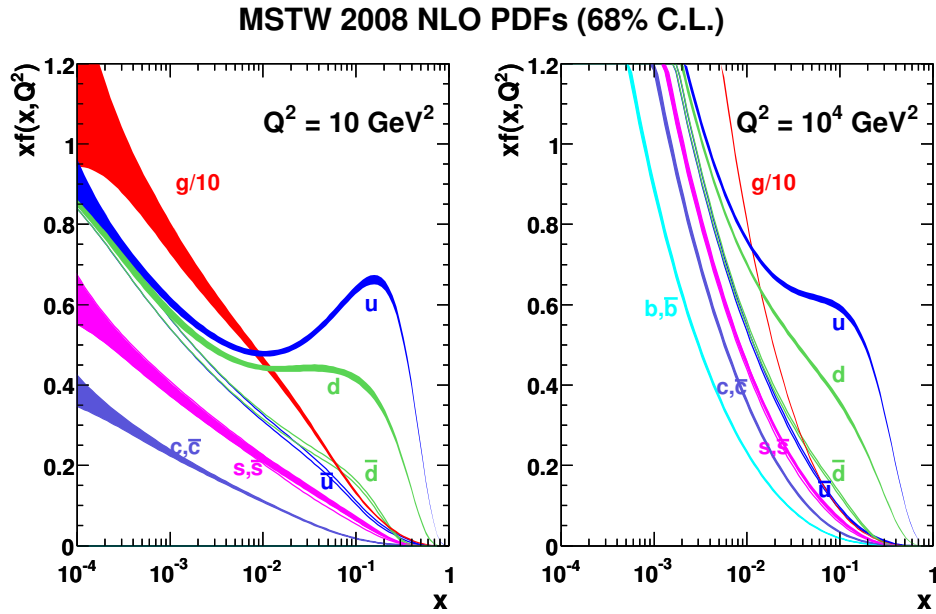
Figure 8.3: *MSTW08 parton density functions as a function of x for two different energy scales Q^2 [221].*

8.1.2   Partonic cross-section: perturbative expansion

The partonic cross-sections are computed with the perturbative QCD framework, whose basic principle is illustrated by Equation 8.4. The Leading Order (LO) contributions are the easier to obtain. The Next to Leading Order (NLO) corresponds to an extra α_S contribution, meaning an additional vertex or radiation.

$$\hat{\sigma} = \alpha_S^k \left(\hat{\sigma}^{LO} + \alpha_S.\hat{\sigma}^{NLO} + \alpha_S^2.\hat{\sigma}^{NNLO} + ... \right) \tag{8.4}$$

In the case of the Higgs production *via* gluon fusion, first computations were made in the Heavy Quarks Effective Theory (HQET), approximating the top mass to infinity and the bottom mass to zero. This is equivalent to considering a point-like interaction as illustrated in Figure 8.4, with one less loop to compute.
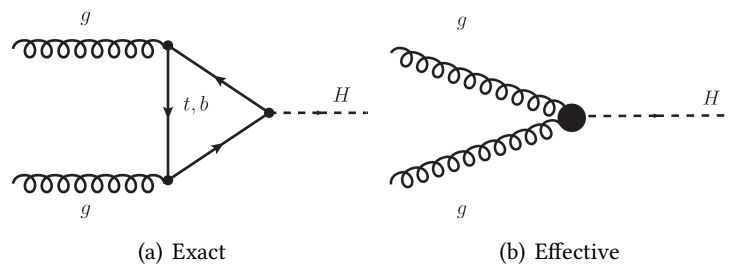
(a) Exact   (b) Effective

Figure 8.4: *Diagrams of the ggH production in the exact and effective theory at leading order in α_S (LO).*

Examples of diagrams contributing to the NLO and NNLO terms in this approximation are presented in Figure 8.5. The last one (number 3), called virtual correction, has a contribution to NNLO because it has the same initial and final state than the diagram labelled 1 (real corrections), and hence interferences between both diagrams have to be accounted for and contribute to the same order than

the second diagram:

$$\begin{aligned}
\sigma_{tot} &\sim (A_1 + A_3)^2 + A_2^2 \\
&\sim A_1^2 + 2A_1 A_3 + A_3^2 + A_2^2 \\
&\sim g_S^2 + 2g_S^4 + g_S^6 + g_S^4
\end{aligned} \tag{8.5}$$
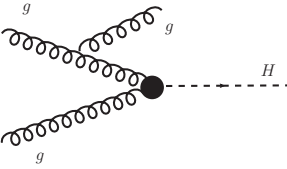
$$A_1 \sim g_S$$
$$\sigma_1 \sim g_S^2 \sim \alpha_S$$
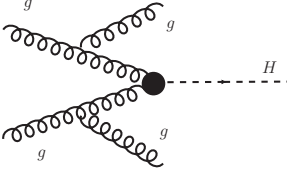
$$A_2 \sim g_S^2$$
$$\sigma_2 \sim \alpha_S^2$$
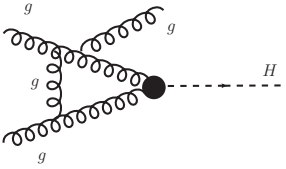
$$A_3 \sim g_S^3$$
$$\sigma_3 \sim \alpha_S^3$$

Figure 8.5: *Example of higher order diagrams to the ggH process.*

Importance of higher terms corrections is illustrated in Figure 8.6. Including the NLO terms increase the cross-section by a factor of ~ 2. When taking into account the NNLO terms, the cross-section increases again by $\sim 20\%$. Each time, the uncertainty band related to the scale dependence of the cross-section decreases, as expected due to the fact that the full computation to all orders should not depend on these arbitrary scales.
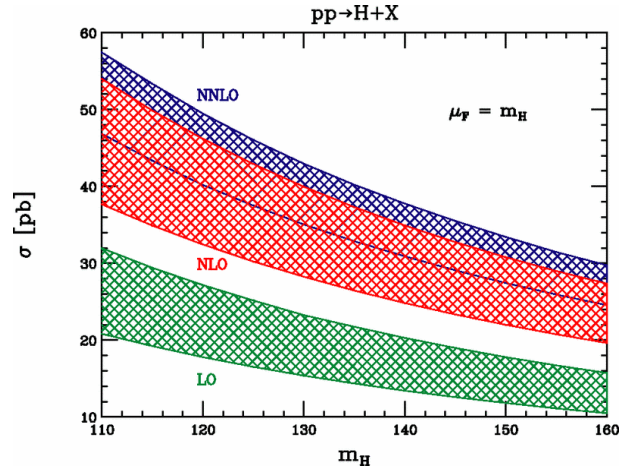
Figure 8.6: *Higher order corrections effect on the ggH cross section as a function of the Higgs mass [224].*

However, the fixed-order computation suffers from divergences in some phase-space regions: virtual corrections (through loops) lead to infinities, that are compensated by the unresolvable real corrections, *i.e.* emissions produced in the soft and collinear limit.
Figure 8.7 illustrates the divergences in the low p_T region of fixed order calculations: NLO tends towards $+\infty$, while NNLO tends towards $-\infty$. Resummation of non-resolvable emissions allows to cancel these divergences and get a finite result on the whole p_T range.

Resummation techniques are based on the observation that the same logarithmically divergent terms are present in all terms of the power expansion, and can hence be exponentiated. In Equation 8.6 [225], the function g_1 corresponds to the Leading Logarithm resummation (LL), g_2 to the Next-to-Leading-Logarithm, etc. L denotes a divergent logarithm, for instance in the case of the Higgs p_T spectrum in the ggH process, $ln\left(\frac{m_H^2}{p_T^2}\right)$.

$$\begin{aligned}
\hat{\sigma} &\propto 1 + \alpha_S(L^2 + L + 1) + \alpha_S^2(L^4 + L^3 + L^2 + L + 1) + \mathcal{O}(\alpha_S^3) \\
&\propto exp\left[Lg_1(\alpha_S L) + g_2(\alpha_S L) + \alpha_S g_3(\alpha_S L) + ...\right]
\end{aligned} \tag{8.6}$$
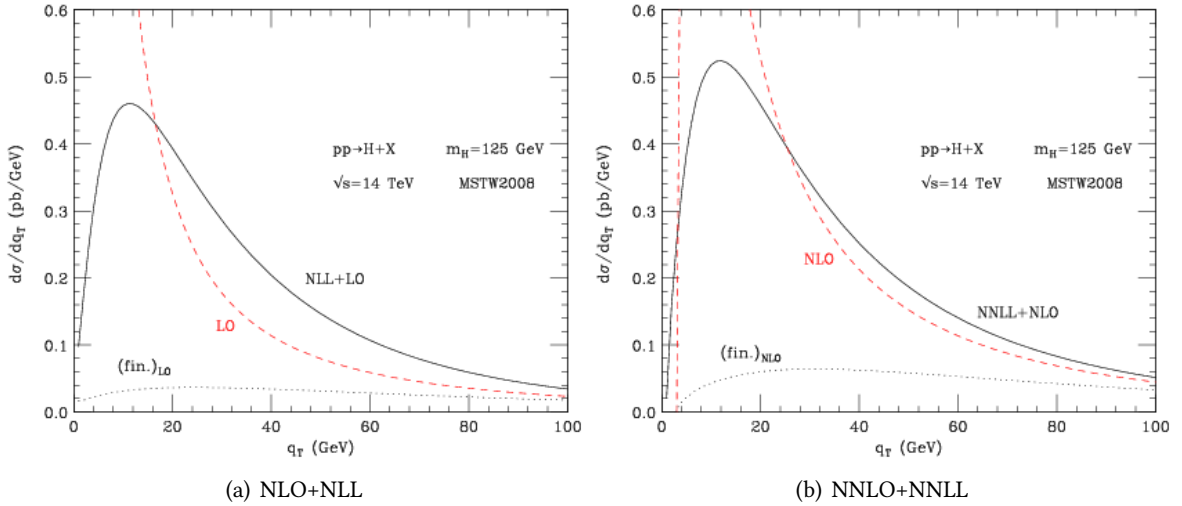
Figure 8.7: *Higgs transverse momentum with resummation compared to the fixed order calculations at $m_H = 125$ GeV in pp collisions at $\sqrt{s} = 14$ TeV [146]. Note that, when considering the Higgs transverse momentum, the leading order diagram always lead to $p_T^H = 0$. For the Higgs to have non zero transverse momentum, one has to go to higher order computations, where it can recoil against a jet emitted in the initial state. For this reason, the inclusive NLO cross-section is sometimes labelled LO at high Higgs p_T as is the case in these plots.*

The ggH process is known up to NNLO with resummation up to NNLL. The computation of higher order terms becoming more and more complex, another approach was developed to approximate the final results, implemented in Parton Shower simulations.

8.2 Monte Carlo simulations and application to the ggH process

When simulating a physical process, the full computation to all orders is the only one able to reproduce reality. However, we are only able to compute the α_S expansion up to a given order. NLO computations are implemented in generators such as `POWHEG` or `MC@NLO` [226]. These programs now implement most of the processes studied at LHC, among which the dominant Higgs production *via* gluon fusion. But NLO is only an approximation to the all-orders computation and higher order terms have a non negligible contribution to the total cross section as the NNLO computation shows (Fig. 8.6).

Technical implementation of higher orders can follow two approaches:

- Exact computation at fixed order (NNLO): these are implemented in numerical codes such as `HRes`, that also includes resummation up to NNLL. They have the advantage to be exact, hence producing reliable results. However, computations are very CPU- and time-consuming and they most often do not take into account other important effects occuring in pp collisions such as multi-parton interactions.

- Parton Shower: the PS programs such as `PYTHIA` [136, 137] or `HERWIG` [227] give an approximation of the higher orders, not only NNLO. For this reason, programs at LO or NLO are interfaced with Parton Shower simulation, that produce higher order radiations. To avoid double counting of radiations that would be produced by both the NLO generator and the PS program, matching algorithms are used. The PS programs also contains non-perturbative effects such as multi-parton interaction and hadronization, *i.e.* recombination of the emitted partons inside stable hadron at long distance.

8.2.1 Exact computations with resummation

Exact computations are available up to NLO in the exact theory and up to NNLO in the HQET. Resummed results are also provided in programs such as `HqT` [228] and `HRes` [229] to bring reliable predictions in the low p_T^H regime. It has to be noted that the resummation included in these programs resums $log\left(\frac{m_H}{p_T}\right)$ terms. It is important in order to provide a reliable prediction in the low p_T region but does not change the overall normalization. It is different from the threshold soft gluon resummation [147, 230] needed to avoid divergences of the inclusive cross-section, that is not taken into account in `HRes`. The global normalization is taken from the most accurate result of [134] which includes the threshold soft gluon resummation.

Resummation techniques consist in dividing the calculations into two parts:

$$\frac{d\hat{\sigma}}{dp_T^2} = \frac{d\hat{\sigma}^{(fin)}}{dp_T^2} + \frac{d\hat{\sigma}^{(res)}}{dp_T^2}$$ (8.7)

$\hat{\sigma}^{(fin)}$ representing the finite part without divergence problems. It can be computed at fixed order. $\hat{\sigma}^{(res)}$ contains all divergent terms and has to be treated separately. The computation is translated into a impact parameter space with a Fourier transformation, where the contributions from each additional emission factorize. The factorization can be defined at the resummation scale Q. The physical result does not depend on Q, but a dependence remains at fixed order in the perturbative theory, similarly to μ_R.

Figure 8.8 shows the predicted p_T^H spectrum form `HqT`, that computes only the p_T^H specturm, and `HRes1.0` that also provided the photons quadrivectors to reconstruct other kinematics variables.
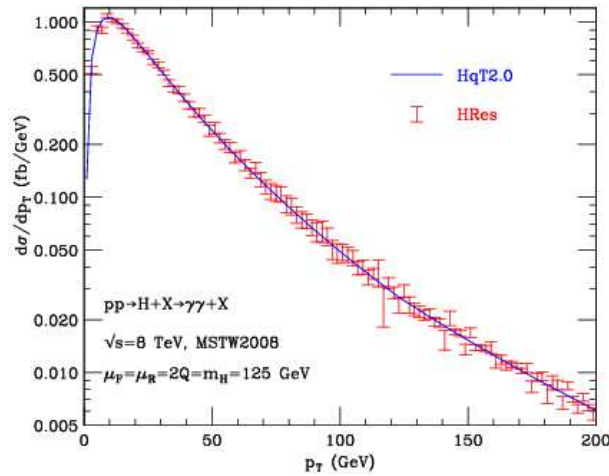
Figure 8.8: *Comparison of `HqT` and `HRes1.0` p_T^H spectra [229].*

8.2.2 NLO + Parton Shower

Several generators implement NLO computations for a large variety of processes and the ggH Higgs production especially. `POWHEG` [231–233] and `MC@NLO` [226] are two examples of such generators used within ATLAS, that allow a matching to parton shower programs.

8.2.2.1 Parton shower principles

Parton shower algorithms rely on the cross-section factorization expressed in Equation 8.8 and illustrated in Figure 8.9. $P_{a\to bc}$ denotes the Altarelli-Parisi splitting functions, a, b, c denote a quark or a

gluon depending on QCD allowed vertex. t is the ordering variable, that can be the momentum of the emitted parton p_a.

$$d\hat{\sigma}_{n+1} = d\hat{\sigma}_n \times \frac{\alpha_S(t)}{2\pi} \frac{dt}{t} dz P_{a\rightarrow bc}(z) \tag{8.8}$$
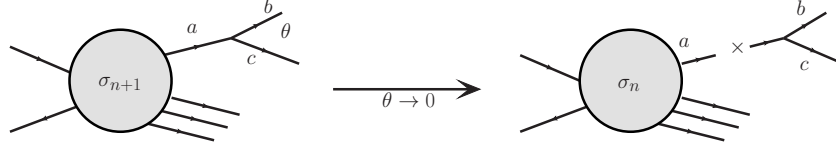
Figure 8.9: *Cross-section factorization.*

The process of Figure 8.9 is repeated iteratively until the virtuality of the last emission become smaller than $\Lambda_{QCD} \sim 200$ MeV, where QCD becomes non-perturbative and hadronization takes place. To avoid double counting, an ordering parameter t is used, and the branchings are chosen such that $t_{n+1} < t_n$. This ordering parameter can be chosen in different ways. The showers used for to simulate the ggH process within ATLAS use the parton p_T as ordering variable.

This result is obtained by using a so-called Sudakov form factor [234–236], characterizing the probability of non-emitting resolvable parton between scale t and t' [237], P being a splitting function:

$$\Delta(t, t') = exp\left\{-\frac{\alpha_s}{2\pi} \int_{t'}^{t} \frac{dt''}{t''} \int \frac{dz}{z} P(z)\right\} \tag{8.9}$$

In practice, the shower algorithm follows several steps:

1. Pick uniformly a number $\rho \in [0; 1]$;

2. Solve $\Delta(t, t') = \rho$. If $t' < t_0$, the infrared cut-off, stop the algorithm since the radiation is not resolvable; else:

3. Generate angular and kinematics variables of the radiated parton according to the spitting functions;

4. Restart from $t = t'$.

8.2.2.2 Matching with NLO: `POWHEG`

Parton Shower programs provide full events simulation at hadron level, but normalization accurate only to LO. On the other side, NLO programs provide accurate high p_T description and reduced scale dependence. It is natural to try to merge the two approaches, keeping the good features of both.

The main problem in merging a NLO result and a Parton Shower is not to double-count radiation: the shower might produce some radiations already present at the NLO level.

`POWHEG`, for POsitive Weight Hardest Emission Generator [231], generates an event with one single emission, at NLO level, and with the correct probability in order not to have double-counting. The p_T of the produced radiation works as an upper cut-off for the p_T's of all the secondary particles produced in the shower.

In addition, a parameter, the h-factor, is introduced to balance the contributions from the regular, fixed order, and singular components to the real cross-section R:

$$R^S = \frac{h^2}{h^2 + p_T^2} R; \quad R^F = \frac{p_T^2}{h^2 + p_T^2} R \tag{8.10}$$

When $p_T > h$, the spectrum is driven by the NLO fixed order computation, while for $p_T < h$, the Sudakov regime dominates. Choosing $h \rightarrow \infty$ is then equivalent to use uniquely the Sudakov formalism.

Tuning the h parameter allows to adjust the p_T^H spectrum and especially improve the agreement between the HqT, or equivalently HRes, p_T^H spectrum and POWHEG. The tuning done in [135] using PYTHIA6 yields:

$$h = \frac{m_H}{1.2} \qquad (8.11)$$

which is the value used to produce the ATLAS ggH samples.

8.2.3 Quark masses effects

Heavy quark masses are included in the cross-section computations and Table 8.1 allows to quantify the contribution of each term to the total ggH cross-section.

The p_T dependence at fixed order is known at NLO. Its effect is shown in Figure 8.10(a). Its implementation at NLL or equivalently in a PS program is more complicated. An implementation exists in POWHEG, where top, bottom and their interferences are considered, on a unique scale basis. HRes2.0 also includes top, bottom and their interferences, but their effect are treated with two different resummation scales: Q_1 for the top quark, of the order of $m_t \approx m_H$ and Q_2 much smaller of the order of the bottom mass (4.75GeV). This leads to slightly different predictions in the low p_T^H regime.

t	b	tb
18.31	0.1206	-1.125

Table 8.1: *ggH cross sections [pb] at 8 TeV for $m_H = 125$ GeV considering only the top contribution, only the bottom contribution or the interference term between top and bottom contributions [134].*

(a) NLO
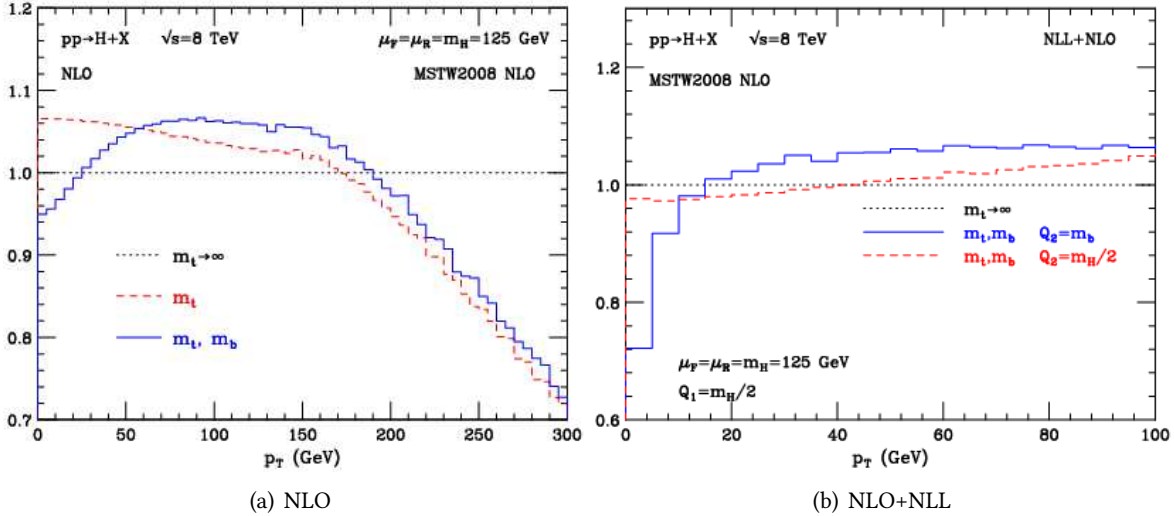
(b) NLO+NLL

Figure 8.10: *Quark mass effect in HRes2.0 at NLO and NLO+NLL. Bottom pad shows the ratio of HRes with top and bottom mass included to HRes in the HQET ($m_t \to \infty$). On the right plot, the red curve is equivalent to the POWHEG treatment [238].*

The current POWHEG version [239] implements an HQ mass effect similar to the one of HRes2.0, with the notable difference that top and bottom effects are treated on the same scale $h \sim m_H/1.2$. It was shown that it is possible to reproduce the same HQ mass effect in POWHEG, but this would require to produce three POWHEG samples, one of them then being assigned negative weights.

Equation 8.12 details the different cases for the treatment of the HQ mass effect in POWHEG:

- It can be run in the heavy quark effective theory approximation, which will be denoted simply $\sigma(h)$;

- The current sample uses the top and bottom mass effect with a single scale, written $\sigma(t + b, h)$;

- The new proposal is to use three different samples (Eq. 8.12):

  1. One sample with only top mass with a large scale of order mH

  2. Another sample including both the top and the bottom mass effect at smaller scale of the order of the bottom mass m_b

  3. Finally, to avoid the double-counting of the top mass effect at scales close to m_b, the contribution from the top only has to be subtracted from the previous term.

$$\sigma_{\text{HQET}} = \sigma(h = m_H/1.2)$$
$$\sigma_{1\text{ sample}} = \sigma(t + b, h = m_H/1.2)$$
$$\sigma_{3\text{ samples}} = \sigma(t, h = m_H/1.2) + [\sigma(t + b, h = m_b) - \sigma(t, h = m_b)]$$

(8.12)

Figure 8.11 shows that the combination of the three `POWHEG` samples described above is able to reproduce the heavy quarks mass effect obtained from `HRes2.0`.
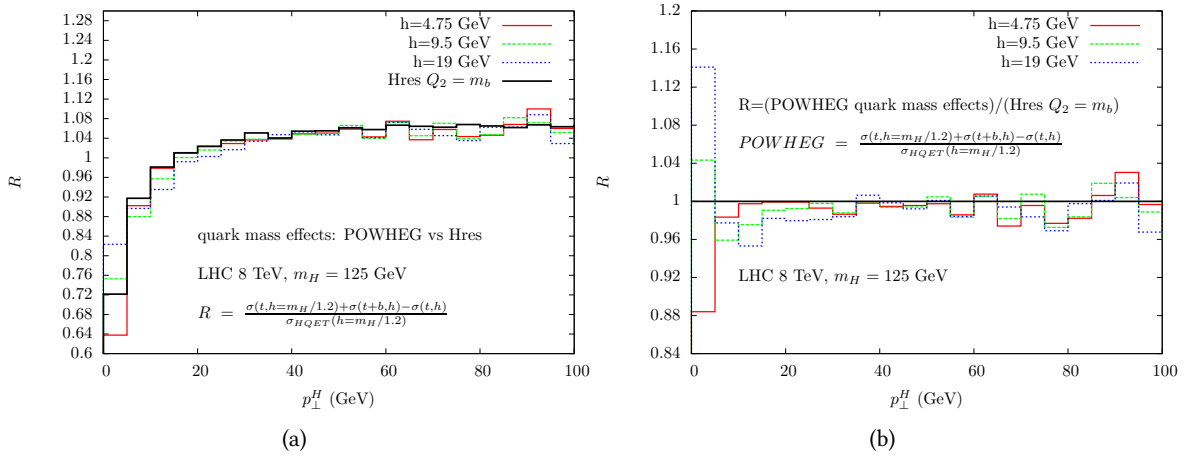
Figure 8.11: *Quark mass effect in* `POWHEG` *with the linear composition of three samples. Ratio of the* p_T^H *spectrum coming from the combination of three* `POWHEG` *samples to the distribution form* `POWHEG` *in the HQET [240].*

8.2.4 Dynamical scale

In the large p_T^H region, fixed renormalization and factorization scales are not justified because the energy involved is not only the mass of the particle. In that case, one should rather use a p_T^H dependant scale defined in Equation 8.13. This is also a way of taking into account part of the next term in the α_S power expansion $\left(\frac{\alpha_S(m_T)}{\alpha_S(m_H)}\right)^3$.

$$\mu_{R,F} = m_T = \sqrt{(p_T^H)^2 + m_H^2}$$

(8.13)

This p_T^H dependence of the scales has been implemented in `HRes2.1` and is also possible with `POWHEG`. Figure 8.12 compares the effect of the dynamical scale in `HRes` and the parametrization of the effect obtained from `POWHEG`, which are very consistent with each other.
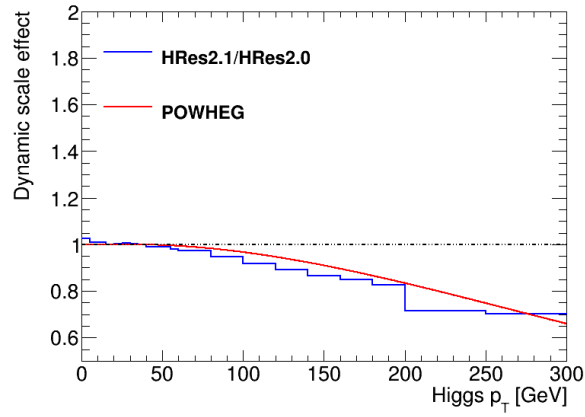
Figure 8.12: *Effect of the dynamical scale in `POWHEG` (from a fit) and `HRes2.1` (histogram). Ratio of the p_T^H distributions with to without dynamical scales.*

Conclusion

The tools described in this chapter allow to predict the ggH cross-section with a better accuracy. The impact of the change in the p_T^H spectrum they imply and the effect on the analysis of the diphoton decay channel of the Higgs in ATLAS are discussed in the next chapter.

9

HIGGS p_T IN THE $\gamma\gamma$ CHANNEL

> ❝ *The most exciting phrase to hear in science, the one that heralds
> new discoveries, is not 'Eureka!' (I found it!) but 'That's funny...'* ❞
>
> ISAAC ASIMOV

Chapter content

9.1 Role of p_T^H in the analysis

Contrarily to other Higgs analyses, no explicit cut on the Higgs transverse momentum is required in the diphoton channel. However, it is sensible to the p_T^H through the use of the diphoton p_{Tt} variable (see definition in Section 6.1.3). Indeed, Figure 9.1 illustrates the high correlation existing between the Higgs p_T and diphoton p_{Tt}, using truth level information.

A change in the modelling of this variable can hence induce migrations of events between low and high p_{Tt} categories. Since these categories have different signal-to-noise ratio, changing the repartition of the events among these categories has an impact on the final measurement of the signal strength. This is quantified in the remainder of this chapter.

(a) Correlation p_{Tt}-p_T^H

(b) p_T^H in the low and high p_{Tt} categories
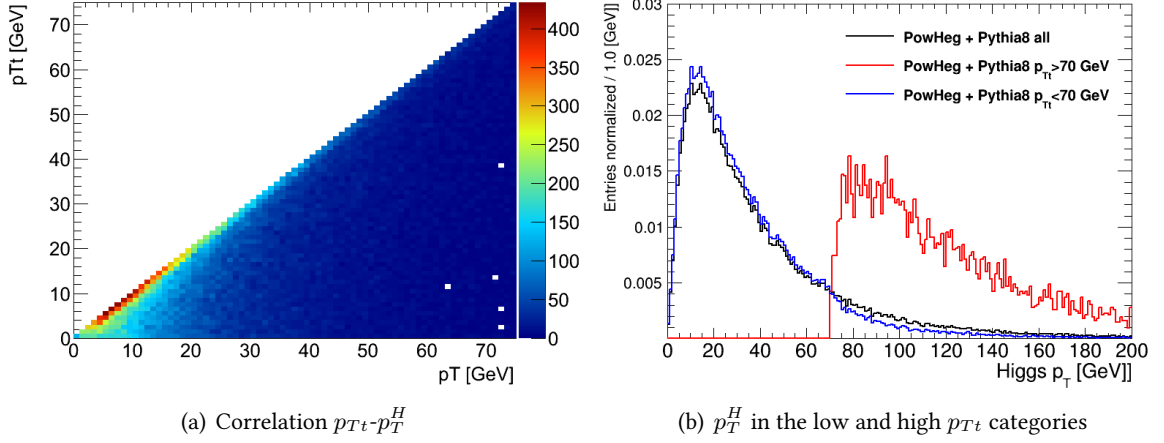
Figure 9.1: *(a): correlation between p_T^H and p_{Tt} at truth level without any acceptance cuts and (b) normalized p_T^H distributions for $p_{Tt} > 70$ GeV and $p_{Tt} < 70$ GeV at truth level.*

9.2 Available Monte Carlo predictions

The official ggH sample is generated using the `POWHEG` generator. The 8 TeV samples use the `POWHEG` version implementing a finite top and bottom mass effects in the loop. It is also parametrized with $h = m_H/1.2$. This `POWHEG` sample is showered by `PYTHIA8`. The 7 TeV samples are generated with a previous `POWHEG` version without h-parameter.

It is compared to the best available prediction of the expected Higgs p_T spectrum that goes up to NNLO+NNLL and is implemented in `HRes`. This programs also has the advantage of producing, for each event, each photon quadri-vector, allowing both to access the p_{Tt} distribution directly and to evaluate the effect of the detector acceptance.

Three different versions of the `HRes` code have been released. The first one uses the effective theory for the top and bottom masses ($m_t \to \infty$ and $m_b = 0$). An exact computation up to NLO+NLL is carried out in the `2.0` release [238]. NNLO+NNLL terms are still included but still computed in the effective theory framework. Version `2.1` allows to use dynamical renormalization and factorization scales ($\mu_{R,F} = \sqrt{m_H^2 + p_T^2}$). This is summarized in Table 9.1.

Generator	HQ mass	# scales	Order	Dynamical scale
POWHEG (Official - 7 TeV)	Yes	1	NLO + PYTHIA6	No
POWHEG (Official - 8 TeV)	Yes	1	NLO + PYTHIA8 (hfact)	No
HRes1.0	No	1	NNLO+NNLL	No
HRes2.0	Yes	2	NLO+NLL (exact t+b) + (NNLO+NNLL) ($m_t \to \infty$)	No
HRes2.1	Yes	2	NLO+NLL (exact t+b) + (NNLO+NNLL) ($m_t \to \infty$)	Yes

Table 9.1: *Generators properties. The number of scales refers to the resummation with heavy quark mass treatment (see text for more details).*

Figure 9.2 shows the initial comparison between the official `POWHEG` sample and the spectrum obtained with `HRes1.0` in the configuration that will be used throughout this chapter, unless otherwise specified:

- Proton-proton collisions at $\sqrt{s} = 8$ TeV;

- $m_H = 125$ GeV:

- $\mu_R = \mu_F = m_H$;

- $Q = \frac{m_H}{2}$

- CT10 parton distribution function.
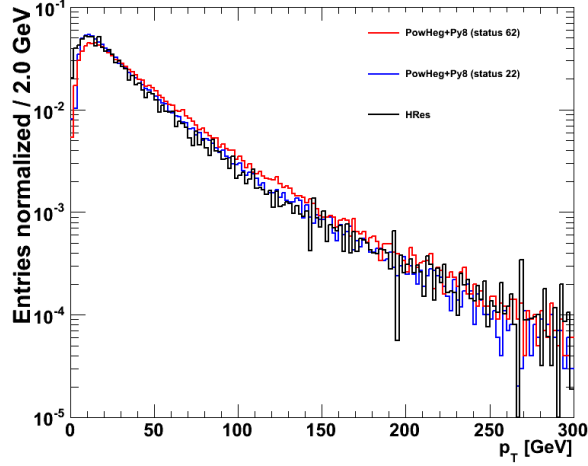
Figure 9.2: *Comparison of the p_T^H spectrum coming out of* `POWHEG+PYTHIA8` *and the* `HRes1.0` *distribution at* $\sqrt{s} = 8$ *TeV. Status 22 refers to the* `POWHEG` *results before the action of the* `PYTHIA` *parton shower; status 62 is the code for the final particle after parton shower.*

A discrepancy is observed between the `HRes1.0` prediction and the `POWHEG+PYTHIA8` spectrum. A reweighting technique is derived in order to take into account the last theoretical progresses in the final analysis of the Run I dataset.

9.3 Reweighting

A method is derived to reduce the difference between `HRes` and our `POWHEG+PYTHIA8` sample based on a reweighting technique. After presenting a simple method, it is tested with the first two versions of `HRes`. Its impact on the $\gamma\gamma$ analysis is also tested. Improvements of this simple method are presented in next section (9.4).

9.3.1 Strategy

`HRes` is a NNLO+NNLL program including or not the exact quark masses depending on the version. `POWHEG+PYTHIA8` uses a `POWHEG` version taking into account heavy quark masses. The first radiation is done with the matrix element computation by `POWHEG`, the following, softer, ones are produced by `PYTHIA8`.

A reweighting can not be done without taking care of these differences and the improvements brought by `PYTHIA` should be taken into account.

The general procedure proposed rely on the following weighting formula:

$$\omega = \frac{H}{P_{off}} \times R_{HQ} \times R_{NP} \tag{9.1}$$

with the following notations:

- P_{off} is the official `POWHEG+PYTHIA8` samples;

- H stands for `HRes`;

- R_{HQ} represents the effect of the exact top and bottom mass effect. It is only present when considering `HRes1.0` that does not implement this effect. It is estimated from `POWHEG` that allow to switch it on and off.

- R_{NP} measures the impact of all `PYTHIA` effects, except the parton shower. It is quantified by turning these effects off in `PYTHIA`, from the same `POWHEG` inputs than the official sample. These non-perturbative effects include MultiParton Interactions (MPI), Final State Radiation (FSR), hadronization and beam-remnant. Their effect on the Higgs p_T spectrum is expected to be small since they only modify the final state environment of the Higgs boson.

Each of these terms is studied further in the next subsections.

9.3.2   Effect of the non-perturbative effects of `PYTHIA`

When interfaced to `POWHEG`, `PYTHIA` generates the emissions that are softer than the parton emitted in `POWHEG`. It also includes:

- Multi Parton Interactions (MPI): soft interactions between the other partons of the interacting protons;

- Final State Radiation (FSR): radiations out of the quarks and gluons generated by Initial State Radiation (for the ggH process, this is the only way to have gluons and quarks in the final state);

- Hadronization and decay: formation of observable hadrons out of the particles in the final state;

- Beam remnants: primordial k_T due to the initial transverse parton motion inside the proton.

When reweighting to `HRes`, these effect that are in `PYTHIA` are not taken into account any more and one has to check their impact on the Higgs p_T spectrum.

Figure 9.3 shows the comparison of `POWHEG` showered by `PYTHIA` with all effects not related to parton shower disabled. A test is performed with `PYTHIA8`. As expected, the impact on the p_T^H spectrum is small, of the order of 2%. It will be neglected compared to the effects considered in the next sections.

(a) `PYTHIA6` (MC11)

(b) `PYTHIA8` (MC12)
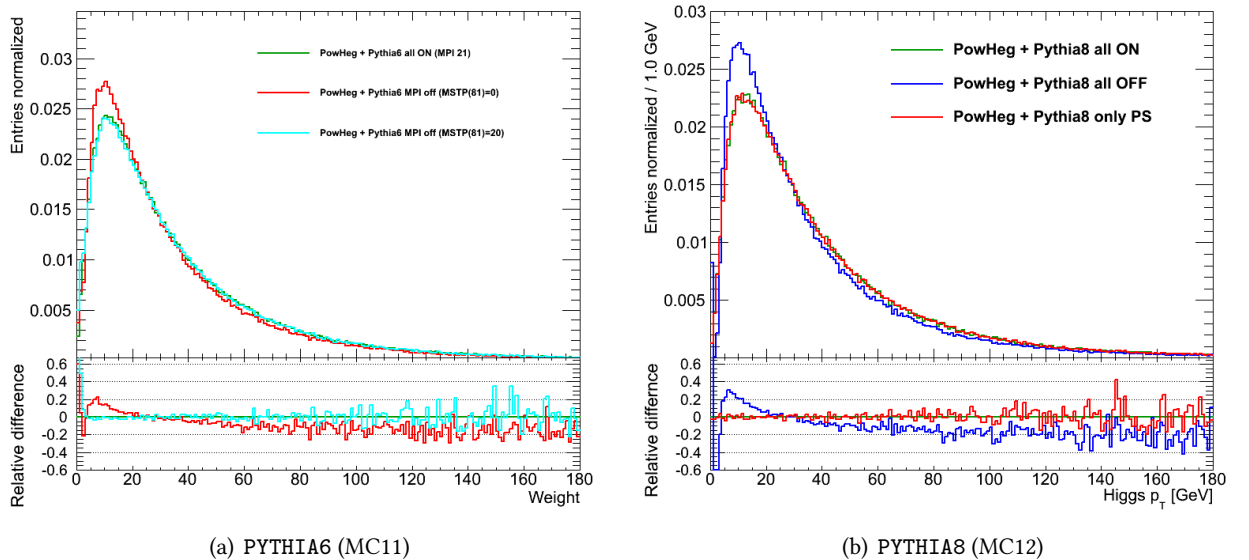
Figure 9.3: *Non perturbative effect in `PYTHIA` shown by the cyan (left) and red (right) histograms. The green lines correspond to the default `PYTHIA` configuration. The blue histogram on the right plot corresponds to the case where the ISR was disabled, hence retrieving the `POWHEG` NLO spectrum.*

9.3.3 Effect of the quark mass effects

For the reweighting to `HRes1.0`, a quark mass effect was extracted from `POWHEG`. The resulting distributions and their ratio are represented in Figure 9.4, in good agreement to the reference study presented in Ref. [135]. This effect gives up to 20% change in the p_T^H distribution.
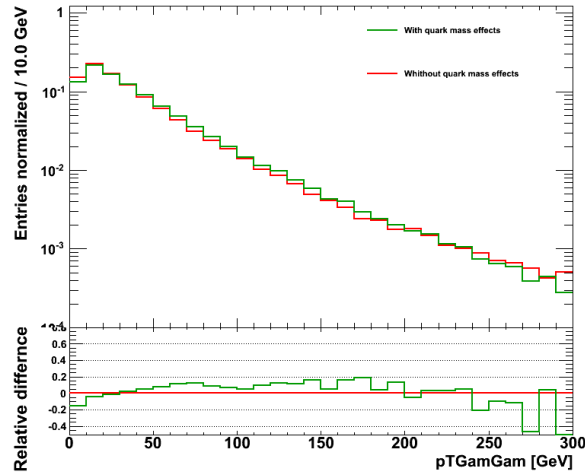
Figure 9.4: *Effect of the top and bottom masses in `POWHEG` (a single scale).*

9.3.4 Reweighting functions

This section shows the weighting function obtained from the different `HRes` versions. Even if only the last one will be used at the end, it is helpful to understand the process.

The effect of MPI, FSR and hadronization is neglected in any case.

9.3.4.1 Reweighting to `HRes1.0`

The reweighting to `HRes1.0` is made in two steps. First, the ratio R between `POWHEG+PYTHIA8` and `HRes1.0` is extracted. Then, the effect of the heavy quark masses is reintroduced by mutiplying R by the ratio shown in Figure 9.4. This is summarized in Figure 9.5 The green histogram represents the ratio of `HRes1.0` to the official `POWHEG+PYTHIA8` sample. The red one shows the effect of the HQ mass derived from `POWHEG`. The total weight is represented by the product of green and red and is represented in black. It includes both the NNLO+NNLL `HRes1.0` precision and the effect of top and bottom masses of `POWHEG`.
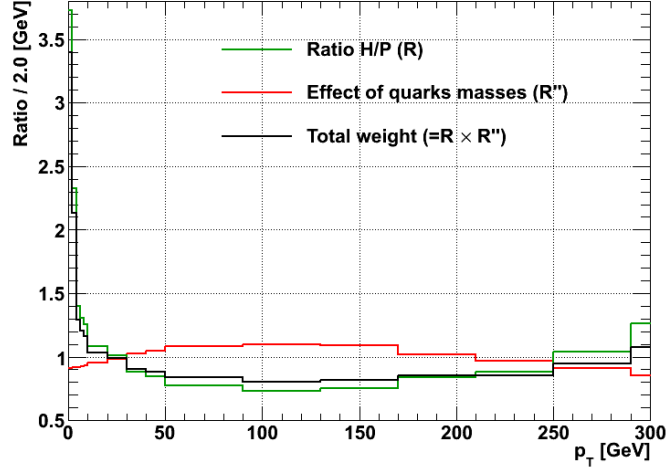
Figure 9.5: *Reweighting `POWHEG+PYTHIA8` to `HRes1.0` at 8TeV for a Higgs mass of 125GeV.*

9.3.4.2 Reweighting to `HRes2.x`

`HRes2.0` is similar to `HRes1.0` with the only difference that it includes the HQ mass effect. The reweighting is thus simplified because only the ratio H/P is needed to have all wanted effects included. Figure 9.6 shows the resulting weights for the 8 TeV `POWHEG+PYTHIA8` sample and a 7 TeV sample showered by `PYTHIA8`. The 7 TeV sample was generated without `hfact`, which explains the larger difference with `HRes` at large p_T^H. These weights are the ones included in the $H \rightarrow Z\gamma$ [241] and $H \rightarrow \mu^+\mu^-$ [242] analyses.

The weight is very similar to the one obtained with `HRes1.0`, except in the very first bin. This is explained partly by the new effect of the bottom mass which is now disentengled from the top and partly by the adaptation of the binning to reduce the statistical uncertainties.

(a) 7TeV

(b) 8TeV
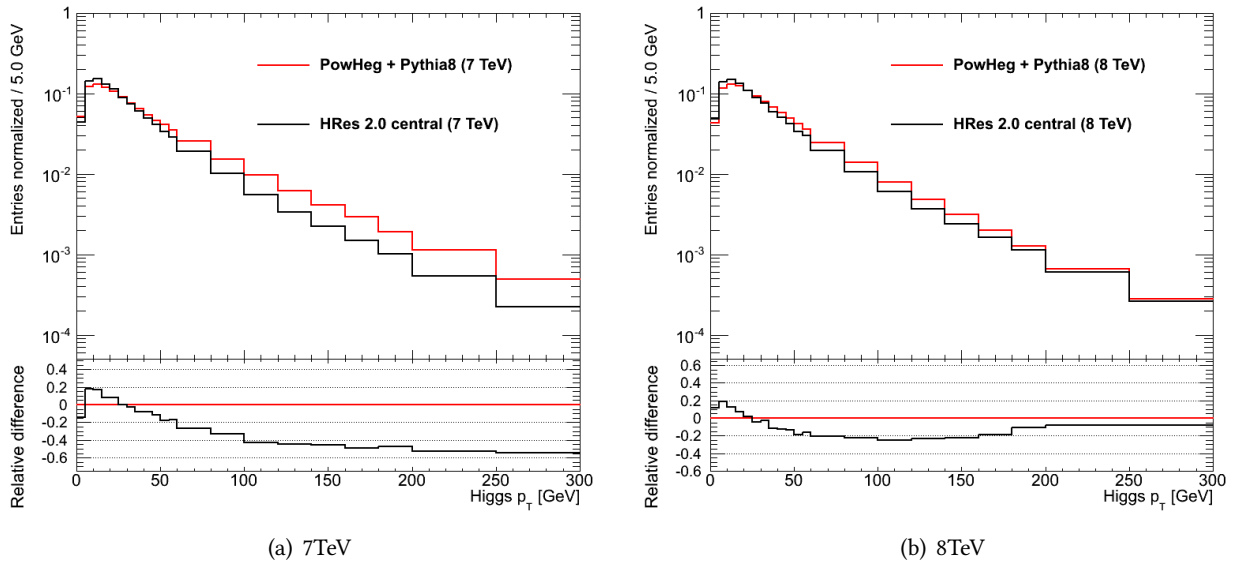
Figure 9.6: *Reweighting `POWHEG` to `HRes2.0` for the 7 and 8 TeV samples.*

Finally, Figure 9.7 shows the comparison of the weights obtained without and with dynamical scale, the latter is the one that is used in the $H \rightarrow \gamma\gamma$ analysis.
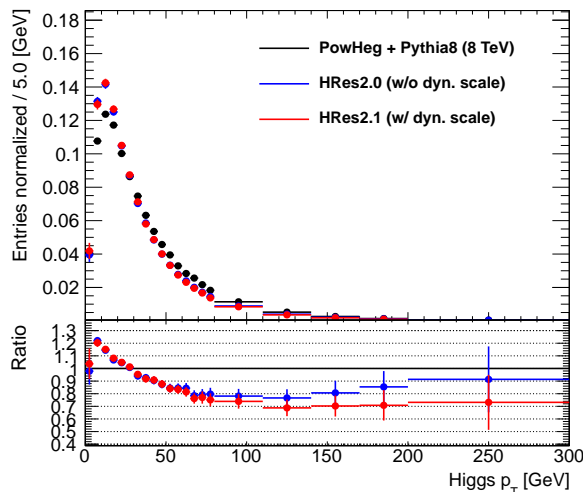
Figure 9.7: *Comparison of the weights obtained with* `HRes2.0` *without dynamical scales and* `HRes2.1` *with dynamical scale.*

9.3.5 Sanity checks of the reweighting method

At this stage, some checks were performed to test the impact of the reweighting on the analysis.

First, thanks to the photon quadrivectors produced by `HRes`, it is possible to test the effect of the acceptance cuts on the weight. Figure 9.8 compares the ratios H/P obtained without any acceptance cut – as was done so far – and after the application of cuts similar to the ones used in the ATLAS $H \rightarrow \gamma\gamma$ analysis, *i.e.*:

- The leading photon should have $p_T > 40$ GeV and the subleading is required to have $p_T > 30$ GeV.

- For each photon, $|\eta| < 2.37$.

The resulting ratios to `HRes1.0` are very similar, showing that the acceptance cuts do not change the relative agreement between the two generators.
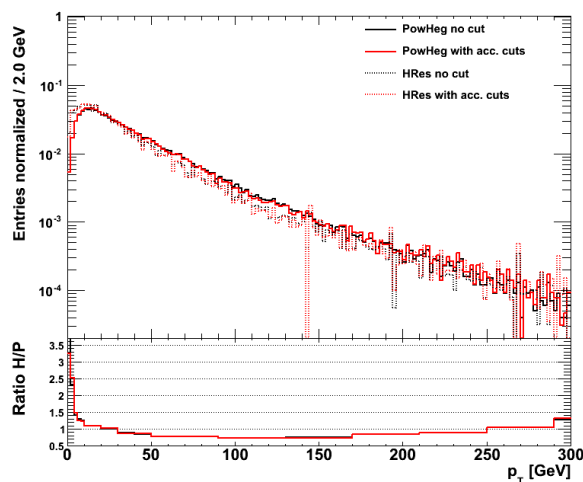
Figure 9.8: *Effect of the acceptance cuts on the reweighting function using* `HRes1.0`*.*

The risk for any reweighting technique is to distort other distributions than the one we are interested in. Some checks are performed here, comparing some distributions without and with weights.

It is shown that, when they are affected, they get closer to the distributions from `HRes`, which is the expected behaviour. This is the case for the leading and subleading photon transverse momentum (Fig. 9.9).

Figure 9.10 is an illustration of the fact that the Higgs rapidity is not sensible to the p_T^H reweighting. The rapidity, related to the longitudinal momentum, is only affected by changes in the structure functions.

(a) Leading photon

(b) Subleading photon
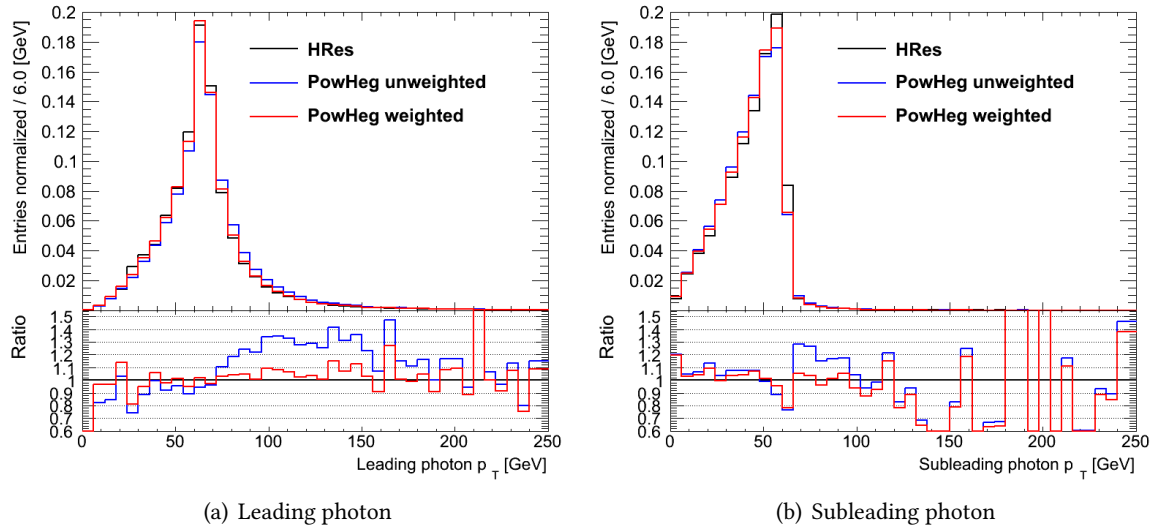
Figure 9.9: *Effect of the Higgs p_T reweighting to `HRes1.0` on single photon transverse momentum.*
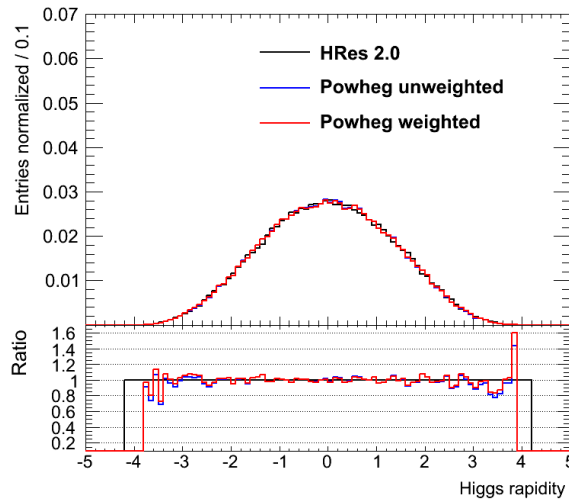
Figure 9.10: *Effect of the Higgs p_T reweighting to `HRes1.0` on the Higgs rapidity.*

9.3.6 Effect on the $H \to \gamma\gamma$ measurements

The effect on the $H \to \gamma\gamma$ analysis is quantified. First, the change of acceptance with the reweighting is tested. Then, the impact on the final signal strength measurement is quantified.

9.3.6.1 Inclusive cross section and acceptance with dynamical scale

The acceptance is defined as the number of events passing the selection with respect to the initial number of signal events. The change in acceptance induced by the change of p_T modelling is quantified by comparing the number of initial and final events with and without reweighting to HRes2.0. This effect is found to be very small (0.4% according to Tab. 9.2) compared to other systematics effects such as the luminosity that introduce a 2% uncertainty.

	Unweighted	Weighted	Ratio [%]
Initial	300000	299929	1,00023
Selected	112796	113271	-
$\sigma \propto \frac{N_{sel}}{N_{init}}$	0,376	0,378	1,0044

Table 9.2: *Effect of the p_T^H reweighting on the $H \to \gamma\gamma$ acceptance.*

9.3.6.2 Change in the μ central value

A wrong estimate of the p_T^H spectrum leads to migration between low and high p_{Tt} categories and can thus change the measured signal strength.

This can be understood by considering a simple example [243]:

We denote by f_i the assumed (wrong) fraction of events in category i and g_i the true fraction of events (unknown). s_0 is the true signal while s denotes the measured (fitted signal). The expected number of background events under the signal peak in category i is called b_i.

We define the following χ^2:

$$\chi^2(s) = \frac{\sum_i f_i \times s + b_i - n_{obs,i}}{b_i} \tag{9.2}$$

Minimizing this χ^2, one can show that the observed (fitted) signal is:

$$s = s_0 \times \frac{\sum_i \frac{f_i g_i}{b_i}}{\sum_i \frac{f_i^2}{b_i}} \tag{9.3}$$

Now, assume we have only two categories:

1. high p_{Tt}, $g_1 = f_1 - \Delta$, the reweighting gives higher weight to low p_T events so $\Delta > 0$

2. low p_{Tt}, $g_2 = f_2 + \Delta$

From the previous formula, one finds:

$$s = s_0 \times \frac{\frac{f_1^2}{b_1} + \frac{f_2^2}{b_2} - \Delta\left(\frac{f_1}{b_1} - \frac{f_2}{b_2}\right)}{\frac{f_1^2}{b_1} + \frac{f_2^2}{b_2}} \tag{9.4}$$

Since $\frac{f_1}{b_1} > \frac{f_2}{b_2}$ (high p_{Tt} categories have better s/b): $s < s_0$, the fitted signal is lower than the true one.

A test of this statement is performed with a pseudo-data to reproduce our measurement situation:

- The pseudo-dataset (Asimov) is generated with model with p_T reweighting with $\mu = 1$ and $\mu = 1.6$ (ie with "true" distribution). It is similar to real data.

- This pseudo-dataset is fitted with the model without p_T reweighting (our "wrong" model).

The results are the following: (estimated with the Moriond 2013 selection and categorization)

$$\text{Asimov with } \mu = 1.6 : \hat{\mu} = 1.562^{+0.362}_{-0.328}$$
$$\text{Asimov with } \mu = 1.0 : \hat{\mu} = 0.973^{+0.313}_{-0.272}$$

The fitted μ is lower than the one used for generation by a few percent, meaning that the number of observed signal events is smaller than the real one, as expected by the previous calculation.

It has to be underlined that, when applying the p_T reweighting in the Monte Carlo and fitting the same, real, dataset, the measured number of signal event will increase.

9.4   Correlation with the number of jets: reweighting improvement

The simple reweighting described in previous section does not take into account the correlation between the Higgs transverse momentum and the number of jets produced in the events. Since the $\gamma\gamma$ channel also use categories relying on the number of jets, this has to be checked and adapted if needed.

Figure 9.11 is an illustration of the correlation between the number of jets and the p_T^H. Jets are defined at truth level with the anti-k_T algorithm, with all stable particles in the final state as inputs. Only final jets with $p_T > 25$ GeV are considered. When no jets is found in the event, in first approximation, this corresponds to the case where only the Higgs is produced, hence without transverse momentum. When one jet is reconstructed, to ensure transverse momentum conservation, the Higgs has to recoil against that jet. Figure 9.11 shows that the Higgs p_T globally increases with the number of jets produced simultaneously in the event.

(a) Relative contribution

(b) Normalized distributions
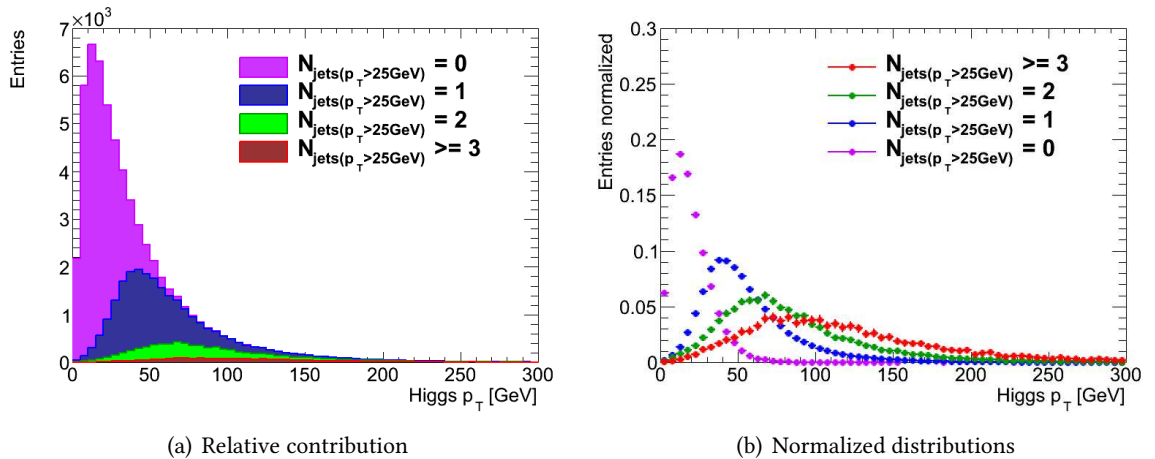
Figure 9.11: *p_T distributions for different jet multiplicities.*

It was observed that applying the simple p_T-reweighting decreases the cross-section for events with at least two jets $\sigma_{\geq 2}$ by 20%. This is not confirmed by computations using the jet veto technique such as the `JetVHeto` program. The discrepancy is illustrated in Figure 9.12. The lines show the cumulative cross-section from `POWHEG` without reweighting and with reweighting to `HRes2.1` (red curve). The points corresponds to the $N_{jets} = 0, 1$ or 2 from `JetVHeto`, where jets are defined with $p_T > 25$ GeV.

(a)   (b)
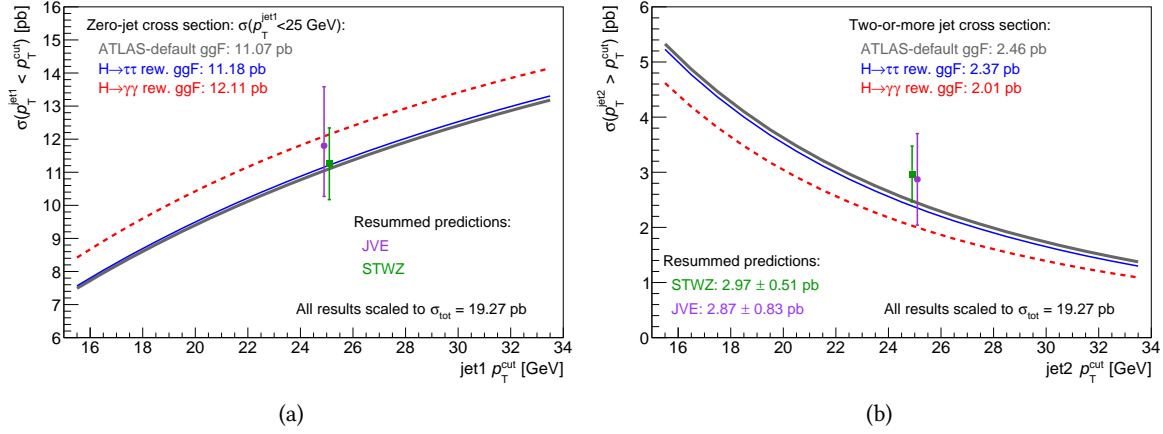
Figure 9.12: *Cumulative cross-section and comparison to* `JetVHeto` *[244].*

A refined method is then derived in order to:

- The inclusive p_T spectrum should match `HRes2.1` spectrum;

- The p_T spectrum in the ≥ 2 jets category should match `MiNLO HJJ` [211], improved `POWHEG` method to produce $H + 2jets$ at NLO, matched with the `PYTHIA8` parton shower;

- The number of jets should match the NNLO predictions from `JetVHeto` [245–247].

The chosen solution is to apply a different weight to events having at least two truth level jets with p_T greater than 25 GeV. The two weighting functions are illustrated in Figure 9.13.

(a) $N_{jets} < 2$ (b) $N_{jets} \geq 2$
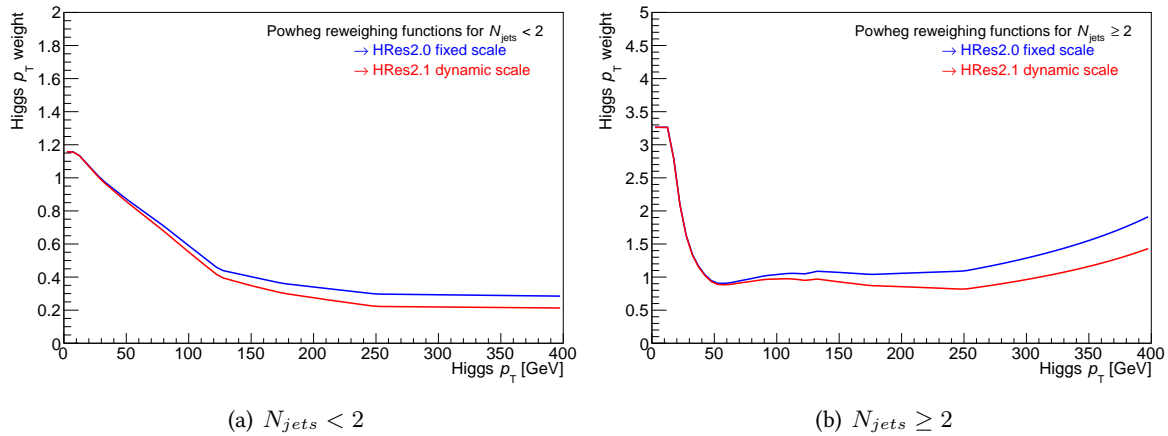
Figure 9.13: *p_T weights for events with 0 or 1 jet (a) and for events with at least two truth jets (b) [105].*

Figure 9.14 shows that the requirements are met: the p_T distribution for the events with more than two jets is consistent with the one coming out of `MiNLO HJJ`, and the jet-bin cross-section is in good agreement with the one obtained form `JetVHeto`.

9.5   Uncertainties

The uncertainty coming from the imperfect knowledge of the Higgs p_T shape can have an important impact on analyses using categories defined with p_T^H cuts. In this case, changing the Higgs p_T can introduce migrations among the categories for events with p_T^H close to thee boundary and have an effect on the measurement.

(a) p_T^H

(b) N_{jets}
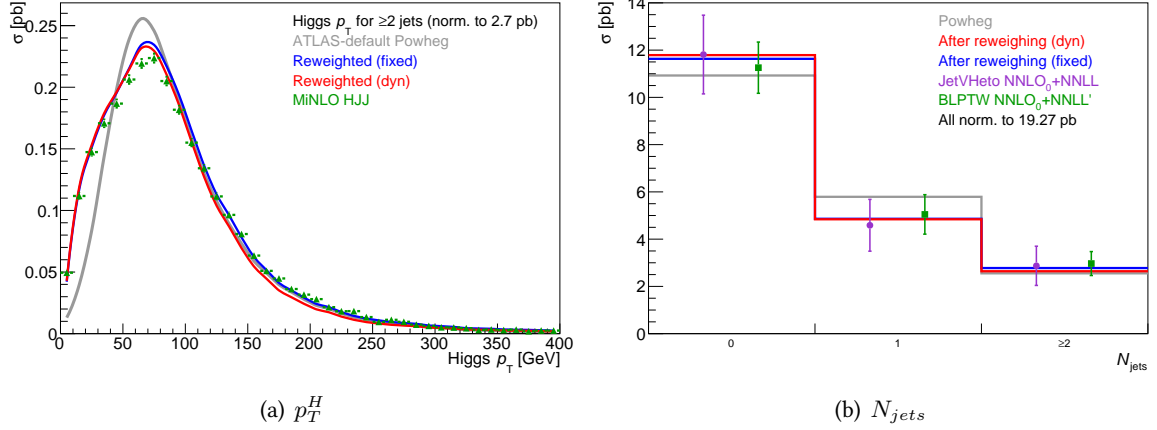
Figure 9.14: *(a) p_T spectrum in events with at least two jets after reweighting, compared to `MiNLO`. (b) jet bin cross-section before and after rewighting compared to `JetVHeto` [244].*

The uncertainty on the Higgs p_T spectrum is estimated with `HRes`. The effect is derived with version `2.0` and is checked to be consistent with the results of the last version `2.1`.

9.5.1 Scales

To quantify the uncertainty coming from scale variations, `HRes` is run with non-nominal scales following the recipe:

- μ_R, μ_F and Q_1 are varied by a factor of 2 around their nominal value, *i.e.*:

  - $\mu_{R,F} = \frac{m_H}{2}, m_H, 2m_H$
  - $Q_1 = \frac{m_H}{4}, \frac{m_H}{2}, m_H$

  Configurations where μ_R and μ_F differ by a factor of 4 are not considered;

- Q_2 is varied by a factor of 3 around m_b.

The usual treatment is to consider only the shape variations induced by the envelope of all scale configurations. The normalization uncertainty is taken inclusively to be $\pm 7.8\%$. This treatment is illustrated in Figure 9.15.

Applied to the $\gamma\gamma$ analysis, changing the reweighting function creates the migration of 10% of the events in the high p_{Tt} categories towards the low p_{Tt} categories, where the number of affected events is $\sim 1\%$ to conserve the total number of selected events: $N_{high}\sigma_{high} = N_{low}\sigma low$, *i.e.* events leaving the high p_{Tt} categories all end up in the low p_{Tt}, and vice-versa.

However, it was realized that the high p_T region suffers from larger normalization uncertainties than the inclusive. We then use non-normalized spectra obtained from the different configurations to compute the envelope. Those variations are illustrated in Figure 9.16.

The evaluated uncertainties in the high p_{Tt} categories from the symmetrized enveloped from Figure 9.16 amounts to $\sim 20\%$. Since it accounts for normalization uncertainties, the inclusive normalization uncertainty is set to 0 is the high p_{Tt} categories. This uncertainty is propagated to the low p_{Tt} categories as a migration. The final results are summarized in Table 9.3.

9.5.2 Structure functions

The impact of the structure functions on the Higgs p_T spectrum is estimated by changing the different eigen-vectors in the CT10 PDF set. The envelope is compared to the scale envelope in Figure 9.17.
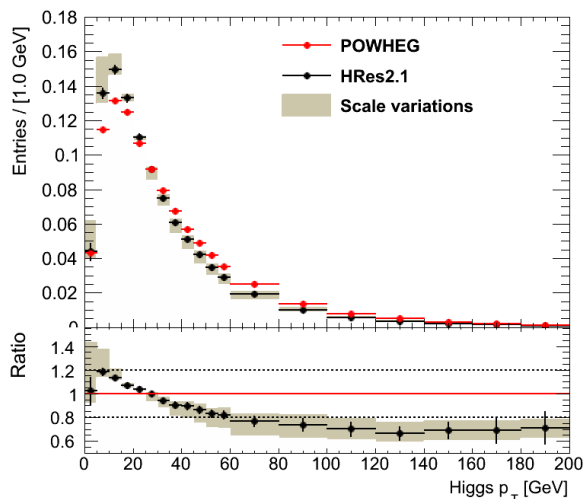
Figure 9.15: *Reweighting function to* `HRes2.1` *and shape uncertainties coming form the scale variations.*
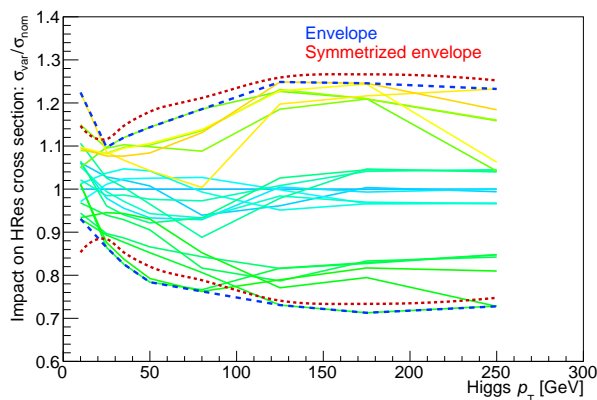
Figure 9.16: *Scale variations from* `HRes2.0`.

	ctrl-low-p_{Tt}	ctrl-high-p_{Tt}	fwd-low-p_{Tt}	fwd-high-p_{Tt}
yield, 7 TeV	7.8	0	7.8	0
p_T^H mig, 7 TeV	-1.4	24.1	-1.4	23.8
yield, 8 TeV	7.8	0	7.8	0
p_T^H mig, 8 TeV	-1.5	24.2	-1.5	23.9

Table 9.3: *Migration uncertainties in percent on the ggF cross section in the p_{Tt} categories from* `HRes2.0`.

Given the smaller impact of the structure functions on the Higgs p_T spectrum, this uncertainty was neglected.

Since `HRes` allows to reconstruct other variables than the Higgs p_T, the impact of the structure functions on the acceptance and mass resolution was also tested by applying a Higgs rapidity y_H-reweighting.

Results presented in Tables 9.4 and 9.5 show that the uncertainty related to the structure functions is negligible with respect to the experimental uncertainties (of the order of 10% on the resolution and 0.1% on the peak position).
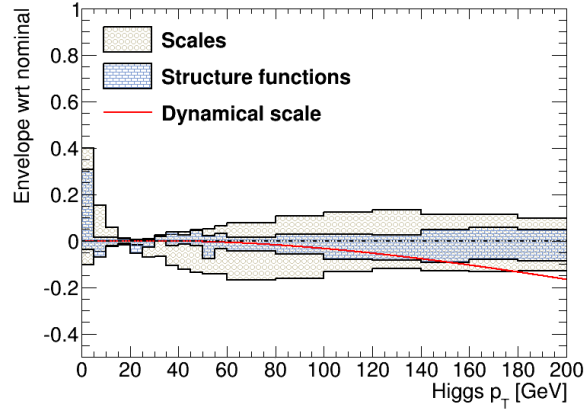
Figure 9.17: *Structure functions shape uncertainties compared to the scale variations uncertainty from* `HRes2.0` *[105].*

(a) Structure function uncertainties

(b) y_H distribution in the $\gamma\gamma$ categories
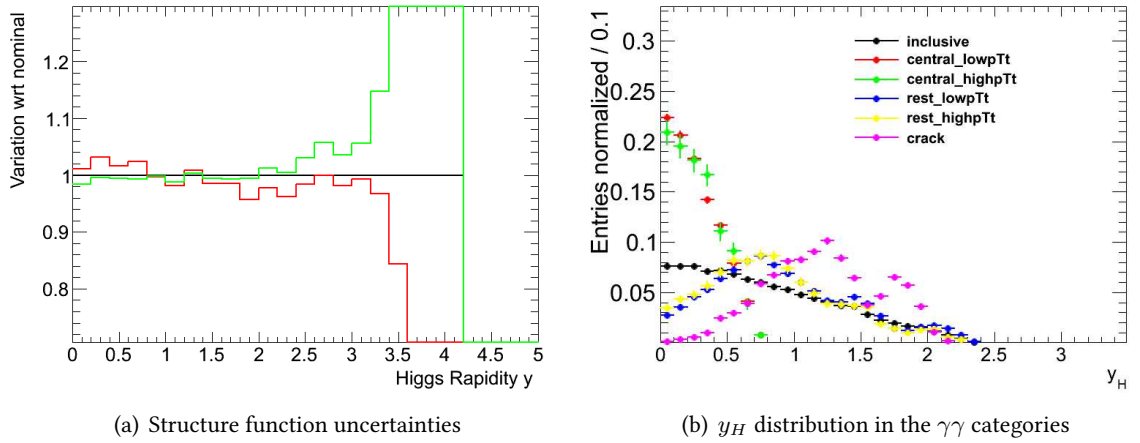
Figure 9.18

Cat	Unweighted	Weighted	$\frac{\Delta\mu}{\mu}$ [%]
inclusive	124.8252	124.8256	-0.0003
central_lowpTt	124.8461	124.8461	0.0000
central_highpTt	124.8584	124.8585	-0.0001
rest_lowpTt	124.8276	124.8277	-0.0001
rest_highpTt	124.8701	124.8700	0.0001
crack	124.7693	124.7701	-0.0006

Table 9.4: *Impact of the rapidity uncertainties on the signal peak position.*

9.6 Differential cross-section measurement with the $\gamma\gamma$ channel

The $H \to \gamma\gamma$ channel has observed about 600 events in the 2012 dataset, enough to start and study the differential distributions of the signal for different variables of interest [248], among which the Higgs p_T spectrum is of particular interest to test the QCD radiation models (the results presented here will soon be updated in a paper using the new calibration [249]).

The measurement strategy is the following:

1. Divide the dataset into several p_T^H bins. The bining is chosen such that they have a similar statistical uncertainty;

Cat	Unweighted	Weighted	$\frac{\Delta\sigma}{\sigma}$ [%]
inclusive	1.8933	1.8903	0.1585
central_lowpTt	1.4972	1.4973	-0.0047
central_highpTt	1.3395	1.3395	0.0007
rest_lowpTt	1.9048	1.9039	0.0485
rest_highpTt	1.6308	1.6304	0.0239
crack	2.4395	2.4398	-0.0129

Table 9.5: *Impact of the rapidity uncertainties on the signal resolution.*

2. After having chosen the background parametrization in a similar way that the one described in Section 6.5.2, an S+B fir is performed in each bin to extract the number of observed signal events N_S, which is reported on the corresponding bin. This is the unfolded distribution that contains the detector acceptance and selection efficiency;

3. An unfolding procedure is applied to get rid of the detector effects. In this low statistics analysis, the chosen unfolding method is a bin by bin correction coefficient based on truth level particle studies. The acceptance cuts considered are the followings:

- Each photon transverse momentum must satisfy $p_T^\gamma > 25$ GeV;

- The pseudo-rapidity range considered corresponds to the detector acceptance $|\eta^\gamma| < 2.57$ (the crack region $1.37 < |\eta^\gamma| < 1.56$ is included in the acceptance.

The results of the analysis for the Higgs p_T are shown in Figure 9.19(a) for the unfolded measurement. The data is compared to several Monte Carlo generators and a shape-only comparison is quantified with a χ^2 test.

The same procedure is applied to the number of jets in the event, where a jet is defined by the anti-k_T algorithm with $R = 0.4$ and $p_T > 25$ GeV. Results are shown in Figure 9.19(b).

(a) Higgs p_T (b) Number of jets
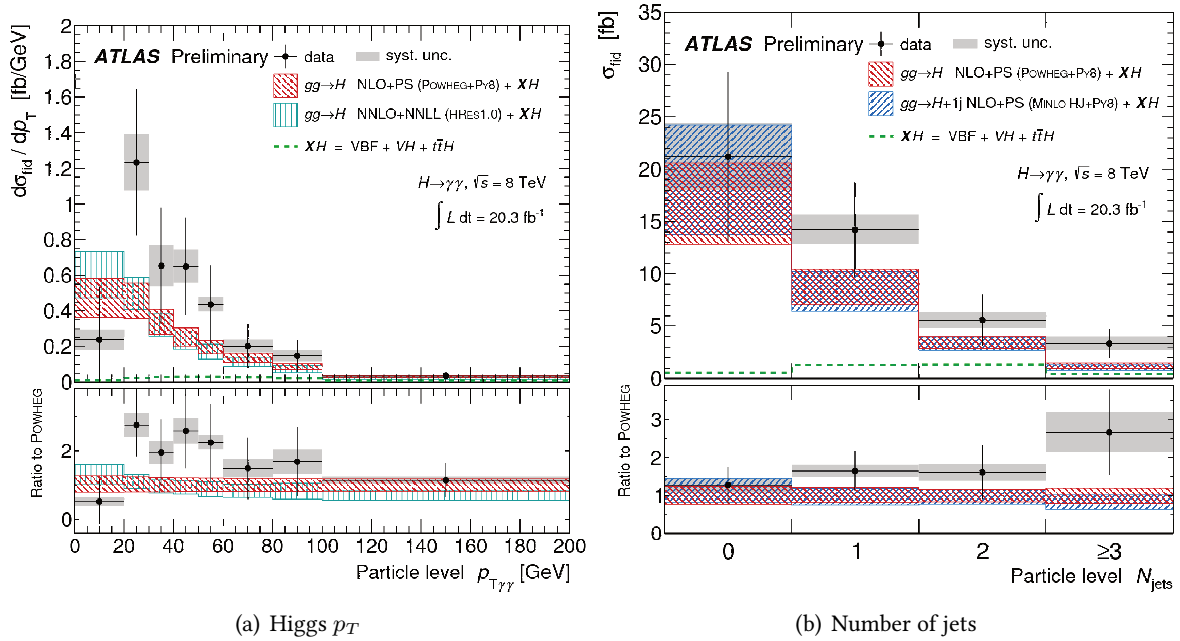
Figure 9.19: *Differential cross section measurement using the diphoton decay channel. After unfolding [248].*

Conclusion

A detailed study of the Higgs transverse momentum at the generation level allowed to take advantage of the last theoretical progresses and present the experimental results with a good knowledge of them. However, the limitations of the reweighting technique are well known and new approaches are already under study to replace it for the next run simulations. In the meantime, first measurements of the Higgs p_T shape have been carried out, still limited by the statistics but next run data will bring much more information in order maybe to understand differences between parton shower and NNLO codes for example. If the first considerations about the relation between this spectrum and other physical observables comes true, this measurement would have much profound implications and allow to access other Higgs properties.

Part V

Outlooks and conclusion

10

FUTURE OF THE HIGGS ERA

Some of the improvements expected in the Standard Model Higgs sector from future LHC runs and next experiments are briefly discussed here.

10.1 LHC

At the end of the LHC Run II, the amount of analysable data is expected to be close to 100 fb^{-1} for each experiment, *i.e.* 4 times more data than the analysis presented here. The energy in the centre of mass frame will be increased to $\sqrt{s} = 13$ or 14 TeV, meaning that the production cross-section of a Standard Model Higgs boson will be increased by a large factor (≈ 2.3 for ggH between 8 and 13 TeV, see Fig. 1.12). With about 9 times more data, the statistical uncertainty on the global signal strength μ will be decreased by a factor of 3, leading to a statistical error smaller than the theoretical and experimental systematics contributions to the total error.

This is also visible in the projections studies performed for 300 and 3000 fb^{-1} of pp collisions at $\sqrt{s} = 14$ TeV [250] (Fig. 10.1).

It is clear that already at the end of Run II, the systematics will become dominant and some efforts have to be made in order to fully benefit from the increase of statistics, both from the theory and experimental sides.

For the former, improvements are foreseen with the N^3LO computations that are close to final, that will, hopefully, decrease the scale dependence of the result. One also have to decrease the structure function uncertainties.

The later is currently dominated by the diphoton mass resolution, itself dominated by the constant term uncertainty measured in $Z \to e^+e^-$ events (see Tab. 7.24 for 8 TeV values). Much more work will be needed in this area in the next few years in order to reduce it. Understanding the mass tails, perform a combined fit of the constant and stochastic terms in the resolution are some possible ways of improvements.

10.2 Future colliders

In the next years, future colliders will be discussed, in particular e^+e^- colliders: the superconducting RF accelerating cavities ILC (International Linear Collider), the two-beam acceleration CLIC (Compact LInear Collider) and the FCC-ee (Future Circular Collider e^+e^-) that could be built in a 100 km tunnel near Geneva. A hadronic collider, FCC-hh, is also considered to be set up in the same tunnel (see [251, 252] for more documented reviews). If we consider the measurement of κ_γ and κ_g (defined in Sec. 7.1.1), FCC-ee gives a priori the lower uncertainties, at percent level, while for κ_t to be measured directly, one needs higher energy colliders.

Generic modifications of the Standard Model couplings are of the form $1/\Lambda^2$ where Λ in the new physics scale. Their magnitude is of the order of 5% for $\Lambda \sim 1$ TeV. However, larger deviations could be present in specific models, for instance with light staus [253].

Figure 10.1: *Expected relative uncertainties on the signal strength for different channels with the data of the LHC Run II. The solid area represents the statistical+ experimental systematics uncertainty while the hashed area represents the theory uncertainty* [250]*.*

Conclusion

This thesis presented several aspects of the search and study of the Higgs boson at a mass of about 125 GeV using its diphoton decay channel at the ATLAS experiment.

The data flow from the LHC collisions to the final physics analysis was presented using the example of the electromagnetic calorimeter. More detailed studies of the calorimeter pointing technique used to reconstruct the unconverted photons direction were also discussed and a strange oscillation effect was observed in the electromagnetic calorimeter end-caps and was corrected, leading to an improvement of the Higgs mass resolution in the diphoton channel of 0.5%.

After the discovery, my work was concentrated on the couplings measurements using the diphoton channel. The analysis consists in isolating each of the main five Higgs production modes using the particles produced in association with the Higgs. Especially, the introduction of a dilepton category tagging $ZH \to llH$ production and the tuning of the existing one lepton and MET categories allow to measure separately the WH and ZH production.

In parallel, the impact on the analysis of the Higgs p_T modelling, in the ggH dominant production mode, was quantified. The last developments from the theory side were taken into consideration by developing a reweighting technique for the Higgs p_T spectrum used in the analysis to match the NNLO+NNLL predictions from `HRes2.1`. A special treatment to preserve the distribution of the number of jets, correlated to the Higgs p_T, is also considered.

The final analysis of the LHC 2011+2012 datasets in ATLAS shows evidence for the spin 0 nature of the discovered particle, confirming its agreement with the Standard Model scalar boson. At the ATLAS combined mass of $m_H = 125.4$ GeV, the measured signal strength is:

$$\mu = 1.15^{+0.28}_{-0.25} = 1.15^{+0.23}_{-0.22} \text{ (stat.) } ^{+0.10}_{-0.08} \text{ (syst.) } ^{+0.12}_{-0.08} \text{ (theory)}$$

Its couplings measurements, with the $\gamma\gamma$ channel alone or combined with five other decay modes, does not show statistically significant deviations from the Standard Model expectations, but error bars of some parameters are still large. For the $\gamma\gamma$ channel only, the ratio of the observed production modes with respect to the Standard Model are: (at $m_H = 125.4$ GeV)

$$\mu_{ggH} = 1.32^{+0.32}_{-0.32}(stat.) \ ^{+0.23}_{-0.15}(syst.)$$

$$\mu_{VBF} = 0.78^{+0.72}_{-0.63}(stat.) \ ^{+0.30}_{-0.29}(syst.)$$

$$\mu_{WH} = 0.97^{+1.64}_{-1.46}(stat.) \ ^{+0.36}_{-0.17}(syst.)$$

$$\mu_{ZH} = 0.13^{+3.62}_{-0.13}(stat.) \ ^{+0.64}_{-0.00}(syst.)$$

$$\mu_{ttH} = 1.55^{+2.62}_{-1.75}(stat.) \ ^{+0.79}_{-0.36}(syst.)$$

From a theory point of view, a Higgs at low mass does not exclude a lot of models, and many extensions of the Standard Model still survive this observation and could explain the still not understood experimental observations outside of the Higgs sector.

The next LHC data taking period starting in 2015 at an increased centre of mass energy of ≈ 13 TeV is expected to decrease the uncertainties on the couplings measurement and bring more constraints on the Higgs and beyond Standard Model processes. However, for precise measurements of the Higgs sector, electron-positron colliders such as the International Linear Collider will be needed.

Bibliography

References for Chapter 1: Standard Model of particle physics

[1] J. Beringer et al. "Review of Particle Physics (RPP)". In: *Phys. Rev.* D86 (2012), p. 010001. DOI: 10.1103/PhysRevD.86.010001 *Cited on pages 8, 13, 26, 74, 76.*

[2] S. L. Glashow. "Partial Symmetries of Weak Interactions". In: *Nucl. Phys.* 22 (1961), pp. 579–588. DOI: 10.1016/0029-5582(61)90469-2 *Cited on page 9.*

[3] A. Salam and J.C. Ward. "Electromagnetic and weak interactions". In: *Physics Letters* 13.2 (1964), pp. 168 –171. ISSN: 0031-9163. DOI: http://dx.doi.org/10.1016/0031-9163(64)90711-5 *Cited on page 9.*

[4] S. Weinberg. "Precise Relations between the Spectra of Vector and Axial-Vector Mesons". In: *Phys. Rev. Lett.* 18 (13 Mar. 1967), pp. 507–509. DOI: 10.1103/PhysRevLett.18.507 *Cited on page 9.*

[5] F. Englert and R. Brout. "Broken symmetry and the mass of gauge vector mesons". In: *Phys. Rev. Lett.* 13 (1964), pp. 321–323. DOI: 10.1103/PhysRevLett.13.321 *Cited on page 9.*

[6] P. W. Higgs. "Broken symmetries, massless particles and gauge fields". In: *Phys. Lett.* 12 (1964), pp. 132–133. DOI: 10.1016/0031-9163(64)91136-9 *Cited on page 9.*

[7] P. W. Higgs. "Broken symmetries and the masses of gauge bosons". In: *Phys. Rev. Lett.* 13 (1964), pp. 508–509. DOI: 10.1103/PhysRevLett.13.508 *Cited on page 9.*

[8] P. W. Higgs. "Spontaneous symmetry breakdown without massless bosons". In: *Phys. Rev.* 145 (1966), pp. 1156–1163. DOI: 10.1103/PhysRev.145.1156 *Cited on page 9.*

[9] "The BEH-mechanism, interactions with short range forces and scalar particles". In: *AAPPS Bulletin* 23.6 (2013), pp. 3–19 *Cited on page 9.*

[10] N. Andari. "Observation of a BEH-like boson decaying into two photons with the ATLAS detector at the LHC". CERN-THESIS-2012-144, LAL12-300. PhD thesis. 2012 *Cited on page 9.*

[11] E. Noether. "Invariant Variation Problems". In: *Gott. Nachr.* 1918 (1918), pp. 235–257. DOI: 10.1080/00411457108231446. arXiv:physics/0503066 [physics] *Cited on page 11.*

[12] C.-N. Yang and R. L. Mills. "Conservation of Isotopic Spin and Isotopic Gauge Invariance". In: *Phys. Rev.* 96 (1954), pp. 191–195. DOI: 10.1103/PhysRev.96.191 *Cited on page 13.*

[13] S. Bethke. "World Summary of α_s (2012)". In: *Nucl. Phys. Proc.Suppl.* 234 (2013), pp. 229–234. DOI: 10.1016/j.nuclphysbps.2012.12.020. arXiv:1210.0325 [hep-ex] *Cited on page 14.*

[14] E. Fermi. "Tentativo di una teoria dell'emissione dei raggi 'beta'". In: *La Ricerca Scientifica* 4.2 (1933), pp. 491–495 *Cited on page 15.*

[15] E. Fermi. "Tentativo di una Teoria Dei Raggi β." In: *Il Nuovo Cimento (8)* 11.1 (1934), pp. 1–19 *Cited on page 15.*

[16] E. Fermi. "Versuch einer Theorie der β-Strahlen. I". In: *Z-Phys.* 88.3–4 (1934), pp. 161–177 *Cited on page 15.*

[17] R.P. Feynman and M. Gell-Mann. "Theory of Fermi interaction". In: *Phys. Rev.* 109 (1958), pp. 193–198. DOI: 10.1103/PhysRev.109.193 *Cited on page 15.*

[18] E.C.G. Sudarshan and R.E. Marshak. "Chirality invariance and the universal Fermi interaction". In: *Phys. Rev.* 109 (1958), pp. 1860–1860. DOI: 10.1103/PhysRev.109.1860 *Cited on page 15.*

[19] N. Cabibbo. "Unitary Symmetry and Leptonic Decays". In: *Phys. Rev. Lett.* 10 (12 June 1963), pp. 531–533. DOI: 10.1103/PhysRevLett.10.531 *Cited on page 15.*

[20] M. Kobayashi and T. Maskawa. "CP-Violation in the Renormalizable Theory of Weak Interaction". In: *Progress of Theoretical Physics* 49.2 (1973), pp. 652–657. DOI: 10.1143/PTP.49.652. eprint: http://ptp.oxfordjournals.org/content/49/2/652.full.pdf+html *Cited on page 15.*

[21] Y. Nambu. "Quasiparticles and Gauge Invariance in the Theory of Superconductivity". In: *Phys. Rev.* 117 (1960), pp. 648–663. DOI: 10.1103/PhysRev.117.648 *Cited on page 16.*

[22] Y. Nambu. "Axial Vector Current Conservation in Weak Interactions". In: *Phys. Rev. Lett.* 4 (7 Apr. 1960), pp. 380–382. DOI: 10.1103/PhysRevLett.4.380 *Cited on page 16.*

[23] J. Goldstone. "Field theories with « Superconductor » solutions". English. In: *Il Nuovo Cimento* 19.1 (1961), pp. 154–164. ISSN: 0029-6341. DOI: 10.1007/BF02812722 *Cited on page 18.*

[24] J. Goldstone, A. Salam, and S. Weinberg. "Broken Symmetries". In: *Phys. Rev.* 127 (3 Aug. 1962), pp. 965–970. DOI: 10.1103/PhysRev.127.965 *Cited on page 18.*

[25] S. Weinberg. "A Model of Leptons". In: *Phys. Rev. Lett.* 19 (21 Nov. 1967), pp. 1264–1266. DOI: 10.1103/PhysRevLett.19.1264 *Cited on page 19.*

[26] S. Schael et al. "Precision electroweak measurements on the Z resonance". In: *Phys. Rept.* 427 (2006), pp. 257–454. DOI: 10.1016/j.physrep.2005.12.006. arXiv:hep-ex/0509008 [hep-ex] *Cited on pages 20, 26.*

[27] S. Dittmaier et al. "Handbook of LHC Higgs Cross Sections: 1. Inclusive Observables". In: *CERN-2011-002* (CERN, Geneva, 2011). arXiv:1101.0593 [hep-ph] *Cited on pages 21–23, 136.*

[28] R. Tanaka. Priv. com. Apr. 2014 *Cited on pages 23, 171.*

[29] W. Hollik. "Quantum field theory and the Standard Model". In: (2010). arXiv:1012.3883 [hep-ph] *Cited on page 24.*

[30] G Abbiendi. "Search for the Standard Model Higgs Boson at LEP". In: *Phys. Lett. B* 565.hep-ex/0306033. CERN-EP-2003-011. CERN-L3-271 (Mar. 2003), 61–75. 22 p *Cited on page 25.*

[31] The CDF, D0 Collaborations, and the TEVNPHWG Working Group. *Combined CDF and Dzero Upper Limits on Standard Model Higgs Boson Production with up to 8.2 fb-1 of Data.* Tech. rep. arXiv/1103.3233. 2011 *Cited on page 25.*

[32] LEP Electroweak working group. http://lepewwg.web.cern.ch/LEPEWWG/ *Cited on page 26.*

[33] S. Schael et al. "Electroweak Measurements in Electron-Positron Collisions at W-Boson-Pair Energies at LEP". In: *Phys. Rept.* 532 (2013), pp. 119–244. DOI: 10.1016/j.physrep.2013.07.004. arXiv:1302.3415 [hep-ex] *Cited on page 26.*

[34] CDF Collaboration. "Observation of Top Quark Production in $p\bar{p}$ Collisions with the Collider Detector at Fermilab". In: *Phys. Rev. Lett.* 74 (14 Apr. 1995), pp. 2626–2631. DOI: 10.1103/PhysRevLett.74.2626 *Cited on page 26.*

[35] D0 Collaboration. "Search for High Mass Top Quark Production in $p\bar{p}$ collisions at $\sqrt{s} = 1.8$ TeV". In: *Phys. Rev. Lett.* 74 (13 Mar. 1995), pp. 2422–2426. DOI: 10.1103/PhysRevLett.74.2422 *Cited on page 26.*

[36] M. Baak et al. "The Electroweak Fit of the Standard Model after the Discovery of a New Boson at the LHC". In: *Eur. Phys. J.* C72 (2012), p. 2205. DOI: `10.1140/epjc/s10052-012-2205-9`. arXiv:`1209.2716 [hep-ph]`   *Cited on page 27.*

[37] ATLAS Public Results. *Summary plots from the ATLAS Standard Model physics group.* Twiki page. `https://atlas.web.cern.ch/Atlas/GROUPS/PHYSICS/CombinedSummaryPlots/SM/`. 2014   *Cited on page 28.*

[38] P.A.R. Ade et al. "Planck 2013 results. I. Overview of products and scientific results". In: (2013). arXiv:`1303.5062 [astro-ph.CO]`   *Cited on page 28.*

[39] S. P. Martin. "A Supersymmetry primer". In: (1997). arXiv:`hep-ph/9709356 [hep-ph]` *Cited on page 29.*

[40] P. Fayet. "Spontaneously Broken Supersymmetric Theories of Weak, Electromagnetic and Strong Interactions". In: *Phys. Lett.* B69 (1977), p. 489. DOI: `10.1016/0370-2693(77)90852-8` *Cited on page 29.*

[41] G. R. Farrar and P. Fayet. "Phenomenology of the Production, Decay, and Detection of New Hadronic States Associated with Supersymmetry". In: *Phys. Lett.* B76 (1978), pp. 575–579. DOI: `10.1016/0370-2693(78)90858-4`   *Cited on page 29.*

References for Chapter 2: Statistical framework

[42] G. Cowan. *Statistical Data Analysis.* Oxford: Clarendon (Oxford), 1998   *Cited on page 31.*

[43] W. Verkerke and D. P. Kirkby. "The RooFit toolkit for data modeling". In: (2003). arXiv:`physics/0306116`   *Cited on page 31.*

[44] R. Brun and F. Rademakers. "ROOT: An object oriented data analysis framework". In: *Nucl. Instrum. Meth.* A389 (1997), pp. 81–86. DOI: `10.1016/S0168-9002(97)00048-X` *Cited on page 31.*

[45] A. Armbruster. "Discovery of a Higgs Boson with the ATLAS Detector ". CERN-THESIS-2013-047. PhD thesis. 2013   *Cited on page 33.*

[46] *Procedure for the LHC Higgs boson search combination in summer 2011.* Tech. rep. ATL-PHYS-PUB-2011-011, CMS-NOTE-2011/005. Geneva: CERN, Aug. 2011   *Cited on page 36.*

[47] ATLAS statistics forum. *Frequentist limit recommendation.* `https://twiki.cern.ch/twiki/pub/AtlasProtected/StatisticsTools/Frequentist_Limit_Recommendation.pdf`. 2012   *Cited on page 36.*

[48] G. Cowan et al. "Asymptotic formulae for likelihood-based tests of new physics". In: *Eur. Phys. J.* C71 (2011), p. 1554. DOI: `10.1140/epjc/s10052-011-1554-0`. arXiv:`1007.1727 [physics.data-an]`   *Cited on pages 36, 37.*

[49] N Andari et al. *Exclusion limits and Systematics.* Tech. rep. ATL-COM-PHYS-2010-844. Geneva: CERN, Sept. 2010   *Cited on page 37.*

[50] A. Armbruster and K.Cranmer. *Private communication*   *Cited on page 39.*

References for Chapter 3: The Large Hadron Collider

[51] L. Evans and P. Bryant. "LHC Machine". In: *JINST* 3 (2008). Ed. by Lyndon Evans, S08001. DOI: `10.1088/1748-0221/3/08/S08001`   *Cited on page 43.*

[52] J. Haffner. "The CERN accelerator complex. Complexe des accélérateurs du CERN". In: (Oct. 2013). General Photo *Cited on page 45.*

[53] AC Team. "Diagram of an LHC dipole magnet. Schéma d'un aimant dipôle du LHC". June 1999 *Cited on page 46.*

[54] ATLAS Public Results. *LuminosityPublicResults.* Twiki page. https://twiki.cern.ch/twiki/bin/view/AtlasPublic/LuminosityPublicResults. 2014 *Cited on pages 47, 64.*

[55] W. J. Stirling. *Private communication* *Cited on page 48.*

References for Chapter 4: The ATLAS experiment

[54] ATLAS Public Results. *LuminosityPublicResults.* Twiki page. https://twiki.cern.ch/twiki/bin/view/AtlasPublic/LuminosityPublicResults. 2014 *Cited on pages 47, 64.*

[56] ATLAS collaboration. *ATLAS Detector and Physics Performance : Technical Design Report.* 1999 *Cited on page 51.*

[57] ATLAS collaboration. "The ATLAS Experiment at the CERN Large Hadron Collider". In: *Journal of Instrumentation* 3.08 (2008), S08003 *Cited on pages 53, 56–59, 77–79.*

[58] D Fournier. "Liquid argon calorimetry". In: vol 3, CERN-90-10,ECFA 90-133 page 356 (Oct. 1990) *Cited on page 60.*

[59] F. Gianotti et al. "Liquid argon calorimetry with LHC-performance specifications". In: *Nuclear Instruments and Methods in Physics Research A.* Vol. 315. LAL 9097. La Biodola, Isola D'Elba, Italie, 1992, pp. 285–293 *Cited on page 60.*

[60] ATLAS Public Results. *LArCaloPublicResults twiki page.* Twiki page. https://twiki.cern.ch/twiki/bin/view/AtlasPublic/LArCaloPublicResultsDetStatus. 2012 *Cited on page 60.*

[61] ATLAS collaboration. "Commissioning of the ATLAS Muon Spectrometer with Cosmic Rays". In: *Eur. Phys. J.* C70 (2010), pp. 875–916. DOI: 10.1140/epjc/s10052-010-1415-2. arXiv:1006.4384 [physics.ins-det] *Cited on page 62.*

[62] ATLAS collaboration. "Performance of the ATLAS Trigger System in 2010". In: *Eur. Phys. J.* C72 (2012), p. 1849. DOI: 10.1140/epjc/s10052-011-1849-1. arXiv:1110.1530 [hep-ex] *Cited on page 63.*

[63] ATLAS Public Results. *Data Quality Information for 2010 and 2011 Data.* Twiki page. https://twiki.cern.ch/twiki/bin/view/AtlasPublic/RunStatsPublicResults2010. 2014 *Cited on page 64.*

[64] S. Agostinelli et al. "Geant4—a simulation toolkit". In: *Nuclear Instruments and Methods in Physics Research Section A: Accelerators, Spectrometers, Detectors and Associated Equipment* 506.3 (2003), pp. 250 −303. ISSN: 0168-9002. DOI: http://dx.doi.org/10.1016/S0168-9002(03)01368-8 *Cited on page 64.*

[65] W Lampl et al. *Calorimeter Clustering Algorithms: Description and Performance.* Tech. rep. ATL-LARG-PUB-2008-002. ATL-COM-LARG-2008-003. Geneva: CERN, Apr. 2008 *Cited on pages 65, 67.*

[66] J.-F. Marchand. "Étude de la recherche du boson de higgs en deux photons dans l'expérience ATLAS au LHC et calibration du calorimètre a argon liquide". CERN-THESIS-2009-127, LAPP-T-2009-001. PhD thesis. 2009 *Cited on page 66.*

[67] ATLAS collaboration. *Expected photon performance in the ATLAS experiment.* Tech. rep. ATL-PHYS-PUB-2011-007. Geneva: CERN, Apr. 2011 *Cited on pages 66, 119, 124.*

[68] HSG1 Group. *Signal studies in H to gamma gamma search with 8TeV data*. Tech. rep. ATL-COM-PHYS-2012-755. Geneva: CERN, June 2012   *Cited on page 66*.

[69] G. P. Salam and G. Soyez. "A Practical Seedless Infrared-Safe Cone jet algorithm". In: *JHEP* 0705 (2007), p. 086. DOI: 10.1088/1126-6708/2007/05/086. arXiv:0704.0292 [hep-ph] *Cited on page 67*.

[70] G. P. Salam. "Towards Jetography". In: *Eur. Phys. J.* C67 (2010), pp. 637–686. DOI: 10.1140/epjc/s10052-010-1314-6. arXiv:0906.1833 [hep-ph]   *Cited on page 67*.

[71] M. Cacciari, G. P. Salam, and G. Soyez. "The Anti-k(t) jet clustering algorithm". In: *JHEP* 0804 (2008), p. 063. DOI: 10.1088/1126-6708/2008/04/063. arXiv:0802.1189 [hep-ph] *Cited on page 67*.

[72] D W Miller, A Schwartzman, and D Su. *Pile-up jet energy scale corrections using the jet-vertex fraction method*. Tech. rep. ATL-COM-PHYS-2009-180. Geneva: CERN, Apr. 2009   *Cited on page 68*.

[73] ATLAS Public Results. *JetEtmissApproved2011PileupOffsetAndJVF*. Twiki page. https://twiki.cern.ch/twiki/bin/view/AtlasPublic/JetEtmissApproved2011PileupOffsetAndJVF. 2012   *Cited on page 68*.

[74] ATLAS collaboration. "Jet energy measurement with the ATLAS detector in proton-proton collisions at $\sqrt{s} = 7$ TeV". In: *Eur. Phys. J.* C73 (2013), p. 2304. DOI: 10.1140/epjc/s10052-013-2304-2. arXiv:1112.6426 [hep-ex]   *Cited on page 68*.

[75] ATLAS collaboration. *Jet energy scale and its systematic uncertainty in proton-proton collisions at sqrt(s)=7 TeV with ATLAS 2011 data*. Tech. rep. ATLAS-CONF-2013-004. Geneva: CERN, Jan. 2013   *Cited on page 68*.

[76] ATLAS collaboration. *Measurement of the b-tag Efficiency in a Sample of Jets Containing Muons with $5 fb^{-1}$ of Data from the ATLAS Detector*. Tech. rep. ATLAS-CONF-2012-043. Geneva: CERN, Mar. 2012   *Cited on page 69*.

[77] ATLAS collaboration. *Preliminary results on the muon reconstruction efficiency, momentum resolution, and momentum scale in ATLAS 2012 pp collision data*. Tech. rep. ATLAS-CONF-2013-088. Geneva: CERN, Aug. 2013   *Cited on page 70*.

[78] ATLAS collaboration. *Performance of Missing Transverse Momentum Reconstruction in ATLAS studied in Proton-Proton Collisions recorded in 2012 at 8 TeV*. Tech. rep. ATLAS-CONF-2013-082. Geneva: CERN, Aug. 2013   *Cited on pages 71, 155*.

[79] ATLAS collaboration. *Letter of Intent for the Phase-I Upgrade of the ATLAS Experiment*. Tech. rep. CERN-LHCC-2011-012. LHCC-I-020. Geneva: CERN, Nov. 2011   *Cited on page 71*.

[80] M Capeans et al. *ATLAS Insertable B-Layer Technical Design Report*. Tech. rep. CERN-LHCC-2010-013. ATLAS-TDR-19. Geneva: CERN, Sept. 2010   *Cited on page 72*.

References for Chapter 5: Electromagnetic calorimeter: from raw data to physics

[1]   J. Beringer et al. "Review of Particle Physics (RPP)". In: *Phys. Rev.* D86 (2012), p. 010001. DOI: 10.1103/PhysRevD.86.010001   *Cited on pages 8, 13, 26, 74, 76*.

[57] ATLAS collaboration. "The ATLAS Experiment at the CERN Large Hadron Collider". In: *Journal of Instrumentation* 3.08 (2008), S08003   *Cited on pages 53, 56–59, 77–79*.

[81] ATLAS Public. *Detector Description.* ATLAS public web page. http://www.atlas.ch/calorimeter.html. 2014 *Cited on page 75.*

[82] B. Rossi. *High energy particles.* New York: Prentice-Hall, 1952 *Cited on page 75.*

[83] R. Wigmans. *Calorimetry.* Oxford, 2000 *Cited on page 75.*

[84] ATLAS collaboration. "Drift Time Measurement in the ATLAS Liquid Argon Electromagnetic Calorimeter using Cosmic Muons". In: *Eur. Phys. J. C* 70.arXiv:1002.4189. CERN-PH-EP-2010-042 (July 2010), 755–785. 30 p *Cited on page 78.*

[85] W.E. Cleland and E.G. Stern. "Signal processing considerations for liquid ionization calorimeters in a high rate environment". In: *Nuclear Instruments and Methods in Physics Research Section A: Accelerators, Spectrometers, Detectors and Associated Equipment* 338.2–3 (1994), pp. 467 –497. ISSN: 0168-9002. DOI: http://dx.doi.org/10.1016/0168-9002(94)91332-3 *Cited on page 80.*

[86] F. Niedercorn. "Recherche de particules supersymétriques dans le canal jets et énergie transverse manquante auprès du détecteur ATLAS au LHC". CERN-THESIS-2011-172, LAL-11-217. PhD thesis. 2011 *Cited on page 80.*

[87] ATLAS collaboration. "Monitoring and data quality assessment of the ATLAS liquid argon calorimeter". In: (2014). arXiv:1405.3768 [hep-ex] *Cited on pages 80, 82, 83.*

[88] Q. Buat. "Recherche de nouveaux phénomènes dans les événements diphoton avec le détecteur ATLAS". CERN-THESIS-2013-175. PhD thesis. 2013 *Cited on page 80.*

[89] ATLAS collaboration. "Characterisation and mitigation of beam-induced backgrounds observed in the ATLAS detector during the 2011 proton-proton run". In: *JINST* 8 (2013), P07004. DOI: 10.1088/1748-0221/8/07/P07004. arXiv:1303.0223 [hep-ex] *Cited on page 84.*

[90] ATLAS collaboration. "Electron performance measurements with the ATLAS detector using the 2010 LHC proton-proton collision data". In: *Eur. Phys. J.* C72 (2012), p. 1909. DOI: 10.1140/epjc/s10052-012-1909-1. arXiv:1110.3174 [hep-ex] *Cited on pages 85, 86, 93.*

[91] ATLAS collaboration. *Electron and photon energy calibration with the ATLAS detector using LHC Run 1 data.* Tech. rep. 2014. arXiv:1407.5063 [hep-ex] *Cited on pages 85–91, 149, 183.*

[92] B Lenzi and R Turra. *Monte Carlo calibration update for electrons and photons using multivariate techniques.* Tech. rep. ATL-COM-PHYS-2013-1426. Geneva: CERN, Oct. 2013 *Cited on page 85.*

[93] G. Unal. *Pedestal shifts.* LAr meeting, https://indico.cern.ch/event/301145/contribution/7/material/slides/0.pdf. 20-02-2013 *Cited on page 87.*

[94] M Aleksa et al. *Calibration stability and uniformity measurements of electrons and photons.* Tech. rep. ATL-COM-PHYS-2013-1421. Geneva: CERN, Oct. 2013 *Cited on page 87.*

[95] M Boonekamp et al. *Electromagnetic calorimeter layers energy scales determination.* Tech. rep. ATL-COM-PHYS-2013-1423. Geneva: CERN, Oct. 2013 *Cited on page 87.*

[96] G. Unal. *Impact of LArOFC on E1/E2.* e/gamma meeting, https://indico.cern.ch/event/310431/contribution/3/material/slides/0.pdf. 2-04-2013 *Cited on page 87.*

[97] I. Koletsou. "Search for the Higgs boson in the diphoton channel at the LHC with the ATLAS detector". CERN-THESIS-2008-047, LAL-08-38. PhD thesis. 2008 *Cited on page 92.*

[98] M. Escalier, L. Fayard, and J.-F. Marchand. *Reconstruction of the z vertex and direction of the photon.* Tech. rep. ATL-COM-PHYS-2009-614. Geneva: CERN, Nov. 2009 *Cited on page 92.*

[99] ATLAS collaboration. *Observation of an excess of events in the search for the Standard Model Higgs boson in the gamma-gamma channel with the ATLAS detector.* Tech. rep. ATLAS-CONF-2012-091. Geneva: CERN, July 2012 *Cited on pages 93, 113, 129.*

[100] J.-F. Marchand and E. Scifo. *Oscillation of calorimeter pointing z position as a function of pseudo-rapidity in the end-cap.* Tech. rep. ATL-COM-CAL-2012-003. Geneva: CERN, Apr. 2012 *Cited on pages 93–101, 103, 104.*

[101] G. Unal. *Private communication* *Cited on page 98.*

[102] N. Lorenzo. *Private communication* *Cited on page 98.*

References for Chapter 6: $H \to \gamma\gamma$ analysis

[27] S. Dittmaier et al. "Handbook of LHC Higgs Cross Sections: 1. Inclusive Observables". In: *CERN-2011-002* (CERN, Geneva, 2011). arXiv:1101.0593 [hep-ph] *Cited on pages 21–23, 136.*

[67] ATLAS collaboration. *Expected photon performance in the ATLAS experiment.* Tech. rep. ATL-PHYS-PUB-2011-007. Geneva: CERN, Apr. 2011 *Cited on pages 66, 119, 124.*

[91] ATLAS collaboration. *Electron and photon energy calibration with the ATLAS detector using LHC Run 1 data.* Tech. rep. 2014. arXiv:1407.5063 [hep-ex] *Cited on pages 85–91, 149, 183.*

[99] ATLAS collaboration. *Observation of an excess of events in the search for the Standard Model Higgs boson in the gamma-gamma channel with the ATLAS detector.* Tech. rep. ATLAS-CONF-2012-091. Geneva: CERN, July 2012 *Cited on pages 93, 113, 129.*

[103] C. J. Seez et al. *Photon decay modes of the intermediate mass Higgs.* ECFA Higgs Working Group. 1990 *Cited on pages 109, 114.*

[104] L. Fayard and G Unal. *Search for Higgs decay into photons with EAGLE. Add. 1 Addendum on the Higgs search with photons. Add. 2 (final?) update on Higgs decay to photons.* Tech. rep. ATL-PHYS-92-001. ATL-GE-PN-1. Geneva: CERN, Dec. 1992 *Cited on page 109.*

[105] The HSG1 Group. *Coupling measurement with the $H \to \gamma\gamma$ channel : Supporting document.* Tech. rep. ATL-COM-PHYS-2014-025. Geneva: CERN, Jan. 2014 *Cited on pages 110, 128, 137, 141, 152, 158, 161–163, 171, 178–180, 188, 190–197, 225, 228.*

[106] ATLAS collaboration. *Search for the Standard Model Higgs boson in the diphoton decay channel with 4.9 fb-1 of ATLAS data at sqrt(s)=7TeV.* Tech. rep. ATLAS-CONF-2011-161. Geneva: CERN, Dec. 2011 *Cited on page 112.*

[107] ATLAS collaboration. "Search for the Standard Model Higgs boson in the diphoton decay channel with 4.9 fb^{-1} of pp collisions at $\sqrt{s} = 7$ TeV with ATLAS". In: *Phys. Rev. Lett.* 108 (2012), p. 111803. DOI: 10.1103/PhysRevLett.108.111803. arXiv:1202.1414 [hep-ex] *Cited on page 112.*

[108] The HSG1 Group. *Improved analysis of the Search for the Higgs Boson Decaying to Two Photons with 4.9 fb-1 of 7TeV data.* Tech. rep. ATL-COM-PHYS-2012-502. Geneva: CERN, May 2012 *Cited on pages 115, 117, 118.*

[109] J. C. Collins and D. E. Soper. "Angular distribution of dileptons in high-energy hadron collisions". In: *Phys. Rev. D* 16 (7 Oct. 1977), pp. 2219–2225. DOI: 10.1103/PhysRevD.16.2219 *Cited on pages 118, 147.*

[110] B. Lenzi. *Impact of tentative p_T cuts on spin and main $H \to \gamma\gamma$ analyses.* HSG1 meeting, https://indico.cern.ch/event/220494/contribution/1/material/slides/1.pdf. 6-12-2012 *Cited on page 118.*

[111] *egamma Public Plots twiki.* https://atlas.web.cern.ch/Atlas/GROUPS/PHYSICS/EGAMMA/PublicPlots/20100721/display-photons/display-photons.pdf *Cited on page 120.*

[112] ATLAS Public Results. *Photon Shower Shapes Data/MC Comparisons from $Z + \gamma$ events.* Web page. https://atlas.web.cern.ch/Atlas/GROUPS/PHYSICS/EGAMMA/PublicPlots/20130522/ATL-COM-PHYS-2013-600/index.html. 2014 *Cited on pages 122, 123.*

[113] ATLAS collaboration. *Measurements of the photon identification efficiency with the ATLAS detector using 4.9 fb^{-1} of pp collision data collected in 2011.* Tech. rep. ATLAS-CONF-2012-123. Geneva: CERN, Aug. 2012 *Cited on page 124.*

[114] *egamma Public Plots twiki.* https://atlas.web.cern.ch/Atlas/GROUPS/PHYSICS/EGAMMA/PublicPlots/20140611/ATL-COM-PHYS-2014-542/ATL-COM-PHYS-2014-542.pdf. 2014 *Cited on pages 124, 125.*

[115] L. Devroye. *Non-Uniform Random Variate Generation(originally published with.* New York: Springer-Verlag, 1986 *Cited on page 124.*

[116] J. Saxon. *Status of Neural Net Photon ID.* HSG1 meeting, https://indico.cern.ch/event/153698/session/1/contribution/26/material/2/0.pdf. 24-11-2011 *Cited on page 124.*

[117] S Laplace and J.-B. de Vivie. *Calorimeter isolation and pile-up.* Tech. rep. ATL-COM-PHYS-2012-467. Geneva: CERN, May 2012 *Cited on page 126.*

[118] M. Cacciari and G. P. Salam. "Pileup subtraction using jet areas". In: *Phys. Lett.* B659 (2008), pp. 119–126. DOI: 10.1016/j.physletb.2007.09.077. arXiv:0707.1378 [hep-ph] *Cited on page 126.*

[119] M. Cacciari, G. P. Salam, and S. Sapeta. "On the characterisation of the underlying event". In: *JHEP* 1004 (2010), p. 065. DOI: 10.1007/JHEP04(2010)065. arXiv:0912.4926 [hep-ph] *Cited on page 126.*

[120] G. Unal. *Average pileup offset vs BCID.* LAr software technical meeting. 5-12-2011 *Cited on page 126.*

[121] ATLAS Public Results. *Calorimeter isolation with TopoClusters versus pileup.* Twiki page. https://atlas.web.cern.ch/Atlas/GROUPS/PHYSICS/EGAMMA/PublicPlots/20120404/TopoIsolation/ATL-COM-PHYS-2012-362/. 2014 *Cited on page 126.*

[122] R. Lafaye. *Private communication* *Cited on page 127.*

[123] ATLAS collaboration. *Observation and study of the Higgs boson candidate in the two photon decay channel with the ATLAS detector at the LHC.* Tech. rep. ATLAS-CONF-2012-168. Geneva: CERN, Dec. 2012 *Cited on pages 126, 129, 132, 136, 147.*

[124] D. Delgove. *An update on the selection of the diphoton vertex.* HSG1 meeting, https://indico.cern.ch/event/166261/contribution/1/material/slides/0.pdf. 23-8-2012 *Cited on page 128.*

[125] ATLAS collaboration. *Measurement of Higgs boson production in the diphoton decay channel in pp collisions at center-of-mass energies of 7 and 8 TeV with the ATLAS detector.* Tech. rep. 2014. arXiv:1408.7084 [hep-ex] *Cited on pages 129, 154, 157–159, 169, 171, 173, 174, 181, 188, 189, 191, 197–199.*

[126] ATLAS collaboration. "Observation of a new particle in the search for the Standard Model Higgs boson with the ATLAS detector at the LHC". In: *Phys. Lett.* B716 (2012), pp. 1–29. DOI: 10.1016/j.physletb.2012.08.020. arXiv:1207.7214 [hep-ex] *Cited on pages 129, 141–143.*

[127] ATLAS collaboration. *Measurements of the properties of the Higgs-like boson in the two photon decay channel with the ATLAS detector using 25* fb^{-1} *of proton-proton collision data.* Tech. rep. ATLAS-CONF-2013-012. Geneva: CERN, Mar. 2013   *Cited on pages 129, 137, 144, 145, 190, 197.*

[128] L. J. Dixon and M. S. Siu. "Resonance continuum interference in the diphoton Higgs signal at the LHC". In: *Phys. Rev. Lett.* 90 (2003), p. 252001. DOI: 10.1103/PhysRevLett.90.252001. arXiv:hep-ph/0302233 [hep-ph]   *Cited on page 131.*

[129] L. J. Dixon and Y. Li. "Bounding the Higgs Boson Width Through Interferometry". In: *Phys. Rev. Lett.* 111 (2013), p. 111802. DOI: 10.1103/PhysRevLett.111.111802. arXiv:1305.3854 [hep-ph]   *Cited on page 131.*

[130] H. Abreu. "Measurement of the inclusive prompt photon cross section and preparation of the search of the Higgs boson decaying into two photons with the ATLAS detector at the LHC ". CERN-THESIS-2011-157. PhD thesis. 2011   *Cited on page 131.*

[131] The HSG1 Group. *Background Studies for the Search of Higgs Boson Decaying to Two Photons with 4.9 fb^{-1} of 7TeV data with the ATLAS Experiment.* Tech. rep. ATL-COM-PHYS-2012-515. Geneva: CERN, May 2012   *Cited on page 132.*

[132] The HSG1 Group. *Update of the observation of an excess of events in the search for the Standard Model Higgs boson in the $\gamma\gamma$ channel and measurement of its properties with the ATLAS detector.* Tech. rep. ATL-COM-PHYS-2012-1488. Geneva: CERN, Oct. 2012   *Cited on pages 132, 134.*

[133] M. Escalier. *Private communication*   *Cited on page 134.*

[134] S. Heinemeyer et al. *Handbook of LHC Higgs Cross Sections: 3. Higgs Properties: Report of the LHC Higgs Cross Section Working Group.* Tech. rep. arXiv:1307.1347. CERN-2013-004. Geneva, 2013   *Cited on pages 136, 152, 176, 178, 180, 209, 211.*

[135] S. Dittmaier et al. *Handbook of LHC Higgs Cross Sections: 2. Differential Distributions.* Tech. rep. arXiv:1201.3084. CERN-2012-002. Geneva, 2012   *Cited on pages 136, 211, 219.*

[136] T. Sjöstrand, S. Mrenna, P. Skands. "PYTHIA 6.4 physics and manual". In: *JHEP* 05 (2006), p. 026 *Cited on pages 136, 208.*

[137] T. Sjöstrand, S. Mrenna, and P. Z. Skands. "A Brief Introduction to PYTHIA 8.1". In: *Comput.Phys.Commun.* 178 (2008), pp. 852–867. DOI: 10.1016/j.cpc.2008.01.036. arXiv:0710.3820 [hep-ph]   *Cited on pages 136, 208.*

[138] S. Alioli et al. "NLO Higgs boson production via gluon fusion matched with shower in POWHEG". In: *JHEP* 04 (2009), p. 002   *Cited on page 136.*

[139] E. Bagnaschi et al. "Higgs production via gluon fusion in the POWHEG approach in the SM and in the MSSM". In: *JHEP* 1202 (2012), p. 088. DOI: 10.1007/JHEP02(2012)088. arXiv:1111.2854 [hep-ph]   *Cited on page 136.*

[140] A. Djouadi, M. Spira, and P.M. Zerwas. "Production of Higgs bosons in proton colliders: QCD corrections". In: *Phys. Lett.* B264 (1991), pp. 440–446. DOI: 10.1016/0370-2693(91)90375-Z *Cited on page 136.*

[141] S. Dawson. "Radiative corrections to Higgs boson production". In: *Nucl. Phys.* B359 (1991), pp. 283–300. DOI: 10.1016/0550-3213(91)90061-2   *Cited on page 136.*

[142] M. Spira et al. "Higgs boson production at the LHC". In: *Nucl. Phys.* B453 (1995), pp. 17–82. DOI: 10.1016/0550-3213(95)00379-7. arXiv:hep-ph/9504378 [hep-ph]   *Cited on page 136.*

[143] R. V. Harlander and W. B. Kilgore. "Next-to-next-to-leading order Higgs production at hadron colliders". In: *Phys. Rev. Lett.* 88 (2002), p. 201801. DOI: 10.1103/PhysRevLett.88.201801. arXiv:hep-ph/0201206 [hep-ph]   *Cited on page 136.*

[144] C. Anastasiou and K. Melnikov. "Higgs boson production at hadron colliders in NNLO QCD". In: *Nucl. Phys.* B646 (2002), pp. 220–256. DOI: 10.1016/S0550-3213(02)00837-4. arXiv:hep-ph/0207004 [hep-ph] *Cited on page 136.*

[145] V. Ravindran, J. Smith, and W. L. van Neerven. "NNLO corrections to the total cross-section for Higgs boson production in hadron hadron collisions". In: *Nucl. Phys.* B665 (2003), pp. 325–366. DOI: 10.1016/S0550-3213(03)00457-7. arXiv:hep-ph/0302135 [hep-ph] *Cited on page 136.*

[146] D. de Florian et al. "Transverse-momentum resummation: Higgs boson production at the Tevatron and the LHC". In: *JHEP* 1111 (2011), p. 064. DOI: 10.1007/JHEP11(2011)064. arXiv:1109.2109 [hep-ph] *Cited on pages 136, 208.*

[147] D. de Florian and M. Grazzini. "Higgs production at the LHC: updated cross sections at $\sqrt{s} = 8$ TeV". In: *Phys. Lett.* B718 (2012), pp. 117–120. DOI: 10.1016/j.physletb.2012.10.019. arXiv:1206.4133 [hep-ph] *Cited on pages 136, 209.*

[148] U. Aglietti et al. "Two loop light fermion contribution to Higgs production and decays". In: *Phys. Lett.* B595 (2004), pp. 432–441. DOI: 10.1016/j.physletb.2004.06.063. arXiv:hep-ph/0404071 [hep-ph] *Cited on page 136.*

[149] G. Degrassi and F. Maltoni. "Two-loop electroweak corrections to Higgs production at hadron colliders". In: *Phys. Lett.* B600 (2004), pp. 255–260. DOI: 10.1016/j.physletb.2004.09.008. arXiv:hep-ph/0407249 [hep-ph] *Cited on page 136.*

[150] U. Aglietti et al. "Two-loop electroweak corrections to Higgs production in proton-proton collisions". In: (2006). arXiv:hep-ph/0610033 [hep-ph] *Cited on page 136.*

[151] S. Actis et al. "NLO electroweak corrections to Higgs boson production at hadron colliders". In: *Phys. Lett.* B670 (2008), pp. 12–17. DOI: 10.1016/j.physletb.2008.10.018. arXiv:0809.1301 [hep-ph] *Cited on page 136.*

[152] P. Nason and C. Oleari. "NLO Higgs boson production via vector-boson fusion matched with shower in POWHEG". In: *JHEP* 02 (2010), p. 037 *Cited on page 136.*

[153] P. Bolzoni et al. "Higgs production via vector-boson fusion at NNLO in QCD". In: *Phys. Rev. Lett.* 105 (2010), p. 011801. DOI: 10.1103/PhysRevLett.105.011801. arXiv:1003.4451 [hep-ph] *Cited on page 136.*

[154] M. Ciccolini, A. Denner, and S. Dittmaier. "Strong and electroweak corrections to the production of Higgs + 2jets via weak interactions at the LHC". In: *Phys. Rev. Lett.* 99 (2007), p. 161803. DOI: 10.1103/PhysRevLett.99.161803. arXiv:0707.0381 [hep-ph] *Cited on page 136.*

[155] A. Denner et al. "Electroweak corrections to Higgs-strahlung off W/Z bosons at the Tevatron and the LHC with HAWK". In: *JHEP* 1203 (2012), p. 075. DOI: 10.1007/JHEP03(2012)075. arXiv:1112.5142 [hep-ph] *Cited on page 136.*

[156] O. Brein, A. Djouadi, and R. Harlander. "NNLO QCD corrections to the Higgs-strahlung processes at hadron colliders". In: *Phys. Lett.* B579 (2004), pp. 149–156. DOI: 10.1016/j.physletb.2003.10.112. arXiv:hep-ph/0307206 [hep-ph] *Cited on page 136.*

[157] O. Brein, R. V. Harlander, and T. J.E. Zirke. "VH@NNLO - Higgs Strahlung at hadron colliders". In: *Comput. Phys. Commun.* 184 (2013), pp. 998–1003. DOI: 10.1016/j.cpc.2012.11.002. arXiv:1210.5347 [hep-ph] *Cited on page 136.*

[158] T. Han and S. Willenbrock. "QCD correction to the $pp \to WH$ and ZH total cross-sections". In: *Phys. Lett.* B273 (1991), pp. 167–172. DOI: 10.1016/0370-2693(91)90572-8 *Cited on page 136.*

[159] L. Altenkamp et al. "Gluon-induced Higgs-strahlung at next-to-leading order QCD". In: *JHEP* 1302 (2013), p. 078. DOI: 10.1007/JHEP02(2013)078. arXiv:1211.5015 [hep-ph] *Cited on page 136.*

[160] O. Brein et al. "Top-Quark Mediated Effects in Hadronic Higgs-Strahlung". In: *Eur. Phys. J.* C72 (2012), p. 1868. DOI: 10.1140/epjc/s10052-012-1868-6. arXiv:1111.0761 [hep-ph] *Cited on page 136.*

[161] W. Beenakker et al. "Higgs radiation off top quarks at the Tevatron and the LHC". In: *Phys. Rev. Lett.* 87 (2001), p. 201805. DOI: 10.1103/PhysRevLett.87.201805. arXiv:hep-ph/0107081 [hep-ph] *Cited on page 136.*

[162] W. Beenakker et al. "NLO QCD corrections to $t\bar{t}H$ production in hadron collisions". In: *Nucl. Phys.* B653 (2003), pp. 151–203. DOI: 10.1016/S0550-3213(03)00044-0. arXiv:hep-ph/0211352 [hep-ph] *Cited on page 136.*

[163] S. Dawson et al. "Next-to-leading order QCD corrections to $pp \rightarrow t\bar{t}h$ at the CERN Large Hadron Collider". In: *Phys. Rev.* D67 (2003), p. 071503. DOI: 10.1103/PhysRevD.67.071503. arXiv:hep-ph/0211438 [hep-ph] *Cited on page 136.*

[164] S. Dawson et al. "Associated Higgs production with top quarks at the large hadron collider: NLO QCD corrections". In: *Phys. Rev.* D68 (2003), p. 034022. DOI: 10.1103/PhysRevD.68.034022. arXiv:hep-ph/0305087 [hep-ph] *Cited on page 136.*

[165] G. Bevilacqua et al. "NLO QCD calculations with HELAC-NLO". In: *Nucl. Phys. Proc. Suppl.* 205-206 (2010), pp. 211–217. DOI: 10.1016/j.nuclphysbps.2010.08.045. arXiv:1007.4918 [hep-ph] *Cited on page 136.*

[166] G. Bevilacqua et al. "HELAC-NLO". In: *Comput. Phys. Commun.* 184 (2013), pp. 986–997. DOI: 10.1016/j.cpc.2012.10.033. arXiv:1110.1499 [hep-ph] *Cited on page 136.*

[167] A. Firan and R. Stroynowski. "Internal conversions in Higgs decays to two photons". In: *Phys. Rev.* D76 (2007), p. 057301. DOI: 10.1103/PhysRevD.76.057301. arXiv:0704.3987 [hep-ph] *Cited on page 137.*

[168] D. A. Dicus and W. W. Repko. "Dalitz Decay $H \rightarrow f\bar{f}\gamma$ as a Background for $H \rightarrow \gamma\gamma$". In: *Phys. Rev.* D89 (2014), p. 093013. DOI: 10.1103/PhysRevD.89.093013. arXiv:1402.5317 [hep-ph] *Cited on page 137.*

[169] C. Rangel-Smith. "Photon performance studies with Radiative Z decays, and the search for the Higgs boson in the $H \rightarrow \gamma\gamma$ and $H \rightarrow Z\gamma$ channels with the ATLAS detector of the LHC". CERN-THESIS-2014-003. PhD thesis. 2014 *Cited on page 137.*

[170] ATLAS Public Results. *Some Displays of Candidate Events Selected in Higgs Search Analyses.* Twiki page. https://twiki.cern.ch/twiki/bin/view/AtlasPublic/EventDisplaysFromHiggsSearches. 2012 *Cited on page 144.*

[171] S. Chatrchyan et al. "Observation of a new boson at a mass of 125 GeV with the CMS experiment at the LHC". In: *Phys. Lett.* B716 (2012), pp. 30–61. DOI: 10.1016/j.physletb.2012.08.021. arXiv:1207.7235 [hep-ex] *Cited on pages 144, 145.*

[172] ATLAS collaboration. "Measurements of Higgs boson production and couplings in diboson final states with the ATLAS detector at the LHC". In: *Phys. Lett.* B726 (2013), pp. 88–119. DOI: 10.1016/j.physletb.2013.08.010. arXiv:1307.1427 [hep-ex] *Cited on pages 145–147.*

[173] ATLAS collaboration. *Updated coupling measurements of the Higgs boson with the ATLAS detector using up to 25 fb^{-1} of proton-proton collision data.* Tech. rep. ATLAS-CONF-2014-009. Geneva: CERN, Mar. 2014 *Cited on page 145.*

[174] G Unal and D Froidevaux. *Higgs mass measurements and uncertainties in 2011 and 2012 data.* Tech. rep. ATL-COM-PHYS-2012-1774. Geneva: CERN, Dec. 2012 *Cited on page 146.*

[175] ATLAS collaboration. *Combined measurements of the mass and signal strength of the Higgs-like boson with the ATLAS detector using up to 25 fb^{-1} of proton-proton collision data.* Tech. rep. ATLAS-CONF-2013-014. Geneva: CERN, Mar. 2013 *Cited on page 146.*

[176] ATLAS collaboration. *Combined coupling measurements of the Higgs-like boson with the ATLAS detector using up to 25 fb^{-1} of proton-proton collision data.* Tech. rep. ATLAS-CONF-2013-034. Geneva: CERN, Mar. 2013   *Cited on page 147.*

[177] L. D. Landau. "On the angular momentum of a two-photon system". In: *Dokl.Akad.Nauk Ser.Fiz.* 60 (1948), pp. 207–209   *Cited on page 146.*

[178] C. N. Yang. "Selection Rules for the Dematerialization of a Particle into Two Photons". In: *Phys. Rev.* 77 (2 Jan. 1950), pp. 242–245. DOI: 10.1103/PhysRev.77.242   *Cited on page 146.*

[179] The HSG1 Group. *Measurement of spin, mass and couplings of the new particle at 126GeV in the diphoton channel.* Tech. rep. ATL-COM-PHYS-2012-1489. Geneva: CERN, Oct. 2012   *Cited on page 148.*

[180] ATLAS collaboration. "Evidence for the spin-0 nature of the Higgs boson using ATLAS data". In: *Phys. Lett. B* 726.1–3 (2013), pp. 120 –144. ISSN: 0370-2693. DOI: http://dx.doi.org/10.1016/j.physletb.2013.08.026   *Cited on pages 147–149.*

[181] ATLAS collaboration. *Study of the spin of the Higgs-like boson in the two photon decay channel using 20.7 fb-1 of pp collisions collected at $\sqrt{s}$ = 8 TeV with the ATLAS detector.* Tech. rep. ATLAS-CONF-2013-029. Geneva: CERN, Mar. 2013   *Cited on page 147.*

[182] ATLAS collaboration. *Study of the spin of the new boson with up to 25 fb^{-1} of ATLAS data.* Tech. rep. ATLAS-CONF-2013-040. Geneva: CERN, Apr. 2013   *Cited on page 147.*

[183] ATLAS collaboration. "Measurement of the Higgs boson mass from the $H \to \gamma\gamma$ and $H \to ZZ^* \to 4\ell$ channels with the ATLAS detector using 25 fb^{-1} of pp collision data". In: *Phys. Rev.* D90 (2014), p. 052004. DOI: 10.1103/PhysRevD.90.052004. arXiv:1406.3827 [hep-ex] *Cited on page 150.*

References for Chapter 7: Couplings measurement

[28] R. Tanaka. Priv. com. Apr. 2014   *Cited on pages 23, 171.*

[78] ATLAS collaboration. *Performance of Missing Transverse Momentum Reconstruction in ATLAS studied in Proton-Proton Collisions recorded in 2012 at 8 TeV.* Tech. rep. ATLAS-CONF-2013-082. Geneva: CERN, Aug. 2013   *Cited on pages 71, 155.*

[91] ATLAS collaboration. *Electron and photon energy calibration with the ATLAS detector using LHC Run 1 data.* Tech. rep. 2014. arXiv:1407.5063 [hep-ex]   *Cited on pages 85–91, 149, 183.*

[105] The HSG1 Group. *Coupling measurement with the $H \to \gamma\gamma$ channel : Supporting document.* Tech. rep. ATL-COM-PHYS-2014-025. Geneva: CERN, Jan. 2014   *Cited on pages 110, 128, 137, 141, 152, 158, 161–163, 171, 178–180, 188, 190–197, 225, 228.*

[125] ATLAS collaboration. *Measurement of Higgs boson production in the diphoton decay channel in pp collisions at center-of-mass energies of 7 and 8 TeV with the ATLAS detector.* Tech. rep. 2014. arXiv:1408.7084 [hep-ex]   *Cited on pages 129, 154, 157–159, 169, 171, 173, 174, 181, 188, 189, 191, 197–199.*

[127] ATLAS collaboration. *Measurements of the properties of the Higgs-like boson in the two photon decay channel with the ATLAS detector using 25 fb^{-1} of proton-proton collision data.* Tech. rep. ATLAS-CONF-2013-012. Geneva: CERN, Mar. 2013   *Cited on pages 129, 137, 144, 145, 190, 197.*

[134] S. Heinemeyer et al. *Handbook of LHC Higgs Cross Sections: 3. Higgs Properties: Report of the LHC Higgs Cross Section Working Group.* Tech. rep. arXiv:1307.1347. CERN-2013-004. Geneva, 2013   *Cited on pages 136, 152, 176, 178, 180, 209, 211.*

[184] ATLAS collaboration. *Improved electron reconstruction in ATLAS using the Gaussian Sum Filter-based model for bremsstrahlung*. Tech. rep. ATLAS-CONF-2012-047. Geneva: CERN, May 2012 *Cited on page 153*.

[185] ATLAS collaboration. *Electron efficiency measurements with the ATLAS detector using the 2012 LHC proton-proton collision data*. Tech. rep. ATLAS-CONF-2014-032. Geneva: CERN, June 2014 *Cited on page 154*.

[186] ATLAS collaboration. "Electron reconstruction and identification efficiency measurements with the ATLAS detector using the 2011 LHC proton-proton collision data". In: (2014). arXiv:1404.2240 [hep-ex] *Cited on page 154*.

[187] ATLAS collaboration. *Performance of Missing Transverse Momentum Reconstruction in ATLAS with 2011 Proton-Proton Collisions at $sqrts$ = 7 TeV*. Tech. rep. ATLAS-CONF-2012-101. Geneva: CERN, July 2012 *Cited on page 155*.

[188] HSG1 Group. *Supporting note for coupling measurements in diphoton channel, for Moriond 2013*. Tech. rep. ATL-COM-PHYS-2013-094. Geneva: CERN, Jan. 2013 *Cited on pages 155, 156, 162*.

[189] G. Cowan and E. Gross. *Discussion and guidelines on significance*. https://twiki.cern.ch/twiki/pub/AtlasProtected/ATLASStatisticsFAQ/SigRec_v1.pdf. 2009 *Cited on page 156*.

[190] D. L. Rainwater, R. Szalapski, and D. Zeppenfeld. "Probing color singlet exchange in Z + two jet events at the CERN LHC". In: *Phys. Rev.* D54 (1996), pp. 6680–6689. DOI: 10.1103/PhysRevD.54.6680. arXiv:hep-ph/9605444 [hep-ph] *Cited on page 157*.

[191] The HSG1 Group. *Supporting note for associated Higgs production in di-photon channel*. Tech. rep. ATL-COM-PHYS-2012-1490. Geneva: CERN, Oct. 2012 *Cited on page 160*.

[192] T. Gleisberg et al. "SHERPA 1. alpha: A Proof of concept version". In: *JHEP* 0402 (2004), p. 056. DOI: 10.1088/1126-6708/2004/02/056. arXiv:hep-ph/0311263 [hep-ph] *Cited on page 165*.

[193] H. Wang. *Private communication* *Cited on page 166*.

[194] The HSG1 Group. *Search for ttH production in the $H \rightarrow \gamma\gamma$ channel at $\sqrt{s} = 8$ TeV with the ATLAS detector*. Tech. rep. ATLAS-CONF-2013-080. Geneva: CERN, July 2013 *Cited on page 169*.

[195] The HSG1/8 Groups. *Search for $t\bar{t}H$ production in the diphoton channel with 20.3 fb^{-1} of data at 8 TeV and 4.5 fb^{-1} data at 7 TeV*. Tech. rep. ATL-COM-PHYS-2014-011. Geneva: CERN, Jan. 2014 *Cited on pages 170, 183*.

[196] ATLAS collaboration. *Search for $H \rightarrow \gamma\gamma$ produced in association with top quarks and constraints on the top quark-Higgs boson Yukawa coupling using data taken at 7 TeV and 8 TeV with the ATLAS detector*. Tech. rep. ATLAS-CONF-2014-043. Geneva: CERN, July 2014 *Cited on page 170*.

[197] ATLAS collaboration. "Search for $H \rightarrow \gamma\gamma$ produced in association with top quarks and constraints on the Yukawa coupling between the top quark and the Higgs boson using data taken at 7 TeV and 8 TeV with the ATLAS detector". In: (2014). arXiv:1409.3122 [hep-ex] *Cited on page 170*.

[198] J. M. Campbell et al. "Higgs-Boson production in association with a single bottom quark". In: *Phys. Rev.* D67 (2003), p. 095002. DOI: 10.1103/PhysRevD.67.095002. arXiv:hep-ph/0204093 [hep-ph] *Cited on page 171*.

[199] S. Dawson et al. "Exclusive Higgs boson production with bottom quarks at hadron colliders". In: *Phys. Rev.* D69 (2004), p. 074027. DOI: 10.1103/PhysRevD.69.074027. arXiv:hep-ph/0311067 [hep-ph] *Cited on page 171*.

[200] R. Harlander, M. Kramer, and M. Schumacher. "Bottom-quark associated Higgs-boson production: reconciling the four- and five-flavour scheme approach". In: (2011). arXiv:1112.3478 [hep-ph] *Cited on page 171*.

[201] F. Maltoni et al. "Associated production of Higgs and single top at hadron colliders". In: *Phys. Rev.* D64 (2001), p. 094023. DOI: 10.1103/PhysRevD.64.094023. arXiv:hep-ph/0106293 [hep-ph] *Cited on page 172.*

[202] J. Saxon. *Private communication* *Cited on page 173.*

[203] J. Baglio and A. Djouadi. "Predictions for Higgs production at the Tevatron and the associated uncertainties". In: *JHEP* 1010 (2010), p. 064. DOI: 10.1007/JHEP10(2010)064. arXiv:1003.4266 [hep-ph] *Cited on page 176.*

[204] J. Baglio and A. Djouadi. "Higgs production at the lHC". In: *JHEP* 1103 (2011), p. 055. DOI: 10.1007/JHEP03(2011)055. arXiv:1012.0530 [hep-ph] *Cited on page 176.*

[205] S. Moch and A. Vogt. "Higher-order soft corrections to lepton pair and Higgs boson production". In: *Phys. Lett.* B631 (2005), pp. 48–57. DOI: 10.1016/j.physletb.2005.09.061. arXiv:hep-ph/0508265 [hep-ph] *Cited on page 176.*

[206] R. D. Ball et al. "Higgs production in gluon fusion beyond NNLO". In: *Nucl. Phys.* B874 (2013), pp. 746–772. DOI: 10.1016/j.nuclphysb.2013.06.012. arXiv:1303.3590 [hep-ph] *Cited on page 176.*

[207] M. Bonvini et al. "Updated Higgs cross section at approximate N^{3}LO". In: (2014). arXiv:1404.3204 [hep-ph] *Cited on page 176.*

[208] C. Anastasiou et al. "Higgs boson gluon-fusion production at threshold in N3LO QCD". In: (2014). arXiv:1403.4616 [hep-ph] *Cited on page 176.*

[209] ATLAS collaboration. "Improved luminosity determination in pp collisions at $\sqrt{s}$ = 7 TeV using the ATLAS detector at the LHC". In: *Eur. Phys. J.* C73 (2013), p. 2518. DOI: 10.1140/epjc/s10052-013-2518-3. arXiv:1302.4393 [hep-ex] *Cited on page 177.*

[210] J-B de Vivie and D Fournier. *Search for Flavour Changing Neutral Currents in $t \to qH$, with $H \to \gamma\gamma$, and limit on the tcH coupling.* Tech. rep. ATL-COM-PHYS-2013-1455. Geneva: CERN, Oct. 2013 *Cited on page 177.*

[211] J. M. Campbell, R. K. Ellis, and G. Zanderighi. "Next-to-Leading order Higgs + 2 jet production via gluon fusion". In: *JHEP* 0610 (2006), p. 028. DOI: 10.1088/1126-6708/2006/10/028. arXiv:hep-ph/0608194 [hep-ph] *Cited on pages 179, 225.*

[212] G. Unal. *Electron and Photon energy resolutions and their uncertainties for run-1 calibration.* Tech. rep. ATL-COM-PHYS-2013-1651. Geneva: CERN, Dec. 2013 *Cited on page 183.*

[213] HSG1 Group. *Mass measurement in the $H \to \gamma\gamma$ channel: Supporting documentation for the Mass Paper.* Tech. rep. ATL-COM-PHYS-2014-018. Geneva: CERN, Jan. 2014 *Cited on page 190.*

[214] M. H. Quenouille. "Approximate Tests of Correlation in Time-Series". In: *Journal of the Royal Statistical Society. Series B (Methodological)* 11.1 (1949), pp. 68–84 *Cited on page 194.*

[215] J. W. Tukey. "Bias and confidence in not quite large samples". In: *Annals of Math. Statist.* 29 (1958), p. 614 *Cited on page 194.*

[216] CMS collaboration. "Observation of the diphoton decay of the Higgs boson and measurement of its properties". In: (2014). arXiv:1407.0558 [hep-ex] *Cited on page 200.*

References for Chapter 8: Monte Carlo tools

[134] S. Heinemeyer et al. *Handbook of LHC Higgs Cross Sections: 3. Higgs Properties: Report of the LHC Higgs Cross Section Working Group.* Tech. rep. arXiv:1307.1347. CERN-2013-004. Geneva, 2013 *Cited on pages 136, 152, 176, 178, 180, 209, 211.*

[135] S. Dittmaier et al. *Handbook of LHC Higgs Cross Sections: 2. Differential Distributions.* Tech. rep. arXiv:1201.3084. CERN-2012-002. Geneva, 2012 *Cited on pages 136, 211, 219.*

[136] T. Sjöstrand, S. Mrenna, P. Skands. "PYTHIA 6.4 physics and manual". In: *JHEP* 05 (2006), p. 026 *Cited on pages 136, 208*.

[137] T. Sjöstrand, S. Mrenna, and P. Z. Skands. "A Brief Introduction to PYTHIA 8.1". In: *Comput.Phys.Commun.* 178 (2008), pp. 852–867. DOI: `10.1016/j.cpc.2008.01.036`. arXiv:`0710.3820 [hep-ph]` *Cited on pages 136, 208*.

[146] D. de Florian et al. "Transverse-momentum resummation: Higgs boson production at the Tevatron and the LHC". In: *JHEP* 1111 (2011), p. 064. DOI: `10.1007/JHEP11(2011)064`. arXiv:`1109.2109 [hep-ph]` *Cited on pages 136, 208*.

[147] D. de Florian and M. Grazzini. "Higgs production at the LHC: updated cross sections at $\sqrt{s} = 8$ TeV". In: *Phys. Lett.* B718 (2012), pp. 117–120. DOI: `10.1016/j.physletb.2012.10.019`. arXiv:`1206.4133 [hep-ph]` *Cited on pages 136, 209*.

[217] J. C. Collins and D. E. Soper. "The Theorems of Perturbative QCD". In: *Annual Review of Nuclear and Particle Science* 37.1 (1987), pp. 383–409. DOI: `10.1146/annurev.ns.37.120187.002123`. eprint: `http://dx.doi.org/10.1146/annurev.ns.37.120187.002123` *Cited on page 203*.

[218] G. Altarelli and G. Parisi. "Asymptotic Freedom in Parton Language". In: *Nucl. Phys.* B126 (1977), p. 298. DOI: `10.1016/0550-3213(77)90384-4` *Cited on page 205*.

[219] Y. L. Dokshitzer. "Calculation of the Structure Functions for Deep Inelastic Scattering and e+ e- Annihilation by Perturbation Theory in Quantum Chromodynamics." In: *Sov. Phys. JETP* 46 (1977), pp. 641–653 *Cited on page 205*.

[220] V. N. Gribov and L.N. Lipatov. "Deep inelastic e p scattering in perturbation theory". In: *Sov. J. Nucl. Phys.* 15 (1972), pp. 438–450 *Cited on page 205*.

[221] A. D. Martin et al. "Parton distributions for the LHC". In: *Eur. Phys. J.* C63 (2009), pp. 189–285. DOI: `10.1140/epjc/s10052-009-1072-5`. arXiv:`0901.0002 [hep-ph]` *Cited on pages 205, 206*.

[222] H.-L. Lai et al. "New parton distributions for collider physics". In: *Phys. Rev.* D82 (2010), p. 074024. DOI: `10.1103/PhysRevD.82.074024`. arXiv:`1007.2241 [hep-ph]` *Cited on page 205*.

[223] J. Gao et al. "The CT10 NNLO Global Analysis of QCD". In: (2013). arXiv:`1302.6246 [hep-ph]` *Cited on page 205*.

[224] C. Anastasiou, K. Melnikov, and F. Petriello. "The Gluon-fusion uncertainty in Higgs coupling extractions". In: *Phys. Rev.* D72 (2005), p. 097302. DOI: `10.1103/PhysRevD.72.097302`. arXiv:`hep-ph/0509014 [hep-ph]` *Cited on page 207*.

[225] E. Laenen. *Resummation.* Theory Meeting, Nikhef, `http://www.nikhef.nl/pub/theory/center-talks/ericlaenen_14-9-07.pdf`. 14-09-2007 *Cited on page 207*.

[226] S. Frixione and B. R. Webber. "Matching NLO QCD computations and parton shower simulations". In: *JHEP* 0206 (2002), p. 029. DOI: `10.1088/1126-6708/2002/06/029`. arXiv:`hep-ph/0204244 [hep-ph]` *Cited on pages 208, 209*.

[227] G. Corcella et al. "HERWIG 6: An Event generator for hadron emission reactions with interfering gluons (including supersymmetric processes)". In: *JHEP* 0101 (2001), p. 010. DOI: `10.1088/1126-6708/2001/01/010`. arXiv:`hep-ph/0011363 [hep-ph]` *Cited on page 208*.

[228] G. Bozzi et al. "The q(T) spectrum of the Higgs boson at the LHC in QCD perturbation theory". In: *Phys. Lett.* B564 (2003), pp. 65–72. DOI: `10.1016/S0370-2693(03)00656-7`. arXiv:`hep-ph/0302104 [hep-ph]` *Cited on page 209*.

[229] D. de Florian et al. "Higgs boson production at the LHC: transverse momentum resummation effects in the $H \to 2\gamma$, $H \to WW \to l\nu l\nu$ and $H \to ZZ \to 4l$ decay modes". In: *JHEP* 1206 (2012), p. 132. DOI: `10.1007/JHEP06(2012)132`. arXiv:`1203.6321 [hep-ph]` *Cited on page 209*.

[230] D. de Florian and M. Grazzini. "Higgs production through gluon fusion: Updated cross sections at the Tevatron and the LHC". In: *Phys. Lett.* B674 (2009), pp. 291–294. DOI: `10.1016/j.physletb.2009.03.033`. arXiv:`0901.2427 [hep-ph]` *Cited on page 209.*

[231] P. Nason. "A New method for combining NLO QCD with shower Monte Carlo algorithms". In: *JHEP* 0411 (2004), p. 040. DOI: `10.1088/1126-6708/2004/11/040`. arXiv:`hep-ph/0409146 [hep-ph]` *Cited on pages 209, 210.*

[232] S. Alioli et al. "A general framework for implementing NLO calculations in shower Monte Carlo programs: the POWHEG BOX". In: *JHEP* 1006 (2010), p. 043. DOI: `10.1007/JHEP06(2010)043`. arXiv:`1002.2581 [hep-ph]` *Cited on page 209.*

[233] S. Frixione, P. Nason, and C. Oleari. "Matching NLO QCD computations with Parton Shower simulations: the POWHEG method". In: *JHEP* 0711 (2007), p. 070. DOI: `10.1088/1126-6708/2007/11/070`. arXiv:`0709.2092 [hep-ph]` *Cited on page 209.*

[234] V. V. Sudakov. "Vertex parts at very high-energies in quantum electrodynamics". In: *Sov. Phys. JETP* 3 (1956), pp. 65–71 *Cited on page 210.*

[235] T. Sjöstrand. "Monte Carlo Tools". In: (2009), pp. 309–339. arXiv:`0911.5286 [hep-ph]` *Cited on page 210.*

[236] A. Buckley et al. "General-purpose event generators for LHC physics". In: *Phys. Rept.* 504 (2011), pp. 145–233. DOI: `10.1016/j.physrep.2011.03.005`. arXiv:`1101.2599 [hep-ph]` *Cited on page 210.*

[237] S. Alioli. *Shower Monte Carlo at the next-to-leading order: the POWHEG method.* Granada, `http://www-theory.lbl.gov/~alioli/talks/Granada.pdf`. 19-02-2009 *Cited on page 210.*

[238] M. Grazzini and H. Sargsyan. "Heavy-quark mass effects in Higgs boson production at the LHC". In: *JHEP* 1309 (2013), p. 129. DOI: `10.1007/JHEP09(2013)129`. arXiv:`1306.4581 [hep-ph]` *Cited on pages 211, 216.*

[239] E. Bagnaschi et al. "Higgs production via gluon fusion in the POWHEG approach in the SM and in the MSSM". In: *JHEP* 1202 (2012), p. 088. DOI: `10.1007/JHEP02(2012)088`. arXiv:`1111.2854 [hep-ph]` *Cited on page 211.*

[240] A. Vicini. Priv. com. July 2013 *Cited on page 212.*

References for Chapter 9: Higgs p_T in the $\gamma\gamma$ channel

[105] The HSG1 Group. *Coupling measurement with the $H \to \gamma\gamma$ channel : Supporting document.* Tech. rep. ATL-COM-PHYS-2014-025. Geneva: CERN, Jan. 2014 *Cited on pages 110, 128, 137, 141, 152, 158, 161–163, 171, 178–180, 188, 190–197, 225, 228.*

[135] S. Dittmaier et al. *Handbook of LHC Higgs Cross Sections: 2. Differential Distributions.* Tech. rep. arXiv:1201.3084. CERN-2012-002. Geneva, 2012 *Cited on pages 136, 211, 219.*

[211] J. M. Campbell, R. K. Ellis, and G. Zanderighi. "Next-to-Leading order Higgs + 2 jet production via gluon fusion". In: *JHEP* 0610 (2006), p. 028. DOI: `10.1088/1126-6708/2006/10/028`. arXiv:`hep-ph/0608194 [hep-ph]` *Cited on pages 179, 225.*

[238] M. Grazzini and H. Sargsyan. "Heavy-quark mass effects in Higgs boson production at the LHC". In: *JHEP* 1309 (2013), p. 129. DOI: `10.1007/JHEP09(2013)129`. arXiv:`1306.4581 [hep-ph]` *Cited on pages 211, 216.*

[241] ATLAS collaboration. "Search for Higgs boson decays to a photon and a Z boson in pp collisions at $\sqrt{s}$=7 and 8 TeV with the ATLAS detector". In: *Phys. Lett.* B732 (2014), pp. 8–27. DOI: `10.1016/j.physletb.2014.03.015`. arXiv:`1402.3051 [hep-ex]` *Cited on page 220.*

[242] ATLAS collaboration. "Search for the Standard Model Higgs boson decay to $\mu^+\mu^-$ with the ATLAS detector". In: (2014). arXiv:1406.7663 [hep-ex]   *Cited on page 220.*

[243] G. Unal. *Impact of systematics on category fractions*. HSG1 EPS 2011 sharepoint. 1-07-2011 *Cited on page 223.*

[244] D. Gillberg. Priv. com. Apr. 2014   *Cited on pages 225, 226.*

[245] A. Banfi, P.-F. Monni, and G. Zanderighi. "Quark masses in Higgs production with a jet veto". In: *JHEP* 1401 (2014), p. 097. DOI: 10.1007/JHEP01(2014)097. arXiv:1308.4634 [hep-ph] *Cited on page 225.*

[246] A. Banfi, G. P. Salam, and G. Zanderighi. "NLL+NNLO predictions for jet-veto efficiencies in Higgs-boson and Drell-Yan production". In: *JHEP* 1206 (2012), p. 159. DOI: 10.1007/JHEP06(2012)159. arXiv:1203.5773 [hep-ph]   *Cited on page 225.*

[247] A. Banfi et al. "Higgs and Z-boson production with a jet veto". In: *Phys. Rev. Lett.* 109 (2012), p. 202001. DOI: 10.1103/PhysRevLett.109.202001. arXiv:1206.4998 [hep-ph] *Cited on page 225.*

[248] ATLAS collaboration. *Differential cross sections of the Higgs boson measured in the diphoton decay channel using 8 TeV pp collisions*. Tech. rep. ATLAS-CONF-2013-072. Geneva: CERN, July 2013   *Cited on pages 228, 229.*

[249] ATLAS collaboration. *Measurement of fiducial and differential cross sections of the Higgs boson in the diphoton decay channel using centre-of-mass energy of 8 TeV*. Tech. rep. ATLAS-HIGG-2013-10-002. Geneva: CERN, July 2014   *Cited on page 228.*

References for Chapter 10: Future of the Higgs era

[250] ATLAS collaboration. *Projections for measurements of Higgs boson cross sections, branching ratios and coupling parameters with the ATLAS detector at a HL-LHC*. Tech. rep. ATL-PHYS-PUB-2013-014. Geneva: CERN, Oct. 2013   *Cited on pages 233, 234.*

[251] S. Dawson et al. "Working Group Report: Higgs Boson". In: (2013). arXiv:1310.8361 [hep-ex] *Cited on page 233.*

[252] F.. Gianotti. *Opportunities and prospects for future high-E colliders*. LHCP 2014, https://indico.cern.ch/event/279518/session/29/contribution/50/material/slides/1.pdf. 6-06-2014 *Cited on page 233.*

[253] M. Carena et al. "Light Stau Phenomenology and the Higgs $\gamma\gamma$ Rate". In: *JHEP* 1207 (2012), p. 175. DOI: 10.1007/JHEP07(2012)175. arXiv:1205.5842 [hep-ph] *Cited on page 233.*

A

INVARIANT MASS DISTRIBUTIONS PER CATEGORY

The following figures display the invariant mass spectra for each of the 12 categories described in Chapter 7 for both the 2011 (left) and 2012 (right) datasets.
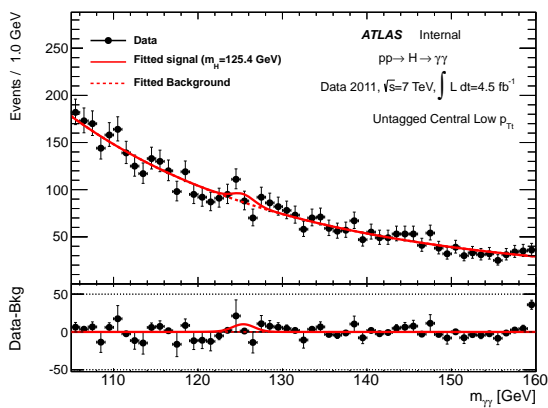
(a) Central low p_{Tt} 2011
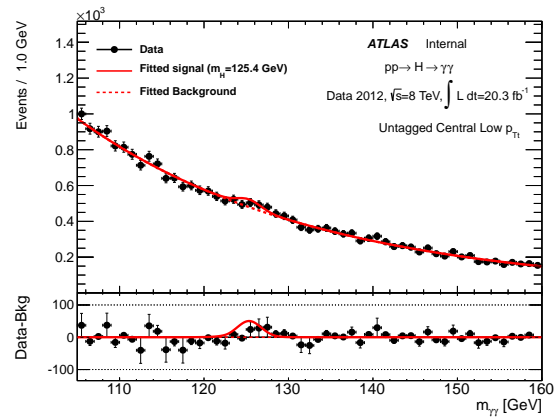
(b) Central low p_{Tt} 2012
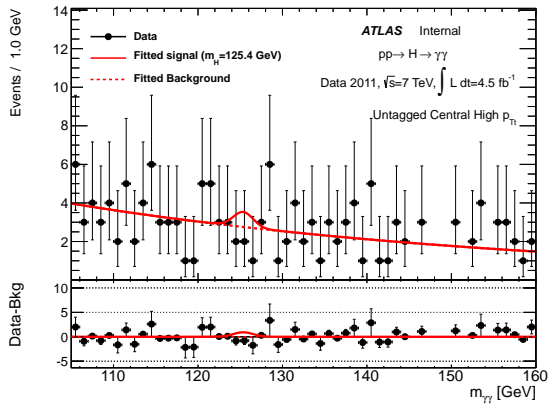
(c) Central high p_{Tt} 2011
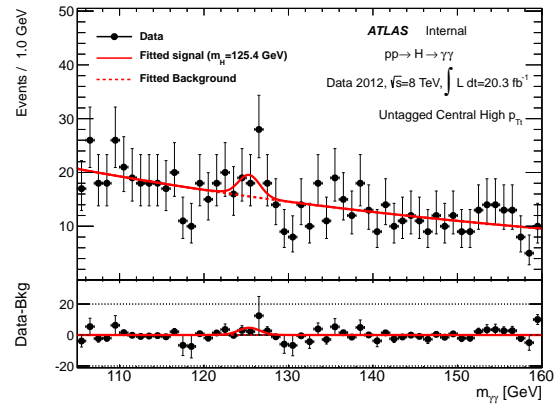
(d) Central high p_{Tt} 2012

Figure A.1: *Invariant mass spectra in the untagged central categories for the 2011 and 2012 datasets.*
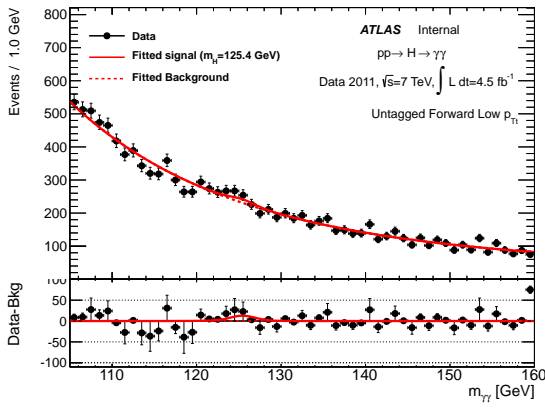
(a) Forward low p_{Tt} 2011
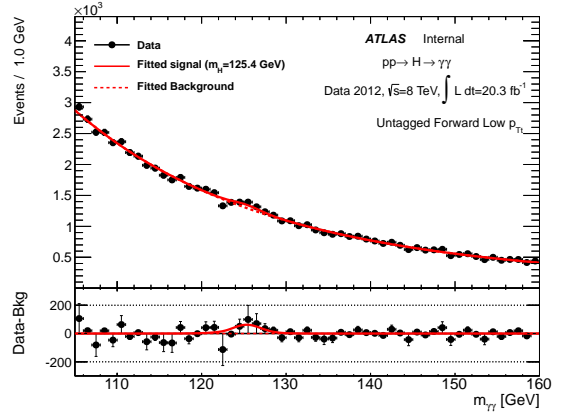
(b) Forward low p_{Tt} 2012
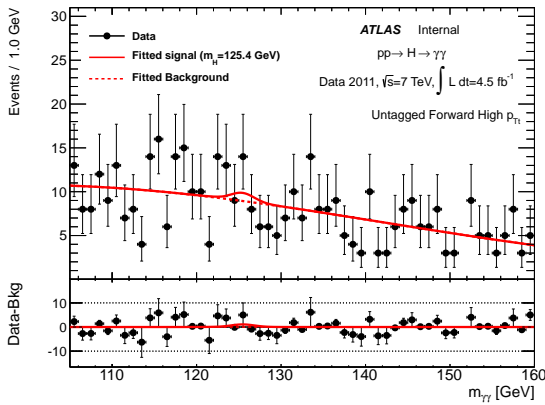
(c) Forward high p_{Tt} 2011
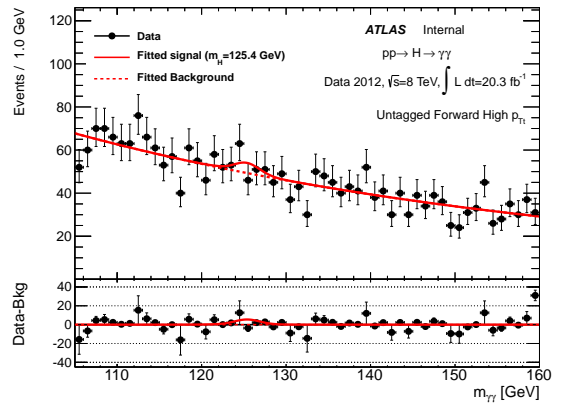
(d) Forward high p_{Tt} 2012

Figure A.2: *Invariant mass spectra in the untagged forward categories for the 2011 and 2012 datasets.*
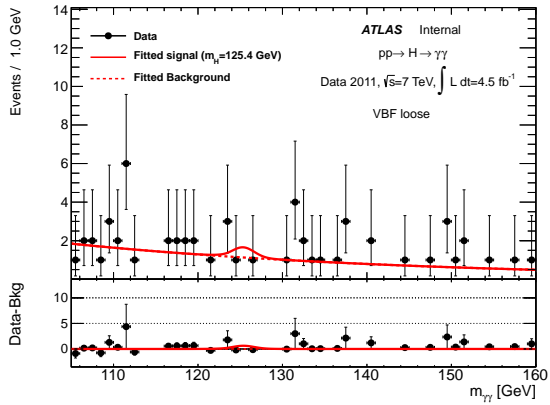
(a) VBF loose 2011
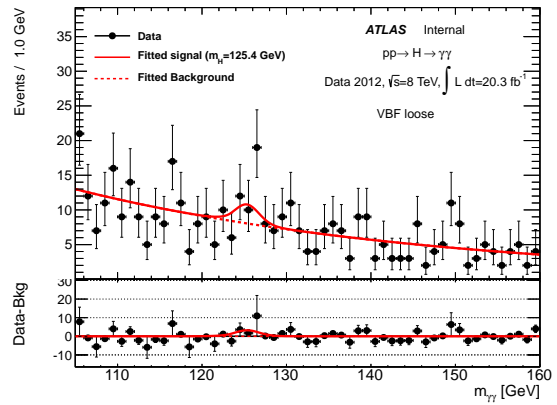
(b) VBF loose 2012
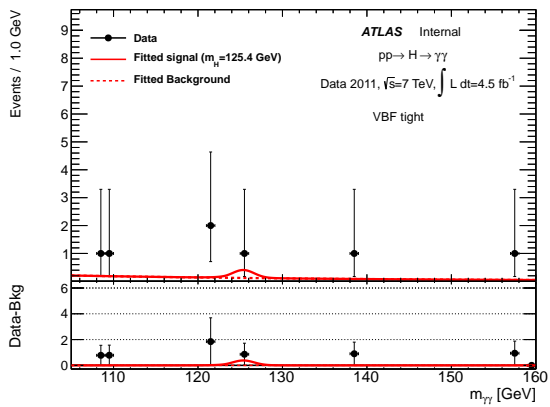
(c) VBF tight 2011
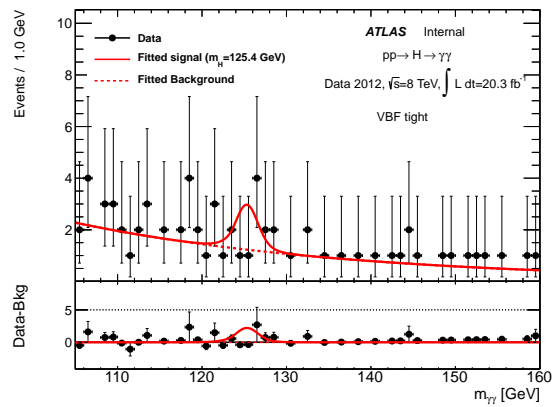
(d) VBF tight 2012

Figure A.3: *Invariant mass spectra in the VBF categories for the 2011 and 2012 datasets.*
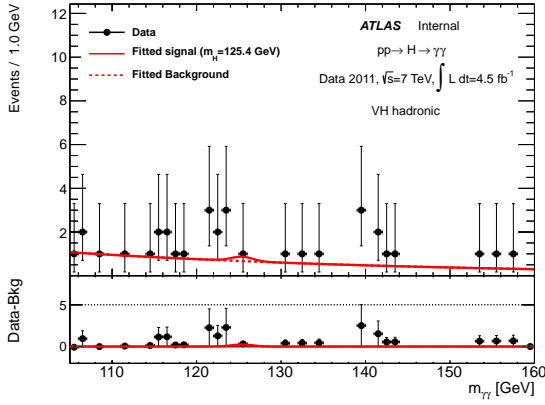
(a) VH hadronic 2011
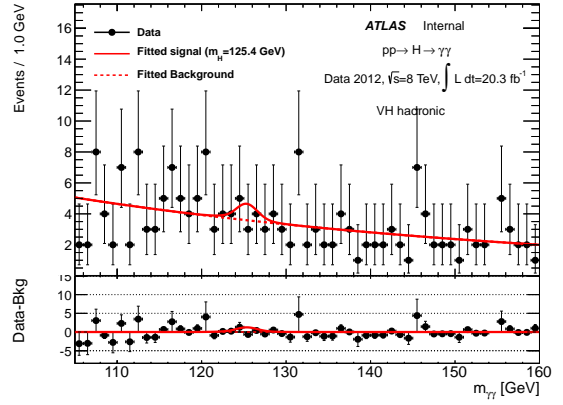
(b) VH hadronic 2012
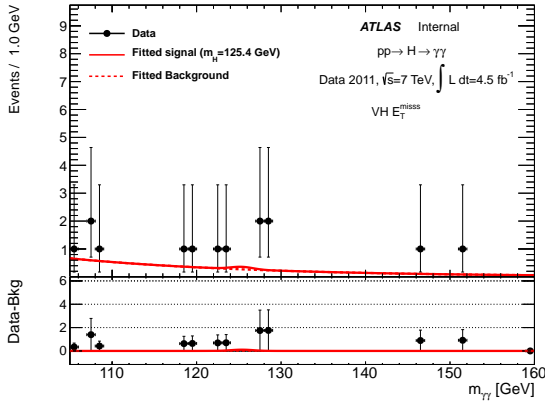
(c) VH E_T^{miss} 2011
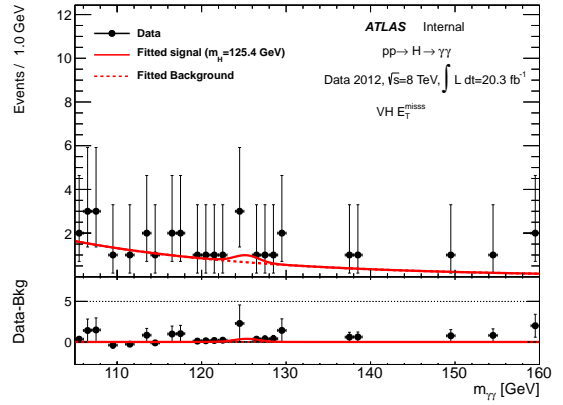
(d) VH E_T^{miss} 2012
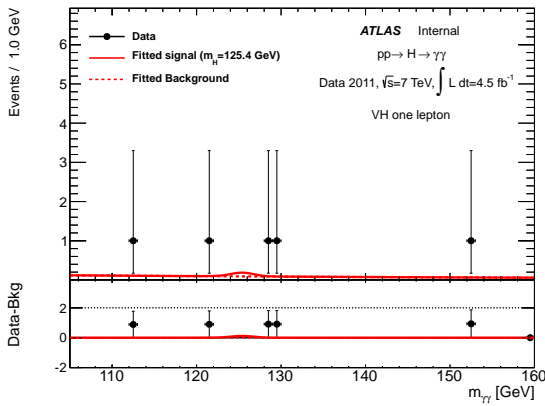
(e) VH one lepton 2011
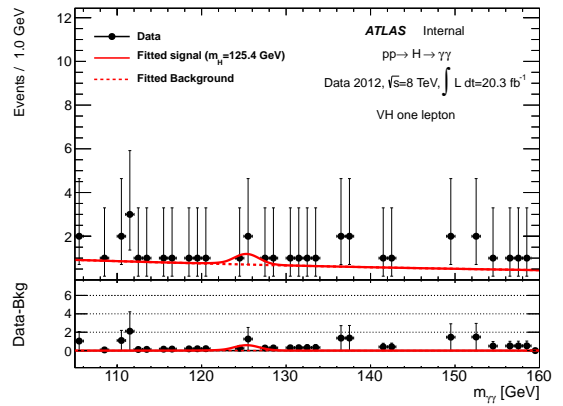
(f) VH one lepton 2012

Figure A.4: *Invariant mass spectra in the VH hadronic, E_T^{miss} and one lepton categories for the 2011 and 2012 datasets.*
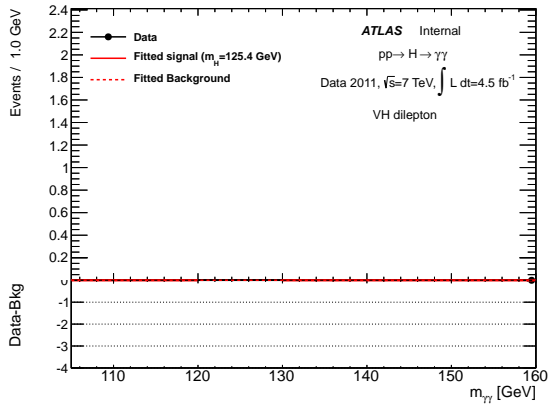
(a) VH dilepton 2011
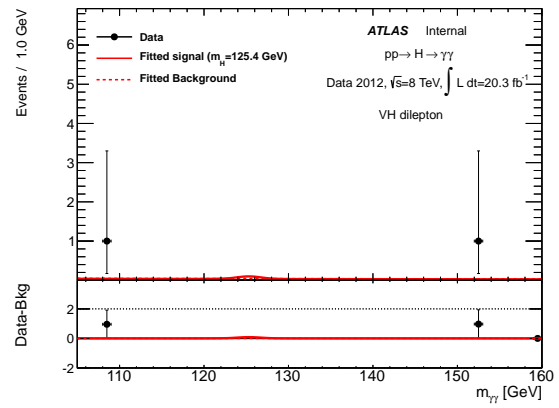
(b) VH dilepton 2012
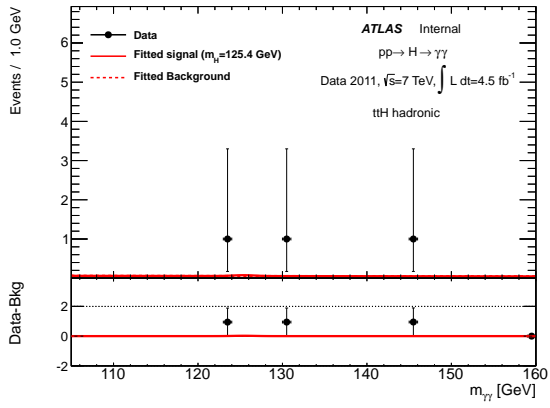
(c) ttH hadronic 2011
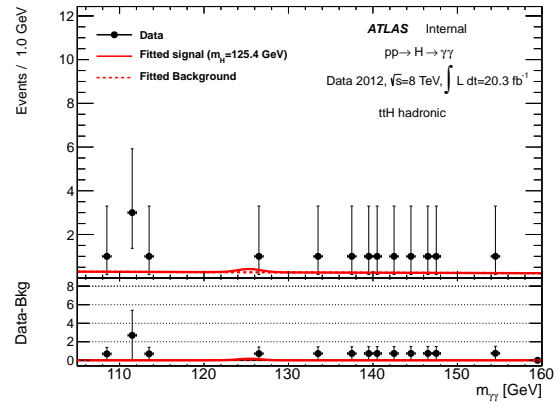
(d) ttH hadronic 2012
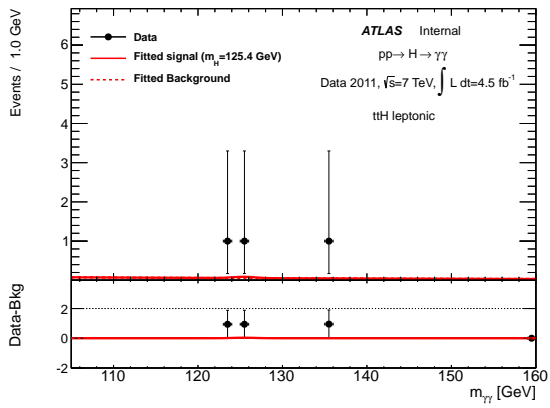
(e) ttH leptonic 2011
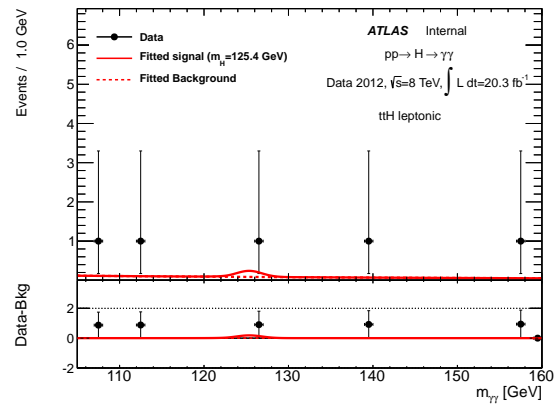
(f) ttH leptonic 2012

Figure A.5: *Invariant mass spectra in the V H dilepton and ttH categories for the 2011 and 2012 datasets.*

REMERCIEMENTS